UNIVERSITY OF CAPE TOWN
IYUNIVESITHI YASEKAPA • UNIVERSITEIT VAN KAAPSTAD

Development and testing of experimental equipment to measure pore pressure and dynamic pressure at points outside a pipe leak

Prepared by:
Nicholas David Bailey

For:
Prof. J.E. van Zyl

In part requirement of:
Master of Science in Engineering

Submission date: 21/05/2015

Institution: University of Cape Town

Faculty: Engineering and the Built Environment

Department: Civil Engineering

Plagiarism declaration

1. I know that plagiarism is wrong. Plagiarism is to use another‟s work and to pretend that it is one‟s own.
2. I have used the Harvard Convention for citation and referencing. Each significant contribution to and quotation in this report that forms the work or works of other people has been acknowledged.
3. This report is my own work.
4. I have not allowed and will not allow anyone to copy my work with the intention of passing it as his or her own work.

Student no: BLYNIC005

Name: NICHOLAS BAILEY

Date: 20/05/2015

Signature: Signed by candidate

Abstract

Leaks in water distribution mains are a major issue throughout the world. The amount of water lost through these leaks is unacceptable for a resource which is becoming ever scarcer. Little is known about the fundamentals which exist outside leaking water distribution mains. These fundamentals are the interaction between the leaking water and the soil surrounding the distribution main. This interaction is known as the leak - soil interaction. Research has found that a phenomenon called internal fluidisation typically occurs in the soils outside of leaks in distribution mains. Internal fluidisation is a complex interaction between the leak and the surrounding soil, whereby the soil losses its intermolecular bonding and becomes displaced by the water jet generated by the leak. It is believed that this complex phenomenon causes large energy losses. Subsequently, many water leaks are not able to propagate to the ground surface where they will be visible. This leads to many such leaks being undetected below the ground surface.

The objective of this study was to develop an experimental setup which simulated the internal fluidisation phenomenon. The setup consisted primarily of an orifice, simulating a leak in a distribution pipe; surrounded by ballotini (glass beads), as the soil medium surrounding the pipe; and the measurement instruments, which were Pitot tubes. When using the experimental setup, pore pressures and dynamic pressures around the leak and therefore within the ballotini bed were measured using two Pitot tubes. The accuracy and repeatability of these measurements were also of importance and were investigated.

The accuracy of the measurements were dependant on the precision of the Pitot tubes in taking measurements. They were found to have an error of up to 4.1 %, although the experiment to test for the accuracy was not fool proof. The repeatability of the measurements was found to have a 3.8 % average difference between the previous and repeated measurements. The measuring of the pore pressures and dynamic pressures resulted in the following findings, which were the most important in the study:

There were large vertical velocities found in the fluidised zone, where outside of this zone they were significantly smaller. The largest pore pressure was found to occur near the top of the fluidised zone. The pore pressures in the bed from a certain distance away from the orifice had a linear distribution, illustrating that Darcy water flow was present. High energy existed in the fluidised zone where it was greatest nearest the orifice and decreased to the top of the fluidised zone. In the ballotini bed outside of the fluidised zone the energy was found to be considerably smaller and decreased further away from the orifice.

Acknowlegements

I would like to take this opportunity to thank the following persons who have guided and helped me throughout this research project:

My Supervisor, Prof J.E. van Zyl for his continual support and for always being available to offer advice;

Civil Engineering Department‟s Technician, Charles Nicholas, for building the experimental setup and for having the patience to do fabrication work on the setup;

University of Cape Town‟s Glass Blower, Andre De Jager, for his kind help in making the nose pieces for the Pitot tubes and supplying the fabricated glass sight tube;

Civil Engineering Department‟s Laboratory staff, led by Noor Hassen, for their ongoing help during the experimentation in the laboratory;

My family for their constant encouragement.

Contents page

List of Figures

List of Tables

List of symbols

A = Izbash‟s coefficient (-)

A_o = Orifice area (m^2)

A_p = Area of particle in contact with flow (m^2)

A_s = Soil flow area (m^2)

a = Forchheimer‟s fluid properties coefficient (-)

B = Izbash‟s coefficient (-)

b = Forchheimer‟s media properties coefficient (-)

C_D = Drag coefficient (-)

C_d = Orifice discharge coefficient (-)

C_L = Lift coefficient (-)

c = General leakage coefficient (-)

c_H = Hazen‟s hydraulic conductivity coefficient (-)

c_p = Viscosity correction ratio (-)

D = Particle diameter (m)

D_{10} = 10 % fine grain diameter (m)

d = Pitot tube outer diameter (m)

d_0 = Jet nozzle diameter (m)

F' = Hydrodynamic force (N)

F_D = Drag force (N)

F_G = Force due to gravity (N)

F_L = Lift force (N)

g = Gravitational acceleration (m/s^2)

g' = Effective gravitational acceleration (m/s^2)

H = Energy (m)

h = Pressure head (m)

h_o = Pressure head at orifice (m)

h_s = Saturated soil head (m)

i = Hydraulic gradient (-)

K = Pitot tube calibration factor (-)

k = Hydraulic conductivity (m^2)

L = Length of flow path (m)

M = Sphere mass (kg)

N = Watanabe‟s coefficient (-)

N_1 = Leakage exponent (-)

n = Porosity (%)

OS = Orifice – Saturated soil number (-)

P = Pressure (kN/m^2)

P_{stag} = Stagnation pressure (kN/m^2)

P_∞ = Upstream pressure (kN/m^2)

Q = Flow rate (m^3/s)

Re = Reynolds number (-)

r = Sphere radius (m)

u = Pore pressure (kN/m^2)

V = Velocity (m/s)

z = Height difference to datum (m)

α = Non-dimensional velocity gradient (-)

Δy = Displacement correction (m)

μ = Dynamic viscosity (N.s/m^2)

v = Kinematic viscosity (m^2/s)

ρ_f = Fluid density (kg/m^3)

ρ_p = Particle density (kg/m^3)

σ = Stress (kN/m^2)

σ^I = Effective stress (kN/m^2)

Φ_s = Particle shape factor (-)

ω = Angular velocity (m/s)

Chapter 1

1 Introduction

1.1 Problem statement

Leaks in buried water distribution mains are a major problem faced by many authorities around the world. The World Bank estimated that as much as 25-30 % of water in a network is lost as non-revenue water, costing $14 billion per year (Freyberg, 2012). New leaks form all the time and need to be detected as soon as possible in order to reduce water leakage. Leakage rate is directly related to the internal pressure in a water main, where a lower pressure will result in a lower leakage rate (Lambert, 2001). Pressure management by altering the internal pressure is an important tool used in reducing the leakage rate. Therefore a clear and accurate understanding of the leak-soil interaction due to a leak from a water main will improve pressure management and therefore improve leakage reduction.

Often leaks become visible on the ground surface. In this case, signs on the surface include surface wetting, piping water flow or a water jet. Leaks that visually show up in this manner are an important leak detection method. It is evident however, that not all leaks are visible on the surface (van Zyl, *et al.*, 2012). This may be due to factors such as leaks being directed downwards, high permeability of soils and water entering other adjacent networks such as stormwater and sewerage networks.

It is thought that water jets directed vertically upwards (Alsaydalani, 2010), or even horizontally (Zoueshitiagh & Merlin, 2007; Ma, 2011) will likely be evident on the ground surface depending on factors such as the leak flow rate and soil type. However a study by van Zyl, *et al.* (2012), found that this may not always hold true. Van Zyl *et al.* found that this is because large amounts of energy head loss occur due to a process called internal fluidisation. Due to internal fluidisation many leaks may not appear on the ground surface.

The meaning of internal fluidisation, applicable to this research, is the process whereby a soil medium becomes completely saturated and loses its intermolecular bonds (van Zyl, *et al.*, 2013). Typically internal fluidisation is caused by a high water velocity jet which creates excess pore water pressure. The excess pore pressure together with shearing forces dislodges the soil by overcoming the intermolecular bonds and friction, and the soil medium experiences fluid properties. The soil medium therefore becomes more mobile and in a sense becomes completely controlled by the fluid.

Internal fluidisation is a complex phenomenon involving geotechnical engineering concerning the soil properties, pore pressures, pore water flow and soil shearing; and hydraulic engineering concerning the complex interaction between soils and fluid flow, and the flow through orifices. This is all covered in the literature together with the design principles of the laboratory experiment used to replicate the internal fluidisation process.

The difficulty in experimenting with internal fluidisation is that it occurs within a confined medium, being the soils which surround buried water distribution mains. This reduces the number of measurement techniques which can be used to investigate the leak – soil interaction. For example the visual and ultrasound measurement techniques are limited in this application. Therefore an intrusive measurement technique which enters into the soil medium surrounding the leak has to be used as the measurement instrument, which was done in this study.

The leak – soil interaction resulting from internal fluidisation is important to understand. This is so that it can be predicted when leaks directed vertically upward in water mains will appear above the ground surface. A better understanding of when such leaks might occur will reduce the number of undetected leaks. Construction factors may even be altered in an attempt to make leaks appear on the ground surface more easily. This could reduce the number of undetected leaks as well as non-revenue water losses.

1.2 Aims and objectives

The goal of this study was to develop an experimental setup and procedure to accurately measure pore pressures and dynamic pressures in the influence zone of a water jet directed vertically upward in an idealised soil medium. The procedure needed to be repeatable, so that the setup can be replicated in the future and will be able to record similar measurements. The pore and dynamic pressure measurements were taken on two axes, because internal fluidisation is considered to be two-dimensional. The study had the following objectives:

- Identifying and developing an appropriate measurement technique by which the pore pressures and dynamic pressures can be recorded;
- Designing of an experimental setup which enabled this measurement technique to be used;
- Constructing and improving the experimental setup;
- Testing and verifying the measuring equipment;
- Measuring the pore and dynamic pressures in the medium surrounding the leak at a fixed flow rate;
- Analysing the pore and dynamic pressures to achieve a better understanding of the internal fluidisation.

1.3 Scope

Only a water jet directed vertically upwards was tested, and the flow rate was kept constant at 2 l/min. An orifice with a diameter of 3 mm was used to replicate the leak in a water distribution pipe. Glass ballotini represented the soil which surrounds buried water distribution pipes. Glass ballotini was the only medium used in the experiments.

The reason for the selection of the aspects detailed here in the scope is that in a previous study by van Zyl, *et al*. (2013), similar aspects were experimented with.

1.4 Layout of dissertation

Chapter 1: Introduction
This chapter included the background and motivation for the study. The goals and objectives were also described.

Chapter 2: Literature review
This is a review of the literature most relevant to this study. Pertinent previous studies on internal fluidisation were also discussed.

Chapter 3: Methodology
The experimental equipment and the verification procedure were discussed. Also included was a description of how the experimental measurements were taken.

Chapter 4: Results and discussion
This Chapter contained a discussion of the results found in the experimental measurements.

Chapter 5: Conclusions and recommendations
Here the results of the study were summarised. Recommendations for further experimentation and alterations to the experimental setup were addressed.

1.5 Terminology used

This section defines the terminology that was used to describe the static pressure and the increase in pressure caused by the internal fluidisation. The pore and dynamic pressures which were measured in the experiments are also defined.

1.5.1 Static pressure

The static pressure is the pressure at a depth should the fluid be static. It is dependent on the height of water (H) above a point and is calculated by the equation $P = \rho_f gH$.

1.5.2 Increased pressures due to internal fluidisation

These are the pressures over and above the static pressure which were caused by the internal fluidisation, thus without fluidisation these pressures would be zero. Furthermore, these were the pressures which were measured in the experiments and are detailed below.

1.5.2.1 Pressure

The pressure was regarded as the increase in ballotini bed pressure created by the internal fluidisation. It was recorded using the Pitot tubes and formed a very important measurement in the experiments. Specifically the Pitot tubes recorded the pressure when the flow direction was at right angles to the Pitot tube"s nose opening. Thus no velocity head was recorded. The pressure is the potential energy component in Bernoulli"s Equation (Equation 4.1).

1.5.2.2 Dynamic pressure

This dynamic pressure was the velocity head caused by the flow in the ballotini bed created by internal fluidisation. As with the pressure, the dynamic pressure was also measured using the Pitot tubes. The dynamic pressure is the kinetic energy component in Bernoulli"s Equation (Equation 4.1).

1.5.2.3 Stagnation or total pressure

The stagnation pressure was the measured value which quantifies the summation of the pressure and dynamic pressure. The pressure and the stagnation pressure were the two measurements which were recorded. The dynamic pressure was later calculated by finding the difference between the pressure and the stagnation pressure. Typically the stagnation pressure was the greater of the pressures, as it included both the pressure and the dynamic pressure.

Chapter 2

2 Literature review

2.1 Introduction

There are many definitions given for the term fluidisation. This is largely due to fluidisation occurring in various disciplines, such as geology, chemical engineering, soil mechanics and earthquake dynamics. One interesting description in the context of soil mechanics was given by Powrie (2004) who claimed that fluidisation is an effect seen as „piping‟ at the soil surface. Terzaghi (1939) provided a general definition for „piping‟ as a process where soil particles are dislodged from the granular bed through erosive forces generated by the seeping water. Another descriptive term in the context of earthquake dynamics that has been used for fluidisation is „liquefaction‟ (Ma, 2011). „Liquefaction‟ occurs when large volumes of saturated soils lose strength and stiffness due to the applied stresses from the earthquake (George, 1985). In chemical engineering, the process of fluidisation is used extensively in mixing gasses with solids. This process occurs in biological reactors where the gasses are injected vertically into a container containing solids which are then injected separately into the gasses. In the chemical engineering context, fluidisation is referred to as the process in which solids act like fluids because of a fluid jet that is directed vertically upward.

There are various terms used to describe the fluidisation process, of which the most relevant are described above. Essentially the differences in the terms arise from the diverse conditions and disciplines in which they occur. Therefore, the term fluidisation can have a variety of meanings. As a result, Ma (2011) referred to fluidisation specifically in the context of the leak-soil interaction occurring outside water pipes as „internal fluidisation‟. Furthermore, the author defined internal fluidisation as when a granular material behaving in a solid like state is brought into a fluid like state due to the drag forces caused by the build-up of pore water pressures within a confined zone. The build-up of pore pressure is induced by the injection of a fluid. Similarly, Alsaydalani (2010) stated that internal fluidisation occurs due to a localised fluid injection, resulting in soil particles losing their stability and moving upwards in a wedged shaped mechanism.

2.1.1 Fundamentals of internal fluidisation with respect to this study

Typically in practice internal fluidisation originates from a leaking pipe orifice through which a fluid is passed and penetrates into a granular bed. This fluid passing through the orifice subsequently increases the granular bed's pore pressure in the vicinity of the orifice. In certain instances if this leak is of sufficient flow rate and pressure, the upward fluid force at the orifice exceeds the total weight of water and particles located in a wedge shape above the orifice. It is at this point that internal fluidisation initiates and the granular bed becomes displaced (Alsaydalani, 2010).

The area outside of a water leak where internal fluidisation occurs is divided into three distant regions. These are the fluidised zone, which is where the granular material becomes completely displaced; surrounding this is the mobile bed zone, which is where the granular material is in continuous motion; and lastly the static bed zone where there is no granular material movement and surrounds the mobile bed zone (van Zyl, *et al.*, 2013). Particularly with a leak that is directed vertically upwards the fluidised zone takes the shape of an inverted cone or a wedge, where the base of the fluidised zone is narrower and widens towards its top. The fluidised zone consists of a fluid jet generated by the leak and transports granular material from the lower regions of the zone up to its top. At the top of the fluidised zone, the fluid jet generally terminates in a vortex movement (Lawrence, 2008). The top of the fluidised zone where often a vortex movement is located is also referred to as the fluidised zone head. The mobile bed zone consists of granular material that is in a continuous circular motion starting from the fluidised zone head and moving down towards the orifice.

2.1.2 Literature review layout

This chapter begins with a review on orifice hydraulics, specifically the flow through orifices. This is followed by an examination of laminar and turbulent flow as well as pressures in saturated soils and leads into the combined flow through orifices and saturated soils. Next is a presentation of fluid and soil particle interaction which discusses the forces acting on a single soil particle due to a flowing fluid. The background theory of air jets directed into solid surfaces which is similar to that of internal fluidisation is then given. The literature then focuses more on the fundamentals of doing an experimental study on internal fluidisation. It includes the various techniques that are used in the laboratory to measure pore pressures and dynamic pressures i.e. flow velocities. The chosen technique and its various designs and correction factors are then discussed in great detail. Fundamental to the successful execution of this experiment is the size of the tank in which the experiment is to be conducted. The chapter ends with a discussion on the most relevant previous studies.

2.2 Orifice hydraulics

Water flow through an orifice is expressed by the orifice equation shown below (Chadwick *et al.*, 2004).

$$Q = C_d A_o \sqrt{2gh_o} \tag{2.1}$$

This equation was proved by Torricelli experimentally in 1643, however Torricelli"s equation is Equation 2.1 in terms of velocity (V) and not flow rate (Q). The orifice equation can also be derived from Bernoulli"s principle which is the Conservation of Mechanical Energy Theorem. In Equation 2.1 Q is the flow rate, A_o the orifice area, g the gravitational acceleration, h_o the piezometric head at the orifice centre, and C_d is the discharge coefficient of the flow through the orifice (Prohaska *et al.*, 2010). The discharge coefficient can be calculated using this equation: $C_d = C_v C_c$ where C_v is the velocity coefficient and C_c the contraction coefficient. Typical values of C_v are between 0.95 and 0.99 and for C_c between 0.6 and 1 (Daugherty & Franzini, 1965). C_c accounts for the contraction of the flow area as the flow passes through the orifice. Initially at the upstream end of the orifice the flow area is the same as the orifice area, the flow area then reduces further downstream. This contraction is known as the vena contracta (Daugherty & Franzini, 1965). C_v accounts for the assumption that the velocity flowing through the orifice is the same at the upstream end of the orifice as it is in the vena contracta.

The flow regime through an orifice can be laminar or turbulent depending on the Reynolds number. The Reynolds number is a dimensionless number which represents the ratio between the inertia and viscous forces (Chadwick *et al.*, 2004). Laminar flow through an orifice occurs with a Reynolds number less than 10 and above 4000 to 5000 for turbulent flow (Idelchik, 1994). The intermediate Reynolds numbers between 10 and 4000 are termed the transitional zone. In the transitional zone the flow behaviour is complex as it is not completely laminar nor is it completely turbulent. Greyvenstein & van Zyl (2007) found that the leakage exponents (N_1) in this transitional zone can vary between 0.5 and 1 (0.5 for the transitional/turbulent boundary, and 1 for the laminar/transitional boundary).

2.3 Flow and pressure in saturated soils

Flow in granular mediums is categorised into two flow types, laminar and turbulent flow. The flow type is dependent on the Reynolds number (Re). The properties of this Re are the same as the Re described previously in Section 2.2. This critical Re number can be calculated using the equation below (Harr, 1962).

$$\mathrm{Re} = \frac{VD\rho_f}{\mu} \tag{2.2}$$

In Equation 2.2 Re is the Reynolds number; V is the average velocity between particles (flow per unit cross section of soil); D the average particle diameter; ρ_f the fluid density; and μ the dynamic viscosity of fluid which is the resistance a fluid exerts to shearing flows. One might notice in Equation 2.2 that the Re is dependent on the characteristic length of the flow path, which in this case is the average particle diameter, D (Miyazaki, 2006). In saturated soils, laminar flow typically occurs at Re numbers below 10 and turbulent flow starts between 60 and 150 (Bear, 1972). Harr (1962) stated that flow changes from laminar to turbulent between Re numbers of 1 to 10.

2.3.1 Laminar flow

Laminar flow through saturated porous mediums is calculated using Darcy"s Law, shown in Equation 2.3.

$$Q = A_s ki \tag{2.3}$$

The flow is mostly dependent on the ease with which water can move through a soil and is known as the hydraulic conductivity k (m/s), which generally varies for different flow directions and soil types (Craig, 2004). The magnitude of k depends on the grain size of the medium"s particles, their shape and orientations, and the structure of the medium (Aysen, 2002). k determines the rate at which excess pore pressures dissipate (Aysen, 2002). The remaining values in Darcy"s equation are: A_s the cross-sectional area of a particular flow path through the soil; i the pressure difference over distance ratio known as the hydraulic gradient; and Q the flow rate for a particular flow path.

The hydraulic gradient, k, can be calculated using Equation 2.4 below which was proposed by Allen Hazen (Aysen, 2002).

$$k = c_H D_{10}^2 \tag{2.4}$$

Here k is in m/s, D_{10} is the grain diameter corresponding to 10% of the fine grains in m (obtained from the particle size distribution curve), and c_H is Hazen"s coefficient that varies from 0.005 for silts to 0.012 for uniformly graded sands. There are tables available where k values can be read off for various soil types, but laboratory tests are preferred for the most accurate results. There are two laboratory experiments that can determine k, namely the constant head test and the falling head test (Aysen, 2002).

2.3.2 Turbulent flow

Darcy"s equation cannot be used for turbulent flow (generally higher flow velocities) because of the linear relationship between flow rate and pressure head which Darcy uses in his derivation. Turbulent flow has a non-linear relationship (Craig, 2004). Therefore, due to the non-linear relationship of turbulent flow, Darcy"s equation was altered. The first to propose an alteration was Forchheimer in 1901, who suggested a second order velocity term shown in Equation 2.5 below (Muskat & Wyckoff, 1937).

$$i = aV + bV^2 \tag{2.5}$$

Here i again is the hydraulic gradient, a and b are coefficients, and V is the flow velocity. Coefficients a and b for a given physical system can be solved (although very difficult) using the partial differential, Navier-Stokes equations (Hlushkou & Tallarek, 2006). The equations are related to pressure and velocity fields and are subject to corresponding boundary conditions (Hlushkou & Tallarek, 2006).

Venkataraman & Rama Mohan Rao (1998) tabulated the previous four decades of work done by various investigators showing their solved a and b values. The table includes results for a large variety of granular mediums ranging from fine sands to different types of rocks with varying particle diameters. The table also shows the amount of voids known as the porosity and also the permeability values for these granular mediums. Venkataraman & Rama Mohan Rao (1998), then verified the correctness of the a and b experimental data with theoretical relationships proposed by Ward (1964) and Ahmed & Sunada (1969). Ward used the method of dimensional analysis, while Ahmed & Sunada used the Navier-Stokes equations to obtain expressions for *a* and *b*. Venkataraman & Rama Mohan Rao (1998) concluded that the theoretical relationships concur with the experimental results of the various investigators. The equations below are Ward"s expressions for coefficients *a* and *b*.

$$a = \frac{1}{k} \tag{2.6}$$

$$b = \frac{6.72\left(1-n\right)}{g\Phi_s D n^{3/2}} \tag{2.7}$$

In Equation 2.6, coefficient *a* is simply the inverse of the hydraulic conductivity, *k*. Equation 2.7 for coefficient *b* is comparatively more complex. Coefficient *b* takes into account the following: the porosity (n) which is a measure of the spaces between particles or voids; the acceleration due to gravity (g); the particle shape factor (Φ_s) which is dimensionless and describes the shape of a particle and is independent of its size (for spheres Φ_s is equal to 1); and the particle diameter (D).

Ergun (1952), in the field of chemical engineering, studied this non-linear relationship between pressure gradient and fluid velocity. He conducted his study using gas flow through crushed porous solids, relating to the importance of flow rate and the properties of the fluid, porosity of the medium, as well as on the orientation, size and shape of particles (Hlushkou & Tallarek, 2006). Ergun obtained the empirical equation shown below which he generalised from Forchheimer"s equation.

$$i = A\frac{\mu}{\Phi_s^2 D^2}\frac{\left(1-n\right)^2}{n^3}V + B\frac{\rho_f}{\Phi_s D}\frac{\left(1-n\right)}{n^3}V^2 \tag{2.8}$$

Here μ is the dynamic viscosity; V the fluid velocity; and ρ_f the fluid density. The remaining subscripts are defined in the previous paragraphs. Ergun stated that the constants *A* and *B* in the equation are 150 and 1.75 respectively (Hlushkou & Tallarek, 2006).

2.3.3 Pore pressures and effective stress

The best way to understand pore pressure is to look at it in conjunction with fluid flow velocities in soils. Craig (2004) describes the two by creating flow nets. Flow nets are drawings consisting of two types of lines: the velocity vectors and the equipotential pressure lines. These two lines cross perpendicularly to each other. In order to draw these lines, the velocity vectors are drawn first in the direction of flow from the source through the soil. Thereafter the pressure lines are drawn. The further away from the flow source the lower the velocity, provided there are no obstructions in the granular medium which disrupt the flow. In addition, this is only true if the area through which the fluid can flow expands as it moves further away from the flow source, which is generally the case. The lower velocities are a result of both the lower pressures and greater flow area which generally exists further away from the flow source.

Pore pressure plays an important role in determining the effective stress in the soil which is the force binding individual soil particles together. The greater the pore pressure, generally due to soil saturation, the lower the effective stress (soil strength). Therefore, the effective stress is the stress in a soil less the pore water pressure (Craig, 2004). Terzaghi in 1925 proposed a relationship for effective stress which is shown in Equation 2.9 below (Craig, 2004).

$$\sigma^{I} = \sigma - u \tag{2.9}$$

In Equation 2.9, σ^{I} is the effective stress, σ is the stress and u is the pore pressure. The above expression plays an important role in understanding the inter-grain stress regarding pore pressures. One might notice in the expression above that if the pore pressure increases, the effective stress decreases. Typically, the pore pressure increases in the presence of a pressurised fluid. There are however cases where the effective stress can increase if subjected to a fluid. In this latter case the pore pressure is negative which occurs when a fluid is drawn upwards above the water level by the forces between the soil particles and the fluid. These forces overcome the gravitational forces that act on the fluid. This upward movement of water is known as capillary action (Aysen, 2002). Examples of this phenomenon can be illustrated both by the strength of sand castles using moist sand, and the resistance to shearing of sand by a vehicle tyre on the beach. This strength or effective stress in moist sand disappears when the sand is completely saturated, due to positive pore pressures. The same happens when the sand is completely dry.

2.4 Combined flow through orifices and saturated soil

Internal fluidisation involves both the flow through an orifice followed by the flow through the surrounding saturated soil. This combined flow therefore forms a very important part of the literature. There have been a number of studies (e.g. Ledwith & Weisman, 1990; Walski *et al.*, 2006; van Zyl & Clayton, 2007; Zoueshtiagh & Merlen, 2007; Noack & Ulanicki, 2008) involving the flow through orifices and the surrounding soils.

Ledwith & Weisman (1990) investigated the internal pipe pressures and flow rates required for internal fluidisation, by means of experimenting with a two dimensional internal fluidisation experiment. In the experiments the sands varied between fine, medium and coarse at bed heights of 254 and 420 mm. Twelve different orifice diameters from 1.59 to 6.35 mm were tested. One of the outcomes of the experiments was that high pressures could be maintained in the pipe before soil became fully fluidised. At the initiation of internal fluidisation the internal pipe pressure dropped significantly.

Zoueshtiagh & Merlen (2007) experimented with a vertical internal fluidising water jet surrounded by a granular bed. The authors categorised the internal fluidisation occurrence into three distinct regimes. The regimes described the different stages leading up to and into the occurrence of internal fluidisation, where these stages were dependant on the granular bed behaviour. They associated the flow rate as being the dependant for these three regimes. The authors described Regime (1) as where seepage flow exists in the granular bed and the bed itself remains motionless, with low flow rates through the orifice. Regime (2) experiences higher flow rates where there is an inherent distortion on the granular bed surface. Zoueshtiagh & Merlen (2007) refer to this regime as the transitional situation where a complex interaction exists at the orifice - particulate interface. Regime (3) experienced even higher flow rates. In Regime (3) they found fluidisation to occur up to and on the granular bed surface. They describe the fluidised zone as being similar to that of a vertical cylindrical chimney.

Walski *et al.* (2006) found an important expression for this combined flow. They conducted their experiments using two sizes of cylinders filled with varied soil samples. A short cylinder of 480 mm high with a diameter of 380 mm, and a tall cylinder of 1.57 m with a diameter of 102 mm were used. The expression determined where the majority of the fluid flow head loss occurred, either in the orifice (h_0) or in the saturated soil (h_s). The expression below is the orifice – saturated soil (OS) expression of Walski *et al.*

$$\mathrm{OS} = \frac{h_0}{h_s} = \frac{kA_sQ}{2gL}\left(\frac{1}{C_dA_0}\right)^2 \tag{2.10}$$

In Equation 2.10 A_s is the area of flow in the soil, L the length of the flow path in the soil, C_d the orifice discharge coefficient, and A_o the area of the orifice. In the expression a small OS value (<0.1) indicates that soil head loss is dominant while a large OS value (>10) means that orifice head loss is dominant (Walski *et al.*, 2006). Walski *et al.* (2006) varied the orifice diameters, flow rates, pressures applied to the cylinders and soil types, in order to obtain a wide range of OS numbers. They discovered that it is unlikely for the soil to experience the dominant head loss (a low OS number). This is because the soil becomes fluidised at high flow rates. In their experiments they avoided internal fluidisation by placing a pressure plate on the soil surface to secure it. In a real world case though, a pressure plate would not be present and internal fluidisation would likely be the result at high flow rates (Walski *et al.*, 2006). They concluded that under certain soil conditions the soil is not likely to control the leakage rate.

Van Zyl & Clayton (2007) expressed their uncertainties about both the conclusion of Walski *et al.* of the soil having no effect on the leakage rate, as well as their OS expression. Van Zyl & Clayton point out that a direct grouping of the orifice equation (Equation 2.1) and the soil seepage equation (Equation 2.3) does not properly define the combination of flows in the OS expression. They state that this is due to orifice flow analysis and soil seepage analysis being incompatible with each other.

The orifice - saturated soil interaction is very complex and limited information is available. Whether the seepage flow through the granular bed is laminar as in Darcy flow or whether it is turbulent is still a contentious issue.

2.4.1 Effect of soil on the orifice equation

As shown in the orifice equation (Equation 2.1), the theoretical flow rate is proportional to the square root of the pressure head. Pressure head is the pressure of a fluid expressed in distance units. A more general version of the orifice equation which accounts for leaks in water networks is shown below.

$$Q = ch_o^{N_1} \tag{2.11}$$

Equation 2.11 uses a leakage coefficient c as in the orifice equation (Equation 2.1), although not the same value; pressure head above the orifice h_o; and a leakage exponent N_1. N_1 values have been found to be substantially larger than the theoretical 0.5 (Lambert as cited by Farley & Trow, 2003). Lambert found the N_1 values to be between 0.5 and 2.79 with an average of 1.15. This illustrates that orifice dynamics are more sensitive to pressure than originally thought (van Zyl & Clayton, 2007).

Van Zyl & Clayton (2007), analysed factors (leak hydraulics, pipe material behaviour, soil hydraulics, and water demand) that could be responsible for a higher range of leakage exponents, N_1, observed in the field. They stated that the interaction between a leaking pipe and the surrounding soil is a very complex problem. This is because different soils vary in permeability as does the range of hydraulic gradients. Van Zyl & Clayton (2007), concluded that the relationship between head loss and the flow through leaks in pipes will not be linear as a result of the following: orifice - soil particles interaction; turbulent flow in the soil; changing geometry of the internal fluidising zone; and the void creation in soils and rock by the pressurised fluid known as hydraulic fracturing and lastly piping. As shown by van Zyl & Clayton (2007), soils can have an influence on the leakage rate from a pipe.

Walski *et al*. (2006) who had done an experimental study described in section 2.4 to determine the OS number suggested otherwise, that the leakage rate is not likely to be controlled by the soil. This is because for the leakage to be controlled by the soil, large leak velocities are required, in which case soil fluidisation of the bed will occur. Furthermore due to the occurrence of soil fluidisation the leak will likely pipe to the soil surface, thus the soil having less of an effect on the leakage rate.

2.5 Fluid and soil particle interaction

The fluid and soil particle interaction is complex. There are various forces, some of which are caused by the fluid and others by external effects, which act on the soil particles. These forces are discussed first. Then the different types of movements which the soil particles experience due to fluid flow, will be discussed. Lastly the effects of suction or flow of water through pipe walls and the base of open channels will be discussed.

2.5.1 Forces on a stationary particle due to horizontally flowing water mass

There are three forces that act on a stationary particle submerged in a flowing fluid. Two of which are hydrodynamic forces caused by the fluid flow and the other which is gravitational. The gravitational force (F_G) is due to the particle"s submerged weight and acts vertically downwards (Dey, 1999). The hydrodynamic drag force (F_D) is in the stream-wise direction, while the hydrodynamic lift force (F_L) is at right angles to the flow, acting towards the strongest flow path (Dey, 1999). The hydrodynamic forces are presented in the following two subsections. Figure 2.1 illustrates the three forces acting on a particle. In the figure, x is the direction of flow u, and F_G, F_D and F_L are the gravitational, drag and lift forces respectively. Dey (1999) described the submerged weight of a particle represented in Equation 2.12 below, where D is the particle diameter and ρ_p the mass density of the particle.

$$F_G = \frac{\pi}{6} D^3 \left(\rho_p - \rho_f\right) g \tag{2.12}$$

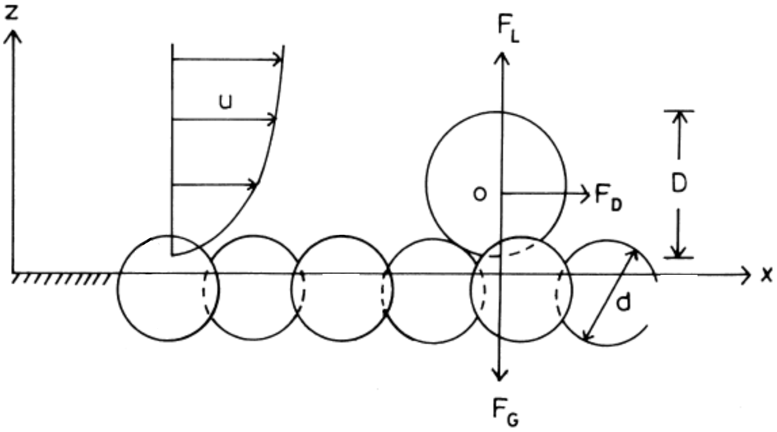

Figure 2.1: Description of the three forces acting on a particle (Dey, 1999)

2.5.1.1 Lift force acting on a particle

Lift forces are caused by the fluid colliding with a granular bed (Liu & Graze, 1983). Fluid flow lines become distorted or deflected when the fluid makes contact with the upstream end of a particle. This distortion causes a flow separation zone which later disappears when the flow lines approach the particle surface again (Liu & Graze, 1983). The lift force is caused by the separation zone where low pressures exist. The low pressure in turn results in a localised uplift force. The maximum normal lifting force was found to occur when particles were in direct contact with the bed and thus there was no gap between the particle and the granular bed where fluid could pass through (Bagnold *et al.,* 1974).

A lift coefficient C_L was derived by both Jeffreys‟ (1929) theoretical approach and Bagnold, *et al.*‟s (1974) experiments. The coefficient is a dimensionless quantity that is used in the lift equation to calculate the resulting lift force (Chadwick *et al.*, 2004). Not much is known about the lift coefficient (Nino & Garcia, 1998), but it is recommended that it be determined experimentally. Bagnold found that his experimental C_L values were much smaller than Jeffreys‟ theoretical values. The reason for this is that Jeffreys‟ theoretical values were relating to an ideal fluid whereas Bagnold‟s experimentation was with a real fluid. Table 2.1 shows the C_L values obtained.

Table 2.1: Ideal and real fluid C_L values (Bagnold, *et al,* 1974)

Theoretical ideal fluid (Jeffreys)	4.5
Real turbulent fluid – contact with bed (Bagnold *et al,* 1974)	0.77
Real turbulent fluid – contact with free surface (Bagnold *et al,* 1974)	0.92

The lift force F_L can be calculated using the expression below.

$$F_L = C_L A_p \frac{\rho_f V^2}{2} \tag{2.13}$$

Where C_L is the lift coefficient, V the shear velocity which is the velocity at the axis of a particle, and A_p the cross-sectional area of the particle in contact with the fluid flow (Liu & Graze, 1983; and Chadwick, *et al*., 2004). Bagnold, *et al.* (1974) derived a similar equation except they did not include the cross-sectional area component.

Lift coefficients quickly tend to zero when the particles are a distance of one particle diameter from the bed and then the lift forces reverse (directional switch) when approaching the free surface (Bagnold *et al.,* 1974). The difference in the C_L values between the bottom bed and top free surfaces proposed by Bagnold *et al*. (1974) can be seen in Table 2.1.

2.5.1.2 Drag force acting on a particle

Drag also has a major effect on the behaviour of particles (Bagnold, *et al.,* 1974). Drag forces act parallel to and in the direction of the fluid flow, therefore at right angles to the lift force F_L. A very similar equation to the lift force (Equation 2.13) is used to calculate the drag force. The drag force equation is illustrated below where the only difference to Equation 2.13 is the drag coefficient, C_D term, which is the drag coefficient (Liu & Graze, 1983; Watters & Rao, 1971; and Dey, 1999).

$$F_D = C_D A_p \frac{\rho_f V^2}{2} \tag{2.14}$$

In many cases a flowing fluid which is bounded by a porous granular bed, may pass through the granular bed between the particles. This occurrence of flow exiting through the granular bed is known as suction flow. There is limited information available concerning the drag coefficient in the presence of suction flow. Suction has an effect, most importantly on the velocity field and shear of a fluid (Prinos, 1995). Suction effects are described in more detail in the section that follows. Of the information available, Liu & Graze (1983) established that the C_D value is simply the difference between the upstream and downstream pressure heads surrounding a particle. Watters & Rao (1971) did extensive experimental testing and found a relationship between the C_D and the Reynolds number (Re). Here this Re relates to the velocity at the flowing fluid and granular bed boundary, also known as the shear zone velocity. Their results which are rather limited in terms of the range of Re, are represented in Figure 2.2. Watters & Rao took into account the Re of the suction flow, which is represented as the effluent Re_S in Figure 2.2.

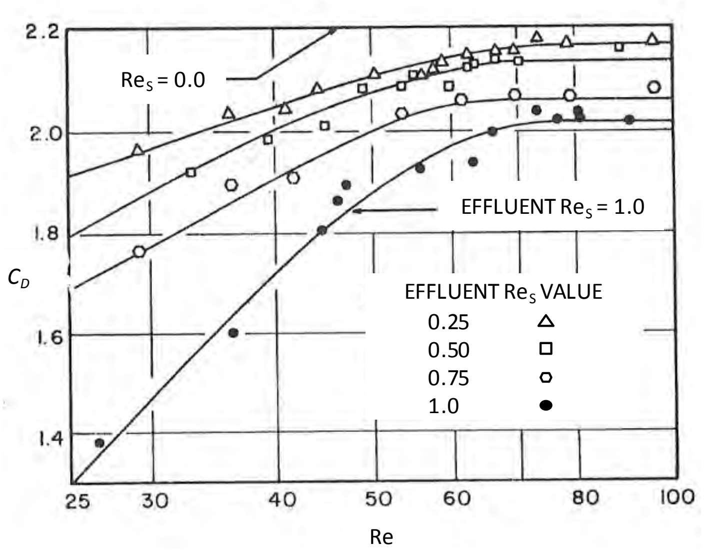

Figure 2.2: Drag coefficients C_D verses Reynolds number Re at different suction Re_s numbers (Watters & Rao, 1971)

Further research regarding the C_D value that does not take suction into account was done by, amongst others: Dallavalle (1948); White (1991); and Schlichting & Gersten (1999). Their findings were very similar. Schlichting & Gersten (1999) graphed the findings of studies done by various researchers (Schiller - Schmiedel, (1929); Liebster, (1927); Allen, (1900); and Wieselsberger, (1921 and 1926)) on the C_D where suction was not taken into account. This graph by Schlichting & Gersten (1999) was redrawn by Robertson & Robertson (2013) and is shown in Figure 2.3. The critical Reynolds number point shown in the figure is regarded as the point at which turbulent flow is reached (Robertson & Robertson, 2013). Dallavalle (1948) derived a model which also did not account for suction, and was represented in an equation for calculating the C_D value. The result of his model is shown in Equation 2.15 below which is only valid for a Re below the critical Re, i.e. laminar and transitional flow, but not turbulent flow.

$$C_D = \left(0.63 + \frac{4.8}{\sqrt{\text{Re}}}\right)^2 \tag{2.15}$$

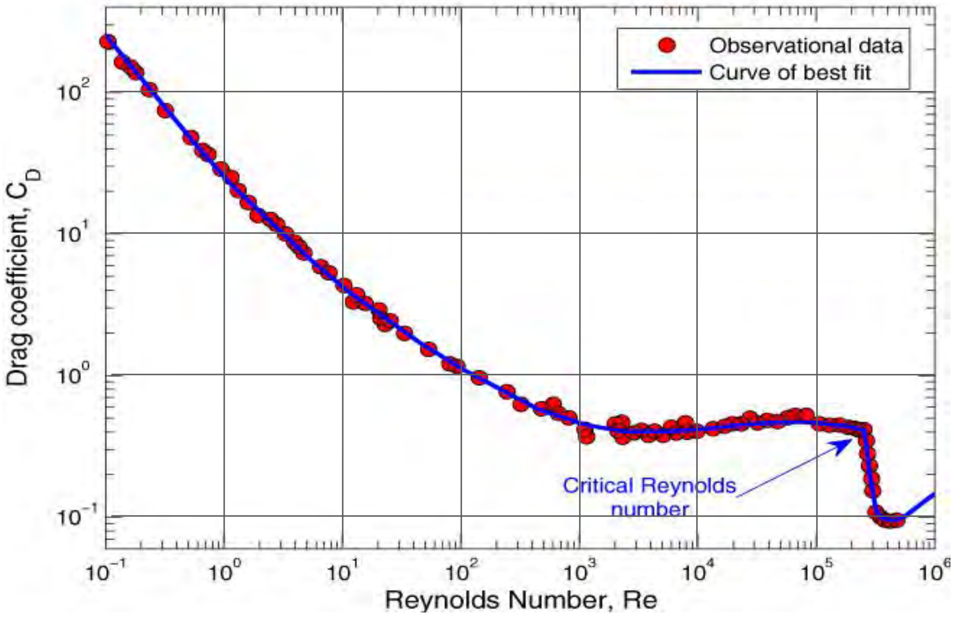

Figure 2.3: Drag coefficients C_D versus Reynolds number Re without suction
(Robertson & Robertson, 2013)

2.5.2 Particle movement caused by horizontally flowing water mass

From as early as 1914, there has been a considerable amount of research done on how a horizontally flowing water mass causes sand particles to be suspended in the flow stream and repositioned further downstream along a sandy bed. Francis (1973) investigated three types of sand particle movements induced by a horizontally flowing water mass, namely rolling, saltation, and suspension.

Particle rolling is caused when the shear stress exerted by the water mass on the bed is just greater than the threshold value. The threshold value is regarded as the force which tends to hold a particle in position. Saltation is one or a series of small jumps that particles experience along a bed. The final type is suspension which is when particles have much longer and higher trajectories away from the bed (Francis, 1973). Figure 2.4 illustrates the difference between saltation and suspension. In all three cases the particles spin about their axes in the direction of the flow, with the spinning slowing down towards the end of their trajectory (Francis, 1973). Of the three movements, saltation is the most relevant and thus further detail is presented below.

2.5.2.1 Saltation

Saltation has been widely studied in the past by Gilbert (1914), Einstein (1950), Danel, *et al.* (1953), and Bagnold (1956). Bagnold (1956) describes the process of saltation as one where sand particles exceeding a certain mass are seen jumping upwards into the fluid flow. The particles are then accelerated in the direction of the flow. The force which causes this upwards "jumping" action into the fluid flow only has an effect for the first part of the particle trajectory. This is generally up to a distance of about half the diameter of the particle (Bagnold, 1956). Later studies by Bagnold, *et al.* (1974), suggest that these forces only stop at a whole particle diameter distance away from the bed. After this initial "jumping" force, gravity and pressure exerted on the particle due to the flow velocity are the only two forces that affect the particle movement, barring the effect of inertia which causes the momentary upward movement (Bagnold, 1956). The saltation height never exceeds a distance of two to four times the grain diameter, as shown in the top illustration in Figure 2.4 (Francis, 1973).

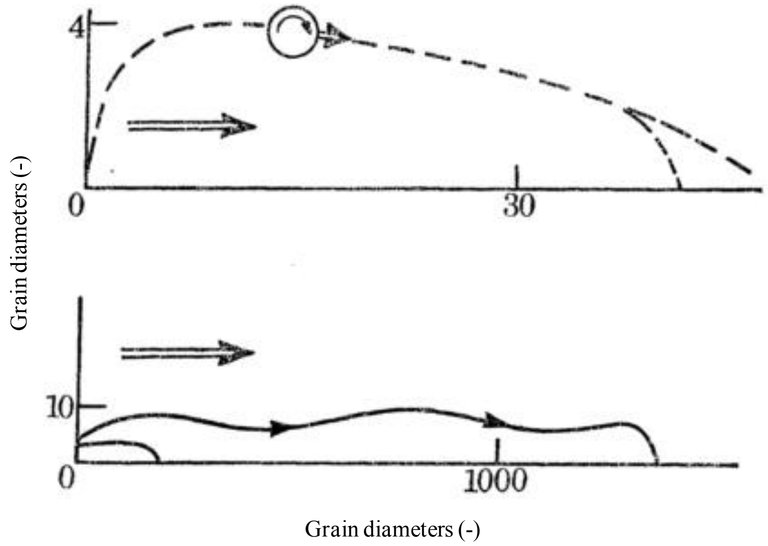

Figure 2.4: Typical saltation trajectory (above) and suspension trajectory (below) relative to grain diameters (Francis, 1973)

According to Bagnold (1956), the impact velocity of the particles reconnecting onto the bed do not cause any rebound, nor does it cause any disturbances of the bed grains. He concludes that this is due to the viscous effects in liquids. Francis (1973) suggests otherwise by stating that particle velocity just before impact with the bed is larger than just after impact, and then the particle is again accelerated due to the fluid drag during the subsequent saltation. Francis deduces that the bed does experience an impact force. Different grain sizes and flow velocities could well be the cause of the discrepancy between the findings of the two authors.

2.5.2.1.1 Forces governing saltation

Francis (1973) conducted an experiment investigating the motion of a sphere in water which flowed at right angles over horizontally placed cylinders. Both the cylinders and the sphere had the same diameter. He grouped the sphere motion into three intricate phases involving the rotation of a sphere on the underlying bed of cylinders. During each phase the magnitude and types of forces acting on the sphere were constantly changing. Phase I was described as when the sphere moved downwards from the crest of an upstream cylinder, here the sphere was propelled by gravity and the hydrodynamic force. Phase II followed on from Phase I when the sphere made contact with the downstream cylinder, thus from when the sphere bridged the gap between the two cylinders. During Phase II there is a reduction in velocity of the sphere. Phase III then starts when the sphere begins its upward movement on the downstream cylinder. During Phase III the force that is driving the sphere is the hydrodynamic force less gravity. Phase III ends when the sphere is on the crest of the downstream cylinder which marks the start of Phase I again. Francis derived the hydrodynamic force which drives the sphere, which is shown below.

$$F' = 0.116Mg' + 1.16Mr\omega^2 \tag{2.16}$$

Equation 2.16 can only be used if the sphere has the same velocity as when it left the previous cylinder‟s crest (known as steady motion). In Equation 2.16, F' is the hydrodynamic force driving the sphere with radius r and mass M, g' is the effective gravity and ω is the angular velocity of the sphere. The effective gravity, g' is the net force exerted by the earth which includes gravity and the acceleration of a body. When the sphere comes to rest in a trough between two cylinders with the angular velocity at zero, the following equation is then used to calculate the force on the sphere.

$$F' = 0.116Mg' \tag{2.17}$$

2.5.3 Seepage through a pipe wall or the bed of an open channel

Seepage is the flow of water, typically from a higher potential to a lower potential, thus there is a potential difference creating the flow. In this particular context, seepage is related to the flow of water through a porous medium, being either holes in pipe walls or a granular bed of an open channel.

There has been a fair amount of research regarding both the seepage through a porous pipe wall and through an open channel bed, and the effects thereof. In these contexts the most important aspect of seepage is the influence it has on the velocity profile. A graphic done by Kinney & Sparrow (1970) showing the affected velocity profile at various seepage rates can be viewed in Figure 2.5. The figure represents flow in a pipe at an Re of 25 000. In the figure, $\bar{v}$ is the average velocity, y is the distance from the pipe wall, r is the radius of the pipe and v_s is the seepage velocity. It is noticeable that at higher seepage velocities, as v_s/v increases, the velocity nearer the pipe wall increases, which is a $v/\bar{v}$ increase.

In addition to Kinney & Sparrow, Prinos (1995) also found that seepage increases the near-bed velocity, resulting in a more evenly spread mean flow profile. The increase in near-bed velocity has subsequent effects on the flow turbulence, pressure gradient and the bed shear stress. Both Oldenziel & Brink (1974), and Abdullah *et al.* (2011), state that seepage increases the bed stability, therefore decreasing particle displacement.

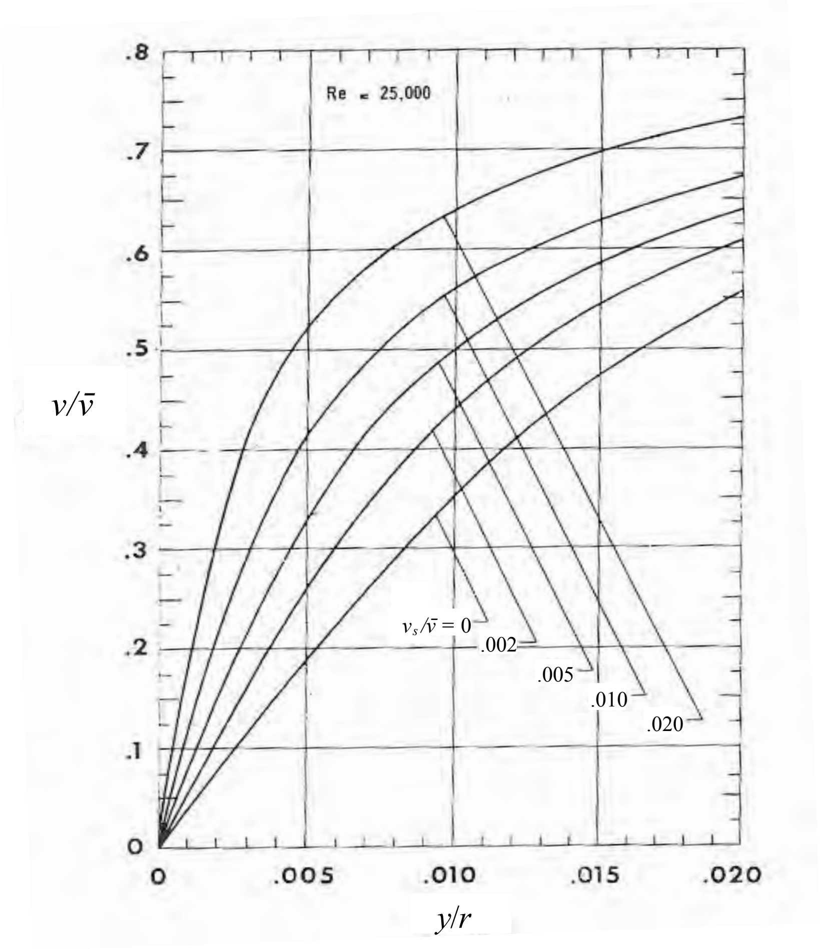

Figure 2.5: Effect of seepage on velocity profile near tube wall at different seepage rates
(Kinney & Sparrow, 1970)

2.5.3.1 Seepage effects on flow turbulence

Bed seepage lowers both the turbulence kinetic energy and the dissipation of the energy in a flow field (Prinos, 1995). Prinos (1995) illustrated that for high seepage rates, up to 9% of the channel flow, the turbulence kinetic energy throughout the channel is reduced more than four times. The lowering of the turbulence energy is said to reduce the sediment transport (Abdullah, *et al.,* 2011).

2.5.3.2 Seepage effects on bed shear stress

Prinos (1995) maintained that due to the higher shear flow velocities caused by seepage there is a resulting higher shear stress on the bed. Maclean & Willetts (1986) suggest that the shear stress doubles in the near-bed region when the seepage velocity is 10 % of the mean flow velocity. Maclean (1991) did further tests, this time including the effects of momentum on the abstracted seepage water. He found that the near-bed shear stress in fact increases between three to six times compared to when there is no seepage. An increase in the shear stress has implications for the bed stability due to the increased hydrodynamic forces at higher velocities.

Abdullah *et al.* (2011) agree that seepage increases the near-bed velocities but that the bed shear stress is reduced due to the increase in bed shear velocity. This differs from the claims of Prinos (1995), Maclean (1991), and Maclean & Willetts (1986). However a study done by Rao, *et al.* (1994) showed that the bed shear stress can either increase or decrease depending on the relative magnitude of seepage applied.

2.6 Theory of air jets directed onto solid surfaces

There have been a number of studies (e.g. Cornaro *et al.* (1999), Eren *et al.* (2006), Terekhov *et al.* (2009), & Yang *et al.* (2011)) that investigated an air jet directed onto a rigid surface. In the case of the experiments by Terekhov, *et al.* the jet was directed vertically downwards into an impermeable concave cavity of fixed dimensions. A basic drawing of their experimental setup is illustrated in Figure 2.6. In the figure, d_o is the diameter of the orifice jet, S is the distance of the jet from the cavity, D_c is the cavity diameter, and r is the radial distance from the cavity centre. The dynamics of the air flow relating specifically to pressures and velocities in the cavity were investigated.

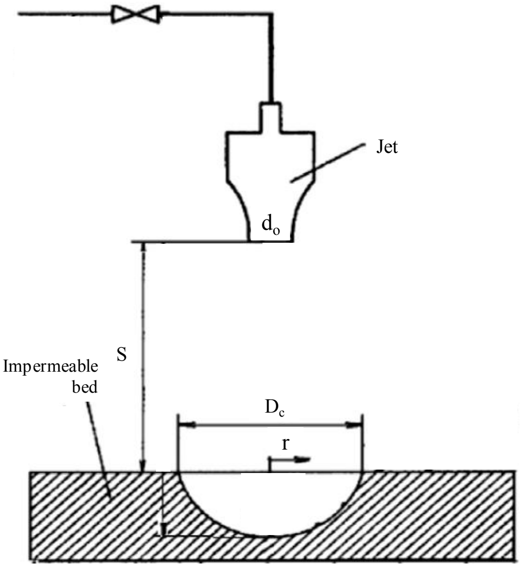

Figure 2.6: Experimental setup of Terekhov, *et al.* (Terekhov, *et al.*, 2009)

Terekhov, *et al.* (2009) found the pressure distribution along a horizontal plane (perpendicular to the jet flow), through the radial centre of the cavity. This horizontal plane is labelled D_c in Figure 2.6. The result is illustrated by the graph in Figure 2.7. In the figure, C_P is the pressure coefficient which is measured and points along the horizontal plane, 2r/Dc. Pressure coefficients are measured for four distances between the jet and cavity, S/d_0. As seen in Figure 2.6, the smaller the distance between the nozzle and the cavity surface, the greater the pressure along the plane. In addition, one may notice the negative pressures which occur at the circumference of the cavity.

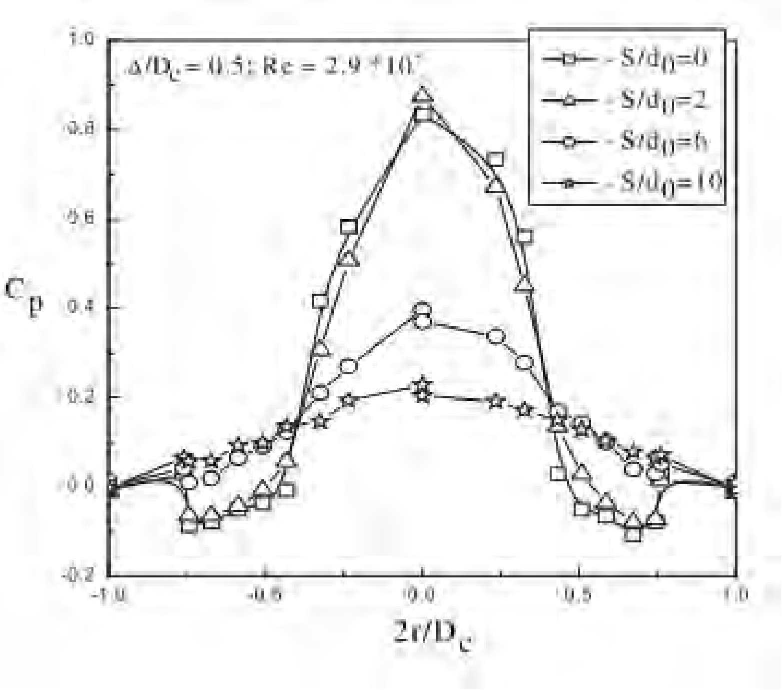

Figure 2.7: Pressure coefficients radially across the cavity with varying nozzle to cavity distances (Terekhov, *et al.,* 2009)

2.7 Measuring velocities and pressures in the laboratory

2.7.1 Introduction

There are two classes of techniques for measuring fluid velocities or pressures in a granular bed. The classes are either intrusive or nonintrusive upon the granular bed. Examples of intrusive techniques are: hot-film anemometers which measure flow velocities and turbulence by gauging the degree of cooling of a heated metal film (Uchiyama & Ide, 2009); velocity bend sensors (VBS) which are a cost effective means of fluid velocity measurement, consisting of a flexible plastic polyimide sheet with an attached electronic resistor (Stewart, *et al.*, 2013); and Pitot-Static tubes which are two concentric tubes which measure fluid pressures in order to calculate the fluid flow velocities (Brown, 2003). Nonintrusive techniques include: laser Doppler velocimetry (LDV) which is a technique where the Doppler shift (shift and reflection of laser beam due to fluid flow) in two laser beams is measured to calculate the velocity in transparent or semi-transparent fluid flows (Fingerson, 1993); acoustic Doppler velocimetry (ADV) which is fundamentally the same as LDV except it uses acoustic sound waves. Both LDV and ADV measure velocity components at a single point; and particle image velocimetry (PIV) which involves inserting tracer particles into a fluid flow, the movement of these particles is traced, and therefore the instantaneous velocity of the particle is obtained (Fingerson, 1993).

PIV is the only method which is able to develop a two-dimensional or even a three-dimensional velocity vector field, while the other methods only measure the velocity at a single point. Nonintrusive techniques are generally limited to transparent or semi-transparent mediums and are therefore not suitable for the confines of a granular bed. Intrusive techniques appear to be better suited for this purpose. Of the intrusive techniques, both hot-film anemometers and velocity bend sensors are not endorsed for use within the confines of a granular bed. This leaves the remaining intrusive technique, the Pitot – Static tube as being best suited, and therefore the literature will be based on this instrument only. From here onwards the Pitot – Static tube will be referred to as the Pitot tube.

2.7.2 Overview and brief history of Pitot tubes

A Pitot tube is a pressure measurement instrument used to measure fluid flow velocities. It is typically used on aircrafts to measure air speed, boats to measure water speed and in industrial applications to measure fluid velocities (Ower & Pankhurst, 1977).

The Pitot tube was invented by the French engineer, Henri de Pitot in 1732 (Brown, 2003). Since then there have been many adaptations to the Pitot tube, the most renowned by Henry Darcy during the 1850‟s and later by Ludwig Prandtl. Often the Pitot tube is referred to as the Prandtl tube due to Prandtl‟s contribution to its development (Goldstein, 1983). Darcy was largely responsible for correcting certain misrepresentations in Henri de Pitot‟s earlier theoretical analysis (Brown, 2003).

2.7.3 Theory of Pitot tube operation

The typical Pitot tube consists of two concentric tubes. Concentric tubes are tubes which share the same axis but have different diameters. The two tubes of the Pitot tube are the impact tube which is the inner tube, and the static tube which is the outer tube (Klopfenstein, 1998). Figure 2.8 illustrates the two tubes (impact and static tubes) separately for illustration purposes. The two tubes will be detailed individually here, starting with the impact tube and followed by the static tube.

The impact tube consists of an opening at the tube's furthermost tip, called the stagnation point. Whereas the furthermost tip on the Pitot tube is called the nose. The impact tube is the top image in Figure 2.8, which shows the stagnation point. At this point the flow velocity comes to rest and the corresponding pressure is transmitted into the tube (Ower & Pankhurst, 1977). This pressure is referred to as the stagnation or total pressure and consists of the static pressure, the pressure and the dynamic pressure. The static tube which is the bottom image in Figure 2.8, consists of a series of circumferential holes, offset from the tube's furthermost tip. The series of holes is called the static points as the flow is at right angles to the holes, and therefore only the static pressure and pressure enter through the holes (Ower & Pankhurst, 1977). Taken individually the stagnation and static pressures would be of little use. However, the difference between these pressures equates to the dynamic pressure, which is used to calculate the velocity of the flow. This velocity is calculated according to Bernoulli's Theorem which is detailed in the following section. The combination of the impact and static tubes which is a typical Pitot tube can be seen in Figure 2.9.

There are Pitot tubes which only consist of the single impact tube or the static tube and thus not the concentric tubes as the typical Pitot tubes have. These Pitot tubes therefore look like the Pitot tubes in Figure 2.8. The top Pitot tube in Figure 2.8 which consists of only the stagnation point was the Pitot tube most relevant in the study as this was the Pitot which was used to take measurements.

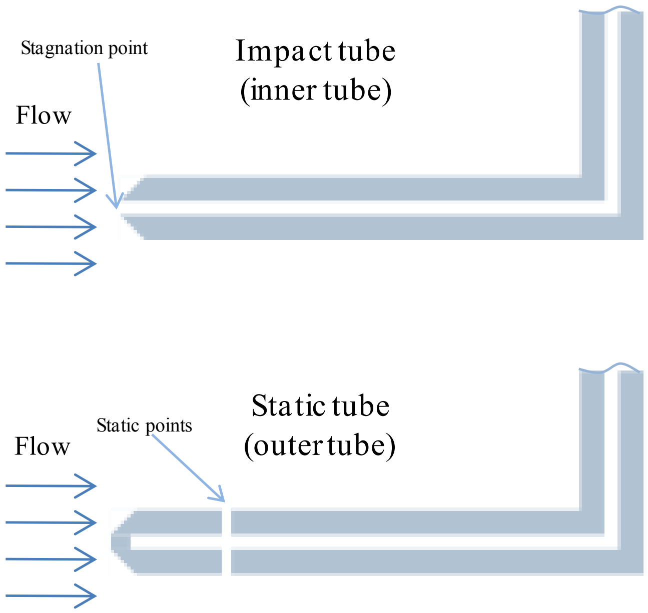

Figure 2.8: Impact and static tubes of a Pitot tube

2.7.3.1 Using Bernoulli’s Theorem for velocity calculation

Bernoulli‟s Theorem is an application of the Conservation of Mechanical Energy Law. The theorem is the conventional means of calculating the velocity of a fluid when using a Pitot tube. The following equation is the Conservation of Mechanical Energy where *H* is the total energy head in meters.

$$H_{(m)} = \frac{V_2^2}{2g} + z_2 + \frac{P_2}{\rho_f g} \tag{2.18}$$

Bernoulli's Theorem enables the equating of energies between two points in an incompressible fluid (Chadwick *et al.*, 2004). In the case of the Pitot tube the two points are points 1 and 2 in Figure 2.9. Point 1 refers to the stagnation point and points 2 refer to the static points of the Pitot tube. Equation 2.18 therefore becomes Equation 2.19 which equates the energy between the two points.

$$\frac{V_1^2}{2g}+z_1+\frac{P_1}{\rho_f g}=\frac{V_2^2}{2g}+z_2+\frac{P_2}{\rho_f g} \tag{2.19}$$

In Equation 2.19, both z_1 and z_2 are equal as the radial centre of the holes at points 2 are the same elevation as point 1. Therefore both z_1 and z_2 cancel each other out. Moreover, V_1 is zero as at the stagnation point the flow comes to rest. Equation 2.19 then becomes the following.

$$\frac{\cancel{V_1}^2}{2g}+\cancel{z_1}+\frac{P_1}{\rho_f g}=\frac{V_2^2}{2g}+\cancel{z_2}+\frac{P_2}{\rho_f g} \tag{2.20}$$

Rearranging Equation 2.20 in terms of V_2 allows one to calculate the flow velocity from the difference between the two pressure readings. This rearrangement is shown in the equation below.

$$V_2=\sqrt{\frac{2(P_1-P_2)}{\rho_f}} \tag{2.21}$$

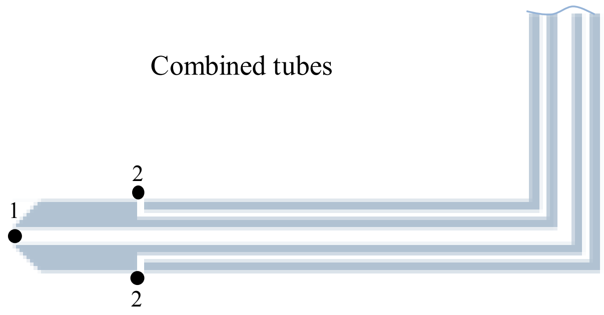

Figure 2.9: Typical Pitot tube with both the impact and static tubes

Figure 2.9 illustrates how the pressures entering through points 1 and 2 are kept separate from each other because of the concentric tubes. In the concentric tubes, it is the elevations of the water surfaces which are used to calculate the pressures. These water elevations are referred to as the pressure heads. The elevations (h) are recorded in mm and are used in the equation below to calculate the corresponding pressure head (P). The corresponding pressure head which is calculated here is what is used in the rearranged Bernoulli equation (Equation 2.21).

$$P=\rho_f gh \tag{2.22}$$

2.7.4 Design of Pitot tube

For both the typical Pitot tube (Figure 2.9) and the Pitot tubes consisting of either the impact or static tube (Figure 2.8), there are two different designs that are in use. These are the L type and the straight type designs. Each of these designs have the same functions and mechanism of measurement. The L type design consists of a 90 degree bend. This bend can be seen in

Figures 2.8 and 2.9. The reason for the two designs is to allow for measurements to be taken in two dimensions.

The nose design of the Pitot tube is very important as it has an effect on the fluid flow. Figure 2.10 shows this effect. In the figure, the top image is a 6/1 ellipsoidal nose and the bottom image is a tapered nose. One might notice that the ellipsoidal nose creates uniform flow and largely parallel flow lines, while the tapered nose creates flow turbulence around the nose. This turbulence is called flow separation and is labelled (1) in the figure. The flow separation can have a dramatic effect on the static points of the Pitot tube, rendering the measurements inaccurate.

The ellipsoidal nose design shown in Figure 2.10 below was developed by the National Physical Laboratory of England. This design is deemed to provide the most accurate measurements due to there being no flow separation (Klopfenstein, 1998).

Figure 2.10: Flow disturbance caused by 6/1 ellipsoidal and tapered nose Pitot tube
(Salter, *et al.* ,1965)

There are a number of companies that manufacture Pitot tubes, such as KIMO, Lambrecht, Dwyer and Okano. These companies may vary their Pitot designs slightly to increase their range of applications. Typically the smallest Pitot tube available has an outer diameter of 3 mm and can have a main shaft length of between 100 to 300 mm.

2.7.5 Pitot tube correction factors

There are a number of correction factors that are continuously being researched and in some cases improved. McKeon, *et al.* (2003) state that there are factors in place to obtain accurate mean velocity profiles when using a Pitot tube. The viscous and displacement corrections are studied here. The viscous correction applies to the contact of the fluid on the Pitot tube and its effect on the fluid flow lines. This correction is a correction factor which is applied to Bernoulli's equation (Equation 2.21). The viscous correction effects the measurement taken at the static point only and therefore is only applied to the Pitot tubes which consist of static tubes. The displacement correction accounts for the disturbance of the Pitot tube's nose on the fluid‟s velocity profile. The displacement correction is simply a shift in the positioning of the Pitot tube for the final measurement. The displacement correction is only applicable to Pitot tubes with the impact tube or which have the stagnation points. Although corrections to the measured pressure readings may be slight, they are nevertheless important for obtaining high levels of accuracy.

2.7.5.1 Viscosity correction

Viscosity is the measure of a fluid's resistance to deformation often caused by other objects moving at different speeds and directions (Chadwick, *et al.*, 2004). The first paper to comprehensively investigate the effects of viscosity is that of Barker in 1922 (Boetcher & Sparrow, 2007). His experimental work showed that at velocities below 60 mm/sec there is a deviation from the adapted Bernoulli‟s law ($P = 0.5\rho_f V^2$), (Barker, 1920). This is due to the viscosity effects that become evident when the kinetic energy is significantly low (Barker, 1920). This low kinetic energy or flow velocity is typically experienced at low Reynolds (Re) numbers (Etemad, *et al.*, 2003). Barker‟s finding has now been recognised as the Barker Effect and is often referred to in more recent studies (Boetcher & Sparrow, 2007). It is therefore at low Re numbers that viscous effects do create errors when simply applying Bernoulli‟s equation. As previously stated, the viscous correction is only applicable for flow over the static points on the Pitot tube.

A correction factor for the application of Bernoulli‟s equation at low Re numbers has since been analysed. Etemad, *et al.* (2003) found a correction factor N which applies to the following equation.

$$V_2 = \sqrt{\frac{\mathrm{N}\left(P_1 - P_2\right)}{\rho_f}} \qquad (2.23)$$

This equation is the refined Bernoulli's equation (Equation 2.21), except the "2" is replaced by the correction factor, N. The reason for this correction factor is that at low Re numbers the frictional losses become prominent over the kinetic energy (Etemad, *et al.*, 2003). Etemad, *et al.* found varying N values for both different Re numbers and distances X. Here X is the distance between the stagnation and static points on the Pitot tube. Figure 2.11 illustrates how these two variables can affect the N value. In the figure it is interesting to note the deviations from N=2, where the N=2 refers to the correction factor in the refined Bernoulli's equation (Equation 2.21).

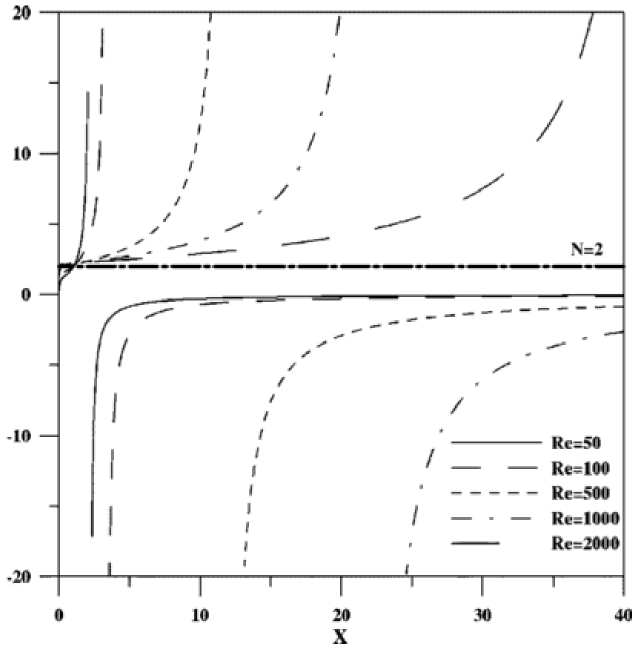

Figure 2.11: Variation of correction factor, N at different distances, X and Re values
(Etemad, *et al.*, 2003)

Boetcher & Sparrow (2007) did a comprehensive study on the effects of viscosity at low Re numbers and were able to establish threshold Re numbers. The tests were conducted using both blunt and hemispherical-nosed Pitot tube head designs. They found the threshold Re numbers to be 65 and 45 for the blunt and hemispherical-nosed Pitot tubes respectively. They state that for Re numbers below these thresholds, the refined Bernoulli equation (Equation 2.21), should be altered whereas Re values above these thresholds need not be altered. The hemispherical and ellipsoidal noses are believed to behave very similarly in the presence of fluid flow (Salter, *et al.*, 1965). Boetcher & Sparrow applied a ratio c_p to Equation 2.21, which is a pressure coefficient defined in Equation 2.24.

$$c_p = \frac{P_{stag} - P_\infty}{\frac{1}{2}\rho_f V_\infty^2} \tag{2.24}$$

c_p is defined as the pressure difference between the upstream or free-stream and the stagnation point of the Pitot tube (Boetcher & Sparrow, 2007). Boetcher & Sparrow suggest a cut-off c_p value of 1.02, which is a 2% deviation and corresponds to an error of 1% in the velocity determination using Bernoulli. The c_p cut-off value was then inspected in terms of the Re numbers for the two respective Pitot tubes. The two threshold Re numbers that were found are shown in Figure 2.12 (Boetcher & Sparrow, 2007). It is recommended that for Re values below these cut-off c_p values, a viscous correction should be applied.

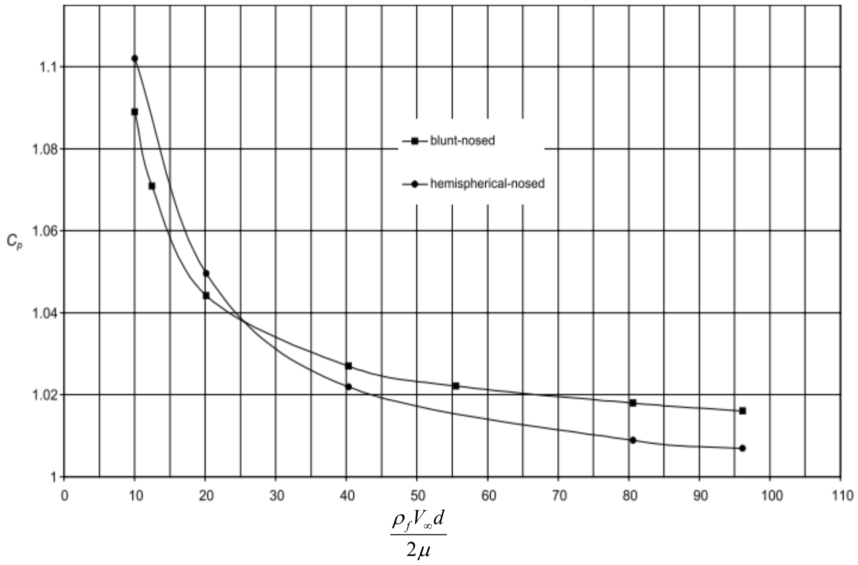

$\mathrm{Re}_{\mathrm{threshold}} \approx 65$ for the blunt-faced tube
$\mathrm{Re}_{\mathrm{threshold}} \approx 45$ for the hemispherical-nosed tube

Figure 2.12: Deviations from Bernoulli at low Reynolds numbers
(Boetcher & Sparrow, 2007)

2.7.5.2 Displacement correction

The presence of a probe such as a Pitot tube in shear water flow causes displacement of the flow (McKeon, *et al.*, 2003). Shear flow is caused by friction acting between the water flow and typically the inner wall of a pipe. The shear creates a curved flow profile known as the velocity gradient, as seen in Figure 2.13. It is due to the velocity gradient that the flow becomes displaced, as shown in the figure. The flow becomes displaced towards the lower velocity flow or towards the boundary layer (typically the pipe wall). The result of this displacement (Δy) is that the Pitot reads a higher pressure than the actual pressure at the geometric centre of the Pitot (McKeon, *et al.*, 2003). This correction is applicable to the impact tube of the Pitot tube, when the stagnation pressure is measured.

There have been a number of equations proposed for estimating the displacement. First MacMillan in 1954, proposed a constant Δy/d value of 0.15; then similar results were obtained by Hall in 1956, Lighthill in 1957, and Chue in 1975. Chue used Patel"s (1965) data to argue that the correction should depend on the local velocity gradient. Chue"s work was formulated into the expression below by Zagarola in 1996 (McKeon, *et al.*, 2003).

$$\frac{\Delta y}{d} = 0.8\alpha\left(1 - 0.17\alpha^2\right) \qquad (2.25)$$

In Equation 2.25, Δy represents the displacement as shown in Figure 2.13; with d the diameter of the Pitot tube; and α the non-dimensional velocity gradient. The non-dimensional velocity gradient will be detailed later (Equation 2.27).

McKeon, *et al.* (2003) argue that the straight lines shown in Figure 2.14 create discontinuity at the pipe's radial centre where flow is very close to uniform (velocity gradient of 0) and there is no shear effect. McKeon, *et al.* subsequently presented a new equation which included a velocity gradient correction, as shown below.

$$\frac{\Delta y}{d} = 0.15 \tanh\left(4\sqrt{\alpha}\right) \tag{2.26}$$

It can be seen that Equation 2.26 equates to a zero displacement for zero shear ($\alpha = 0$) and then asymptotes to the MacMillan correction of 0.15 for large shear ($\alpha \rightarrow 1$) (McKeon, *et al.*, 2003). In Figure 2.14, ---- represents the MacMillan correction; ······ Chue correction; – · · – Hall (1956); – · – Lighthill (1957); and —— the new McKeon correction.

In both Equations 2.25 and 2.26 above, α is the non-dimensional velocity gradient or shear gradient which is defined below; where d is the diameter of the Pitot tube; V the mean velocity; and y_c the distance from the boundary to the Pitot tube centreline (McKeon, *et al.*, 2003).

$$\alpha = \frac{d}{2V\left(y_c\right)} \left.\frac{dV}{dy}\right|_c \tag{2.27}$$

The velocity gradient is typically much greater near the boundary and then decreases towards the centre of the flow. This change in the velocity gradient can be seen in Figure 2.13. Equation 2.27 is applicable for the whole flow profile, this is where the expressions from previous studies were inadequate.

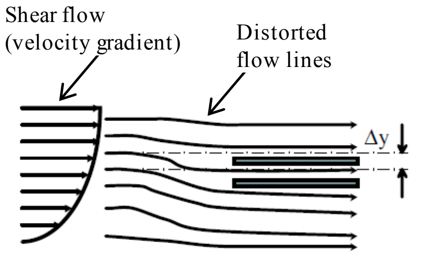

Figure 2.13: Pitot tube displacement in shear flow (McKeon, *et al.*, 2003)

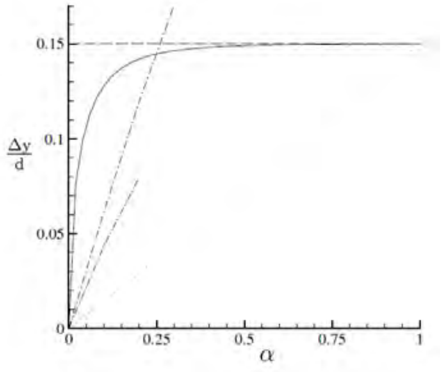

Figure 2.14: Correction factor $\frac{\Delta y}{d}$ vs velocity gradient α (McKeon, *et al.*, 2003)

2.7.6 Calibration factors of different Pitot tube head designs

This calibration factor is a K value that is applied to the Bernoulli Equation (Equation 2.21) similar to the N of the viscosity correction, and becomes the following equation (Ower & Pankhurst, 1977).

$$V_2 = \sqrt{\frac{2(P_1 - P_2)}{\mathrm{K}\rho_f}} \tag{2.28}$$

The head design only affects the measurement taken through the static point and the factor is therefore only applied to the static tube. Modern Pitot tubes can be produced with an already calibrated correction factor. This factor is usually issued by the supplier and can be directly used in the calculations. As previously stated, the ellipsoidal nose design has very little disturbance to the flow and therefore produces a K factor of one (Klopfenstein, 1998).

2.7.7 Calibration procedures of Pitot tubes

Very often, such as in Al-Deen, *et al.* (1996); Uchiyama & Ide, (2009); and Yamanoi, (2011), Pitot tubes are used as calibrators to test and verify other flow measuring instruments like the hot-film anemometer. Apart from ascertaining the initial K calibration factor of a Pitot tube, it is not often that the Pitot tubes need to be calibrated. Typically this calibration is done by comparing the actual readings taken by the Pitot tube with calculated numerical values.

However, there have been some studies involving the calibration of a Pitot tube. One particular study by Klopfenstein (1998), describes the method of calibrating a Pitot tube in a pipe using air flow. The author explains that the Pitot tube should be placed at the location of average velocity which is determined as being at a 0.147d distance away from the wall of the pipe (d being the pipe diameter). The average velocity in the pipe can be calculated by knowing the flow rate and diameter of the pipe. This velocity can then be compared to the velocity recorded by the Pitot tube. The author concludes that the test should be done for various velocities and the subsequent varying Reynolds numbers in order to obtain an accurate comparison of the velocities. This calibration technique is employed in accordance with the National Institute of Standards and Technology (NIST) of the United States (Klopfenstein, 1998).

Another method of calibration is proposed by Boetcher & Sparrow (2007) and Etemad, *et al.* (2003), who calibrated a Pitot tube by solving the full Navier-Stokes equations under laminar, constant property flow conditions. The equations determine flow velocity paths in a stream, which are then related to the actual readings from the Pitot tube. The authors found this method to be adequate at lower turbulence levels, but caution must be taken with the correction factors (detailed in Section 2.7.5) that should be applied to the Bernoulli equation (Equation 2.21). Furthermore the authors determined that this method of calibration cannot be used for a turbulent stream.

2.8 Adequate experimental tank size

This section investigates the size and geometry of tanks in which fluidising experiments have been conducted. The correct size of the tank is of importance in order not to disturb or confine the normal flow paths surrounding a fluidising jet. Lima Neto, *et al.* (2008), experimented with both water jets directed vertically upwards into a water bed. This process is widely used to promote circulation and turbulent mixing in aeration tanks for the chemical industry, reservoir water circulation and in other water bodies. They particularly focused on the water flow surrounding the jet. This helped them to understand the effect that tank geometry and size had on this flow, and were thus able to determine what size of tank would be sufficient in order to limit this effect.

In their experiments, Lima Neto, *et al.* used flow rates of 120 and 180 l/h with an orifice diameter of 3 mm. These two flow rates had calculated Reynolds numbers of 14 140 and 21 231 respectively. Both flow rates were tested in two different size tanks−one square tank of 1.2 m sides and another rectangular tank of 1.2 by 1.8 m sides. An Argon ion laser was used to record the velocity fields and streamlines surrounding the jets. The authors put emphasis on the circulation cells which the streamlines formed. Figure 2.15 illustrates these cells, in which z is the vertical distance and r is the radial distance from the jet orifice.

In Figure 2.15 A refers to the streamlines found in the square tank of 1.2 m sides; B and C the streamlines in the rectangular tank of 1.2 by 1.8 m sides, where B is the 1.8 m side and C the 1.2 m side.

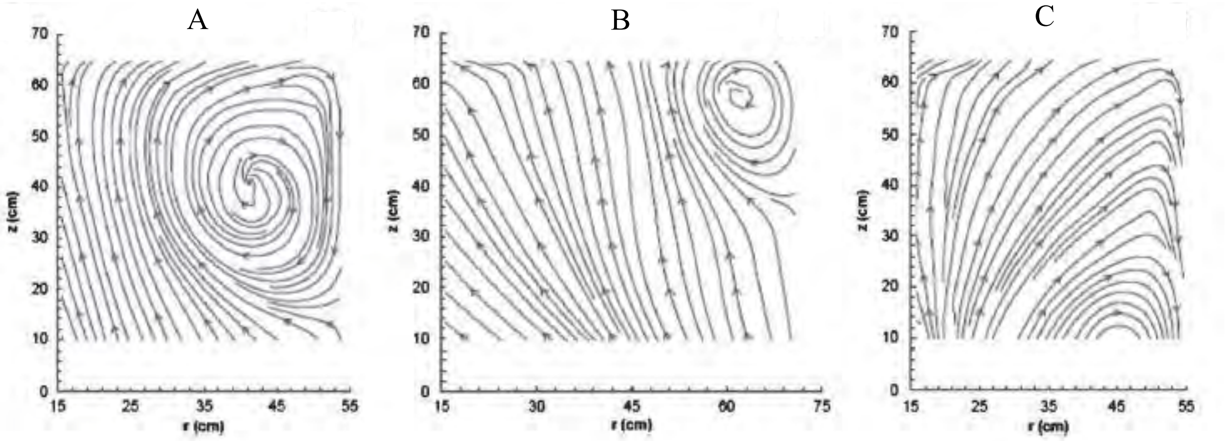

Figure 2.15: Streamlines due to the water jet in square tank (A), rectangular tank's longer planes (B), and shorter planes (C) (Lima Neto, *et al.*, 2008)

Lima Neto, *et al.* found that a rectangular tank produces 3D flow, caused by the different side wall lengths. This 3D flow can be seen by the difference in the streamlines of Figure 2.15 B and C. Another important aspect that was found is that the streamlines fill the entire tank volume, even though proportionally the tank is far larger than the jet. Lima Neto, *et al.*

concluded that more extensive research needs to be conducted in order to determine the actual threshold tank size at which flow becomes disturbed.

2.9 Previous studies on internal fluidisation

There has not been a considerable amount of literature that focuses on internal fluidisation which is relevant to this research. Of what there is available, the most relevant literature for this study is that of: Zoueshitiagh & Merlin, (2007), Alsaydalani, (2010), Ma, (2011), and van Zyl *et al.*, (2012). Descriptions of these studies and their results are given below.

2.9.1 Vertically flowing water jet under a bed of glass beads by Zoueshitiagh & Merlin, (2007)

Zoueshitiagh & Merlin (2007) experimented with the effects of a water jet penetrating vertically upwards underneath a granular bed. Typical application of this process is found in coastal engineering where navigable waterways are kept open. In their experiments the bed consisted of either granular material or glass beads. They analysed their experimental results by comparing them with previously developed theoretical and numerical models. The water jet was varied by changing the flow rates, orifice diameters and granular bed height.

The experimental setup, which can be seen in Figure 2.16, consisted of a vertical Plexiglas cylinder with an internal diameter of 240 mm. Interchangeable sub-cylinders which are pointed out in the figure, have internal diameters of 3, 15 or 35 mm and fitted centrally on a disk. Together this formed the base of the vertical cylinder. The sub-cylinders then formed the different diameter orifices. A grid of 210 μm was placed above each sub-cylinder to avoid bed material from entering the water source. The water level in the cylinder was kept above the varying height of the bed, to ensure complete bed saturation. The bed was monitored using a CCD video camera set at two locations.

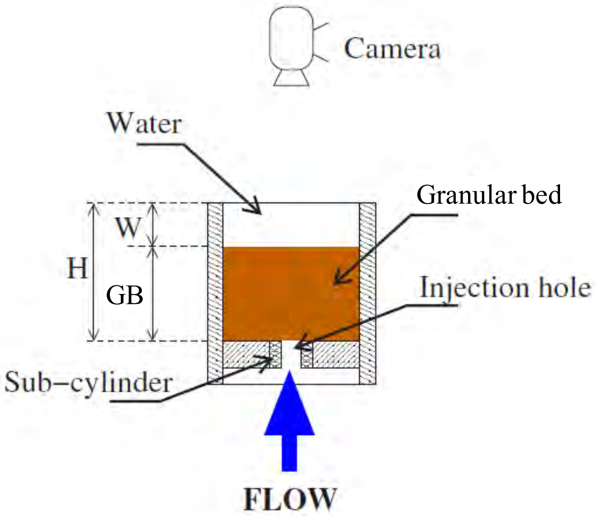

Figure 2.16: Zoueshitiagh & Merlin's experimental setup

Zoueshitiagh & Merlin (2007) grouped their findings from the experiments into three regimes. These regimes were influenced by the increasing flow rates fed into the system. Regime one consisted of a motionless bed occurring at low flow rates. Regime two was when the bed deformed locally. This was only apparent at large enough flow rates, and formed a bump shape on the bed surface. It was found that the deformation was less noticeable when using the glass beads. Most importantly the authors state that in this regime there is likely to be internal fluidisation located at the injection of the jet. This regime therefore has potential for further research on internal fluidisation.

The third regime was observed to have local fluidisation to the surface of the granular bed. This regime occurred at flow rates greater than those of Regime two. Material in this regime moved in a chimney or wedge shape motion above the orifice and up to the bed surface while the material surrounding the chimney was at rest and acted as a solid porous skeleton. Figure 2.17 contains two images captured directly above the granular bed at different stages in Regime three. Image B reflects a higher flow rate than image A. In the figure one can see fluidisation appearing on the bed surface.

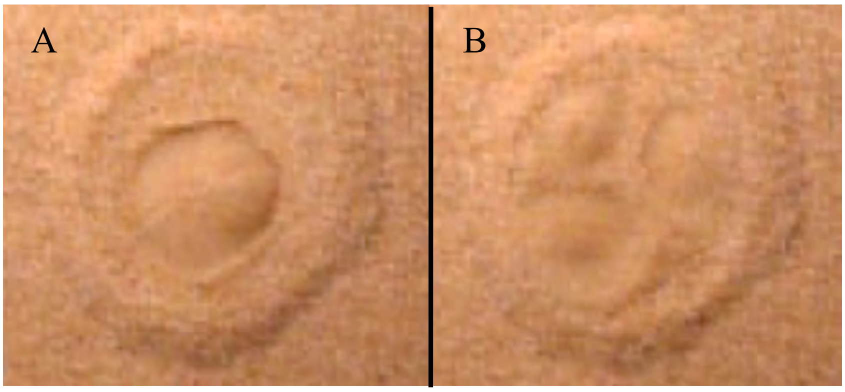

Figure 2.17: Fluidisation reaching the granular bed surface (Zoueshitiagh & Merlin, 2007)

Zoueshitiagh & Merlin"s test findings using both a granular bed and glass beads are listed below:

- Chimney diameter is almost independent of the orifice size at a given flow rate.
- The flow rate required for the start of internal fluidisation is dependent on the bed height.
- In the case of sand grains, the water supply pressure at the start of internal fluidisation is approximately 3 times the pressure needed to maintain internal fluidisation
- In the case of glass beads, the water supply pressure at the start of internal fluidisation is only 1.24 times the pressure needed to maintain internal fluidisation.

2.9.2 Internal Fluidisation of Granular Material by Alsaydalani, (2010)

Alsaydalani (2010) investigated the effect of a water jet positioned vertically upwards penetrating a granular bed of sand. In the experiments the author varied three parameters: the jet flow rate, the orifice dimensions and the granular medium (particle size and shape). These tests were done in order to develop an understanding of the mechanics behind internal fluidisation of granular mediums.

The experiments were conducted in a Plexiglas tank, of dimensions 1060 mm x 550 mm x 153 mm. A machined aluminium box was attached to the bottom of the tank. This box was designed with an idealised longitudinal crack that served as the orifice. It had dimensions 330 mm x 152 mm x 105 mm. The remaining equipment included a pump, pressure gauges, measuring cylinders, tubes and a sight tube panel assembly. Figure 2.18 is a representation of the experimental setup used by Alsaydalani.

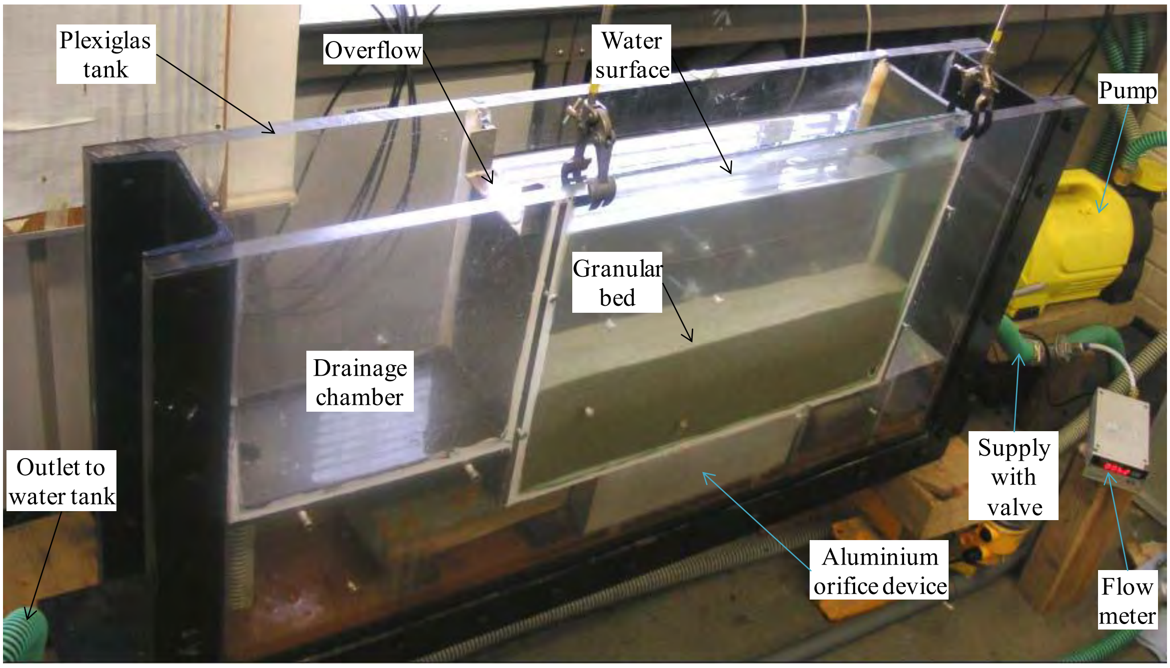

Figure 2.18: Schematic of Alsaydalani's experimental setup (Alsaydalani, 2010)

Two types of granular mediums i.e. Silica sand and Leighton Buzzard Sand (LBS) were tested separately. These mediums have average particle diameters of 0.9 mm and 1.6 mm respectively. With the use of a funnel, the mediums were rained into the seepage tank which was partially filled with water. This prevented any air pockets from forming within the granular bed.

The experiment was monitored using sight tubes and Particle Image Velocimetry (PIV). The sight tubes were used for pore pressure measurement during the preliminary tests. This measurement was done through six holes which were drilled through the back wall of the tank. The holes were located directly above the orifice at 10, 53, 102, 150, 220 and 300 mm. Needles with a 2 mm inner diameter were then fed in through the holes. The needles were connected to the sight tubes where the pressures relating to the water elevation could be read. The PIV technique was used to monitor the behaviour of granular mediums in the internal fluidisation. The PIV consisted of a light source, a camera, a board with gridlines, and image processing software to track the movement of the particles.

Experiments were run with increasing flow rates until complete fluidisation up to the granular bed surface was observed. Alsaydalani described the process he observed as follows: initially there was no observable grain movement. As the flow rate was increased though, an uplift mechanism occurred, moving particles away from the orifice and providing a small internal fluidised zone where particles could move rapidly and freely. As the flow rate increased further, the internal fluidised zone grew taller until eventually with an even greater flow rate the fluidised zone reached the granular bed surface. Figure 2.19 shows the fluidised zone reaching the bed surface.

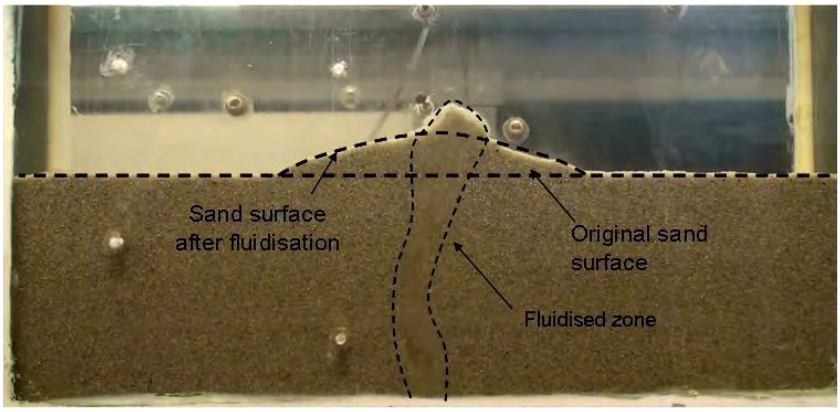

Figure 2.19: Fluidised zone with a bed depth of 150 mm and a 0.33 mm thick orifice (Alsaydalani, 2010)

By observing the fluidisation process, Alsaydalani drew the following conclusions:

- A static cavity which is a localised zone of displaced particles, forms prior to the onset of internal fluidisation. The cavity allows particles to circulate which at higher flow rates caused internal fluidisation.
- Greater flow rates are required to initiate internal fluidisation in a coarser granular bed. Particle size does therefore have an effect on fluidisation.
- Neither the size of the orifice nor the depth of the bed has any effect on the fluidised zone.
- The weight of material displaced at the start of internal fluidisation is approximately equivalent to the uplift force exerted by the fluidising jet.

2.9.3 Internal fluidisation due to horizontal seepage by Ma, (2011)

This study by Ma was a continuation of the study by Alsaydalani (2010). Ma did modifications to Alsaydalani's experimental setup to investigate fluidisation from a horizontal jet of water injected into a bed of sand, which might occur through a defective sheet pile. Ma's experimental setup functioned similar to Alsaydalani's, except the water was injected from the side of the tank and not from below, thus creating a horizontal internal fluidising jet.

Ma's experimental setup is illustrated in Figure 2.20 which is similar to Alsaydalani's setup shown in Figure 2.18. In Figure 2.20, Tube A to Tube E illustrate the locations where the jets could be individually injected into the sand bed, although Tube A was not used in the experiments. This allowed for different sand bed heights to be investigated. In the experiments two types of Leighton Buzzard Sands of different diameter ranges were used. The two diameter ranges were 0.6 to 1.18 mm and 0.09 to 0.15 mm. In the experiments the injected flow rate through the different tube locations was increased from 0 l/min until the internal fluidisation reached the bed surface.

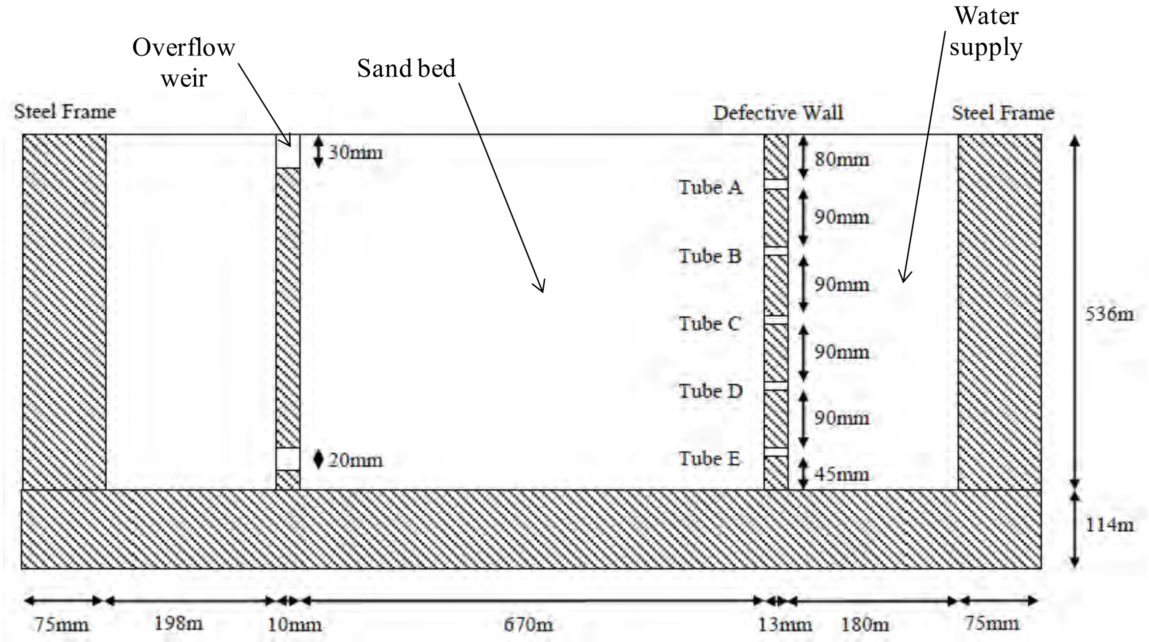

Figure 2.20: Side view drawing of experimental setup (Ma, 2011)

Ma examined the occurrences at the increasing flow rates for the two types of sands. He described the 0.6 - 1.18 mm diameter sand's first occurrence by forming a cavity outside of the orifice at low flow rates. When the flow rates increased further, internal fluidisation began to occur. At even higher flow rates the internal fluidisation broke through the bed surface. The flow rates at the formations of the cavities, internal fluidisation and when fluidisation reached the bed surfaces were recorded and analysed. The occurrences for the 0.09 - 0.15 mm diameter sand was slightly different. At a low flow rate a very small cavity appeared. Where at increasing flow rates the cavity directly transformed into an open fluidised bed. An open fluidised bed is when the fluidisation reached the sand bed surface. Therefore a stable internal fluidisation area did not occur for the smaller diameter sand sample.

The experimental results were analysed by assessing the affects of air bubbles, bed height and particle size on the cavity, internal fluidisation and the open fluidised bed. The pressures within the tank, in the absence of the sand bed, at various flow rates were also analysed.

Figure 2.21 is a plot showing the flow rates for the formation of internal fluidisation at the different bed heights for both the sand samples. Whereas Figure 2.22 is a plot of the pressure within the tank at various flow rates. These pressure readings were taken when the sand was removed from the tank, thus the water jet penetrated a bed of water.

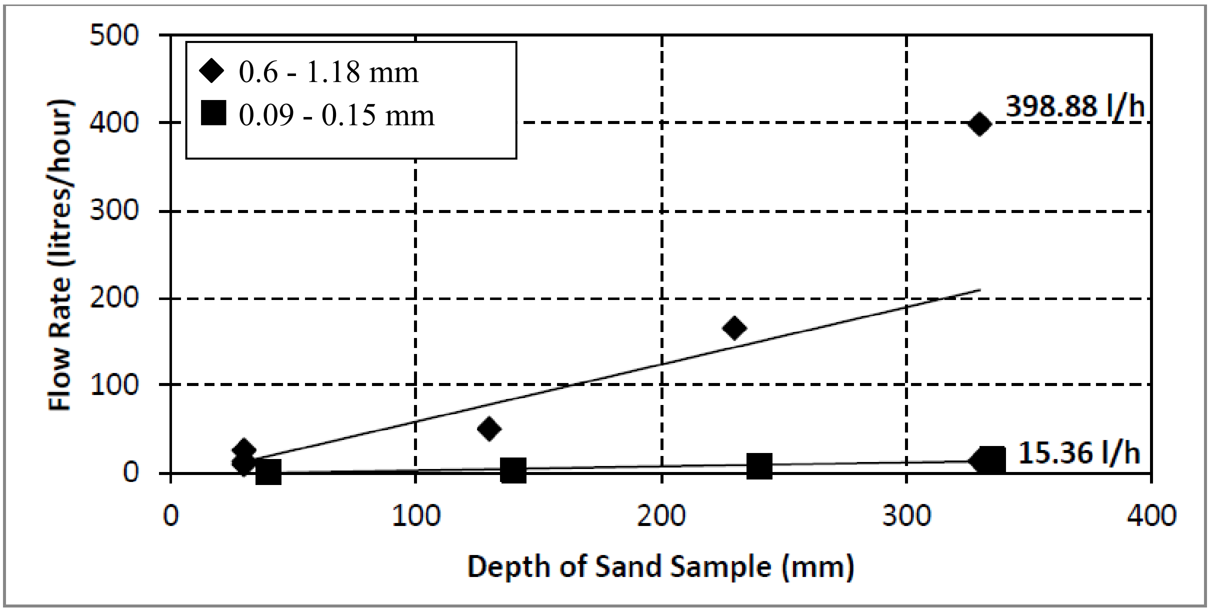

Figure 2.21: Flow rates at formation of fluidised zones at different bed heights (Ma, 2011)

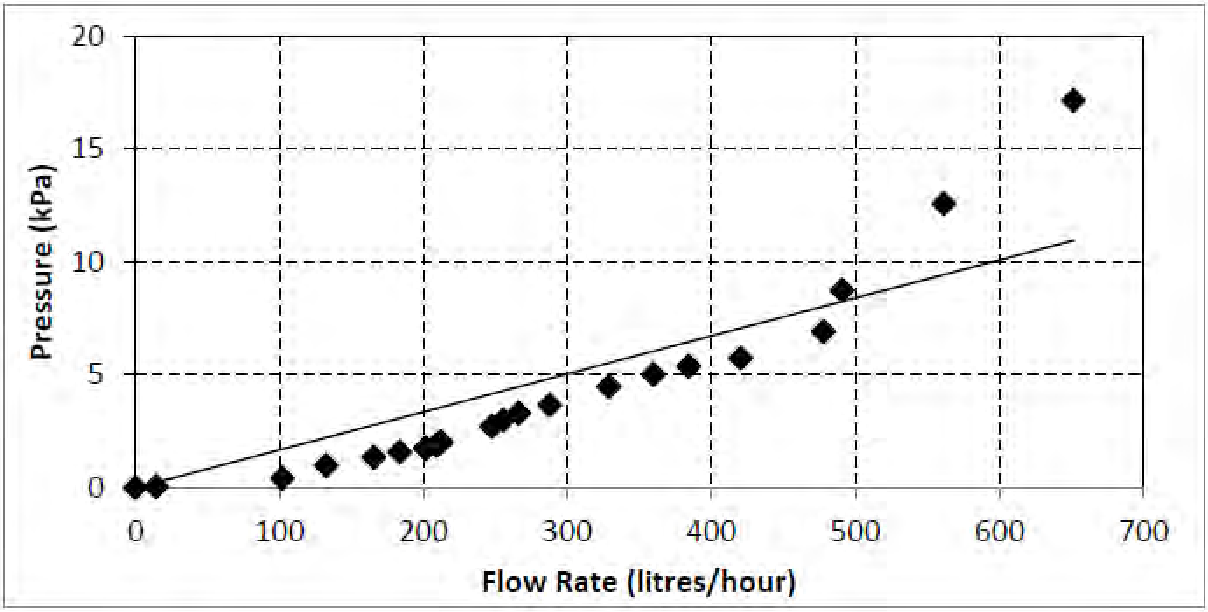

Figure 2.22: Pressure of injected water at various flow rates (Ma, 2011)

Ma concluded the following from the study of a horizontal internal fluidising jet:

- The geometry of the internal fluidisation was dependant on the following: the profile of the injected flow; the bed height (depth of jet); and lastly the injected flow rate.
- The formation of the cavities and the internal fluidisation were achieved at lower flow rates in the smaller diameter sand sample.
- The greater the bed height, the greater the flow rate required to form a cavity and subsequently internal fluidisation.
- At increasing flow rates of the jet, increasing pressures were found.
- The addition of air bubbles in the injected jet resulted in the increase in size of the internal fluidisation area.

2.9.4 Preliminary observations of fluidisation in distribution pipes by van Zyl, *et al.* (2013)

This research was done as a preliminary study to investigate the effect soil has on a leaking water pipe. They investigated an internal fluidising water jet positioned vertically upwards, penetrating a bed of glass beads (glass ballotini). The jet was produced by a single round orifice of varying diameters (2, 4 and 8 mm). The experiment was conducted in an 8 mm thick walled Perspex tank with the dimensions 1 000 x 200 x 500 mm high. The interchangeable orifice was placed 2 mm from the front wall of the tank and protruded 98 mm vertically into the tank. The position of the orifice can be seen in both the side and front views of the experimental setup shown in Figure 2.23. In their experiments the excess water pressure in the bed was measured.

This was done by a number of 1 mm diameter drilled holes in the front wall of the tank. The holes are labelled “pressure tapings” in Figure 2.23. Blunted hypodermic syringe needles with 0.9 mm internal diameters were introduced through these holes. The needles were then connected to sight tubes where pressure readings could be taken. The holes were drilled on one side of the orifice centreline, due to the symmetry of the fluidised zone.

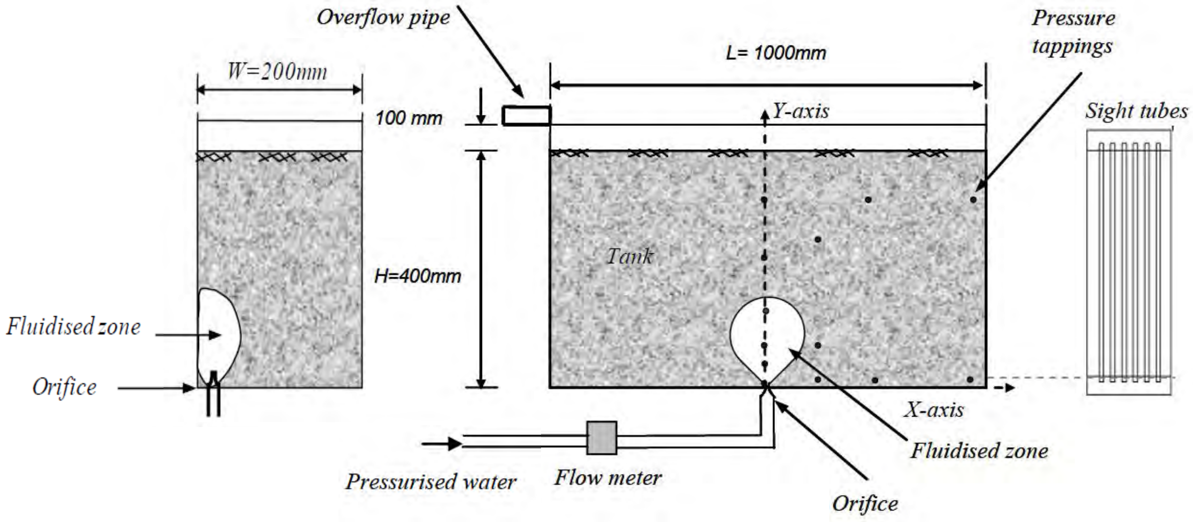

Figure 2.23: Experimental setup of van Zyl, *et al.*− side and front view
(van Zyl, *et al.*, 2013)

The experiment was prepared by filling the tank with water first and then adding the ballotini to a depth of 400 mm. The flow rate was increased in steps from a minimum of 220 l/h to a maximum of 850 l/h. An electromagnetic flow meter was placed upstream of the orifice to record the flow rates. The size of the internal fluidised zone for the allocated flow rates and the corresponding pressure head in the ballotini bed was recorded.

One of the objectives of the experiments was to assess the geometry of the internal fluidised zone and so the orifice setup in this experiment differed slightly. A 60 mm long, 6 mm diameter tube was cut in half laterally and fixed to the front wall of the seepage tank. This allowed for accurate visual inspection through the Perspex wall of the tank. Three distinct zones were observed in these experiments: the fluidised, mobile and static bed zones. These zones can be seen at three different flow rates in Figure 2.24.

Fluidised zone:

This zone was a high velocity water jet, starting from the orifice and ending in a vortex movement. ballotini particles entered the zone at the orifice. They were then deposited back into the mobile bed zone at the head (top) of the jet. The body of the fluidised zone was found to be stable, whereas the head tended to move from side to side.

Mobile zone:

This zone surrounded the fluidised zone. Ballotini particles were observed moving steadily from the fluidised zone head down towards the orifice at which point they were picked up by the fluidised zone again.

Static zone:

This was the outermost zone, where the ballotini remained unaffected by the water jet.

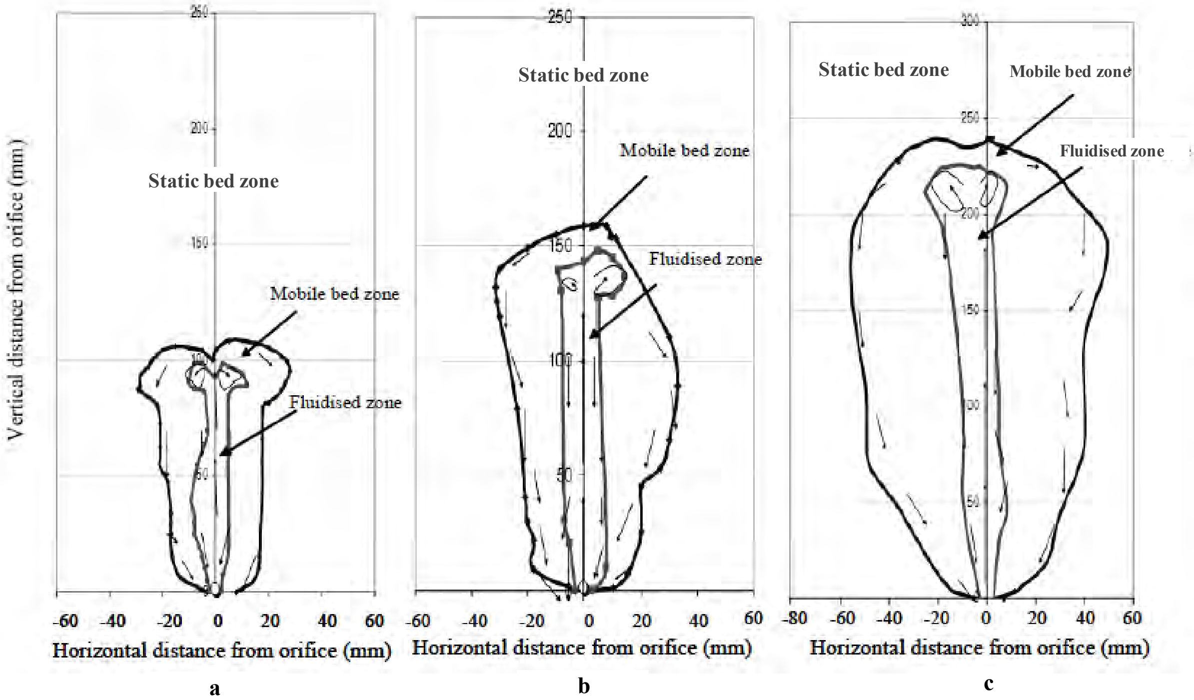

Figure 2.24: Visual observations of the three distinct zones for flow rates: (a) 130; (b) 220; and (c) 320 l/h (van Zyl, *et al.*, 2013)

The following list contains the findings of van, Zyl *et al.* (2013).

- The majority of the head loss existed in the fluidised bed and mobile bed zones. Orifice head loss was less in these two zones, but still substantially more than the head loss in the static bed zone, which had the least.
- It is the orifice flow rate rather than the orifice diameter which controls the excess pore water pressure at various depths in the bed, as well as the height of the fluidised zone.
- Under ideal conditions, the soil surrounding water distribution pipes is unlikely to have much impact on the pressure-leakage relationship.
- High pressure heads can be sustained by a granular bed without visible piping at the ground surface and this may well be the reason for many leaks going undetected.

2.10Literature summary

Fluidisation has been found to occur in a number of applications, specifically in chemical engineering, soil mechanics, earthquake dynamics and geology. In the context of the leak-soil interaction, fluidisation has been referred to as internal fluidisation which exists in the soil outside of a leak in a buried water distribution main (Ma, 2011). Internal fluidisation is caused by a localised fluid injection and results in soil particles losing their stability creating their movement (Alsaydalani, 2010).

Research conducted specifically on internal fluidisation to analyse the leak-soil interaction is limited. The research which is available is that of Lawrence, (2008); Alsaydalani, (2010); Ma, (2011); van Zyl, *et al*. (2013); and Cui, *et al.*, (2014).

Van Zyl, *et al*. (2013) experimented with a leak directed vertical upwards in ballotini (glass beads). They identified three zones in the leak-soil interaction space: a fluidised zone outside the leak with particles moving at high velocity to a terminating head, a mobile bed zone where tightly packed particles move slowly back to the origin of the jet and a static bed zone. The study found that the majority of the mechanical energy in the leakage jet is dissipated through the orifice and the two inner (fluidised and mobile bed) zones. Surplus pressure in the fluidised zone increased rapidly and reached a maximum at the terminating head. Finally, the study concluded that substantial pressures may be sustained within the pipe without the fluidised zone extending to the surface of the ballotini bed. This means that even leaks directed upwards may not become visible on the soil surface, making them more difficult to detect.

Alsaydalani (2010) did an experimental study on internal fluidisation using different types of sands. The author increased the flow rate until internal fluidisation initiated, which was found to be the point where the seepage force exceeds the buoyant weight of the particles located in a wedge shape above the orifice. The seepage force which controls the onset of internal fluidisation was found to be dependent on the flow rate, particle size, sphericity, bed height and permeability.

Ma (2011) continued Alsaydalani‟s work by experimenting with a horizontal water leak into different sands, and found similar results. Cui, *et al.*, (2014) did a numerical study on internal fluidisation and found good correlations with Alsaydalani‟s experimental results, both for the onset of internal fluidisation and the angle of the fluidisation wedge.

In the author's knowledge, to date there has not been an experimental study which quantifies the pore and dynamic pressures due to an undisturbed water jet (jet away from experimental tank walls) in a three dimensional space. Furthermore, an experimental method which can accurately and repeatedly measure pore and dynamic pressures in the confinement of a ballotini bed has not been presented. Therefore, this study was aimed at both developing an experimental method to measure pore and dynamic pressures, and to quantify these pressures in an undisturbed bed.

Chapter 3

3 Methodology

An experimental study was done to investigate the internal fluidisation phenomenon occurring in a granular bed, typically caused by a leak in a water distribution pipe. Internal fluidisation involves a complex interaction between the leaking water and the soil surrounding the pipe. The experimental setup that was developed consisted of a glass tank which contained the granular bed surrounding a water leak. Instruments which were supported by the glass tank were then inserted into the granular bed where they measured pore pressures and dynamic pressures which is the flow velocities, generated by the water leak. The experimental setup therefore facilitated the analysis of this complex interaction where pore pressures and flow velocities were measured. In the experiments the granular bed represented the soil surrounding a distribution pipe.

This chapter firstly contains an overview of the experimental setup, followed by details of each piece of apparatus used. After this the calibration and verification procedures conducted on some of the apparatus are detailed. Then the repeatability of the experimental results are analysed, followed by a methodology review of how the measurements were taken. Lastly, the experimental observations are discussed.

3.1 Overview of experimental setup

This section briefly describes the experimental setup and its functionality.

The experiments were conducted in a glass tank filled with glass ballotini, where the ballotini represented the granular bed surrounding a water distribution pipe. The glass tank can be seen in Figures 3.1 and 3.2, and the ballotini can be seen in Figure 3.2. Two holes in the base of the glass tank consisted of orifices through which water passed and made up part of the inlet network. With the use of a valve shown in Figure 3.2, water was directed via pipes to either one of these orifices, creating a vertical fluidising jet in the ballotini bed. This fluidising jet simulated the occurrence of a leak in a water distribution pipe. One of the holes was located in the centre of the tank base and the other at the front edge of the base (against the front wall of the tank). Figure 3.1 is a plan view photograph of the experimental setup. The photograph was taken before the tank was filled with ballotini and therefore the two inlet holes are visible and are labelled in the figure. Also in Figures 3.1 and 3.2 one might notice the drainage hole, which was a third hole in the base of the glass tank. The drainage hole served to drain the tank of its water after the experiments were completed.

In order to measure pore pressures and dynamic pressures in the influence zone outside of the leak caused by the fluidising jet, two types of Pitot tube instruments were used. Each Pitot tube was used separately by vertically inserting them into the ballotini bed. Measurements were taken by one Pitot tube at a time. The Pitot tubes were secured by the Pitot tube positioning system. This positioning system which is labelled in both Figures 3.1 and 3.2, was mounted on the top four corners of the glass tank. The system consisted of individual supporting, levelling and positioning components. The supports were aluminium corner support blocks that slotted onto the four top corners of the glass tank and provided a base for the remainder of the Pitot tube positioning system. The levelling components were placed on each of the aluminium corner support blocks. Finally, the positioning components were placed on top of the levelling components. The purpose of the Pitot tube positioning system was to allow for movement in the X, Y and Z planes of the Pitot tube, while still securing the Pitot tube when measurements were taken. The Pitot tube positioning system also included three steel rules. These steel rules, which can be seen in Figure 3.1, enabled the geo-referencing of the Pitot tube. Therefore, the precise position of the Pitot tube measuring point would be known when it was in the granular bed.

The top end of the Pitot tube was connected to clear flexible tubing, where the other end of the tubing was connected to a glass sight tube. The subsequent pore pressures and dynamic pressures which the Pitot tubes measured were transmitted via the clear tubing into the sight tube. Figure 3.2 is a labelled photograph of the complete experimental system.

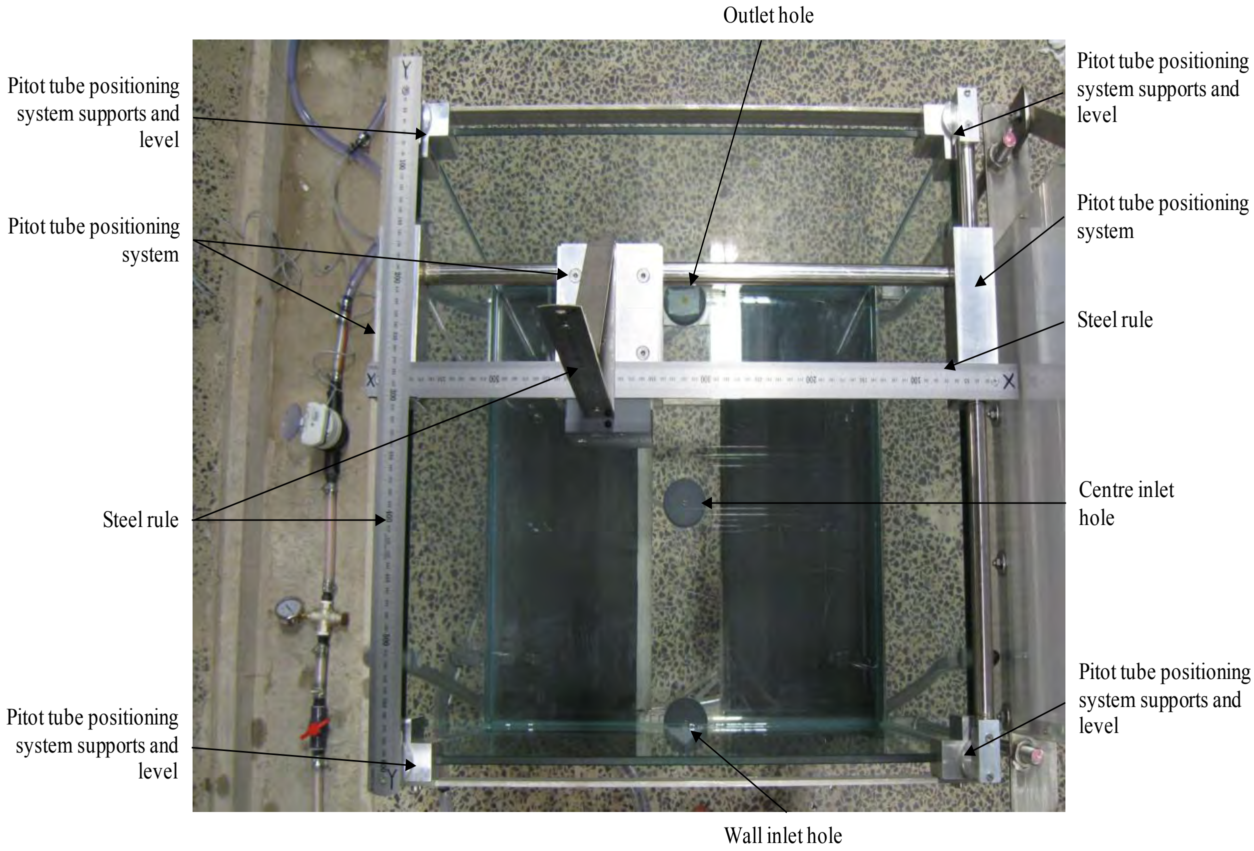

Figure 3.1: Photograph of complete experimental system (plan view)

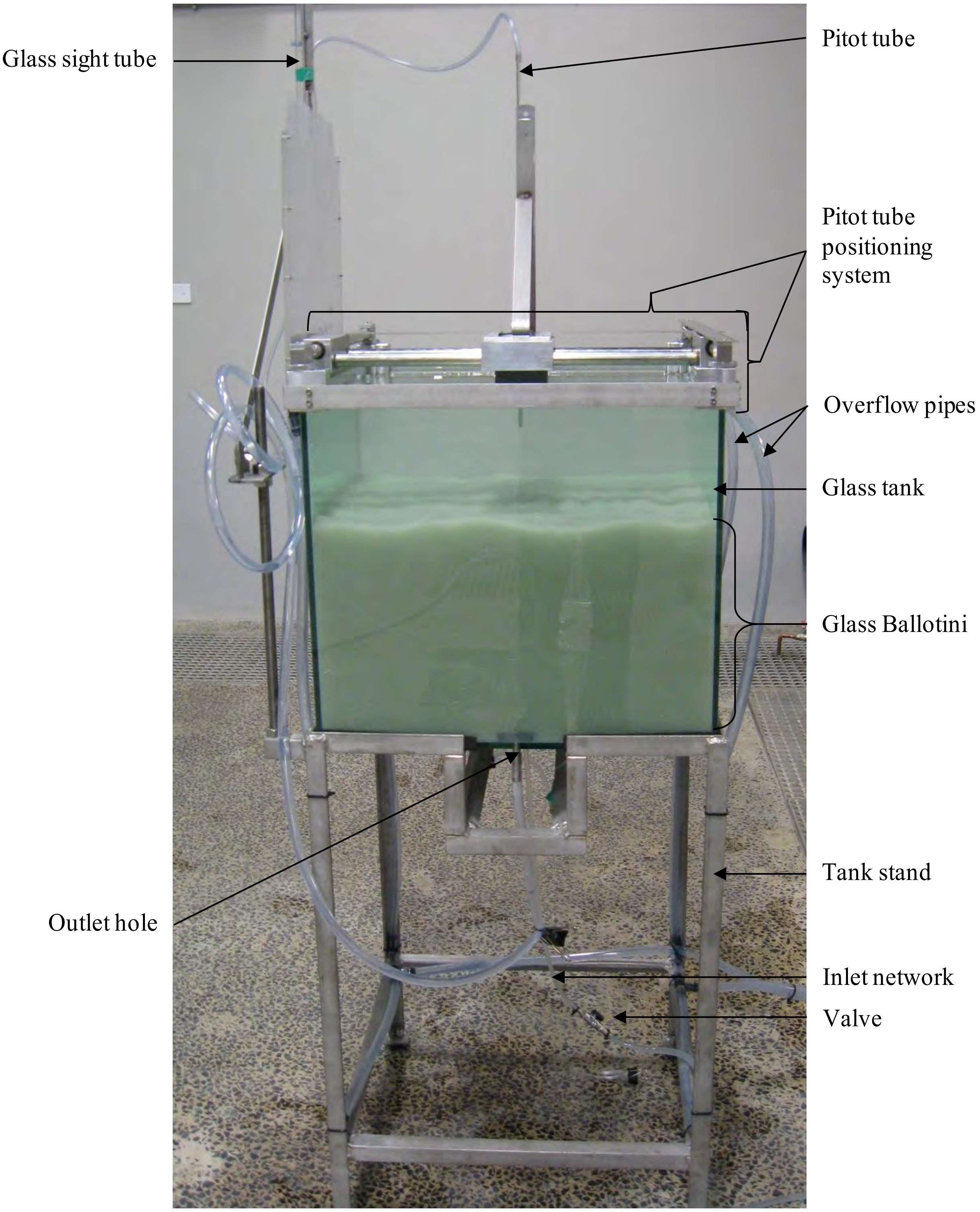

Figure 3.2: Photograph of complete experimental system (side view)

3.2 Detailed design of complete experimental setup

What follows is a list of all the equipment that were used in the experiments. A detailed description of the equipment is included after the list.

- Glass tank
- Glass ballotini (glass beads)
- Inlet network
- Outlet network
- Flow meter
- Valves and gauges
- Water supply
- Pitot tubes
- Pitot tube positioning system
- Glass sight tube
- Steel rules
- Stand

3.2.1 Glass tank

The glass tank served to contain the glass ballotini. It also served as a support for the Pitot tube positioning system. Furthermore the tank had holes in its walls and base which served as connections for both the inlet and outlet network pipes. The glass tank can be seen in Figures 3.1 and 3.2. The connection points on the tank for the inlet network were two holes in base of the tank. One of the holes was in the centre of the base while the other hole's centre was 3 mm from the front wall of the tank. A third hole which was a drainage hole was in the tank base and was part of the outlet network. An additional four holes were located on the upper regions of two of the tanks side walls, which were also part of the outlet network. These holes serve as the overflows to maintain a constant water height in the tank. The precise positioning of all the holes in the tank can be seen in the design drawings found in Appendix A.

The tank was made from glass as it is scratch-resistant and transparent. The outer dimensions of the tank were 566 mm square by 488 mm high. The tank size ensured that the tank walls had little or possibly no disturbance on the flow of water through the granular bed. During the designing of the tank, care was also taken to ensure that enough ballotini were available to fill the tank to the required depth.

The thickness of the glass was calculated using an Excel based glass calculator, supplied by Marine Aquariums South Africa. Figure 3.3 shows a preview of the calculator in Excel.

Although the calculator was designed for aquarium tanks which typically have a sand layer of not more than 100 mm on their base, large safety factors were applied in order to counter this. These large safety factors can be seen in the green shaded blocks in the figure. The tank was built to a final wall thickness of 8 mm and a base thickness of 12 mm.

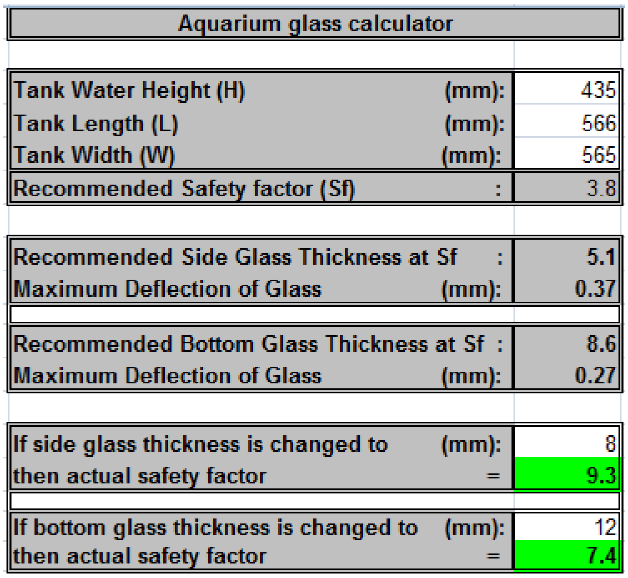

Aquarium glass calculator		
Tank Water Height (H)	(mm):	435
Tank Length (L)	(mm):	566
Tank Width (W)	(mm):	565
Recommended Safety factor (Sf)	:	3.8
Recommended Side Glass Thickness at Sf	:	5.1
Maximum Deflection of Glass	(mm):	0.37
Recommended Bottom Glass Thickness at Sf	:	8.6
Maximum Deflection of Glass	(mm):	0.27
If side glass thickness is changed to	(mm):	8
then actual safety factor	=	9.3
If bottom glass thickness is changed to	(mm):	12
then actual safety factor	=	7.4

Figure 3.3: Glass thickness calculator preview (Marine Aquariums South Africa, 2014)

3.2.2 Glass ballotini (glass beads)

The granular bed consisted of glass ballotini which are glass beads. Typically water distribution pipes are laid with a surrounding bed of sand. In the experiments, the ballotini replaced the sand and represented an idealised sand medium. Certain characteristics such as density and grain order size of the ballotini are similar to sand. In previous studies by van Zyl *et al.* (2013) and Lawrence (2008) the same ballotini was used, logically this ballotini was therefore used in these experiments too. The fluidising jet penetrated into this granular bed of ballotini.

In the experiments, the ballotini were placed in the glass tank to a depth of 300 mm, and the subsequent total volume of ballotini was 0.0908 m^3. The ballotini consisted of a diameter range from 0.6 mm to 0.8mm. This range is shown in the particle size distribution curve in Figure 3.4. A magnified photograph of a sample of ballotini is shown in Figure 3.5. In Figure 3.5 the difference in particle diameter can be observed, as well as the interesting sphericity of the particles.

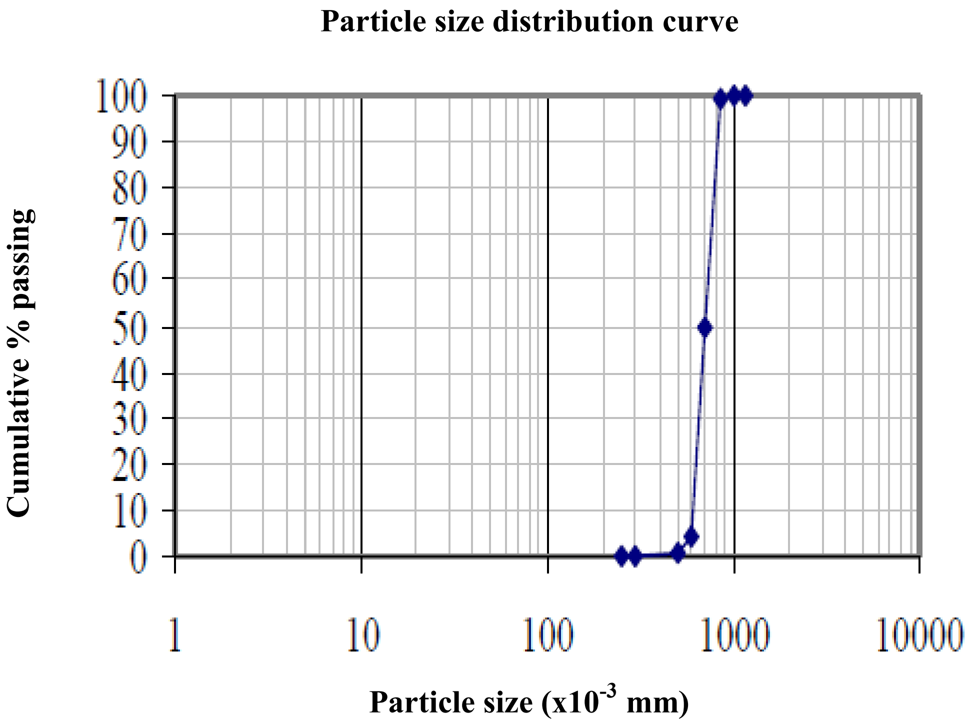

Figure 3.4: Particle size distribution curve (Lawrence, 2008)

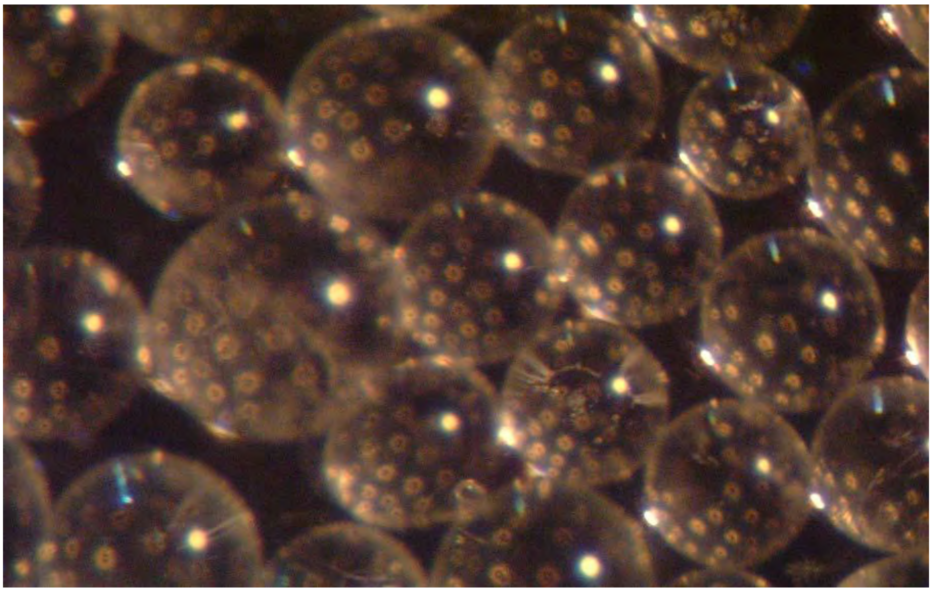

Figure 3.5: Microscopic view of glass ballotini (Lawrence, 2008)

These particular ballotini had been subject to soil tests prior to being used in these experiments. The results of the tests are shown in Table 3.1.

Table 3.1: Glass ballotini specifications

Specification	Value
Bulk density (Lawrence, 2008)	14.74 kN/m^3
Particle density (Lawrence, 2008)	23.40 kN/m^3
Porosity (Lawrence, 2008)	0.39
Sphericity (Lawrence, 2008)	0.988 (sphere = 1)
Hydraulic conductivity (Lawrence, 2008)	0.199 cm/s

3.2.3 Inlet network

A water supply network conveyed water to two orifices located in the base of the glass tank. Only one of the orifices received water at a time, while the other was closed off. A section view of one of the orifices is shown in Figure 3.6. The orifice located against the front wall and the orifice at the centre of the tank base had internal diameters of 2.8 mm and 3 mm respectively. An important consideration in the design of the orifices was to ensure that the flow passing through the orifices was undisturbed. This was accounted for by ensuring that the upper end of the orifices had a constant inner diameter for a length over 10D, where D was the internal diameter. This constant diameter is evident in Figure 3.6.

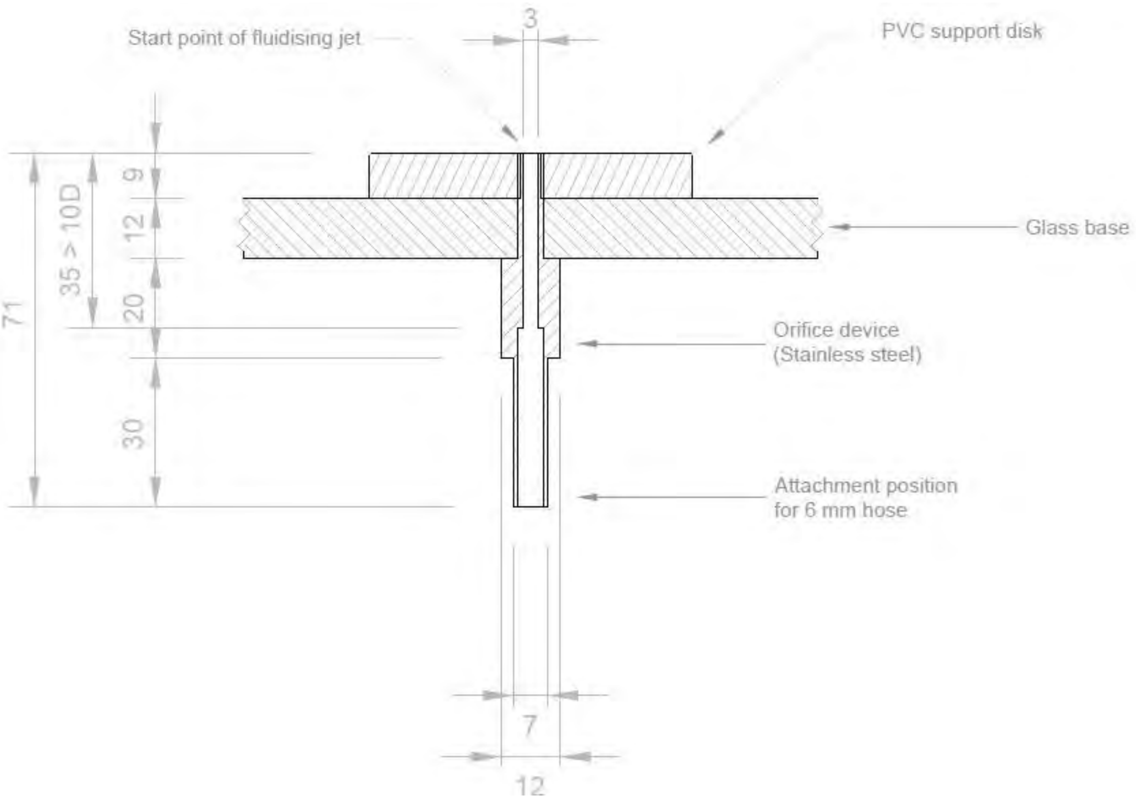

Figure 3.6: Section view of the orifices

The inlet network leading to the orifices supplied the water via a 20 mm (or ¾ inch) diameter clear flexible hose. This hose had various meters and valves attached which are explained in more detail in sections 3.2.5 and 3.2.6. The 20 mm hose was then reduced in two intervals to a similar hose of 6 mm in diameter. The 6 mm hose was then attached to a valve. This valve could be attached to either one of two separate 6 mm hose sections that were connected to the two orifices.

3.2.4 Outlet network

This network transported water away from the apparatus. It consisted of two sub systems, one being the drainage orifice and the other the overflow. The drainage orifice enabled the tank to be completely drained of its water. It was positioned in the base of the tank and can be seen in the design drawings in Appendix A. The drainage orifice itself looks similar to the orifice shown in Figure 3.6, except it had a larger internal diameter of 7.5 mm. Clear flexible hose was attached to the orifice which conveyed the water to a drain.

The other sub system was comprised of four overflow holes located on two of the glass tank walls. The precise position of these holes can again be seen in the design drawings in Appendix A. The overflow holes maintained a constant static head of water in the tank, by the continuous expulsion of water. Water that flowed through the overflow holes was conveyed to a drain via clear flexible hose.

3.2.5 Flow meter

An Aquadis+ Composite Itron flow meter was used in the experiments for recording the flow rate through the orifices. This piston type volumetric flow meter is typically used for household water metering. At the flow rates tested in the experiments the flow meter has an accuracy of 1.5 % (Itron, 2014). A V2 type Itron Cyble Sensor, was attached to the flow meter. The Itron Sensor was connected to a Sensus Cosmos Data Logger which calculated the flow rate. The three metering components are shown in Figure 3.7.

Figure 3.7: Itron flow meter with attached Cyble Sensor and Sensus data logger

3.2.6 Valves and gauges

The inlet network had a ball valve and a Pressure Reducing Valve (PRV) with an attached pressure gauge. These components, which are pictured in Figure 3.8, were positioned upstream of the flow meter on the 20 mm diameter inlet network hose.

The ball valve controlled the water flow rate. It also allowed for the complete closure of the water supply to the apparatus. An additional ball valve, not pictured in Figure 3.8, was located on the 6 mm diameter hose of the inlet network. This valve which was much smaller and different in shape to the one in Figure 3.8, enabled the fine tuning of the flow rate.

The PRV controlled the pressures in the inlet network. It ensured that in the event of a blockage caused by the ballotini in the orifice structures, the pressure build-up in the network would not become too high. High pressures would be detrimental to the thin walled 6 mm diameter hose of the inlet network.

Figure 3.8: Setup of Ball valve and PRV with attached Pressure gauge

3.2.7 Water supply

Water from the municipal reticulation network was used in the experiments. The water flow rate was controlled by the two ball valves, and monitored with the flow meter. The PRV controlled the pressure of this water supply. The water was directed to either one of the two orifices, which created the fluidising jet in the ballotini bed.

3.2.8 Pitot tubes

The Pitot tubes were the instruments used to measure the pore and dynamic pressures in the ballotini bed caused by the fluidising jet. There were two types of Pitot tubes, both manufactured at the University of Cape Town. The two types, namely the L type and straight type Pitot tubes are pictured in Figure 3.9. Each of the Pitot tubes consisted of two parts − a thicker stainless steel tube and a thinner glass tube. The glass tube fitted inside the steel tube and was secured there by a PVC collar. This setup can be seen in the figure, while the dimensional drawings are in Appendix A. For both the Pitot tubes, the contact surfaces between the two parts and the PVC collar were secured with clear silicon sealant, ensuring a watertight seal. Therefore the Pitot tubes had two openings, one at the nose piece in the glass tube and the other at the opposite end of the Pitot, in the steel tube. Unlike the Pitot - Static tubes described in the literature these Pitot tubes did not have a series of radial holes offset from the nose piece.

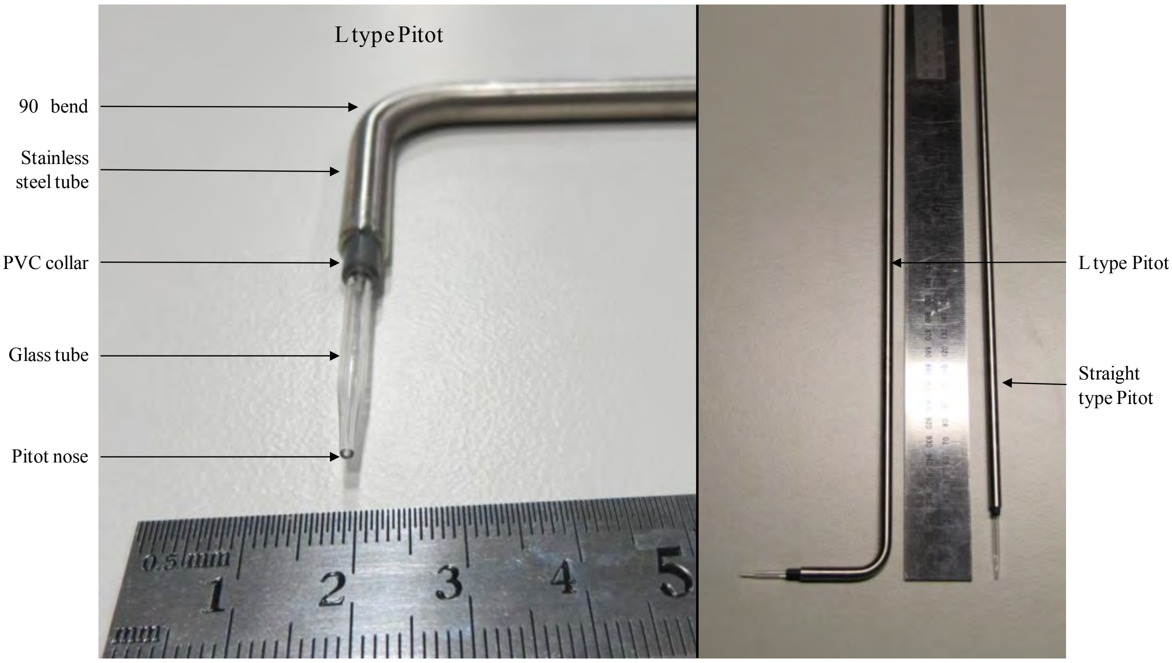

Figure 3.9: L and straight type Pitot tubes

The dimensions of the Pitot tubes were as follows: the stainless steel tube had an outer diameter (OD) of 6.35 mm and an inner diameter (ID) of 4.57 mm; the glass tube had an OD of 3 mm and an ID of 1.5 mm, with the tapering section creating a 0.5 mm ID at the nose piece. The length of each glass tube was 70 mm. The PVC collars were each 35 mm long and had tight tolerances with the steel and glass tubes. Essentially, the reason for having the thicker stainless steel tubes was to provide rigidity and strength to the Pitot tubes, while the thinner glass tubes had very little disturbance on the fluid and ballotini flow.

The nose ends of the Pitot tubes were inserted into the ballotini bed, while the Pitot tubes were secured in the Pitot tube positioning system. The Pitot tube positioning system is explained in detail in section 3.2.9. The open tubes of the Pitot noses were therefore subjected to the pore and dynamic pressures caused by the fluidising jet. However at the same time the noses prevented the ballotini from entering the Pitot tubes as the noses were tapered down to inner diameters of about 0.5 mm, whereas the ballotini had a particle diameter greater than 0.6 mm. The distinct tapering of the Pitot noses can be seen in Appendix A.

3.2.9 Pitot tube positioning system

Essentially this system was the most intricate of the whole experimental setup. It served to secure each of the Pitot tubes so that the noses of the Pitot tubes could be exactly positioned within the ballotini bed. This meant that if for example the L type Pitot tube was removed from the system it could later be repositioned in exactly the same place again. The system also allowed for the movement of the Pitot tubes in the X, Y and Z directions within the ballotini bed. The movement in the three directions was accurately recorded using three steel rules (one for each direction), mounted on the positioning system. This position was important as it determined where in the ballotini bed each reading was being taken with respect to the orifice (regarded as the origin, 0,0,0).

The whole positioning system was mounted on the four top corners of the glass tank. On each of these corners were aluminium corner support blocks, which formed the basis of the positioning system. The blocks contained machined slots to a depth of 25 mm, which the glass fitted into. Figure 3.10 contains a cross sectional drawing and a photograph of the complete corner structures which were placed on each of the four corners of the glass tank. The aluminium corner support blocks can be observed in the figure, as well as the slot for the glass. Detailed explanations of the remaining corner structure relating to Figure 3.10 continues in the subsequent paragraph.

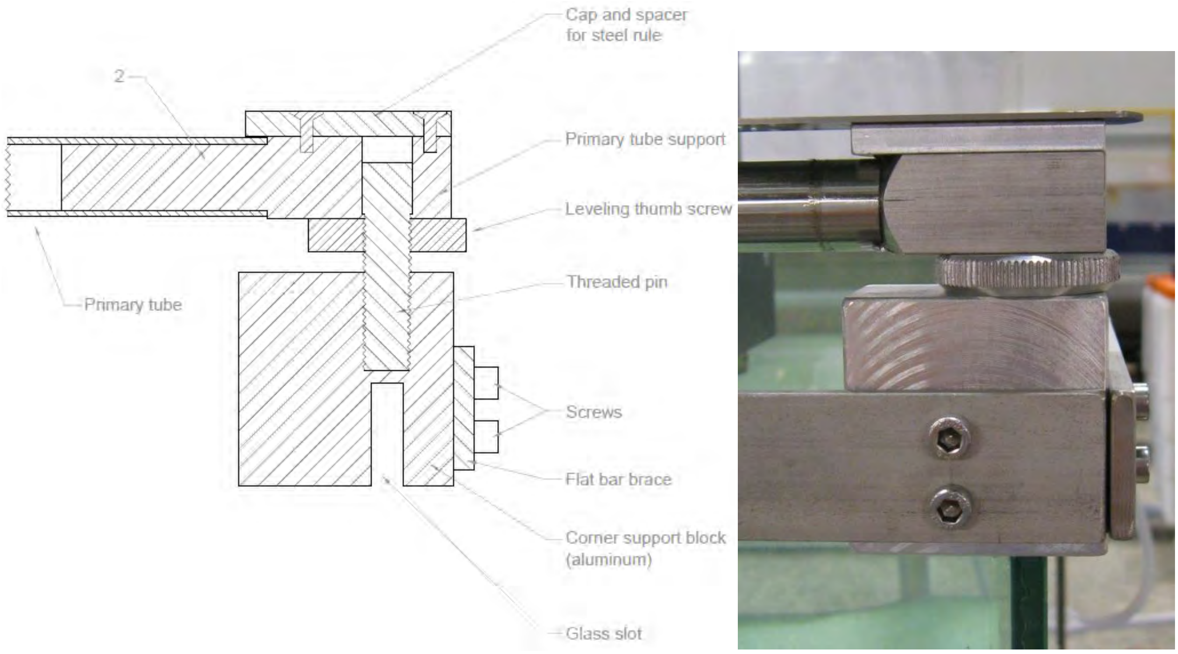

Figure 3.10: Vertical cross section and photograph of the Pitot tube positioning system corner structures

Embedded in the corner blocks to depths of 24 mm were threaded pins. The pins served as supports for the remaining components of not only the corner structure, but also the complete positioning system. The upper 13 mm of the pins were not threaded and therefore were solid round bars. The round bars fitted into primary tube supports which were drilled to receive the pins. Placed on the threaded parts of the pins were levelling thumb screws. When these thumb screws were turned, it vertically adjusted the primary tube supports which sat directly on the screws. The whole positioning system was levelled in turn as well. The primary tube supports consisted of a 16.05 mm diameter round bar part which fitted inside and secured the primary tubes. There were two primary tubes, where both of their ends were supported by two corner structures. The two primary tubes were therefore positioned parallel to two of the glass tank side walls, where the other two side walls were left free from any tubing. On top and attached to all four of the primary tube supports were caps which prevented unwanted material from falling into the drilled pin holes, while also providing attachments for the Y steel rule. The primary tubes supported the remaining components of the positioning system. This completed the components of the four corner structures shown in Figure 3.10.

The two primary tubes that were attached to and supported by the primary tube supports, ran parallel to each other in the Y direction. Running over these primary tubes were primary slides, one slide on each of the primary tubes. The primary tubes therefore served as runners or guides for the movement of the primary slides. This setup can be seen in Figure 3.11. Each of the primary slides consisted of rectangular aluminium blocks which were bored to fit two bearings with their seals. The primary tubes then passed through the bearings and seals. The bearings and seals limited the amount of play between the tube and slide and also prevented any unwanted dirt from entering. Apart from the primary slides enabling the movement of the Pitot positioning system in the Y direction, they also secured two secondary tubes. These secondary tubes ran parallel to each other and perpendicular to the primary tubes, as shown in Figure 3.11. They therefore connected the two primary slides, enabling the exact movement of both the slides in the Y direction. This movement of the primary slides was monitored using the Y steel rule. Figure 3.11 shows a mark on the X steel rule which was used as the datum to record this movement of the slide. The secondary tubes‟ attachments onto the two primary slides were set below the radius of the primary tubes. This setting below the radius of the primary tubes allowed two attachment bolts to pass through the slides, clear of the primary tubes. The two bolts on each of the slides secured the two secondary tubes, as shown in Figure 3.11.

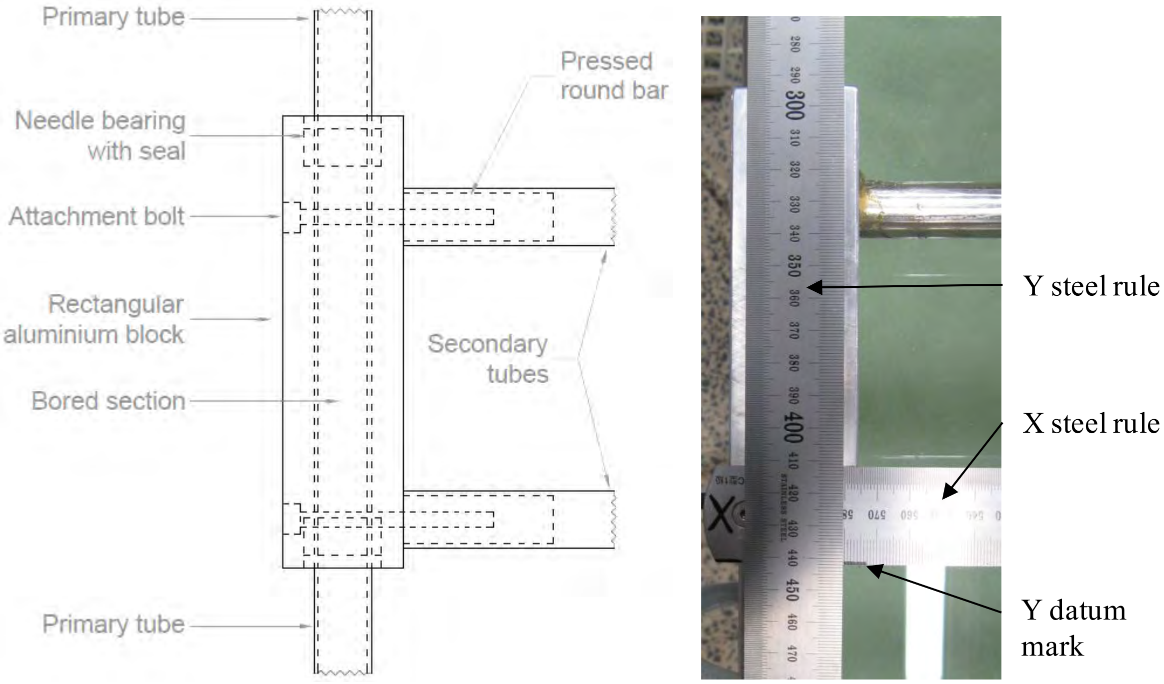

Figure 3.11: Drawing and photograph of primary tube slide

Similar to the primary slides, a single secondary slide ran over both the secondary tubes. The secondary slide can be seen in Figure 3.12. The figure shows the secondary slide, where the secondary tubes can also be seen. The secondary slide ran on both the secondary tubes which prevented its rotation and enabled movement in the X direction only. This movement in the X direction was monitored using the X steel rule together with the X datum mark shown in Figure 3.12. The secondary slide was made from aluminium and was bored at two locations to receive the secondary tubes. As with the primary slides, the secondary slide was also fitted with bearings and seals. Attached to the front side of the aluminium block was a PVC Pitot tube brace. The brace secured either the L type or the straight type Pitot tubes, depending on which Pitot was being used at the time. The brace also allowed the Pitot tube movement in the Z direction and could be locked in position by means of a locking nut. Furthermore attached to the top of the aluminium block was the Z steel rule support, which supported the Z steel rule. This steel rule enabled recording of the Pitot tube‟s Z position.

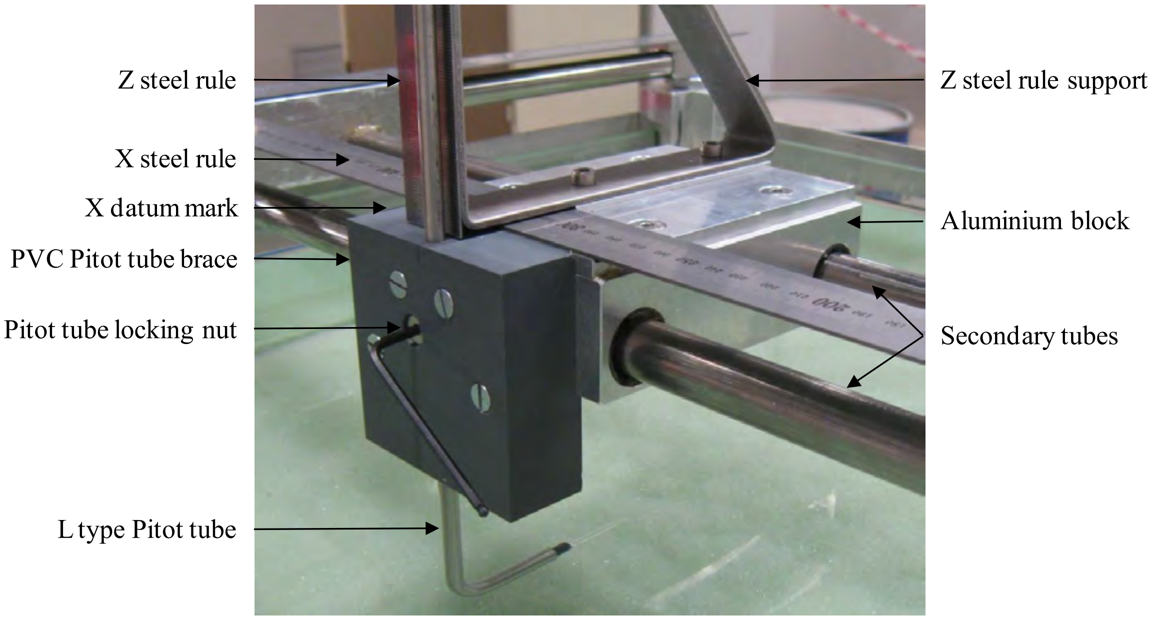

Figure 3.12: Image of secondary slide

Figure 3.13 is a photograph taken from above the complete Pitot tube positioning system. In the figure one can see the four corner configurations on the top corners of the glass tank, which support the two primary tubes. The primary slides can also be seen together with the secondary tubes and the single secondary slide. The figure also gives a good perspective of how the system enables three dimensional movement of the Pitot tubes. This concludes the individual components of the Pitot tube positioning system. Dimensional drawings of not only the Pitot tube positioning system but of the whole setup can be found in Appendix A.

Figure 3.13: Photograph of the complete Pitot positioning system

3.2.10 Glass sight tube

The glass sight tube functioned as the piezometer in the experiments, allowing water pressure head measurements to be taken. This was possible as the bottom end of the glass sight tube was attached to a length of clear flexible tubing, where the other end of the flexible tubing was connected to whichever of the Pitot tubes was being used at the time. This created a continuous airtight system with openings only at the nose of the Pitot tube and at the top end of the sight tube. This meant that water pressures experienced at the Pitot nose were transmitted into the sight tube. The water elevation (pressure head) in the sight tube could then be recorded and the corresponding pore pressures and dynamic pressures could be calculated.

The glass sight tube was mounted onto a length of steel flat bar. The flat bar was hinged by means of a pin at its bottom end, and at its mid length it was attached to a pivot arm. A wing-nut secured the attachment with the pivot arm. This setup is shown in Figure 3.14. The wing-nut could be adjusted by hand which subsequently allowed for the changing in inclination of the flat bar and the sight tube. This allowed the sight tube‟s inclination to be changed through 90^0.

The inclination of the sight tube meant that smaller increments of the water elevation in the tube could be read, making the system more accurate. A 90° protractor was installed with its origin at the centre of the pivoting hinge, providing the angle of inclination. Also, ruler increments were placed on the steel flat bar, behind the glass tube. The ruler was used to read the increase in water elevation in the sight tube, and therefore the subsequent pressures and dynamic pressures could be calculated.

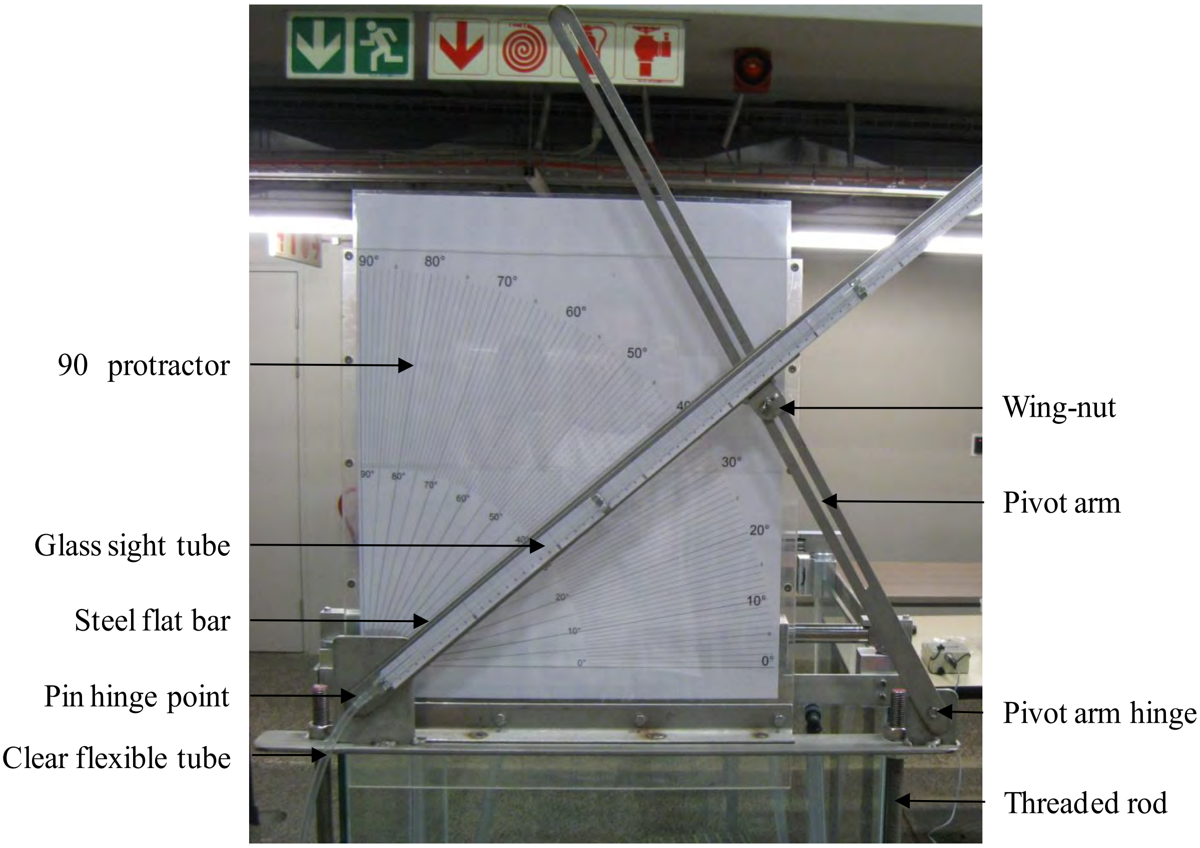

Figure 3.14: Photograph of glass sight tube with mounting system

3.2.11 Steel rules

In total there were three steel rules included in the experimental setup. All three were positioned on the Pitot tube positioning system. These three steel rules were responsible for the X, Y and Z position of the Pitot tube; in particular the position of the Pitot tube with respect to the centre orifice, while in the ballotini bed. The steel rules can be seen in Figure 3.13, where the X and Y rules are marked with an X and Y respectively and the Z rule is angled out of the page.

3.2.12 Stand

The stand supported the complete experimental setup. It was made from stainless steel equal-leg angle iron and flat bar sections. The feet of the stand were adjustable, which enabled the stand to be levelled, therefore ensuring the levelling of the glass tank. The stand platform which the glass tank rested on had cut out sections, therefore not being one solid platform or plate. At one of the cut out sections the drainage and inlet orifices were connected onto the base of the tank. The stand also supported the glass sight tube mounting system, which was attached to its side.

3.3 Calibration and verification procedures

These procedures ensured that the experimental equipment functioned correctly, therefore confirming that the readings taken were as accurate as possible. Both of the procedures were done prior to any experimental testing. The calibration procedure involved zeroing the Pitot tube positioning system. This included referencing both the Pitot tubes with respect to the centre inlet orifice (origin) in the glass tank. The verification procedure was done to determine the errors, if any, that might be incurred when using the Pitot tubes.

The results of the verification procedure for the L type Pitot tube are detailed following the description of the verification procedure.

3.3.1 Calibration of Pitot positioning system

The purpose of this procedure was to enable the accurate positioning of the Pitot tubes‟ noses, when concealed by the bed of ballotini in the tank. For this calibration the experiment was set up as it was for the final experiment, except the ballotini were not placed into the glass tank. Therefore visually one could observe where the noses of the Pitot tubes were located within the glass tank. Each of the Pitot tubes was calibrated separately. Therefore the process described below was followed for each of the two Pitot tubes.

For the calibration the Pitot positioning system was adjusted so that the Pitot tube nose was located directly above the centre and just in contact with the centre orifice. The centre of the centre orifice was regarded as the origin for the area in the glass tank. When each of the Pitot tubes was placed in this particular position at the origin, it was regarded as having been zeroed. Furthermore, the readings on the X, Y and Z steel rules were regarded as the datum readings for the Pitot tubes. Therefore when the glass tank was filled with the ballotini, the datum readings on the steel rules could locate the exact position of the Pitot tube. This calibration process for each of the Pitot tubes was undertaken at the centre orifice only, as this is where the measurements were taken from.

3.3.2 Verification of L type Pitot tube

The verification of the Pitot tubes was a more complex process than the calibration of the Pitot placement system. Typically Pitot tubes built by specialised manufacturers are calibrated in-house and are issued with a constant calibration error if there is one at all. In this study however, the Pitot tubes had to be verified as they were built at the University of Cape Town.

The verification process involved a temporary experimental setup done in the University of Cape Town‟s Laboratory. The process was not successful for a number of reasons which will be discussed in the results section (section 3.3.3). A decision was taken not to pursue the process in order to improve the results because: the errors found were in the same range as the variation in the velocities tested; secondly these errors with an average of 3.3 % were very small and would have had a minor effect on the results. What follows is a brief explanation of the L type verification which was done.

3.3.2.1 L type Pitot tube verification method

An accurate and effective way of verifying the precision of a Pitot tube is by doing a simple experiment. The experiment which was done here involves moving the Pitot tube at a known constant velocity down a channel filled with a static water medium. This is in contrast how a Pitot tube is typically used, with the Pitot in a static position and the water moving. The reason for using this reverse method is that if say the Pitot tube was stationary in water flowing down a channel, the channel walls would have a frictional effect on the flow profile of the water flow. It therefore becomes very difficult to know the true velocity of the water.

In the experiment, the nose opening of the Pitot tube was essentially faced in the direction of the Pitot movement, which enabled the fluid to flow directly into the Pitot tube. This flow that entered was in fact the dynamic pressure which was measured and then calculated into velocity terms. This calculated velocity was then compared to the actual velocity at which the Pitot tube moved along the channel. Ideally if these two velocities were the same then the Pitot was accurate, otherwise if not, a ratio of the difference could be found and applied as a calibration factor. The verification followed this process and is explained below.

The verification involved a temporary setup done in the University of Cape Town‟s Civil Engineering Laboratory. The setup consisted of an Armfield hydraulics flume, which was positioned horizontally and was filled with water to a depth of 180 mm. A platform was manufactured to support the Pitot tube. This platform consisted of ball bearings which enabled the platform to move along the channel while being guided and supported by the channel walls.

The movement of the platform was created by a thin cable wire running through a pair of pulleys, where the one end of the cable was attached to the platform and the other end to a suspended weight. One of the pulleys was fastened to one end of the flume while the other pulley was attached to the laboratory crane. The pulley on the crane was elevated almost directly above the first pulley. This setup can be seen in Figure 3.15. When the setup was loaded, the weight was suspended just below the elevated pulley, and the platform securing the Pitot tube was positioned at the opposite end of the flume from the first pulley. This loaded setup is illustrated in Figure 3.15. The suspended weight resulted in the cable being taut. At this loaded position the platform was held stationary by hand and then released. The platform moved along the flume resulting in a water rise in the Pitot tube.

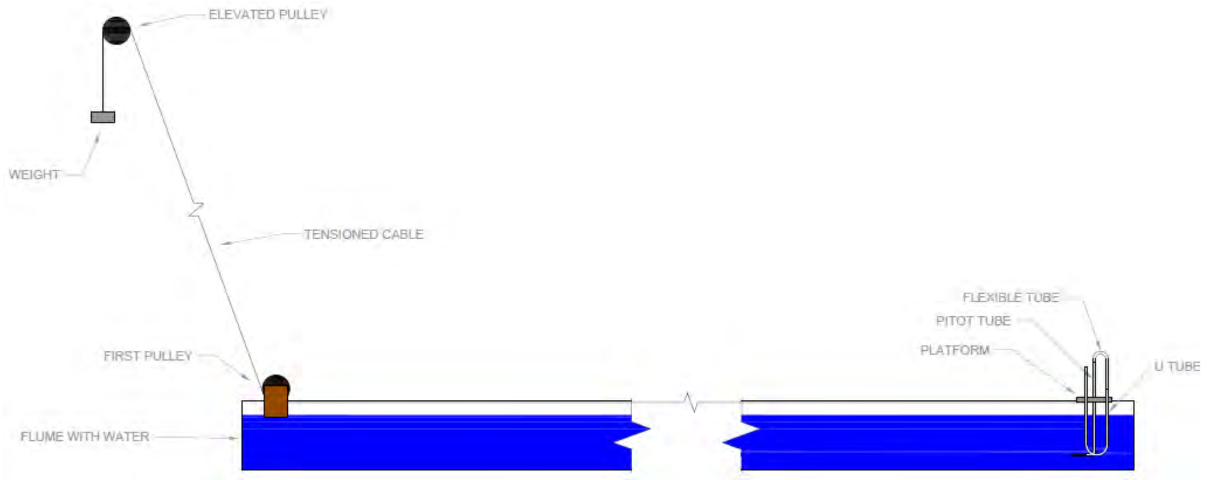

Figure 3.15: Schematic of the temporary verification setup

The water rise experienced by the Pitot tube was small due to the low velocities tested. With the main, larger tube of the Pitot tube being stainless steel this small rise would not be visible. Not being able to see the water rise in the Pitot tube was an issue. The problem was solved by connecting a length of clear flexible tubing to the top end of the Pitot tube. The tubing was then bent downwards, and then upwards again creating two U bends. From here the tube was connected to a vertical PVC sight tube. The length of tubing was filled with water, with the top of the PVC sight tube being open to the atmosphere. When the system was at rest, the water elevation in the sight tube was the same as the water elevation (water surface) in the flume, except for the addition of water capillary rise in the PVC sight tube. This setup can be seen in the photograph of the platform together with its attachments in Figure 3.16. Both the flexible tubing and the sight tube were braced onto the platform.

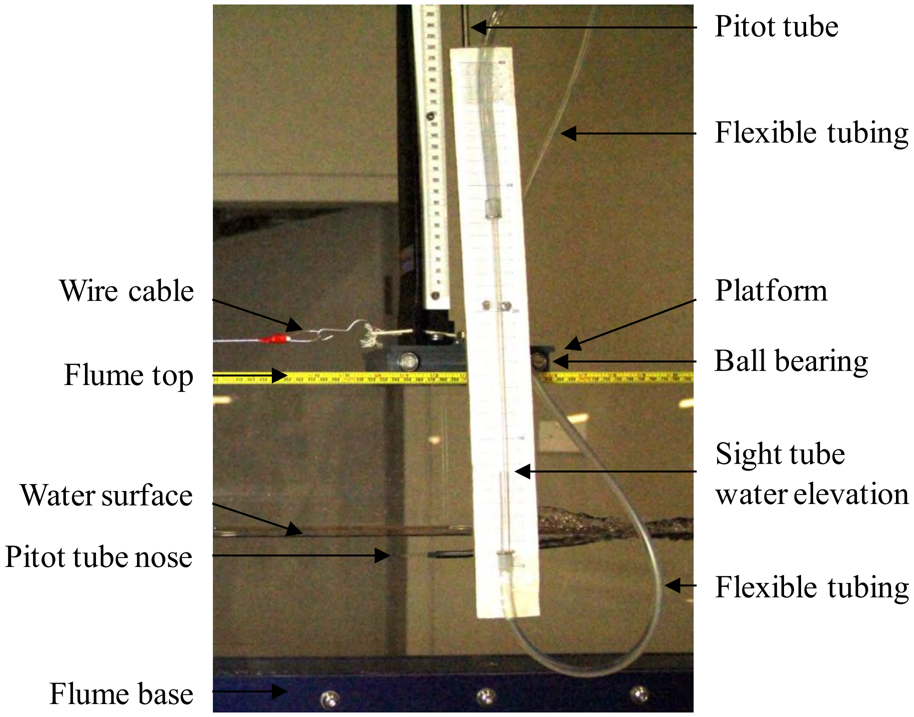

Figure 3.16: Photograph of platform securing Pitot tube

In the verification experiments, three velocity category tests were undertaken using this experimental setup. In each of the velocity category tests, there were 20 runs. A run was regarded as the movement of the platform along the length of the flume, through which a reading was taken. For each of the runs the platform which was held by hand at one end of the flume was released, at which point the platform reached terminal velocity and moved to the other end of the flume up to the first pulley. The velocity of the platform ($V_{Platform}$), which was the velocity at which the platform moved along the flume, was calculated using its travel distance over time. The travel distance was marked with red tape on the flume while the travel time of the platform over this distance was recorded with a stopwatch.

The water rise directly reflected the velocity head which entered the Pitot tube. As mentioned previously, this was because the nose opening of the Pitot tube was in the same direction as the motion of the Pitot. This implies that the static water entered the Pitot tube. Equation 3.1 is the kinetic energy formula used to calculate the velocity from the water rise in the sight tube. This velocity was termed the measured velocity ($V_{Measured}$). Essentially this measured velocity was the most important unknown in the experiments, as the accuracy of the Pitot tube needed to be verified.

$$H = {V^2}/{2g} \qquad 3.1$$

Before initiating the verification runs it had to be determined whether the platform had reached terminal velocity before water rise readings were taken. The platform velocity was thus calculated for two separate runs using the distance over time method. In the two runs the distances were different - 0.6 m and 1.1 m. These different distances meant that the platform‟s recorded time of travel would be different, but if the calculated velocities were the same then a constant terminal velocity had been reached. The water rise readings were thus taken after it had been noted at what distance along the length of the flume the platform had reached terminal velocity. This process was followed for each of the three testing weights.

Following the testing for terminal velocity, the verification runs were done. In the verification runs, a number of high speed photographs were taken as the platform securing the Pitot tube passed through the demarcated distance with red tape. These photographs were then later analysed to read off the water rise in the sight tube. As mentioned, the calculated velocity was found from the water rise. This calculated velocity was then compared to the platform velocity for each of the respective runs of the Pitot tube. The difference in the two velocities is therefore the accuracy of the Pitot tube.

3.3.3 Verification results of L type Pitot tube

The following section describes and analyses the results of the verification procedure. First the results of Test 1 are analysed. These are followed by a comparative analysis of tests 1, 2 and 3. Additional raw data and analysis that is not included here for Tests 1, 2 and 3 can be found in Appendix B.

3.3.3.1 Test 1 results

It was noticed that the platform velocity ($V_{Platform}$) varied considerably, sometimes by as much as 0.118 m/s. This illustrates that conditions were constantly changing in each of the runs, resulting in different velocities. These conditions can be largely ascribed to shifting frictional forces acting on a number of components in the experimental setup. Figure 3.17 shows the wide distribution of $V_{Platform}$ obtained in the 20 runs in Test 1. There was however a peak in distribution in the range of 0.339 to 0.373 m/s, which occurred within the median.

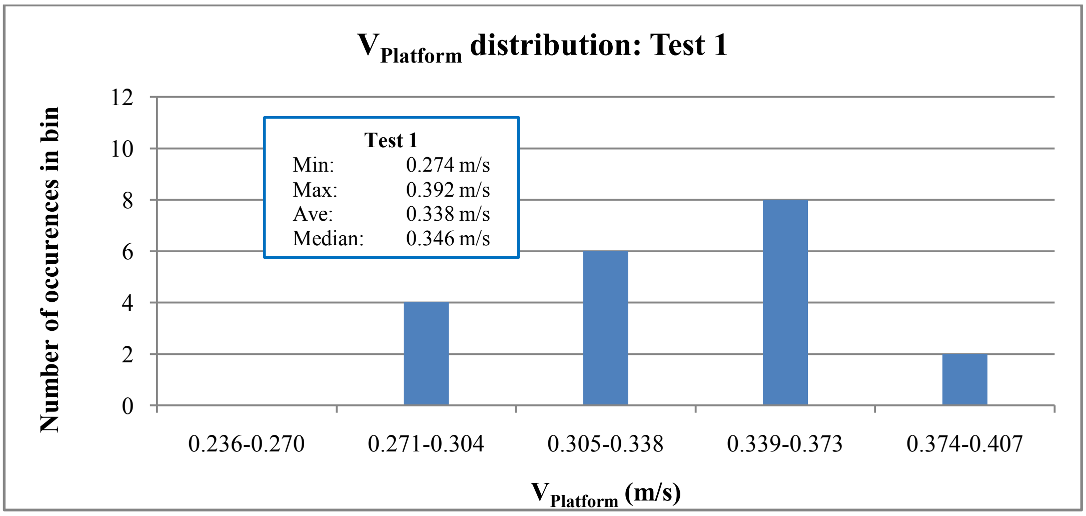

Figure 3.17: $V_{Platform}$ distribution in Test 1

To illustrate the wide range of $V_{Platform}$ obtained, Figure 3.18 depicts the difference between each run"s $V_{Platform}$ and the average $V_{Platform}$, represented as a percentage. The range of percentages is particularly wide (as much as 37 %). There was however a peak in this figure similar to that found in Figure 3.17. One might notice that the peaks in both Figures 3.17 and 3.18 are skewed to the right.

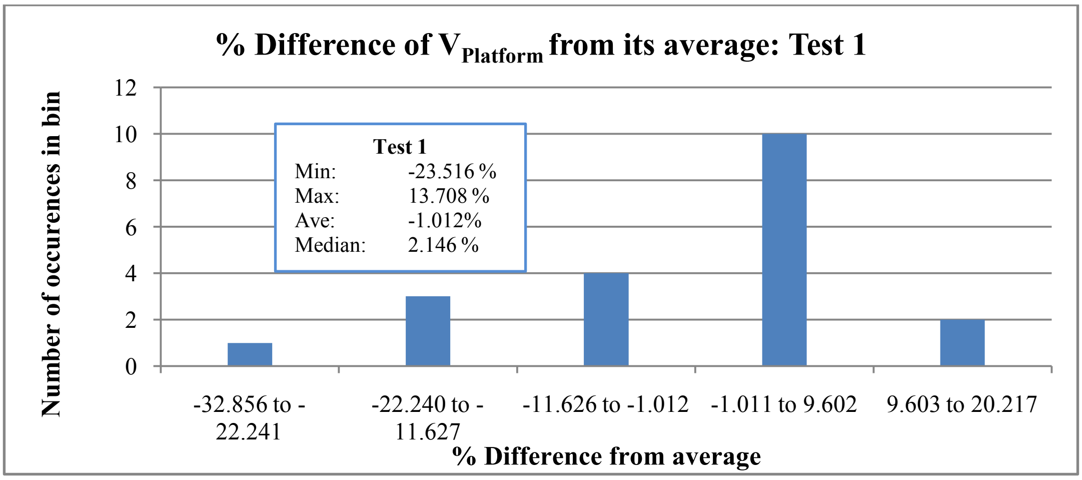

Figure 3.18: % Difference of $V_{Platform}$ from its average for Test 1

The fact that there was such discrepancy in the $V_{Platform}$ was not too critical. The reason for this was that the $V_{Platform}$ was individually compared to the $V_{Measured}$ in each run. In other words in each separate run the $V_{Platform}$ which was calculated from the stopwatch, and the $V_{Measured}$ which was calculated from the water rise in the photographs, were compared with each other. Figure 3.19 shows the relationship between the $V_{Platform}$ and the $V_{Measured}$ obtained in Test 1. The figure reflects a considerable spread of values. This is due to both the varying $V_{Platform}$ as well as the errors between the $V_{Platform}$ and $V_{Measured}$ values. The solid black line in Figure 3.19 represents the y=x or perfect relationship where $V_{Platform}$ and $V_{Measured}$ are equal. However, many of the points are far from this line, which shows the errors between the two velocities. The blue line represents the trend line, which is nearly parallel to the perfect relationship line. It is interesting to note that the trend line is to the right and below the perfect relationship line. A possible reason for this is that the $V_{Measured}$ values are smaller than they should be, implying that the water rise in the sight tube was not sufficient.

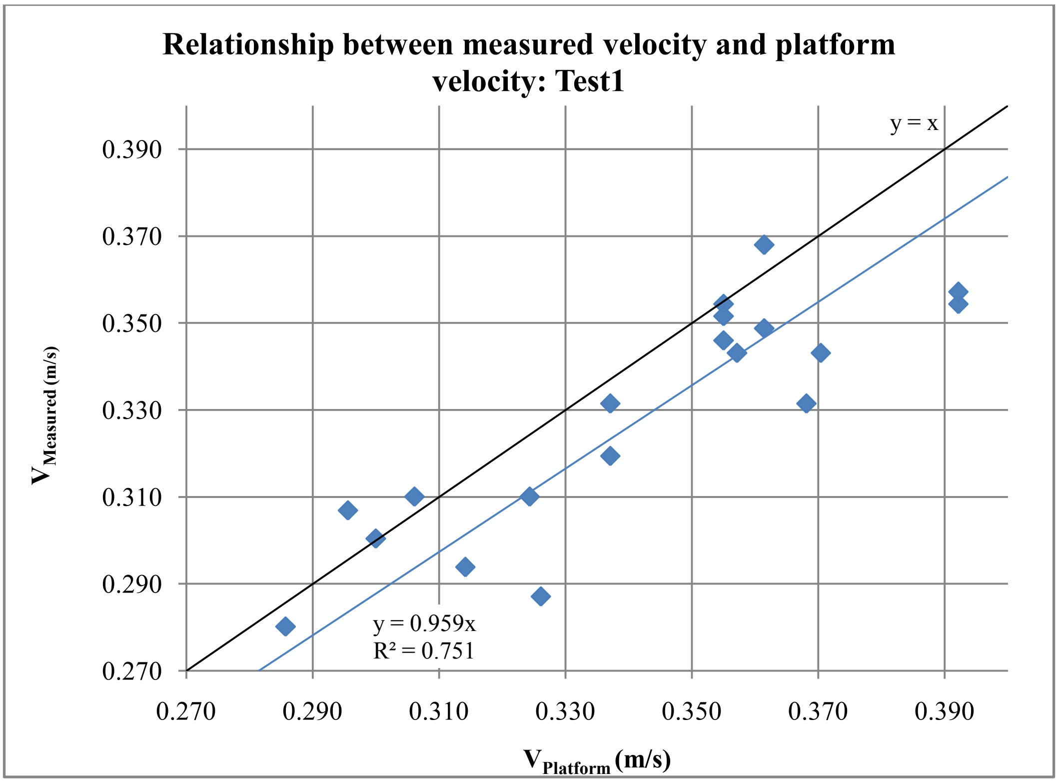

Figure 3.19: Relationship between $V_{Platform}$ and $V_{Measured}$ for Test 1

Figure 3.20 shows the percentage error between the $V_{Platform}$ and $V_{Measured}$ values. The negative errors show the $V_{Measured}$ values to be lower than the $V_{Platform}$ values. This also illustrates that the water rises in the sight tube had not reached their desired heights for each of the runs. A possible reason for the majority of readings having low water rises is that the water height in the sight tube took time to stabilise sufficiently before the photo was taken. Typically the water would rise rapidly in the sight tube when there was a large potential difference, but when the water approached its desired height, and the potential was lower, the water rise would slow down considerably.

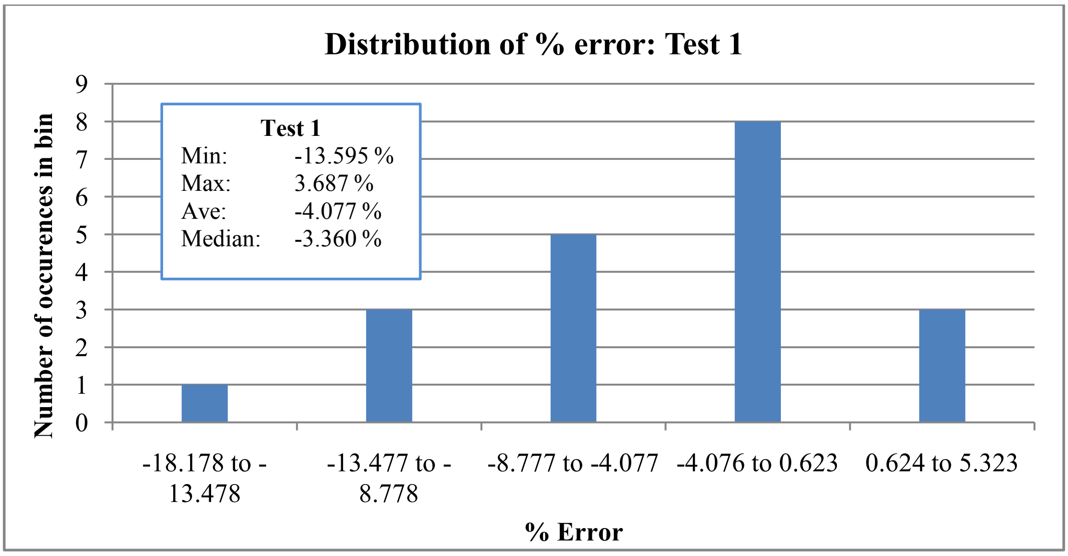

Figure 3.20: % Error for Test 1

It is interesting to note that an error of 1 % in Figure 3.20, reflected on average a 0.0033 m/s velocity difference and a 0.11 mm pressure head difference. Here the velocity difference is the difference between $V_{Platform}$ and $V_{Measured}$, and the pressure head difference is the difference between the actual water level in the sight tube and the level it should have stabilised at for 0 % error.

3.3.3.2 Comparative results of Tests 1, 2 and 3

Figure 3.21 shows the relationship between the $V_{Platform}$ and $V_{Measured}$ for each of the 20 runs in the three tests. The different colours in the figure represent the three tests where different weights were used. Interestingly one can see a greater spread of values at the greater velocities. This is shown by the lower and upper limit trend lines, which widen at the greater velocities. A possible explanation for this is that at the greater velocities more water had to enter the sight tube to reach the desired height, and there was less time for the water height in the sight tube to stabilise.

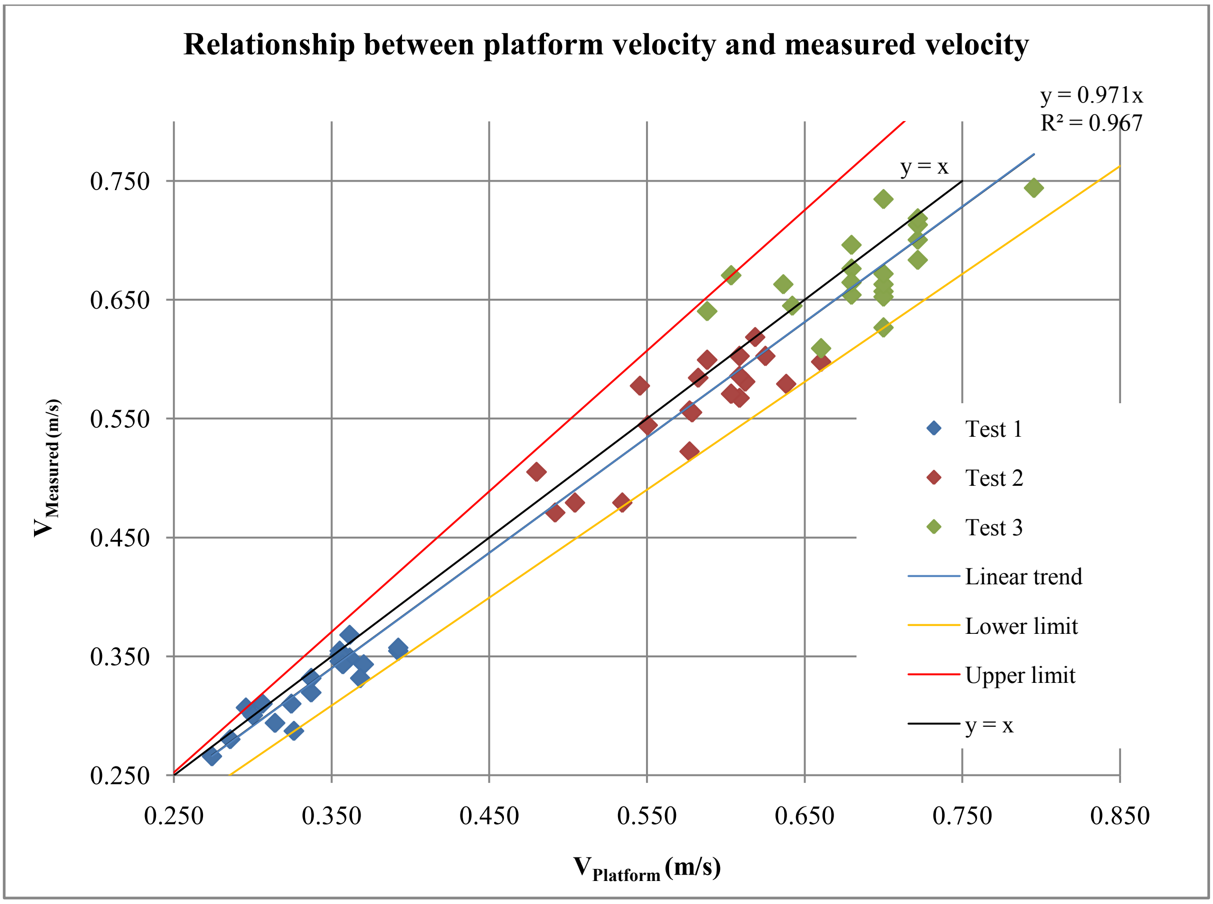

Figure 3.21: Relationship between $V_{Platform}$ and $V_{Measured}$ for all three tests

Table 3.2 consists of comparative data obtained in the three tests. The % error again is negative, generally due to a lower water level in the sight tube than the required water level which corresponds to the platform velocity. One can see that the % error significantly decreases from Test 1 to 3 (at the greater velocities). Figure 3.21‟s greater spread at greater velocities would suggest that the % error would increase, but in fact it does the opposite. What is also interesting is the decrease in the coefficient of variability at the greater velocities.

Table 3.2: Comparative velocity data from Test 1, 2 and 3

Test velocity data		Average (m/s)	Median (m/s)	Standard deviation	Coefficient of Variability	% Error
Test 1	$V_{Platform}$	0.338	0.346	0.034	0.101	-4.077
	$V_{Measured}$	0.325	0.331	0.029	0.090	
Test 2	$V_{Platform}$	0.580	0.585	0.049	0.084	-3.792
	$V_{Measured}$	0.559	0.574	0.045	0.080	
Test 3	$V_{Platform}$	0.687	0.700	0.046	0.067	-1.910
	$V_{Measured}$	0.674	0.667	0.035	0.052	

3.3.4 Conclusions from the Pitot tube verification

It was established from the L type Pitot tube verification that the water level in the sight tube does have a delayed stabilisation. This has been deemed as one of the inaccuracies in the L type Pitot tube verification. However in the experiments that follow, it is expected that there will be continuous small pressure fluctuations which will enter the Pitot tube. Due to the delayed stabilisation of water the fluctuations are not expected to be noticeable in the glass sight tube, and the water level will directly reflect the average.

In all three of the tests the V_{Platform} varied considerably. As previously mentioned, the reason for the variances is largely due to the changing frictional forces acting on the platform as it moves along the flume. The % error likewise had a similar variance for the three tests. It would therefore be unsatisfactory to find an accurate average % error to be applied to the Pitot tube due to the inconsistency of V_{Platform} as well as the water level stabilisation.

Typically Pitot tube errors or calibration factors as they are formally known, are the result of the disturbance the nose of the Pitot causes to the fluid flow. Ellipsoidal shaped noses are said to cause very little or even no flow disturbance (flow separation) over the static port holes (refer to Figure 2.10) of the Pitot tube (Ower & Pankhurst, 1977). The Pitot tubes used in these experiments do not have these static ports. Therefore what disturbance the Pitot tubes have on the flow should not have had any effect on the readings.

Due to the delayed stabilisation of the water level in the sight tube and the varying velocity of the platform, the verification experiments were deemed to be unsuccessful. However the experiments were not pursued any further in an effort to improve the results. The reasons for this are as follows: the errors found were in the same range as the variation range of V_{Platform}; and based on the Reynolds number that would be used in the experiments, it was assumed that the Pitot tubes would be accurate without a calibration factor, no literature was found which contradicts this assumption.

3.4 Repeatability analysis

The repeatability of the measured pore and dynamic pressures was an aspect that needed to be considered to verify the accuracy of the experimental method. It was done to assess whether or not the measurements which were taken can be measured again and be similar in magnitude. For this analysis a number of random measurements at the centre orifice were taken again. These repeated measurements were taken in separate experimental setups, where the experiment was re-setup following the procedure explained in section 3.5.2. A total of 20 measurements were repeated at random locations in the ballotini bed for both the L type and straight type Pitot tubes.

The differences between the previous (original) measurements and the repeated measurements were compared, specifically by looking at the difference between the two measurements. These comparisons are presented in the graphs in Figure 3.22 for the L type Pitot tube and in Figure 3.23 for the straight type Pitot tube. In both the graphs the differences between the previous and repeated measurements are shown.

It is noticeable in the graphs that repeated measurement number 10 for the L type Pitot tube, and number 4 for the straight type Pitot tube, have the largest differences between the previous and repeated measurements. However, both these measurements were the highest pressure measurements that were repeated. This was expected, as with greater measurements greater differences will be found. Interestingly though, the percentage differences between the previous and repeated measurements for these measurements are not high when compared to some of the other percentage differences. These percentages were 6.8 % and 4.5 % for the L type and straight type Pitot tubes respectively. The combined average percentage difference for both the Pitot tubes was 3.8 %. This shows that although these measurements contain significant differences between the previous and repeated measurements, the percentage differences are still reasonable, which makes the repeated measurements quite accurate.

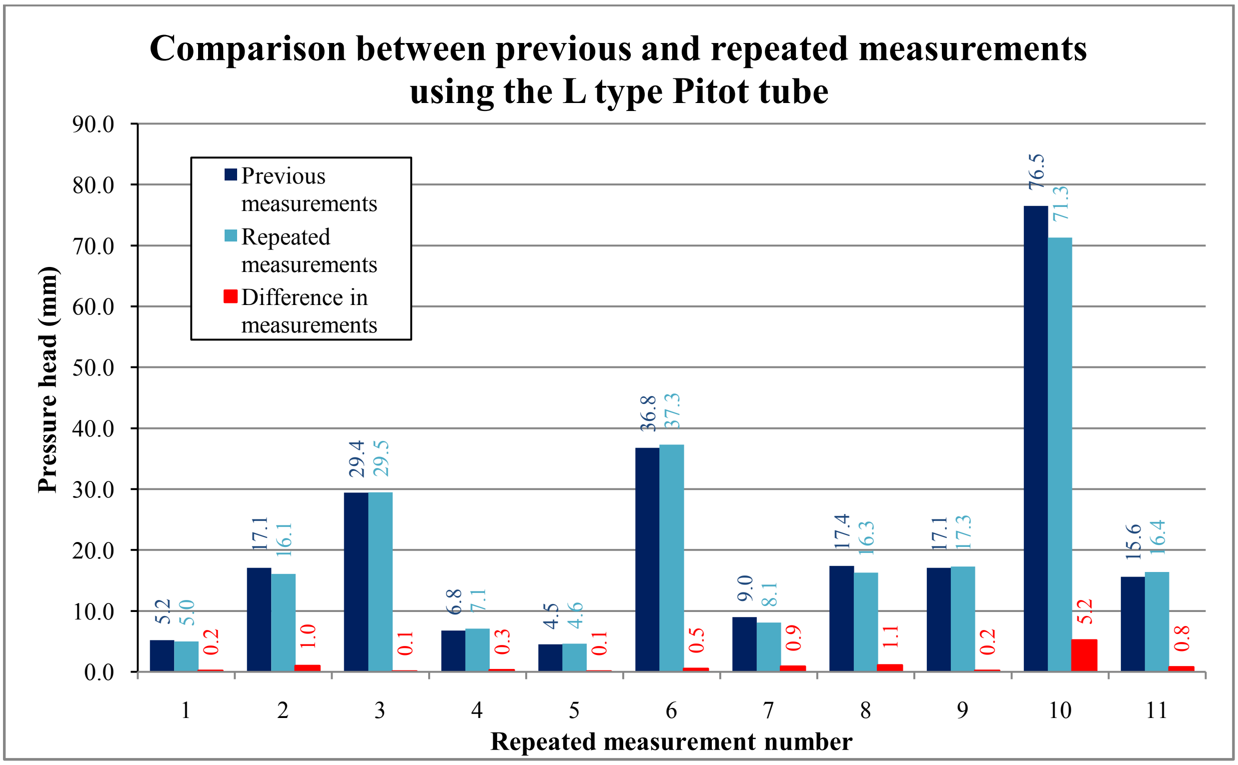

Figure 3.22: Repeated measurements using the L type Pitot tube

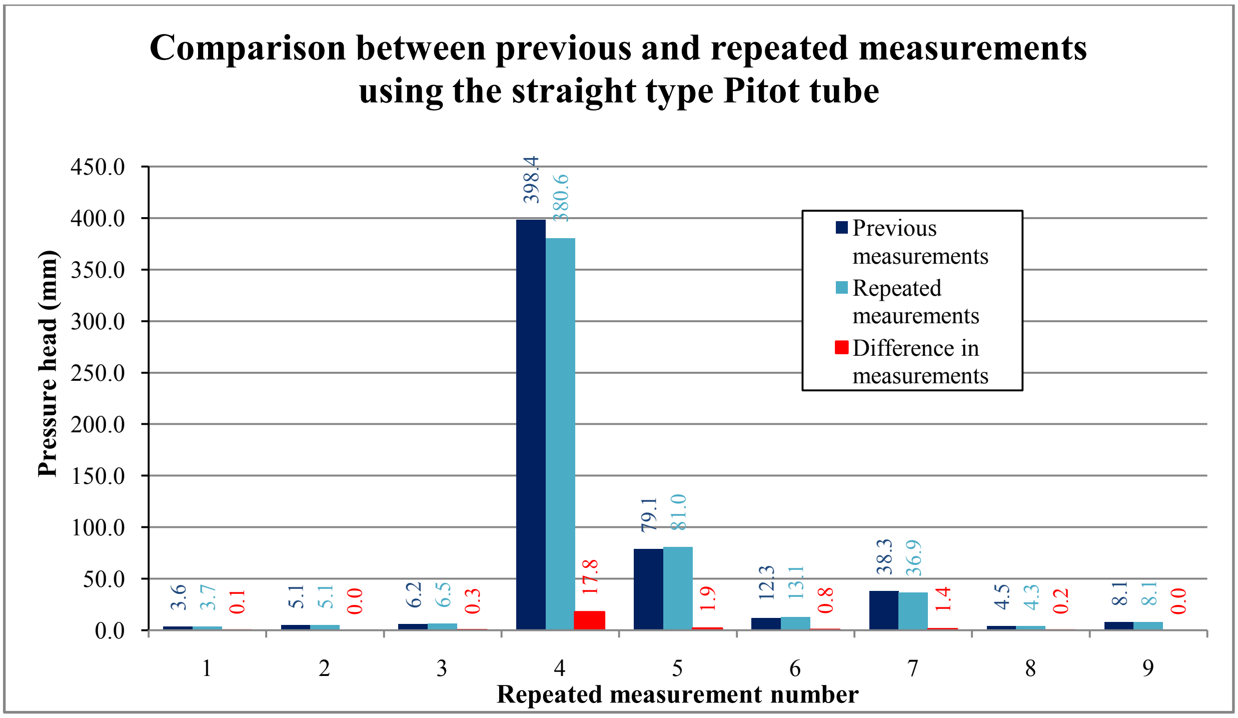

Figure 3.23: Repeated measurements using the straight type Pitot tube

3.5 Experimental standards and procedures

3.5.1 Experimental assumptions and limitations

- The fluidised zone which occurred at the centre orifice was considered to be two dimensional, therefore symmetrical around any vertical plane through the centre of the orifice.
- All tests were done in the glass ballotini only, which represented an idealised soil medium. The ballotini filled the glass tank to a height of 300 mm, which was maintained for all the experiments.
- Only one flow rate of 2 ℓ/min was tested at the centre orifice, while at the wall orifice flow rates of 1, 2 and 4 ℓ/min were tested.
- The flow rates were controlled to an accuracy of ± 0.03 ℓ/min.
- The centre orifice‟s diameter was 3 mm, while the wall orifice‟s diameter was 2.8 mm. The difference in diameters was due to the difficulties in boring the orifices.
- The static water height in the glass tank was kept constant throughout the experiments.

3.5.2 Pre experimental setup procedures

These procedures are a guide to what steps were followed in setting up the experimental equipment so that measurements could be taken.

- Firstly the Pitot tube positioning system was calibrated as per section 3.3.1. Thereafter the datum values on the X, Y and Z steel rules were recorded. In this setup the datum values were regarded as when the Pitot tubes were located at the very centre of the orifice. The calibration was done for each of the Pitot tubes at the centre orifice only. Therefore there were two datums, one for each Pitot tube, where the datums reflected their respective 0.0.0. points.
- The glass tank was filled with water up to the overflow holes, with the drainage hole closed.
- Glass ballotini was rained (sprinkled) into the glass tank. The raining of the ballotini prevented any air entrapment between the particles, while also ensuring a uniform compression and distribution of the ballotini.
- The water supply was then turned on and directed to the centre orifice. Initially the orifice was blocked by the ballotini falling down into the orifice. It was unblocked by probing a piece of wire into the orifice from above to dislodge the ballotini.
- The flow rate of the water supply was controlled using two ball valves, one larger valve on the 20 mm hose for large adjustments in flow, and a smaller valve on the 6 mm hose for fine adjustments. The flow rate was monitored with the flow meter.
- The pressure was controlled using the Pressure Reducing Valve (PRV) and monitored with its attached pressure gauge.
- The L type Pitot tube was used first followed by the straight type. Therefore the L type together with the flexible hose connecting it to the glass sight tube, was primed with water. The Pitot tube was subsequently attached to the Pitot tube brace. Later, once all the measurements using the L type Pitot tube were obtained, the same priming process was repeated for the straight type Pitot tube.
- This essentially completed the experimental setup. Experimental measurements were conducted, where first the centre orifice was analysed and then the wall orifice.

3.5.3 Experimental procedure

Below is a detailed explanation of what experimental measurement procedures were followed for both the centre and side orifice experiments.

3.5.3.1 Centre orifice

- Initial checks

First initial checks were done on the experimental setup. These included checking the flow rate; that there were no air bubbles in the Pitot tube, flexible hose and glass sight tube; and finally that there were no air bubbles entrapped in the ballotini bed. These checks were done frequently throughout the experiments.

- Static water reading

This reading was the water elevation in the glass sight tube when the Pitot tubes‟ noses were positioned above the ballotini bed, but still surrounded by the water. Therefore, the flow through the orifice had no effect on the reading in the sight tube. Furthermore, this reading directly reflected the water elevation in the glass tank. The reading was taken periodically− typically before measurements from the orifice jet, and after the initial checks.

- Measurement process

Measurements were taken at 10 mm and 20 mm intervals on a grid layout. This grid occurred in the positive YZ plane. The grid layout can be seen in Figure 3.24, where the black dots represent measurement points, and point (0,0) the centre orifice. Only one half of the fluidised jet, along a two dimensional plane (positive YX plane) was measured due to the assumed symmetry of the jet. As seen in Figure 3.24, measurements were taken in the vertical Z plane at 10 mm intervals up to an elevation of 200 mm. Along the horizontal Y plane, measurements were taken at 10 mm intervals from 0 to 20 mm, and then at 20 mm intervals from 20 to 60 mm.

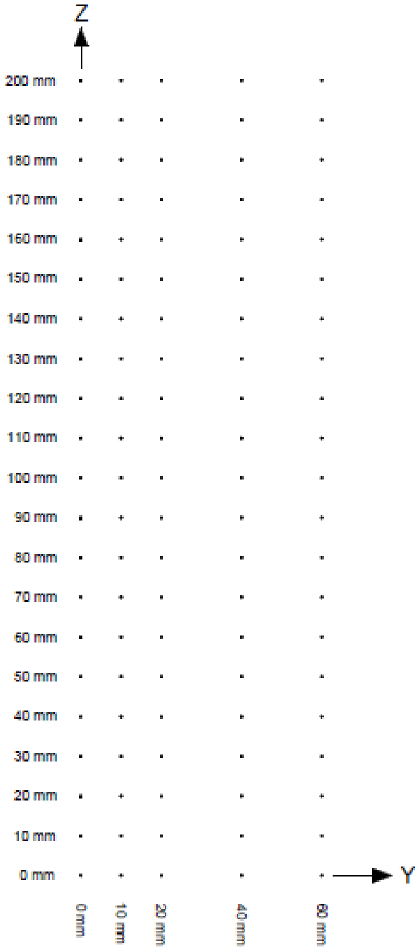

Figure 3.24: Grid layout of measurement points

Measurements were taken along the vertical planes starting at Y, Z position (0, 200) and moving down to (0, 0) in 10 mm intervals. However, in some cases measurements started at the bottom and moved vertically upwards, rather than downwards. The Pitot positioning system was then adjusted 10 mm in the Y direction to the next set of vertical measurements. The same process was repeated for all five of the vertical sets which is a total of 105 measurement points. This measurement process was followed for all of the measurements which totalled between 315 and 420 measurements depending on the number of repeated pressure measurements.

- Taking measurements

Water elevation readings were taken in the glass sight tube for all of the measurements. Before each reading was taken, the water in the sight tube was allowed to stabilise. This was due to water often taking time to pass through the small noses of the Pitot tubes. The readings were subsequently recorded in Microsoft Excel.

3.5.3.2 Side orifice

The measurement process at the side orifice was much simpler than the process at the centre orifice. This is because at the side orifice the Pitot tubes were not used for any of the measurements. The glass wall"s interference with the Pitot tube positioning system, prevented the Pitot tubes from being positioned close to the side orifice.

Therefore at the side orifice, monitoring of the internal fluidisation was done through the glass wall. This was possible as the orifice"s centre was 3 mm away from the glass. The monitoring involved taking measurements of the internal fluidisation geometry in the ballotini bed. The movement of the ballotini caused by the fluidising jet was also monitored. For these measurements, both photographs and videos which could be analysed later, were taken through the glass.

There were three flow rates, 1, 2 and 4 l/min, which were tested at this side orifice. For the three flow rates the geometries of the fluidised and mobile bed zones were analysed by calculating their contact areas on the glass and their volumes. The volumes were regarded as the volume of ballotini which was either displaced or in motion due to the internal fluidisation. In other words the volume for the fluidised zone was the volume of ballotini which was completely displaced in this zone. Similarly, the volume for the mobile bed zone was the volume of ballotini which was in motion, and surrounded the fluidised zone while being contained by the static bed zone.

In order to calculate these volumes, firstly the contact area on the glass wall of the fluidised and mobile bed zones was calculated. These areas were then divided into several horizontal rectangles of known width. Each of the rectangles represented horizontal slices of the fluidised and mobile bed zones. The length of each rectangle, which was bounded by the outer edges of the respective zones, was calculated by using the scale rule which was included in the photographs. These lengths were the diameters for each horizontal slice. The diameter was used to calculate the area of each slice. Once the area for each slice was found, it was then multiplied by the width. This equated to the volume for each horizontal rectangular slice. The individual volumes were summed which equated to the total volumes for the fluidised and mobile bed zones.

3.5.4 Measurement technique using the Pitot tubes

The fluidising jet was assumed to be symmetrical about any vertical plane passing through the central axis of the jet (centre of the orifice). Therefore only one side, positive or negative of either the XZ or YZ planes was used to measure the pore and dynamic pressures. In the experiments the measurements were taken along the negative Y and positive Z planes. The reason for this was that with this experimental setup this was the easiest plane along which to take the measurements. This chosen plane along which the measurements were taken is illustrated in Figure 3.25, the figure also shows the typical fluidised zone which occurred.

The chosen YZ plane comprised of many predetermined points where at each point the measurements were taken. An illustration of these points is shown in Figure 3.24 and is described in Section 3.5.3.1. At each measurement point either three or four measurements were taken where for each measurement the Pitot tubes were positioned at the point differently. The first measurement which was taken was the stagnation pressure in the Z direction and was recorded using the straight type Pitot tube as illustrated by figure 1 in Figure 3.26. The second measurement was the pressure, which was the increase in pressure over and above the static pressure. The pressure was recorded using the L type Pitot tube as shown by figure 2 in Figure 3.26. The pressure measurement could be taken with the L type Pitot tube positioned in two different ways. These two positions are shown by the two figures labelled 2 in Figure 3.26. Only occasionally were two pressure measurements taken like this. This is because of the two pressure measurements being the same it was unnecessary to take both measurements. The final measurement was the stagnation pressure in the Y direction and was recorded using the L type Pitot tube as illustrated by figure 3 in Figure 3.26.

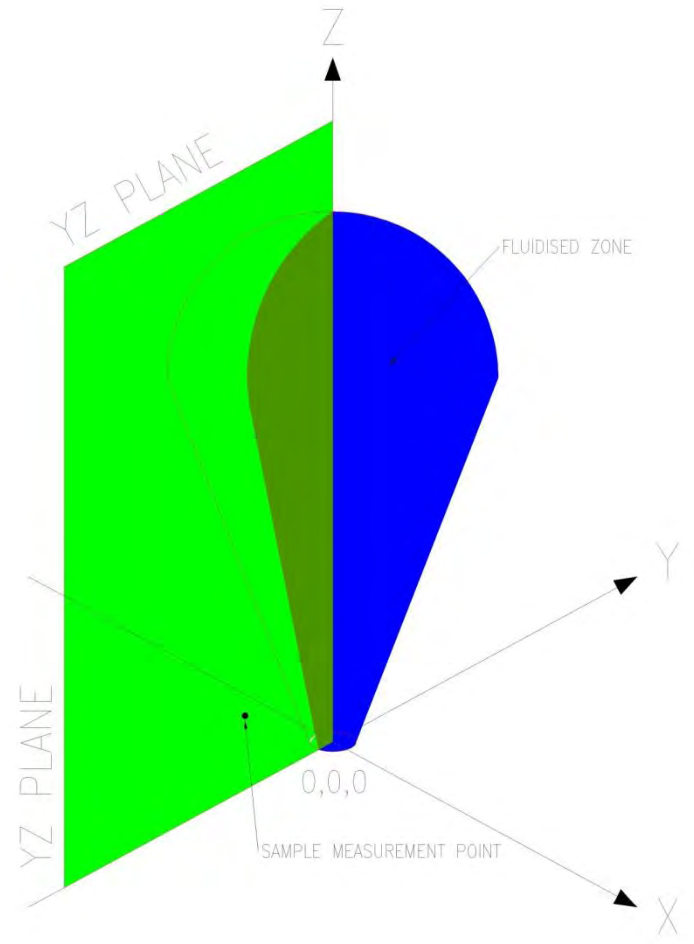

Figure 3.25: Isometric view of YZ measurement plane

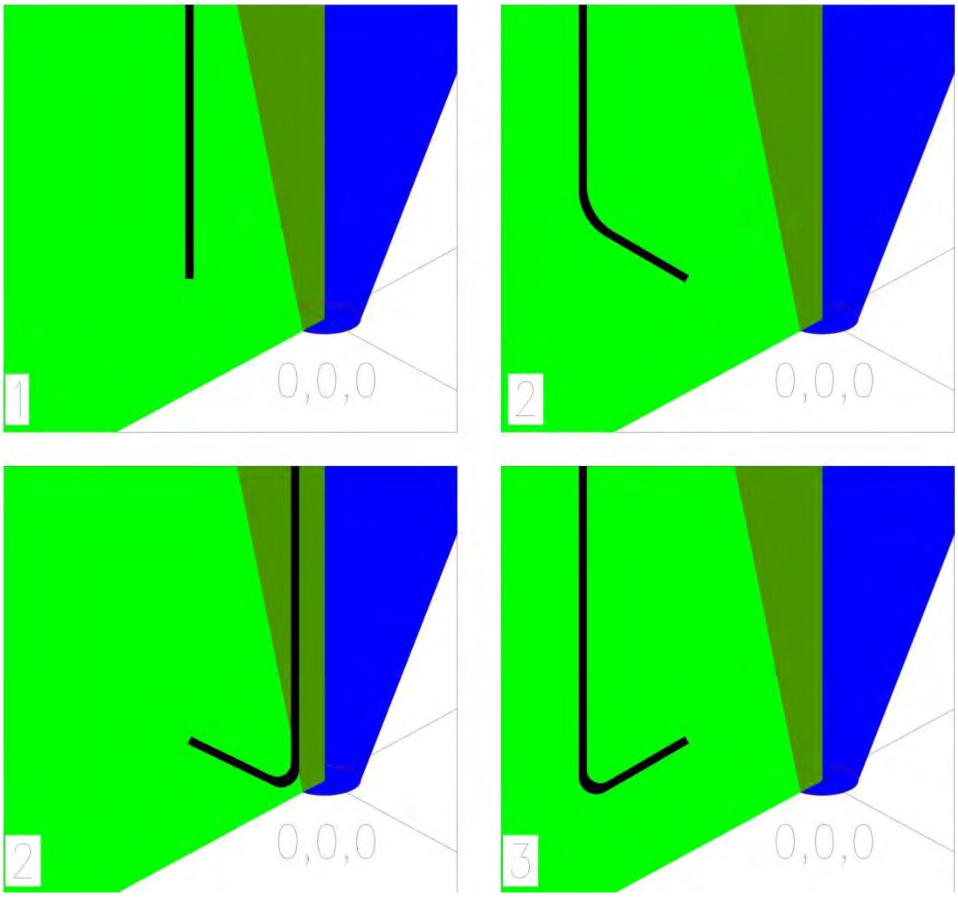

Figure 3.26: Placement of Pitot tubes at a sample measurement point

The means in which the Pitot tubes were able to measure the pressure, the Z and Y directional stagnation pressures separately was as follows and is illustrated in Figure 3.27. The pressures were measured when the flow was at right angles to the Pitot tube's nose piece opening, thus no flow entered into the Pitot tube but the pressure did. The Z directional stagnation pressure was measured as the Pitot tube's nose piece opening was open to the Z direction, therefore both the pressure and Z directional flow entered the Pitot tube. No Y directional flow entered the Pitot tube as the flow was at right angles to the opening of the Pitot tube. The Y directional stagnation pressure was measured as Pitot tube's nose piece opening was open to the Y direction, therefore both the pressure and Y directional flow entered the Pitot tube.

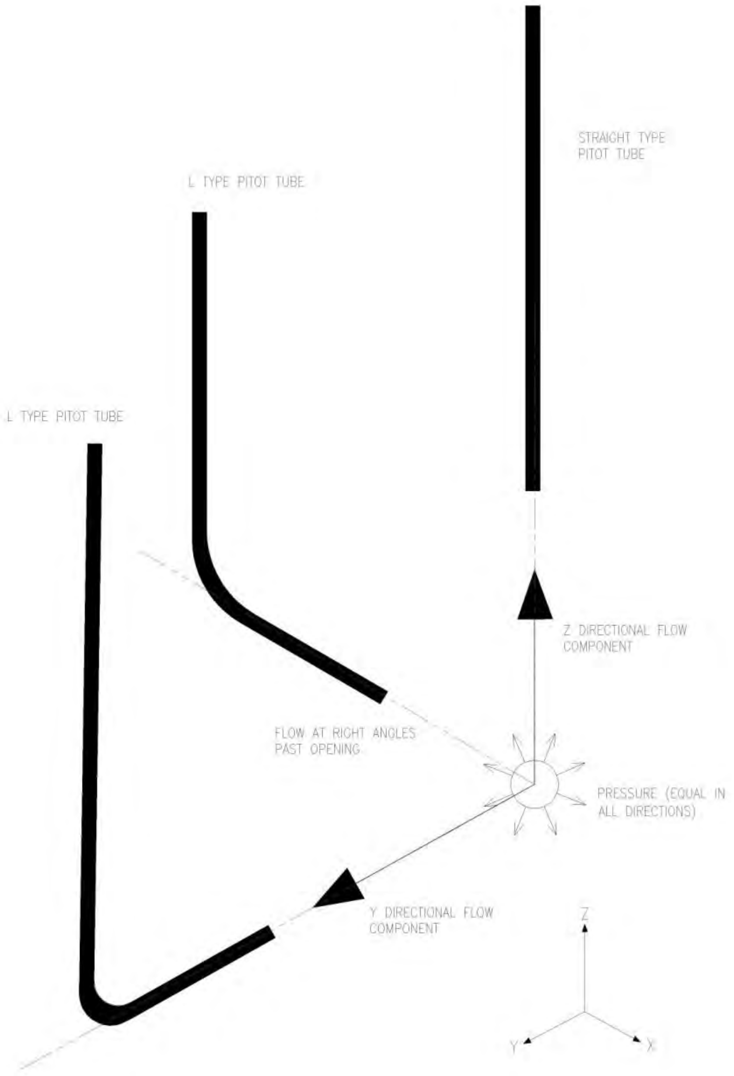

Figure 3.27: Illustration of the Pitot tubes measuring the pressures and directional flow components

It must be noted that the direction of flows shown in Figure 3.27 are the flow components of the resultant flow direction, as illustrated by the example in Figure 3.28.

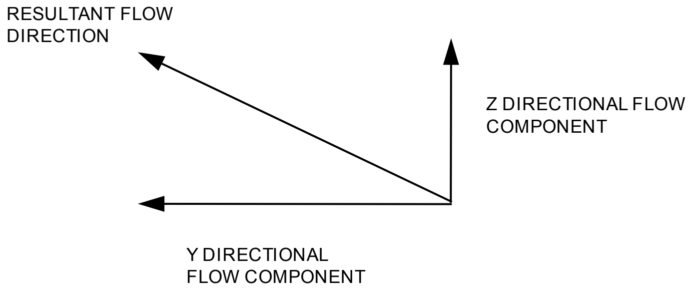

Figure 3.28: Example of the resultant flow with the Y and Z flow components

By taking measurements of the Y and Z directional flow components of the resultant, the resultant could be calculated. Furthermore, by subtracting the pressure measurement (recorded using the L type Pitot tube shown by figure 2 in Figure 3.26), from the stagnation pressure measurements (recorded using the L type and straight type Pitot tubes shown by figures 1 and 3 in Figure 3.26), the dynamic pressures in the Y and Z directions were calculated. From the dynamic pressure which was the velocity head, the velocity could be calculated.

3.6 Experimental observations

During the running of the experiments and taking the measurements, a number of interesting observations were made. Some of these observations pointed to problems which were addressed during the experiments. These observations, as well as their effects and how they were overcome are described here.

3.6.1 Air bubble entrapment in ballotini bed

After running the experiment for some time, large numbers of air bubbles were seen to be entrapped in the ballotini bed. Most of these bubbles were located near to the orifice. This meant that the bubbles were likely entering via the water supply. Essentially these air bubbles restricted the flow of water between the ballotini beads. This resulted in a pore pressure build up in the bed, which led to inaccurate measurements.

The water used in the experiments was supplied by the municipal network which often contains small amounts of dissolved air. The dissolved air then dissipates into the bed surrounding the orifice where it gets entrapped and congregates to form air bubbles. In order to prevent these air bubbles from being created the water should be de-aired prior to being supplied to the experiment.

Figure 3.29 is an image of the centre orifice taken from below the glass tank looking upwards at the ballotini bed. In the figure the shiny white patches are the entrapped air bubbles. It is noticeable in the figure that there is a higher concentration of air bubbles near to the orifice. Also, a brown colour is evident near to the orifice. This brown colour was dirt build up from the inlet water supply. The dirt was caught by the ballotini as the ballotini acted as a filter.

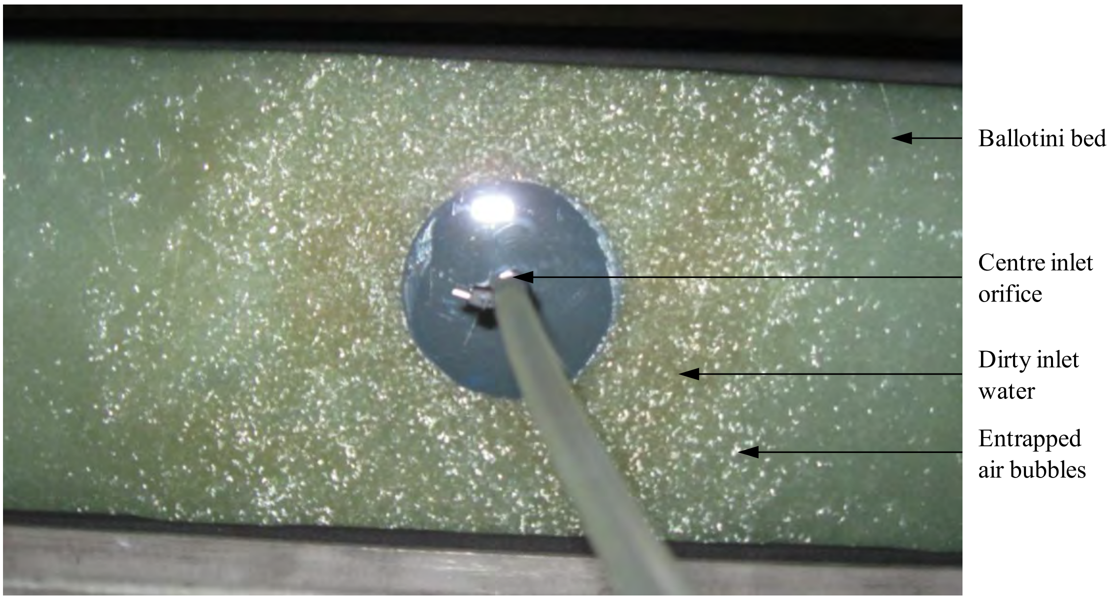

Figure 3.29: Entrapped air bubbles in the ballotini bed

In an attempt to dissipate this air entrapment, approximately half the ballotini were removed from the glass tank at regular intervals. Thereafter the remaining ballotini in the tank were mixed around by hand, which released the entrapped air and allowed the air to rise to the water surface. After sufficient air had been removed, the removed ballotini were replaced by being rained into the tank. The raining method prevented any air from being entrapped between the beads when entering the tank again. Once this process had been completed, the experimental testing could commence again.

3.6.2 Orifice blockage by ballotini

When there was no flow through the orifices the ballotini had a tendency to fall down into the orifice. This posed problems when the water flow had to be switched off after experimentation, or when the orifice that was not being used at the time had no flow through it. When experimentation started again and the flow was switched on, the ballotini still in the orifice caused a blockage. This prevented fluidisation from occurring. The blockage resulted in pressure build-up in the inlet hose, upstream of the blockage.

In order to unblock the orifice, a length of thin wire was used to prod down into the orifice while the water flow was on. This dislodged the ballotini and allowed the water to pass through the orifice more freely. Once the orifice was free of ballotini and fluidisation occurred again, no ballotini fell back down into the orifice to cause a blockage.

3.6.3 Nose pieces of Pitot tubes blocked by ballotini

The glass nose pieces of each of the Pitot tubes often got blocked by a single ballotini bead. The ballotini had a particle diameter distribution of between 0.6 and 0.8 mm, however there were some beads which had smaller diameters, typically 0.5 mm. It was these smaller beads which got lodged inside the glass nose pieces.

It was noticed that the noses became more frequently blocked when the Pitot tubes were moved in the bed from a point of low pressure to a point of high pressure. The movement of the Pitot tubes between two points of this nature induced a large water rise in the glass sight tube, caused by the pressure increase. At times this rise was up to 1 m in the sight tube. A rise as large as this required a large amount of water to flow through the nose pieces. The flow was likely to have carried the ballotini bead into the nose of the Pitot tube and blocking it.

It was quickly realised that the nose pieces were blocked when there was a delayed or very slow water rise in the glass sight tube. This was especially the case when the Pitot tube"s nose was set in position to anticipate a high pressure and then a slow water rise was experienced instead. In most instances when this slow water rise was experienced, sufficient time was given to allow the water in the sight tube to stabilise, before taking the sight tube"s water elevation measurement. However, in other instances there was practically no water rise in the sight tube at all. In such cases the ballotini beads had been tightly lodged in the nose piece and had not allowed any water to enter the Pitot tube.

A number of trial and error techniques were tried to dislodge the beads. Firstly, the clear flexible tubing connecting the top of the Pitot tube and the glass sight tube was rapidly squeezed. The squeezing created a very small pressure increase down to the Pitot tube"s nose, which at times was enough to dislodge the bead. Another technique which was used if the squeezing did not work, was to tilt the glass sight tube. A tilted sight tube meant that a greater water volume had to enter the Pitot tube, so that the sight tube"s water elevation would reflect the pressure at the Pitot tube"s nose. Once the sight tube"s water had risen to a substantial level, the sight tube was rapidly tilted back to vertical. Then the water elevation in the sight tube was too high which meant that water had to flow out of the Pitot tube rather than into it. This rapid flow out of the Pitot tube often pushed the bead outwards thus dislodging it, which allowed the measurement to be taken.

If these two techniques did not work then the Pitot tube had to be completely lifted out of the ballotini bed where various other methods were tried. These methods involved prying the bead off the nose, blowing compressed air through the Pitot tube and prodding the bead with a thin piece of wire through the opposite end of the nose. Only once the bead was dislodged, could experimental testing commence again.

3.6.4 Water surface fluctuations observed in glass sight tube

An observation was made that when taking readings of the water surface elevation in the glass sight tube, the water surface would tend to fluctuate. The fluctuations generally occurred when medium to high pressure measurements were being taken, typically near to or inside the fluidised zone. These fluctuations were found to be up to 1 mm where medium pressures were measured. However, when high pressures were measured, typically inside the fluidised zone, these fluctuations were up to 10 mm. The higher fluctuations made it particularly difficult to take the water elevation readings in the sight tube. When this was the case, the average between the surface fluctuations was recorded.

The fluctuations are likely to have been the result of the continually changing dynamics of internal fluidisation. It is also possible that when the ballotini beads collided with the opening of the Pitot tube"s nose piece, this caused a pressure spike. Therefore a water rise in the sight tube was experienced, followed by a water drop again. Another possible cause for the fluctuations was the fact that the experiment made use of water supplied directly from the municipal network. Municipal networks are known to have pressure fluctuations, which are caused by taps being opened and closed continuously.

3.6.5 Fluctuations in inlet flow rate

The water flow supplied to the experiment"s centre orifice was found to vary between 1.97 l/min and 2.03 l/min. Often the flow rate would automatically return to the required 2 l/min. However, sometimes this did not happen and the valve on the inlet network would have to be physically adjusted.

Chapter 4

4 Results and discussion

This chapter presents and discusses all the results found from the internal fluidisation experiments described in Chapter 3. First the details of how the measured data was processed is described followed by the results and the analysis of the results. The analysis of the results specifically looked at the fluid flow velocities, pressures and surplus energies caused by the internal fluidising jet, followed by the geometries of the fluidised and mobile bed zones.

4.1 Data processing

The recorded measurements in the experiments were processed in a slightly different method to what was described in the literature. Specifically Equation 2.19 was not used to calculate the flow velocities in the ballotini bed. The reason for this is that the Pitot tube had a different design to the typical Pitot tube used in industry. The difference was that the Pitot tubes used here did not consist of the static pressure points which are the series of holes on the circumference of the tube offset from the tube"s nose. The Pitot tubes therefore only consisted of the openings in the nose, known as the stagnation points. The typical double tube Pitot tube was not used as the pressure measurements needed to be taken at exactly the same point which would be impossible due to the offset distance between the tube's nose (stagnation point) and the series of static holes on the circumference.

As stated previously, at all the measurement points the pressure and dynamic pressure were measured in a combined reading which equalled the stagnation pressure, and in a separate measurement only the pressure was recorded. Therefore the dynamic pressure was the first calculation to be done, which was simply the difference between the combined and separate readings above. After the pressure and the dynamic pressure were found as pressure heads in mm, the pressures in Pa and the velocity in m/s needed to be calculated.

Instead of using Equation 2.19, the individual components of Bernoulli"s Equation (Equation 4.1) were used to separately calculate the pressure in Pa and the velocity in m/s. For example, the pressure in Pa was calculated using the potential energy or the flow work component shown in Equation 4.2. Likewise, the velocity in m/s was calculated using the kinetic energy component shown in Equation 4.3. For each of the potential energy and kinetic energy components in Equations 4.2 and 4.3 respectively, the H was the water elevation recorded in the glass sight tube. The following is a description of how the individual components were calculated using all the measurements at a sample point.

$$\mathrm{E}_{(m)} = \frac{V^2}{2g} + \frac{P}{\rho_f g} + z \tag{4.1}$$

$$\mathrm{H}_{(mm)} = \frac{P}{\rho_f g} \tag{4.2}$$

$$\mathrm{H}_{(mm)} = \frac{V^2}{2g} \tag{4.3}$$

Sample measurement point: X, Y, Z = (0, 10, 40) mm

Measurements taken:

Stagnation pressure (Horizontal direction) = 33.2 mm	*(1)*
Stagnation pressure (Vertical direction) = 34.9 mm	*(2)*
Pressure = 29.3 mm	*(3)*

Calculated dynamic pressures:

Horizontal = 3.9 mm	*(1-3)*
Vertical = 5.6 mm	*(2-3)*

Calculated pressure (Pa) using Equation 4.2:

*$P=\rho_f gH$ = 1*9.81*29.3 =* ***287.43 Pa***

Calculated velocity (m/s) Equation 4.3:

Horizontal: $V=\sqrt{(2gH)}$ = $\sqrt{(2*9.81*0.0039)}$ = ***0.277 m/s***

Vertical: $V=\sqrt{(2gH)}$ = $\sqrt{(2*9.81*0.0056)}$ = ***0.331 m/s***

4.2 Experimental results

4.2.1 Velocity distribution

This measurement was the velocity of the fluid flow through the ballotini bed, caused by the fluidising jet. The measurements were taken at the centre orifice using both the Pitot tubes. From the recorded measurements, the dynamic pressure was calculated by subtracting the pressure from the stagnation pressure. The velocity was then calculated by equating the dynamic pressure in Equation 4.3. At each measurement point, measurements were taken in the Y and Z directions which were the two velocity vector components. The resultant vector could be found at each of the points. The velocity vectors are discussed next, followed by the vertical and horizontal velocity vector components. A description of how the vertical and horizontal velocities were calculated is illustrated in Section 4.1 and a description of how the velocity vectors were calculated is illustrated below.

Calculated velocity (m/s) Equation 4.3:

Horizontal: $V=\sqrt{(2gH)} = \sqrt{(2*9.81*0.0039)} = \mathbf{0.277\ m/s}$

Vertical: $V=\sqrt{(2gH)} = \sqrt{(2*9.81*0.0056)} = \mathbf{0.331\ m/s}$

Vector velocity (m/s)

Vector: $V=\sqrt{(0.277^2+0.331^2)} = \mathbf{0.290\ m/s}$

4.2.1.1 Velocity vectors

The resultant vectors were plotted and are presented in Figure 4.1. The vectors are colour coded from the smallest velocity of 0 m/s in blue to the largest velocity of 5.24 m/s in red. At points (0;0), (0;10) and (0;20) there are three large red vectors of different thicknesses plotted on top of each other. This is because the vectors were scaled up to make the smaller vectors visible. Of these three vectors, the thinner red vector represents the vector from (0;0), the thicker vector from (0;10) and the thickest vector from (0;20). The blue dots in the figure represent zero velocity. In Figure 4.1 the vectors on the left side plane of the orifice are a mirror image of the vectors on the right side plane which is the measured data. Therefore the vectors on the left side were not measured.

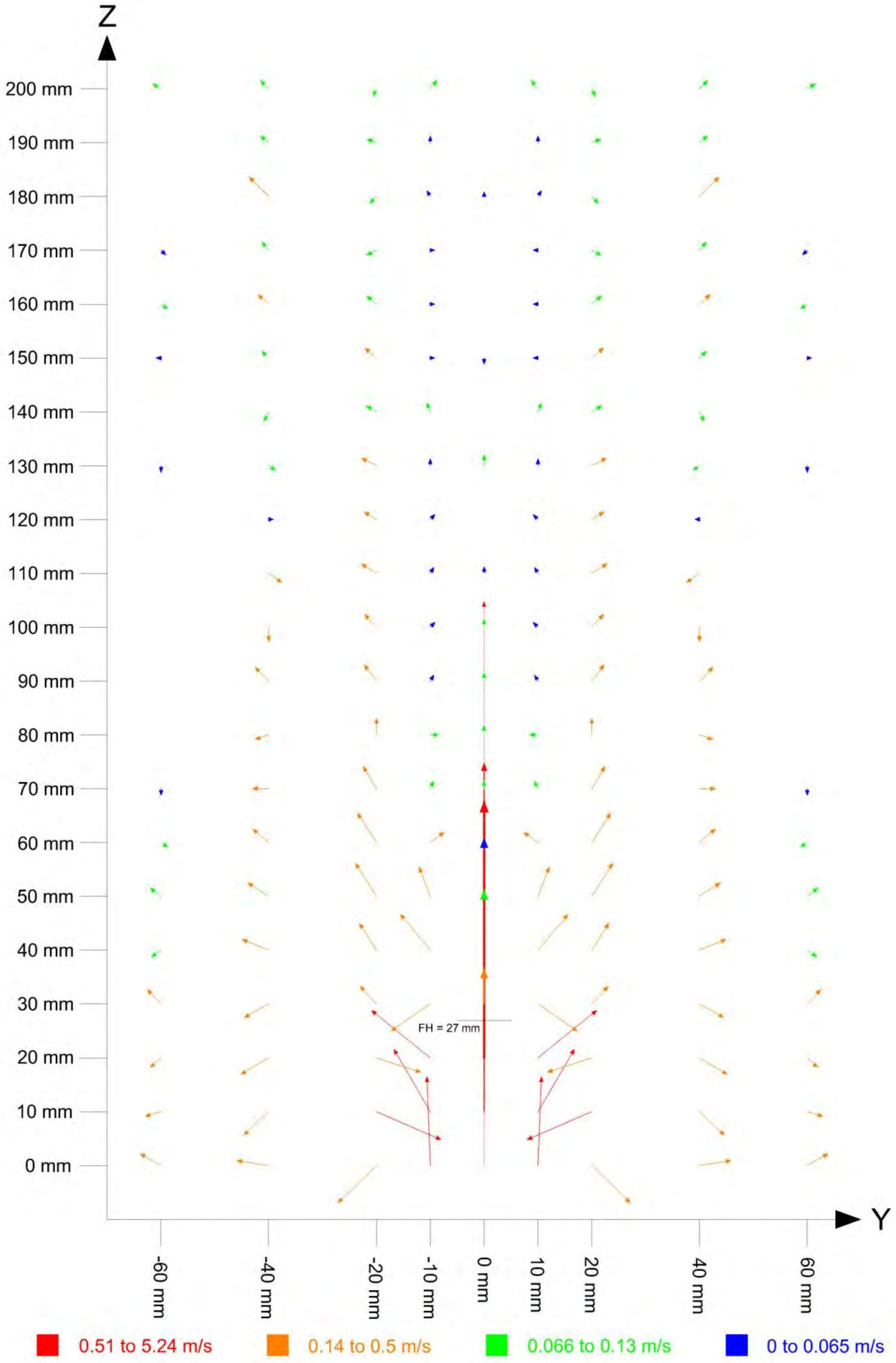

Figure 4.1: Velocity vector plot

In Figure 4.1 the solid black line labelled FH = 27 mm is the fluidisation height, which is the estimated height the fluidised zone reached. This height was regarded as the point at the top of the vortex movement which was the top of the fluidised zone. In the experiments the fluidisation height was found to be 27 mm. This height was found by inserting the Pitot tubes from directly above the orifice into the ballotini bed. When the Pitot tubes entered into the fluidised zone a distinctive scramble noise could be heard, which was transmitted through the Pitot tubes. The fluidisation height was marked as the point at which the noise became audible.

In Figure 4.1 it is interesting to note that directly above the FH the vertical velocities drop off suddenly, as the localised area of green and blue vectors and dots show. However, moving horizontally away from this localised area the orange vectors show the velocities to be greater. This is evidence that the vectors are deflected outwards at roughly 45° from the top of the fluidised zone.

Figure 4.2 is an illustration of the fluid flow streamlines in the ballotini bed. The streamlines were estimated by judgement of the vectors shown in Figure 4.1. The literature on fluidisation generally refers to the mobile zone as the movement of ballotini from the top of the fluidised zone in a circular trajectory down to the orifice. At the orifice the ballotini then join the fluidised zone and are transported to the top of the fluidised zone, where this process repeats itself. Similar trajectories of the ballotini are illustrated by the flow streamlines in Figure 4.2. However the flow streamlines and ballotini trajectories are not likely to be the same. The trajectories of the ballotini will be later analysed in the geometry of the influence zone shown in Figure 4.11.

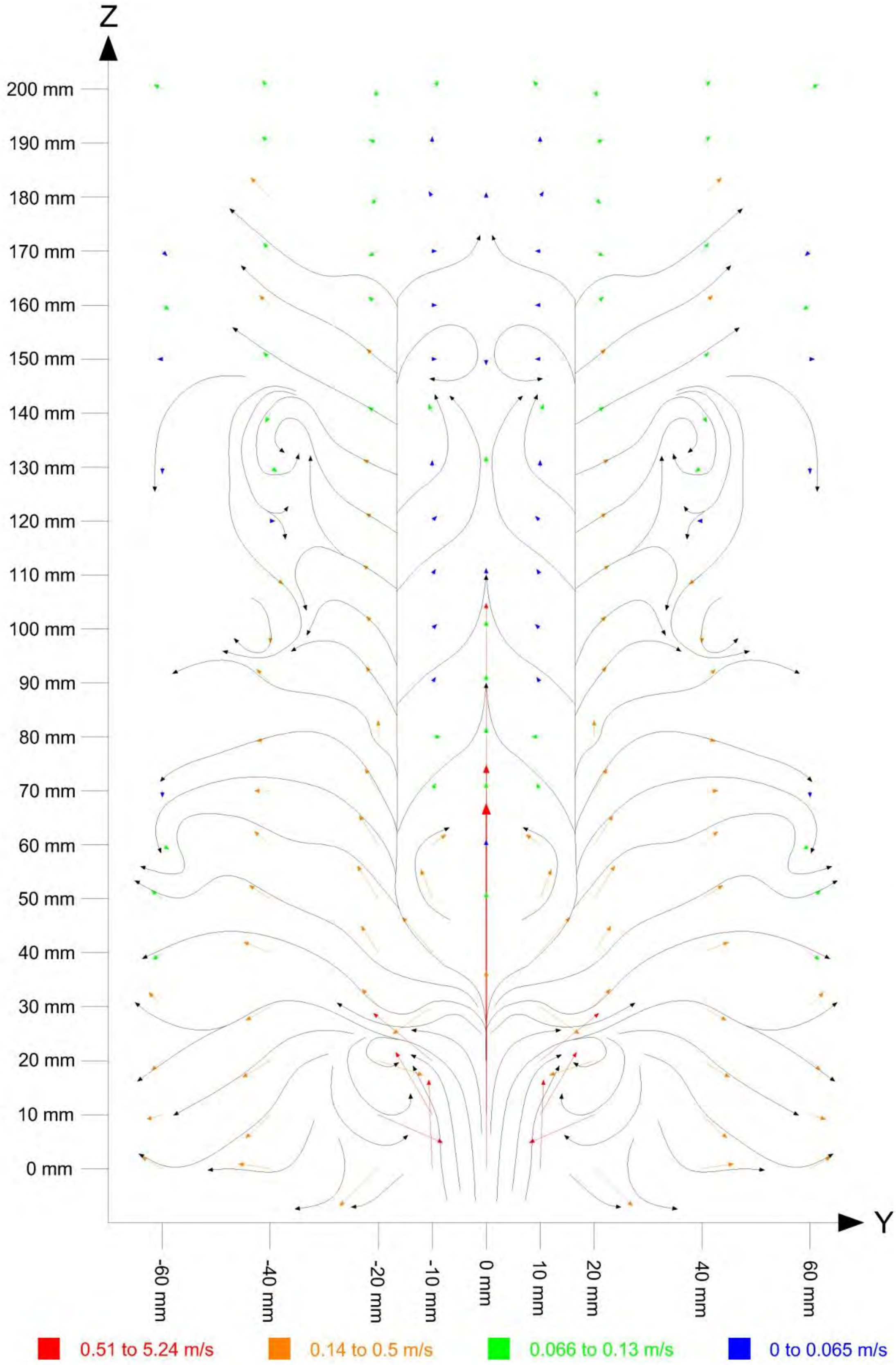

Figure 4.2: Predicted flow streamlines

4.2.1.2 Velocity components

- Vertical velocities

This is the vertical velocity component of the vectors that were presented previously. These vertical components are presented in Figure 4.3. In the figure, each line interconnecting its points represents the vertical velocity along a horizontal slice above the orifice, therefore perpendicular to the fluidising jet. The horizontal slices are represented as Z=0 up to Z=200 mm. The slices can be visualised as horizontal planes or horizontal disks stacked on top of each other above the orifice. In Figure 4.3 there are a number of points that are indistinguishable. Figure 4.4 is a scaled up graph of this dense region which excludes the horizontal slices of Z=0 up to Z=30 mm.

It is interesting to note when looking at the points and their interconnecting lines in Figures 4.3 and 4.4, that there are similar trends in many of the vertical velocities. For example in Figure 4.3 the vertical velocities for horizontal slices Z=0, 10 and 20 mm are closely grouped at horizontal distances 10, 20, 40 and 60 mm. Another example is in Figure 4.4 where the horizontal slices Z=80, 100, 110, 130 and 140 mm have similar points and subsequent line trajectories over the whole horizontal slice. Apart from a couple of the points, they generally do compare well with each other where similarities between the interconnecting lines can be seen.

The vertical velocity measured at the orifice, the Y,Z location (0,0) was of particular importance. The reason for this was that at this location the vertical velocity could also be calculated using the known flow rate and the known orifice area. Therefore the measured and calculated velocities could be compared with each other. Here the measured velocity (V_M) was found to be 5.253 m/s as shown in Figure 4.3., while the calculated velocity (V_C) was 4.716 m/s. This reflects a difference of 0.537 m/s which is quite large. There are two likely reasons for the higher measured velocity. The first possibility is when the ballotini moves in the mobile bed zone from the top of the fluidised zone down towards the orifice. At the point when the ballotini sits alongside the orifice and is being picked up by the fluidising jet thus entering the fluidised zone is it likely that the ballotini impinges on the jet. The impingement reduces the jet flow area and therefore increases the flow velocity.

The second possibility for the higher velocity measured at the orifice could be the effect of friction on the flow passing through the orifice. Here this flow field had a circular cross section as it passed through and exited the circular orifice. It was along the edges or perimeter of this flow field that the flow experienced friction on the orifice wall, and possibly downstream of the orifice where there was friction on the ballotini bed. This friction resulted in the flow velocity at the perimeter to be lower than the velocity at the centre. When taking this velocity measurement at the orifice, the Pitot tube was placed at the centre of this flow, where the velocity was greatest. The measured velocity was therefore higher than the calculated velocity, where the calculated velocity was the average velocity over the whole flow field.

There is another possibility which is unlikely to occur, however it is still interesting to consider. This is the effect that the thickness of the glass wall of the Pitot tube's nose has by reducing the flow area of the fluidising jet as it exits the orifice. This therefore increases the localised pressure at this point, which in turn increases the velocity. In order to estimate what affect the glass thickness could have, the known flow area through the orifice can be reduced by the area of the glass wall. Once this has been done the new velocity can be calculated with the reduced known flow area. Here the new velocity, V_{NC} was calculated as 5.344 m/s. This equates to a difference of 0.09 m/s between the V_M and V_{NC}. This is a far smaller difference than when the possible influence of the Pitot tube's nose was not accounted for. The difference of 0.09 m/s is a 1.7 % error from the V_M of 5.253 m/s.

There is an interesting consideration which could result in the Pitot tubes reading higher values than what actually occur. This is when the Pitot tube is placed in the bed, it could create local fracturing of the bed. Such fracturing would then have created a flow path for the flow to pass through, which would ultimately have increased the flow velocity past the Pitot tube. This is likely to occur in the static zone of the ballotini bed thus outside of the fluidised and mobile bed zones. This is a typical result of an intrusive measuring device like the Pitot tube.

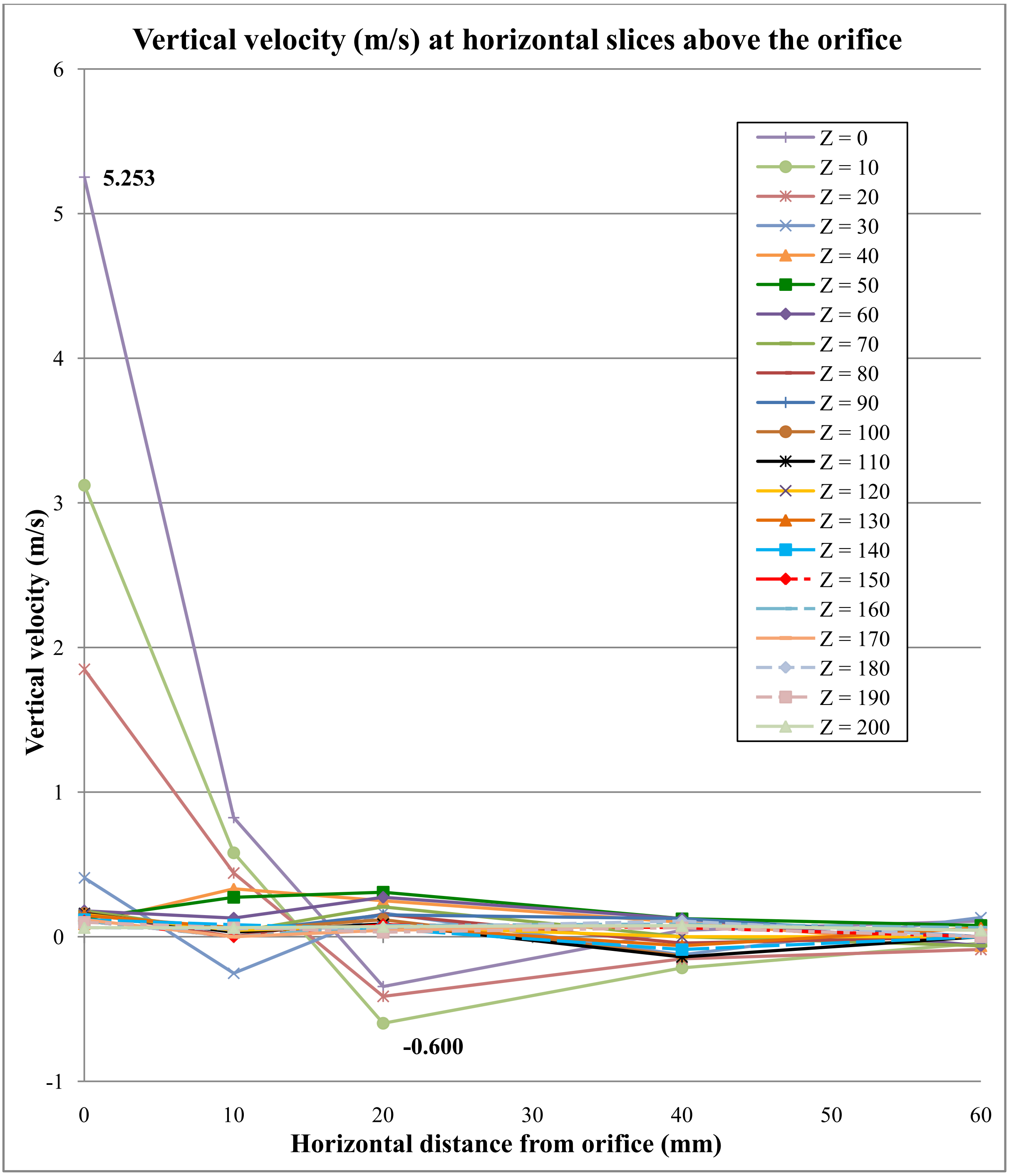

Figure 4.3: Vertical velocity for horizontal slices Z=0 to Z=200 mm

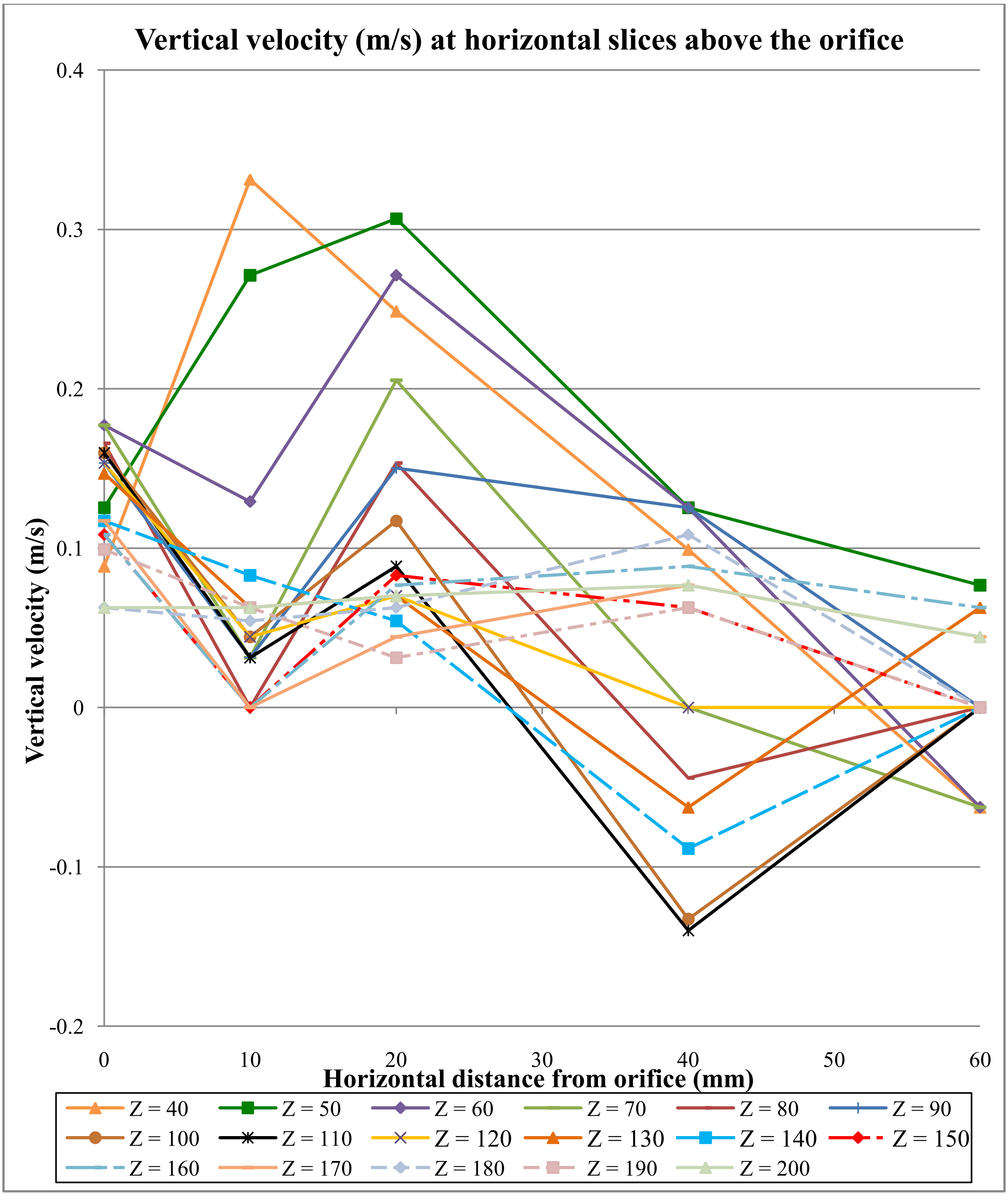

Figure 4.4: Vertical velocity for horizontal slices Z=30 to Z=200 mm

- Horizontal velocities

The horizontal velocities are the other component of the velocity vectors. The horizontal components are graphed in Figure 4.5 and are presented in vertical slices away from the orifice. The horizontal velocity components portray a different picture from the vertical velocity components. This is largely because there are no similarities between the points along the vertical slices as there are in the vertical velocities.

However a similarity that was expected, was the general trend of decreasing horizontal velocity at increasing vertical distance from the orifice. Another interesting observation in Figure 4.5 is the negative velocities, experienced along the Y=20 vertical slice at heights 10 and 20 mm in particular. The negative velocities experienced at this location facilitate an understanding of the flow motion close to and inside the fluidised zone. In addition, the horizontal velocity at points along the Y=10 vertical slice at heights 10, 20 and 30 mm, also highlights the flow motion in this region. The height of the fluidised zone is labelled FH in Figure 4.5. This height was 27 mm above the orifice.

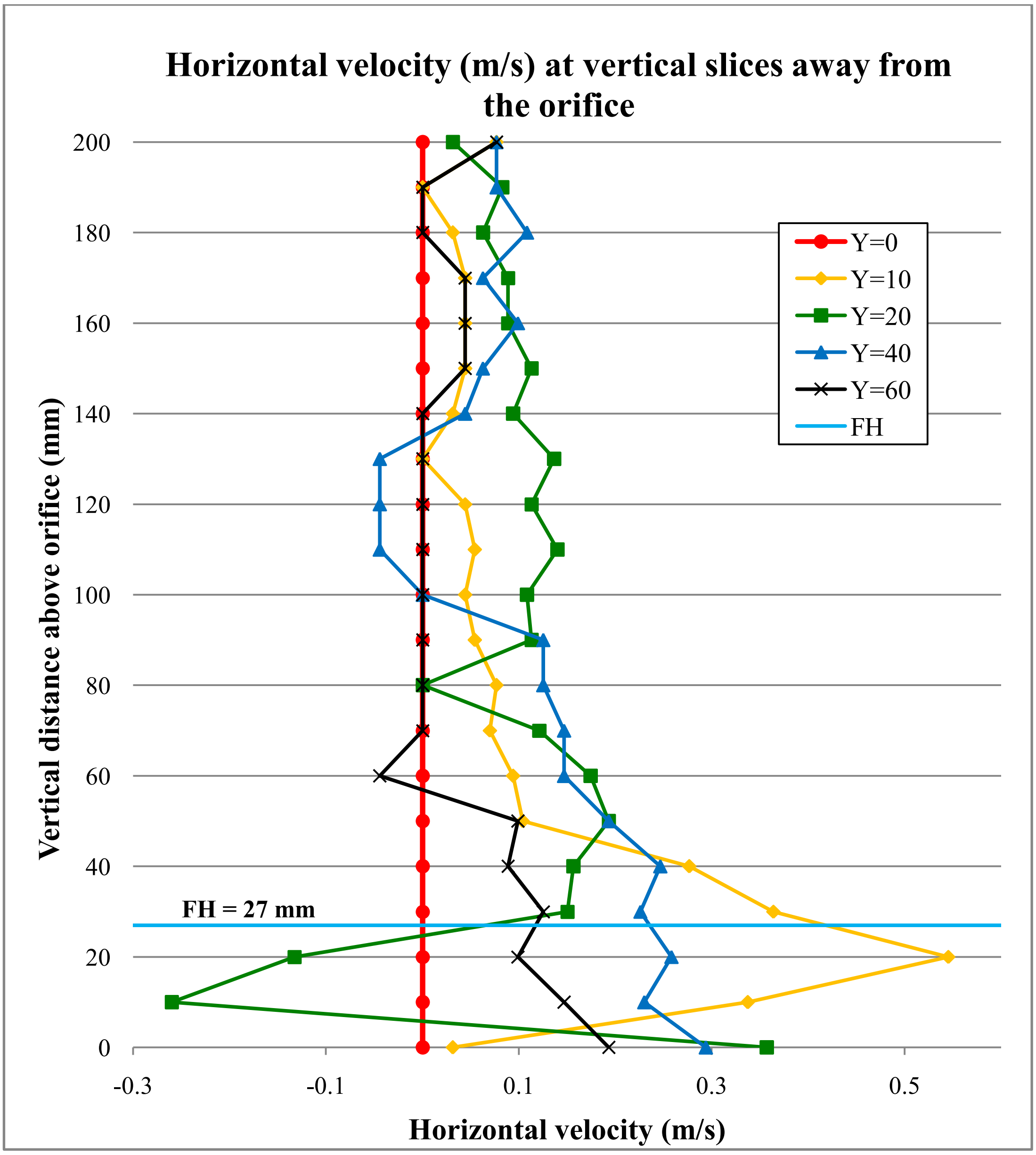

Figure 4.5: Horizontal velocity at vertical slices

4.2.2 Pressure distribution

The pressure distribution is the measured increase in pressure, therefore over and above the static pressure in the ballotini bed. The pressure at a particular point is equal in all directions, unlike the velocities which have components in different directions. In this section the pressures are presented as pressure head (mm). Figure 4.6 is a graph showing the pressure head distribution along horizontal slices above the orifice. As with the velocity distribution, the horizontal slices are at 10 mm intervals between heights of Z=0 and Z=200 mm.

In Figure 4.6 the maximum pressure head in the ballotini bed of 110.6 mm exists directly above the orifice at point Z=20 mm. The maximum pressure is expected to exist near the top of the fluidised zone or the fluidising head. This in fact is the region where the vortex action occurs. The graph shows how the pressures rapidly decrease from this point of maximum pressure with increasing elevation, and also the lower pressures at points Z=0 and Z=10 mm. It may be noticeable in the graph that the horizontal slices from Z=40 to Z=200 mm in particular have very similar interconnecting line trajectories. The only difference between the trajectories of these horizontal slices, is the decreasing pressure at increasing elevation.

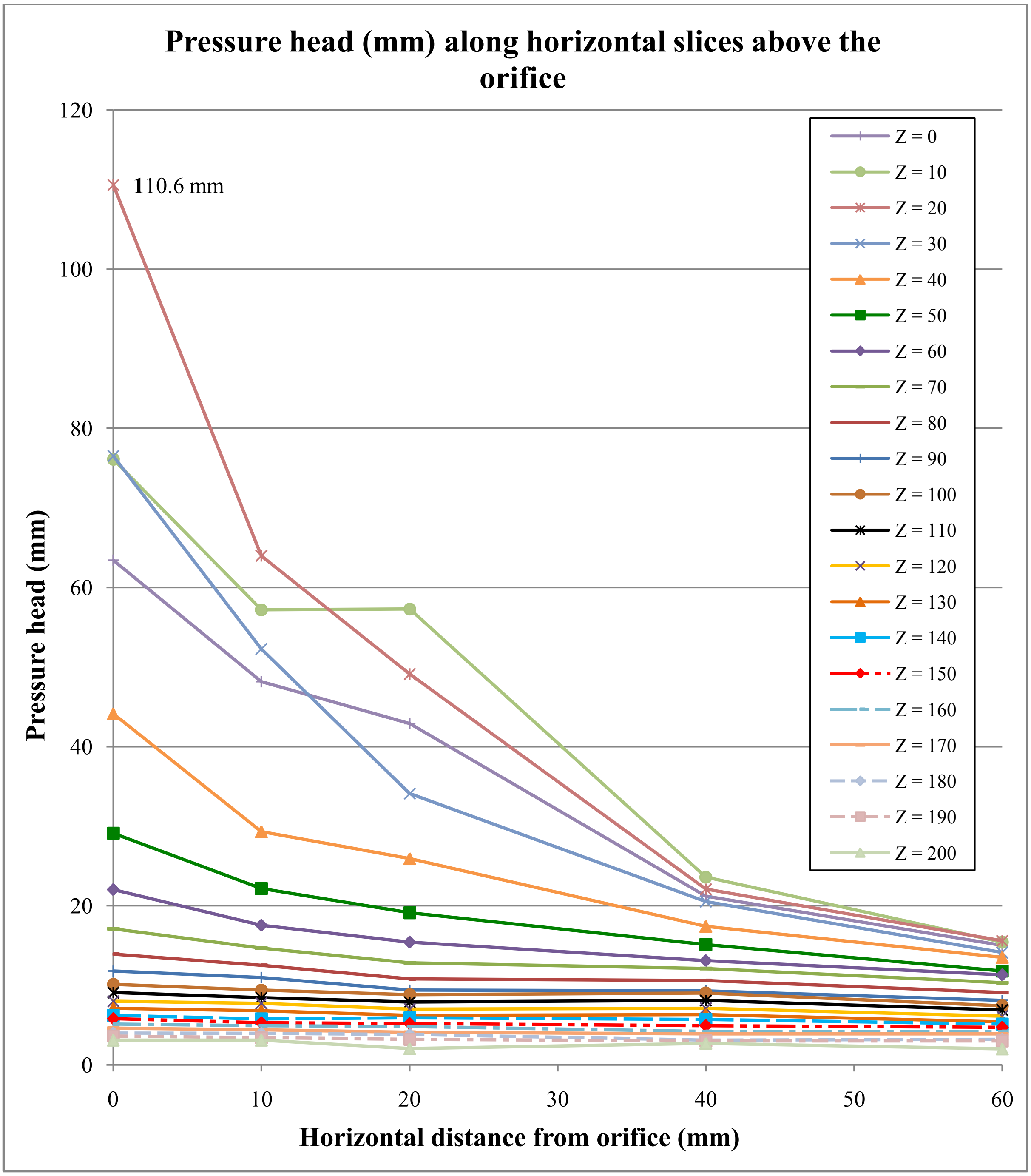

Figure 4.6: Pressure head along horizontal slices above the orifice

Figure 4.7 is a graph plotting the pressure head along vertical slices Y=0 to Y=60 mm. The maximum pressure occurs along the Y=0 mm slice. The locations of the maximum pressures for each vertical slice are of particular interest. The graph shows that these maximum pressures along each vertical slice occur at points (0,20), (10,20), (20,10), (40,10) and (60,20). These maximum pressures may not necessarily be found at the exact heights of Z=10 or 20 mm as indicated here, they may in fact be some distance above or below these heights. For example the maximum pressure at point (0,20) may in fact be at point (0,22) or (0,17) for instance. However, even though the maximum pressures may not exist exactly at the points shown; it should still be noted that there is a general trend of the maximum pressures being at Z=20 mm nearer the orifice, which then moves lower to Z=10 mm further away from the orifice. This trend is shown by the max pressures line in Figure 4.7. A possible reason for this trend is due to the influence of the glass tank base on the fluid flow. When the flow from the fluidised zone head circles down towards the orifice, the base may disturb this flow. This would result in a localised increase in the pressure nearer to the glass, as shown in the graph. This circular flow motion is described in the velocity distribution section and is referred to again later in the analysis of the geometry of the influence zone.

The dashed bright green line in Figure 4.7 is a linear trend-line for all the readings at measurement points above elevation Z=100 mm. The trend-line shows that all these points mentioned generally have a linear distribution of pressure in the ballotini bed. However, generally the readings at measurement points below this elevation of Z=100 mm move off this linear trend-line. At these lower measurement points a nonlinear distribution of pressure in the ballotini bed is therefore experienced. This is with the exception of the vertical slice at Y=60 mm, which tends to almost maintain a linear trend of pressure as shown. It is possible that where in the ballotini bed the pressures have a linear distribution as described here, that the water flow here is Darcy flow, thus being laminar flow. This is because in Darcy flow the hydraulic gradient, which is the ratio of the pressure difference between two points over their characteristic distance, has a linear relationship. Furthermore this means that over the regions in the bed where the pressures have a nonlinear distribution, the flow must be nonlinear and therefore turbulent flow must be present.

The fluidised height (FH) is labelled in Figure 4.7 at the Z=27 mm height. It is noticeable that the maximum pressures were all recorded below this height, typically at Z=20 and 10 mm. Although as mentioned previously these maximum pressures may be slightly above or below these heights. However, as described in the literature, the very top of the fluidised zone was found to be slightly higher than the point of maximum pressure. Terekhov, *et al.* (2009) amongst others, found that the maximum pressure did in fact exist at the centre of a jet head, which is the centre of the vortex movement. However, in a jet directed vertically upwards, the centre of the jet head is slightly below the top of the jet head. These results then would seem to be keeping with the literature.

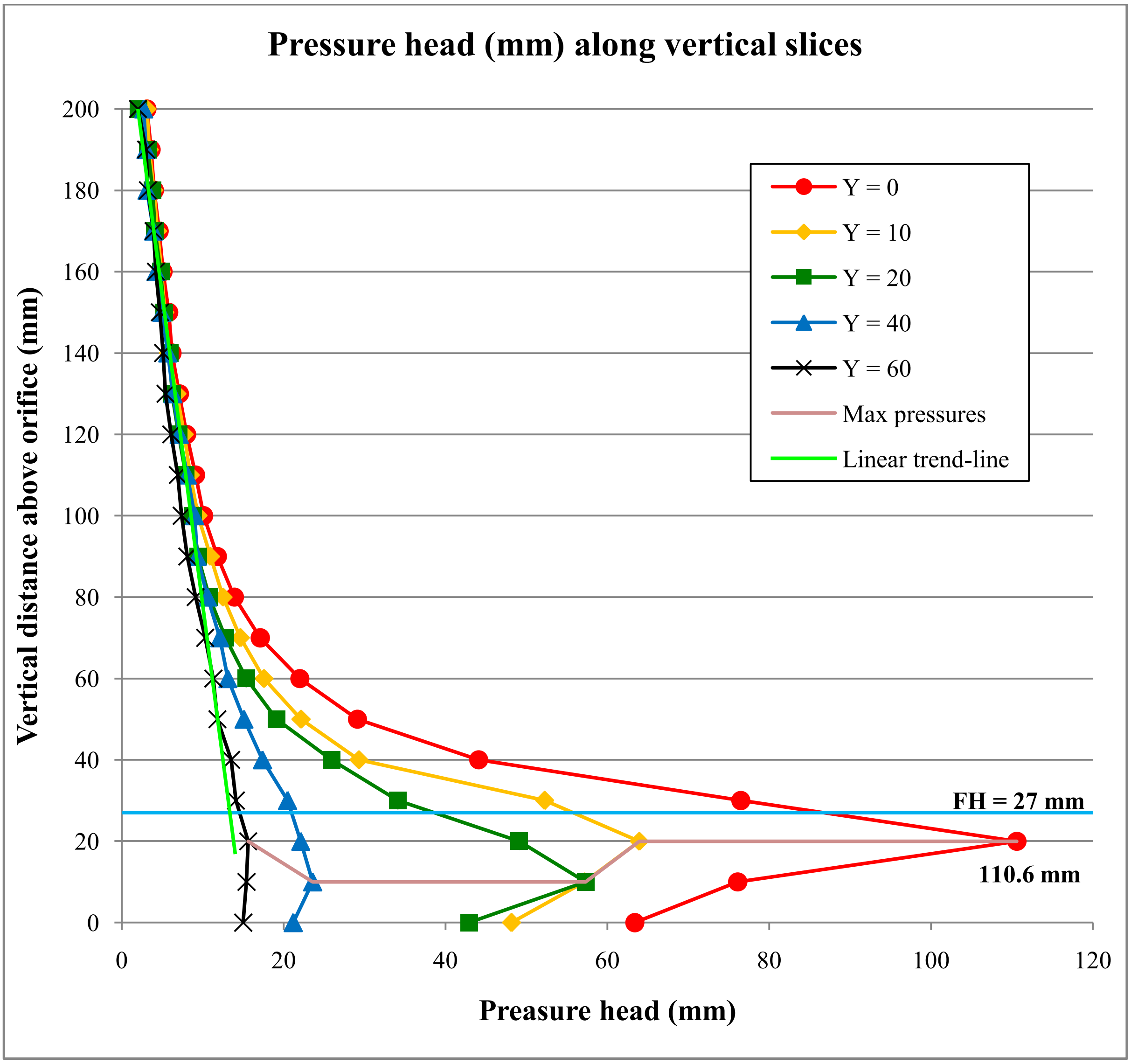

Figure 4.7: Pressure head along vertical slices

4.2.3 Energy distribution

This is the energy measured in the ballotini bed which is the increase in energy over and above the static energy. The static energy is the same everywhere in the ballotini bed which is explained by Bernoulli's Theorem. Basically the theorem portrays that at increasing depth thus a loss in elevation results in a lower energy, however the pressure increases which results in an increase the energy, therefore the energy remains unchanged.

Figure 4.8 is a graph of the energy along the vertical slices. The graph includes the ballotini bed surface as well as the static water surface in relation to where the measurements were taken. The energy at the ballotini bed surface is regarded as being zero. From elevation Z=200 down to Z=0 mm where the measurements were taken, the energies increase with depth. The graph contains an insert which is a magnification of the region. The insert shows the detail for the slices from the orifice to elevation Z=100 mm.

In the graph it is interesting to note that there is a large amount of energy which exists in the region directly above the orifice, up to an elevation of Z=20 mm. The bulk of this energy is from the vertical velocity component. The energy then rapidly decreases outside of this region. Evidently the region is very similar in size to the fluidised zone. More detail of the fluidised zone is given in section 4.2.4. The graph shows that a large amount of energy is contained in this region of the fluidised zone. This is clearly shown in the graph by how much lower the energy is at points higher up and away from directly above the orifice to elevation Z=20 mm. This finding that large amounts of energy can be sustained in a bed surrounding a water jet of this nature, concurs with what previous studies by van Zyl, *et al*. (2013) have found.

In Figure 4.8 and in particular in the insert, it is noticeable that the energy at point (10;10) is possibly an error. The energy at this location is less than the two energies on the same vertical plane above and below this location. The energy here is 75 mm whereas above and below this location they are 82 and 83 mm respectively. The reason for this point having a lower energy is due to a low pressure measurement which was taken at this point. This location of (10;10) is very near to the orifice. It is also very near to the region where the circular flow from the top of the fluidised zone rejoins the fluidised zone at the orifice. At this rejoining point near the orifice, there are likely to be suction or low pressures which are caused by the vertical fluidising jet sucking in water and ballotini. Therefore the low pressure measurement at this location could well be the result of the suction.

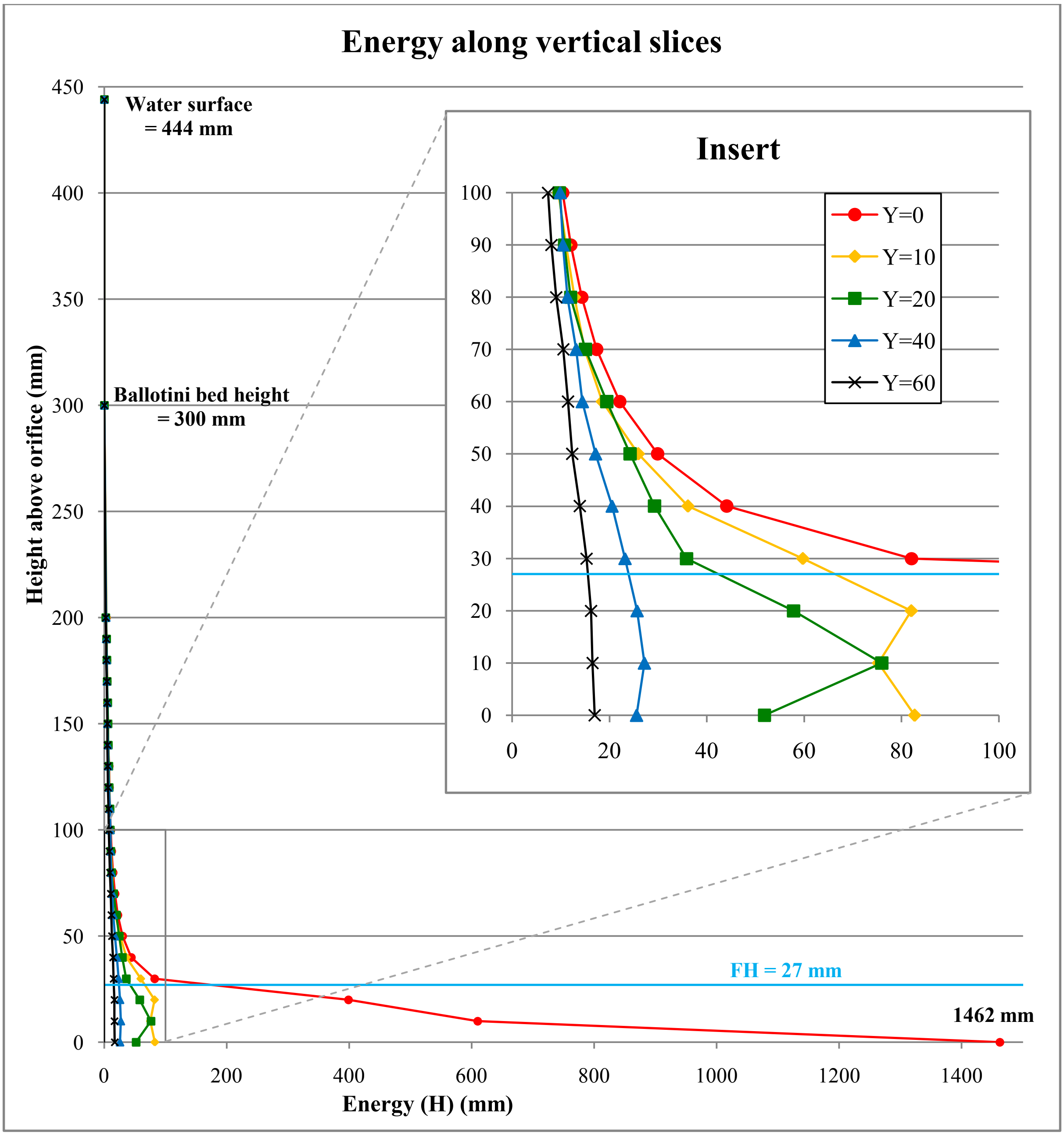

Figure 4.8: Energy along vertical slices

Figure 4.9 is a plot of the energy along the vertical slice Y=0 mm. The plot shows the zero energy at the ballotini bed surface of Z=300 mm. Also on the plot is a dashed blue line. This blue line is a linear trend-line of the energies at the measurement points between elevations Z=160 and Z=200 mm. On the graph, both the trend-line's equation and the R^2 value are shown. It is interesting to note that the R^2 value is 1, which shows that the energy has a linear distribution in the bed at these elevations.

The equation of the linear trend-line in Figure 4.9 has a Y intercept of 262 mm, as shown on the graph. If the energy were to follow this trend line at elevations above Z=200 mm, then the energy would become zero at this elevation of Z=262 mm, which is below the surface of the ballotini bed. This however is unlikely as there is energy up to the surface of the ballotini bed due to the flow from the fluidising jet which has to flow to the overflow holes in the glass tank, where the holes are above the bed surface. The flow which passes through the bed surface towards the overflow holes is however low. The average flow velocity is 0.11 m/s which would result in a water rise in the glass sight tube of 6x10^{-4} mm. It is most likely that the Pitot tubes are not able to record such low pressures which is the likely reason for this discrepancy.

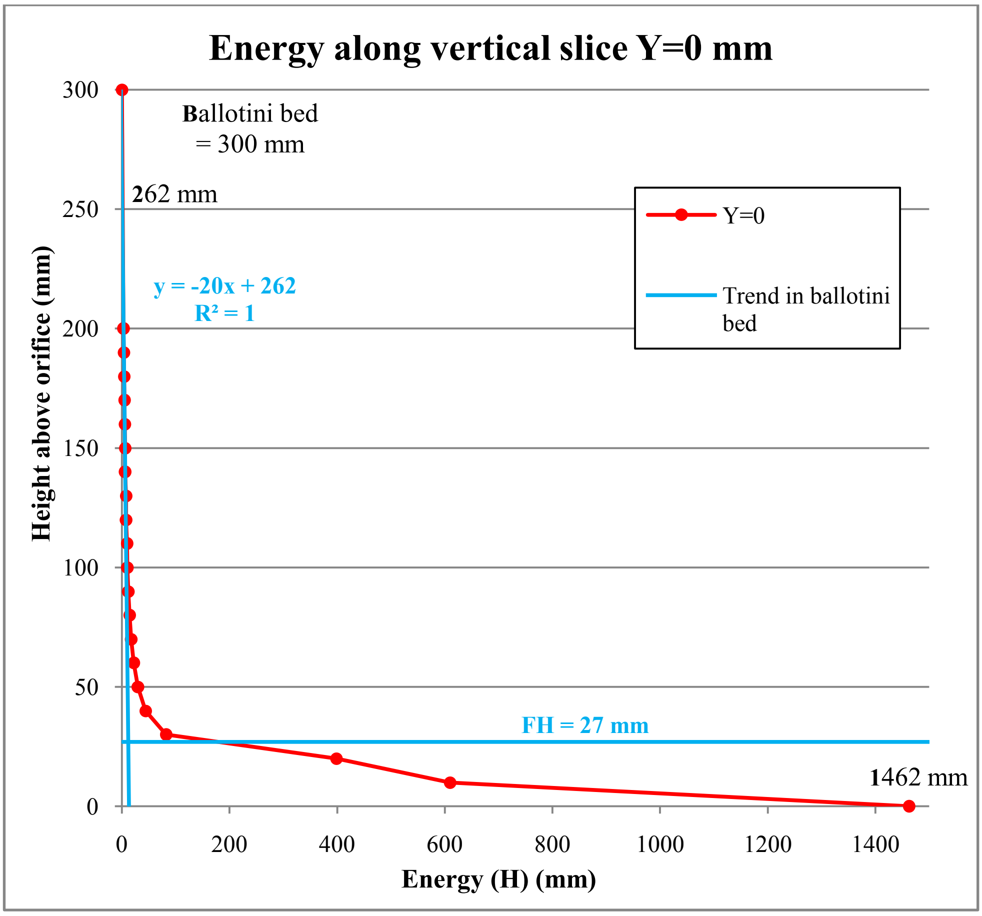

Figure 4.9: Energy along vertical slice Y=0 mm

The energy along horizontal slices above the orifice is presented in the graph in Figure 4.10. The graph also consists of a zoomed insert, showing the region from Y=0 to Y=60 mm for energies from 0 to 100 mm. It is noticeable in the graph that the horizontal slices from Z=200 down to Z=30 mm or even possibly Z=20 mm, have similar trajectories to those of the interconnecting lines between the measurement points. However, the horizontal slices of Z=0 and Z=10 mm, have trajectories that are not as similar to those of the interconnecting lines. These non-similarities exist due to the energies at points (10;10) and (20;10). The point (10;10), as explained previously, has lower energy due to the possible suction caused by the fluidising jet.

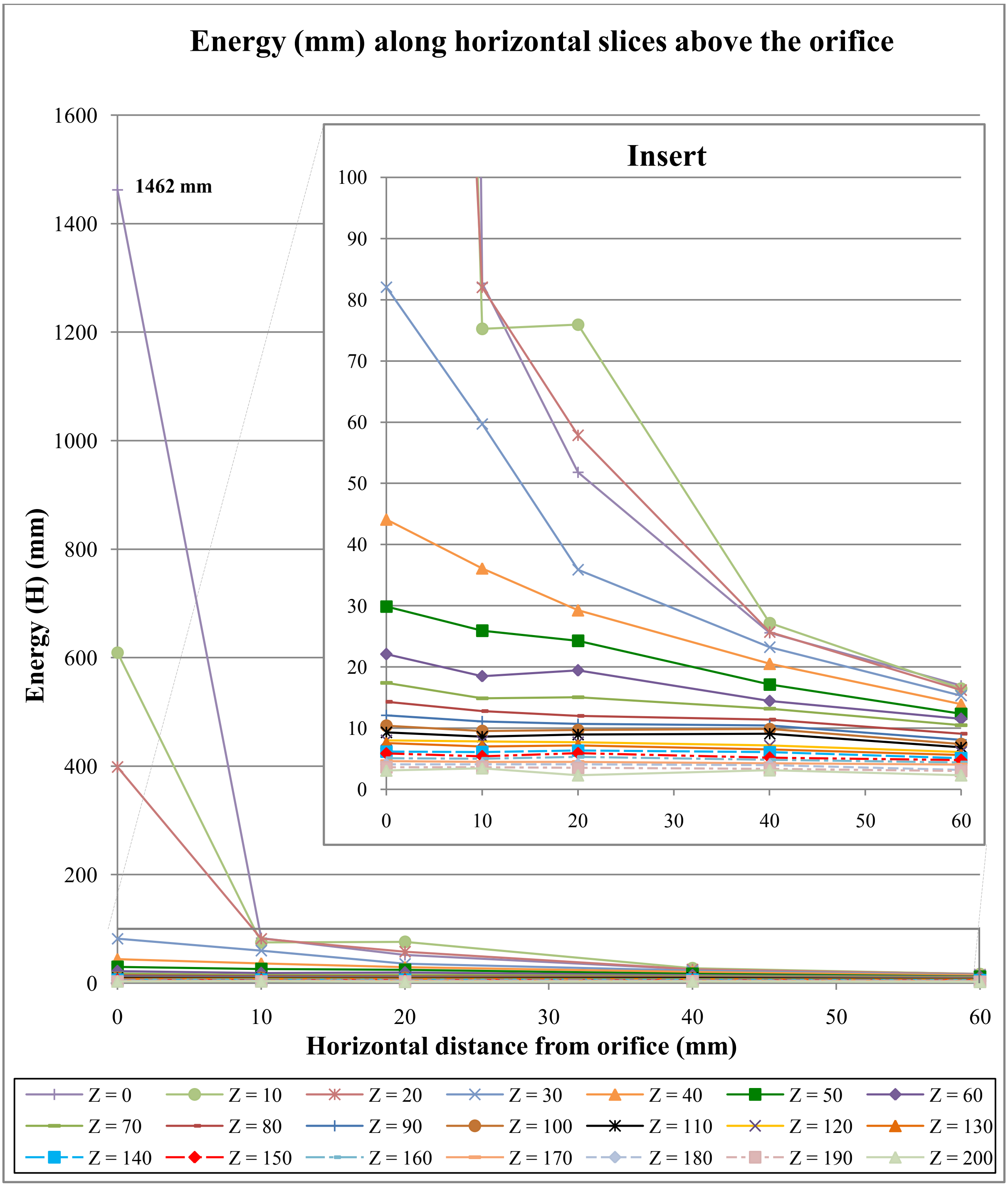

Figure 4.10: Energy along horizontal slices

From the energy graphs along both the vertical and horizontal slices, it is clear that there are large energies that are contained in the fluidised zone. The energies in this region seem to be contained by the ballotini bed which prevents them from being easily dissipated. The graphs illustrate how the energies then quickly decrease when moving out of the fluidised zone.

4.2.4 Side orifice observations

At the orifice located against the tank wall, no measurements were taken using the Pitot tubes as they were at the centre orifice. Instead, due to the orifice being close to the glass wall of the tank, visual monitoring of the influence zone was done through the glass. Three flow rates were tested through this orifice. Where for each flow rate, both videos and photographs were taken through the glass of the influence zone.

4.2.4.1 Motion of the ballotini

The dynamics of the ballotini's circular motion which was observed at the side orifice is of particular interest. What was observed is the circular motion of ballotini moving from the head of the fluidised zone where the ballotini were passed from the fluidised zone into the mobile bed zone. In the mobile bed zone the ballotini moved in a circular motion down towards the orifice. At the orifice the ballotini re-entered the fluidised zone where the jet transported them upwards. This motion is illustrated in Figure 4.11.

It is likely that the beads are entrained into the vertical water jet in the fluidised zone due to the drag and lift forces caused by the jet. A void is created at the point where the ballotini gets picked up and enters the fluidised zone. This void is then likely to be filled by a nearby bead, likely a bead above it or a bead away from the fluidised zone. Similarly, at the head of the fluidised zone the bead which enters the mobile bed zone pushes the bead which it collides with. The beads then continue their motion from the head of the fluidised zone in a circular ark down to the base of the fluidised zone. This ballotini movement continuously occurs in the mobile bed zone which was evident through the tank's glass wall. The motion of the ballotini from the head of the fluidised zone circling down towards the base of the zone could have been accelerated by gravity acting on the ballotini beads.

4.2.4.2 Geometry of the influence zone

The photographs taken through the glass wall were scaled and were used to determine the volumes for the three flow rates that the fluidised and mobile bed zones occupied in the ballotini bed. Also the contact areas against the glass wall of the fluidised and mobile bed zones, and the fluidising height were determined.

As described in Chapter 3, the centre of the side orifice was 3 mm away from the tank wall. Therefore, as the orifice had a diameter of 2.8 mm, the wall of the orifice was 1.6 mm from the inside of the tank wall. The projection of both the fluidised and mobile bed zones on the tank wall may thus have been disturbed by the wall. The degree of disturbance, if any, by the wall is unknown. With the three flow rates having been tested, comparisons between the measurements of the three flow rates could be done. Figure 4.11 illustrates the contact with the glass of the fluidised zone and mobile bed zone for the 2 l/min flow rate. In the figure, the left image is a photograph of the occurrence and on the right is the edited photograph used to calculate the areas and the volumes of the two zones. The flow lines are also drawn in on the image on the right to show the circular motion of ballotini from the top of the fluidised zone down to the orifice.

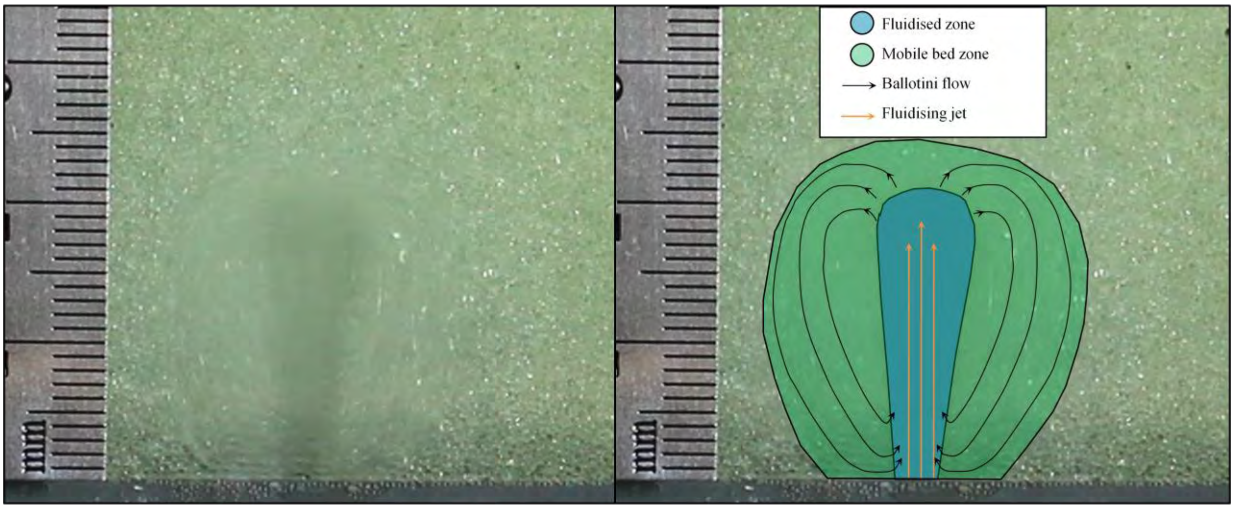

Figure 4.11: Influence zone for the 2 l/min flow rate

Comparisons of the three flow rates are presented in the graph in Figure 4.12. The graph plots the volumes of both the fluidised and the mobile bed zones for the three flow rates. The method of obtaining these volumes is described in Section 3.5.3.2. In the graph the red points and line refer to the mobile bed zone and the blue points and line refer to the fluidised zone. The volumes represent the volumes of the two zones, where the zones were bounded by the ballotini bed and the tank wall.

It is noticeable from the trend-line for the mobile bed zone that a volume of 0 mm^3 is found at a flow rate of 0.06 l/min. This demonstrates that only from a flow rate of 0.06 l/min does movement of the ballotini bed occur. However, this flow rate cannot be seen as the threshold at which internal fluidisation begins to occur. This is due to the flow rate required to initiate fluidisation being larger than the flow rate to maintain fluidisation, which is what Zoueshitiagh & Merlin (2007) found in their studies. In other words fluidisation should initiate at a flow rate greater than 0.06 l/min. This possibly indicates that the cohesion between the ballotini beads needs to be initially broken, or the uplift force needed to displace the ballotini beads is initially greater than when fluidisation is maintained.

The trend-line for the fluidised zone shows that at a flow rate of 0 l/min there is a ballotini displacement volume of 95 mm^3. This is impossible as at a zero flow rate there will be no internal fluidisation and subsequent ballotini displacement. However there are many factors that can influence the relationship between the displacement volume and flow rate whether is it a linear or a non-linear relationship. It is possible that the relationship between the ballotini displacement volume and flow rate is non-linear at lower flow rates than what were tested here.

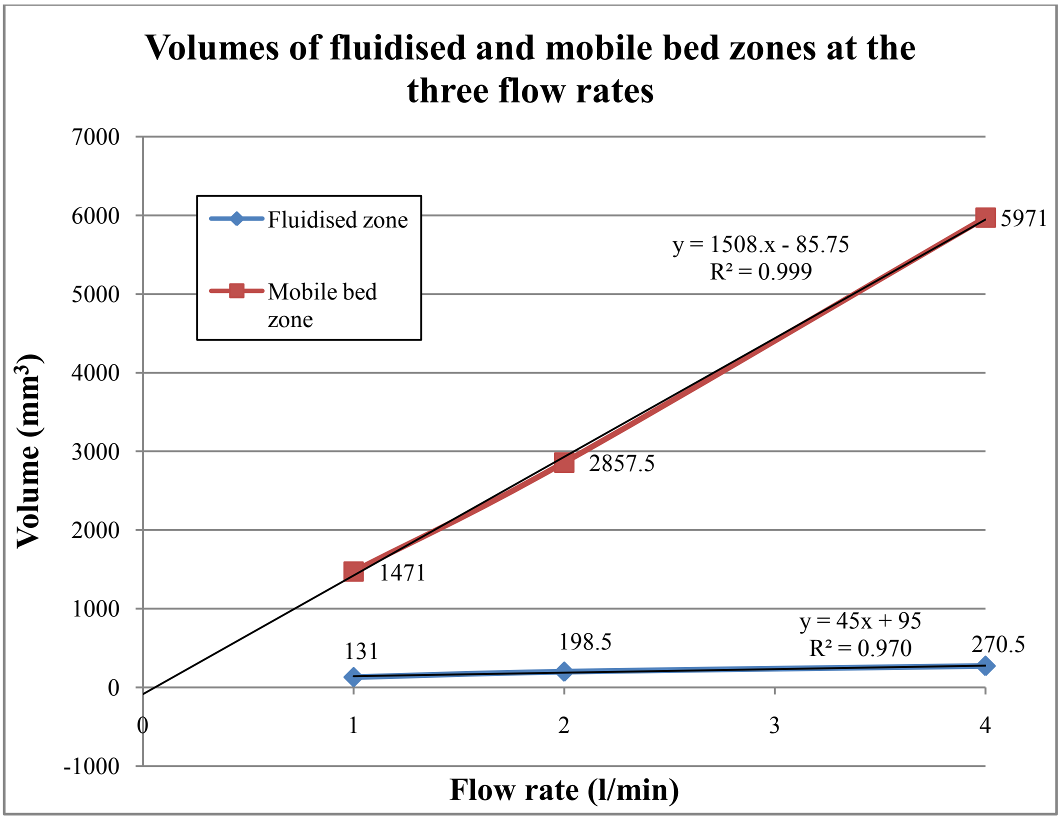

Figure 4.12: Volumes of fluidised and mobile bed zones for the three flow rates

Figure 4.13 is a graph illustrating the contact areas of the fluidised and mobile bed zones, similar to the volume graph in Figure 4.12. The graph in Figure 4.13 has R^2 values of 0.996 and 0.851 for the mobile bed and fluidised zones respectively to the linear trend-lines. These values are close to 1, showing that the relationship between the area and flow rate for the fluidised and mobile bed zones might be linear.

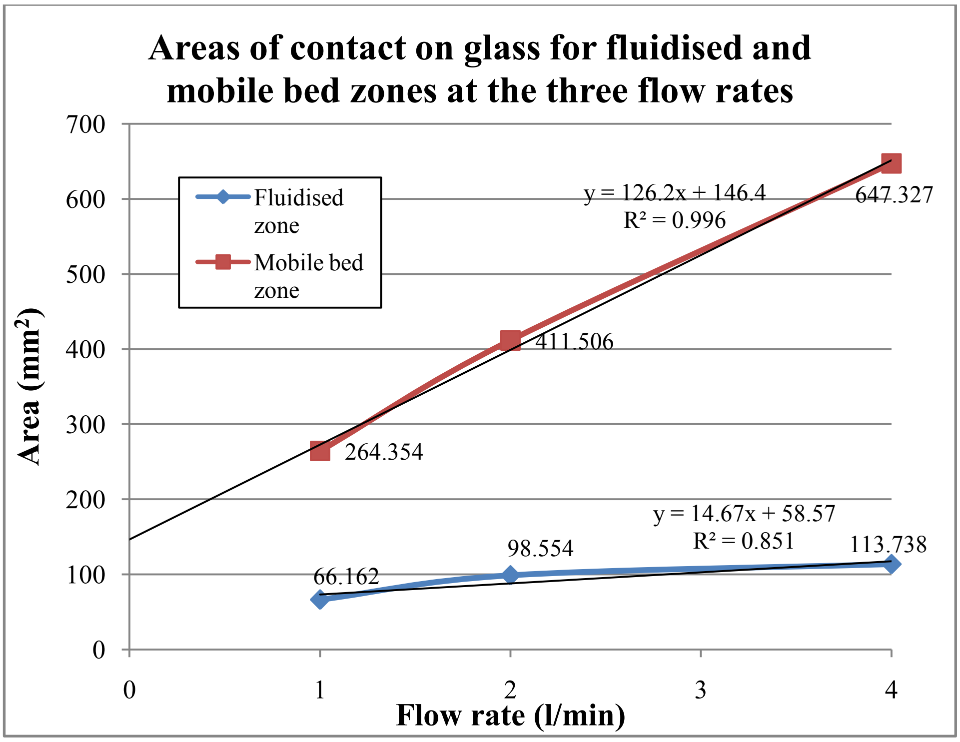

Figure 4.13: Glass contact areas of fluidised and mobile bed zones for the three flow rates

Figure 4.14 contains a graph showing the fluidisation heights (heights of the fluidised zone, FH) measured against the glass at the side orifice for the three flow rates. It is interesting to note for the 2 l/min flow rate that the FH found here of 20.8 mm was different from the FH found at the centre orifice of 27 mm. The exact reason for this is unknown.

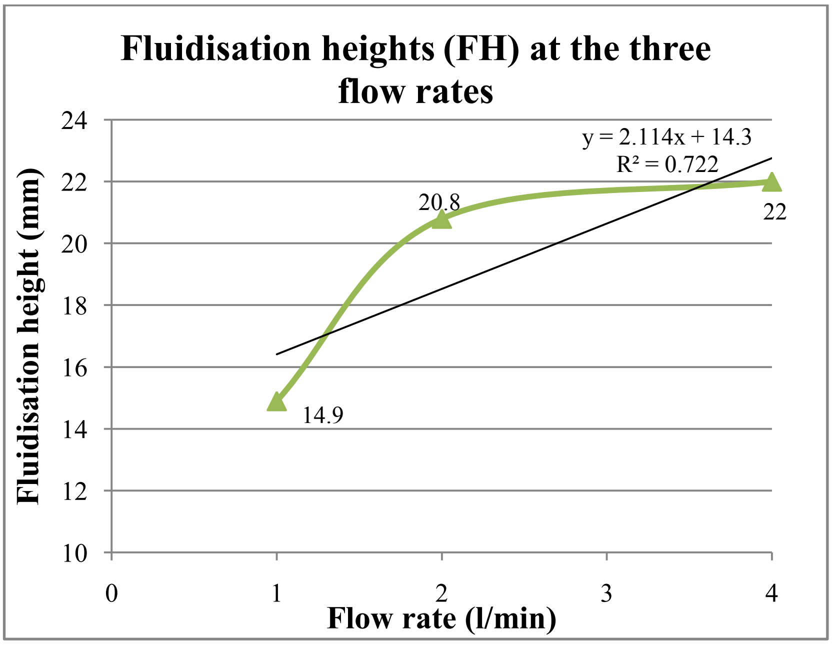

Figure 4.14: Fluidisation heights for the three flow rates

4.2.5 Other observations

At the side orifice, observations were made of the effect that pressing down on the surface of the ballotini bed had on the fluidised zone. This pressing down on the surface of the ballotini bed was done by hand and potentially increased the density of the ballotini bed, which is similar to increasing the ballotini bed height. By increasing the density of the bed the voids between the beads are subsequently decreased. The void reduction reduced the area through which the fluid could flow and therefore increased the pore pressures. When pressing down on the bed the fluidised zone decreased in height significantly. This is illustrated by the image on the right in Figure 4.15. The fluidising height (FH) was greatly decreased as shown in the figure when comparing it to the image on the left in Figure 4.15 where no downward pressure was applied.

In addition to applying downward pressure, some of the ballotini beads were lifted upwards by hand. This reduced the density of the ballotini bed. The fluidising height significantly increased when the beads were lifted and in fact the jet reached the ballotini bed surface. This observation suggests that the fluidised zone is sensitive to the bed pressure which may be effected by the bed height.

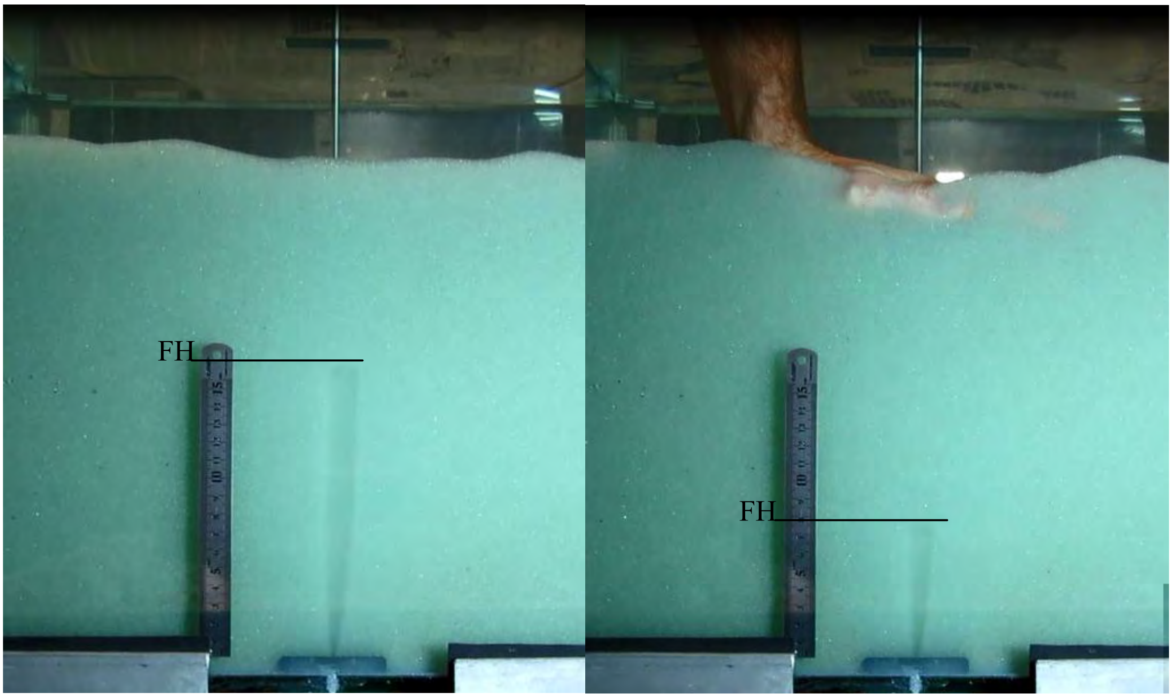

Figure 4.15: Effect of bed pressure on fluidised zone

Chapter 5

5 Conclusions and recommendations

5.1 Summary of study

Internal fluidisation is not a new phenomenon. It is however a relatively new field in Civil Engineering being researched, but it is becoming an increasingly important topic. In the field of Civil Engineering, internal fluidisation may occur outside of leaking water distribution pipes. The effects of internal fluidisation can be severe, in some cases eroding away the pipe bedding material, or damaging the foundations of nearby structures.

Some pipe leaks have been known to not show any physical evidence of the leak on the ground surface (van Zyl, *et al.* 2013). This is because of the internal fluidisation phenomenon which can prevent the leak from reaching the ground surface. Other aspects such as the direction of the leak leaving the pipe, or if the leaking water enters other conveyance systems, may also be reasons why these leaks do not reach the ground surface. This means that many leaks are undetected below the ground surface. These undetected leaks may only be recognised once complete failure of the structure has occurred. This study was therefore done to gain a better understanding of internal fluidisation, particularly in the field of Civil Engineering.

The occurrence of internal fluidisation due to a pipe leak was experimentally investigated in this study. The experimental setup replicated a leaking water pipe buried below the ground surface, under controlled conditions. The setup consisted primarily of a glass tank filled with glass ballotini which created a typical soil medium that surrounds water pipes. On top of the glass tank was a positioning system which supported and controlled the movement of the measurement instrument, where the measurement instrument was either one of two Pitot tubes. Pitot tubes are an intrusive measurement technique as in these experiments they were inserted into the ballotini bed.

In the base of the glass tank were two orifices through which water flowed and entered the glass tank. Water was allowed to flow through one of the orifices at a time, while the other was blocked off. One orifice was located in the centre of the tank base while the other was against one of the tank walls. At the centre orifice the pore and dynamic pressures created by internal fluidisation were measured using the two Pitot tubes. At the side orifice, against the tank wall, the internal fluidisation was visually analysed through the glass wall. The flow rate through the centre orifice was maintained at 2 l/min, while at the side orifice three flow rates of 1, 2 and 4 l/min were tested.

For the flow rate of 2 l/min tested at the centre orifice, large vertical velocities were found to exist near to the orifice, which then rapidly decreased further away from the orifice. The large velocities clearly occurred within the fluidised zone, where outside of this zone, generally in the static bed zone the velocities were much smaller. These large vertical velocities ended at the same elevation as the predicted fluidised height (FH), where the fluidised height was at the top of the fluidised zone. This elevation was also the top of the circular vortex movement which occurred due to the internal fluidisation.

The velocity vector plot (Figure 4.1) shows some vectors which are very different to the vectors surrounding them - particularly some of the vectors which are further away from the orifice. These vectors are not parallel to each other as they have different directions. The vectors seem to reflect a circular movement of the fluid. It might seem that these vectors are inaccuracies in the measurements. Conversely, if the measurements are accurate, these vectors might suggest that there are a number of vortices occurring in the ballotini bed as illustrated by the flow streamlines in Figure 4.2.

The direction and magnitude of the velocities measured near to the orifice which are shown by a number of graphs is of particular interest. At a number of locations in the bed the flow velocity was found to be directed downwards and in places towards the orifice. The flow streamlines in Figure 4.2 illustrate these fluid flow velocities well by showing the direction of these flows. This flow is called the circular flow motion which is typical of a fluidising jet such as this. The flow circles from the head of the fluidised zone where the vortex movement is located, and moves down towards the orifice. At the side orifice where the motion of the ballotini beads were visually monitored through the glass, a similar circular motion of the ballotini to the fluid flow was observed. The ballotini movement is shown in Figure 4.11. The motion of the ballotini and fluid flow streamlines is however not the same, but at some locations in the bed such as in the mobile bed zone the two do appear to be quite similar.

The height at which the fluidised zone ended, which is the fluidisation height (FH) was found to be 27 mm above the orifice where the very top of the vortex was at 27 mm. The FH was found by lowering the straight Pitot tube from directly above the orifice to the point when a scramble noise could be heard, this was the point at which the Pitot tube makes contact with the moving ballotini in the fluidised zone. The pressure plots demonstrate that the maximum pressure is located just below the FH, where the maximum pressure occurred in the head of the fluidised zone. Additionally, there is a large difference in the velocities below and above this height.

The pressure distribution plots suggest that from a height of 100 mm above the orifice there is very near to a linear pressure distribution in the ballotini bed. Through this region of linear pressure distribution, the flow will likely follow Darcy laminar flow properties whereas below this region the flow will likely have turbulent properties. This height of 100 mm is considerably close to the orifice, which shows that the ballotini bed together with the internal fluidisation has a large pressure damping effect.

The effect that the internal fluidisation has on the energy is similar to its effect on pressure. The energy plots show that there is a steep decrease in the bed energies when moving away from the orifice. Interestingly the higher energies seem to exist within the fluidised and mobile bed zones whereas outside of these zones, typically in the static bed zone, the energies are considerably lower. This shows that in the case of a leak, internal fluidisation can drastically reduce the energies in a bed.

The experimental setup was found to operate successfully. However, this was only the case if sufficient time and patience was taken by the operator when taking the measurements. Issues did arise which hampered the experimental process considerably. These issues were: blockage of the Pitot tube nose pieces by the ballotini; the build-up of entrapped air in the ballotini bed; blockage of the inlet orifices; and the variance in flow rate of the water supply. However, if care is taken to prevent these problems or ideally if the setup could be modified so as to prevent them, then this method of experimentation would be more successful.

5.2 Main findings and conclusions of the study

- Large vertical velocities existed in the fluidised zone and were contained inside this zone. Outside the fluidised zone the vertical velocities were significantly lower.
- The fluidised zone also contained large pressures where outside of the fluidised zone the pressures were substantially lower.
- From approximately 100 mm above the orifice and higher a linear distribution of pressure was found in the ballotini bed, suggesting that laminar Darcy flow was evident.
- The fluidising height (FH) which was the height the fluidised zone reached, was found to be approximately 27 mm above the orifice.
- Both the fluid flow and the ballotini movement had circular trajectories away from the head of the fluidised zone then circling down towards the orifice.
- The maximum energy was found to exist at the orifice, it then rapidly decreased higher up in the fluidised zone. The energy in the mobile and static bed zones was significantly lower than inside the fluidised zone, illustrating that internal fluidisation incurs a substantial amount of energy head loss.
- The repeatability of the measurements obtained when using this experimental method was found to have an average variance in measurements of 3.8 %.

5.3 Recommendations

This study was an initial study where a large percentage of the research went into the designing and building of the experimental equipment. Then by using the experimental equipment measurements were taken. Also the repeatability of these measurements was analysed. As a result there are a number of recommendations for improving the design of the experimental equipment and suggestions for further experimentation.

5.3.1 Experimental equipment design recommendations

- Needle roller bearings

In total there were eight roller bearings in the experimental setup. The bearings were located on the primary and secondary tubes and aided in the movement of the three aluminium blocks. The bearings were the needle bearing types which are suited for rotational movement around a circular tube. However, in the experimental setup the aluminium blocks were slid along the tubes, and not rotated around the tubes. Therefore, the incorrect bearing type was used. The bearings did not function correctly which hampered the operation of the experimental setup.

It is suggested that cylindrical bushes be used rather than needle bearings. The bushes would increase the slide ability of the aluminium blocks on the tubes, while still maintaining small tolerances to prevent over sliding and play.

- Pitot tube nose pieces

By making the inner diameter of the glass nose piece slightly smaller the ballotini would be prevented from blocking the nose piece. Alternatively the ballotini could be sieved to remove the smaller beads that are less than 0.5 mm in diameter.

- Inlet orifice structures

As illustrated in Figure 3.6, there is a shoulder along the inner diameter of each of the orifice structures. The shoulders are created where two different inner diameters meet. Where the smaller diameter is on the downstream side of the shoulder, there is a reduction of diameter in the flow direction. When the flow through the orifice is stopped the ballotini tend to fall some distance down into the orifice. When the flow is switched on again the ballotini remain in the orifice and prevents internal fluidisation from occurring. It is most likely that the shoulders in the orifice are creating the build-up of the ballotini and preventing them from exiting the orifice.

It is recommended that these shoulders be completely removed from the orifice structures. If the drill bit length is not sufficient, the overall length of the orifice structure could be reduced. This would prevent the ballotini build-up in the orifice.

- Flow meter and control valve

The inlet flow was controlled by the ball valves positioned upstream of the orifices. These ball valves however where very sensitive which made it very hard to make small flow adjustments by hand. The process to obtain the required flow rates became time consuming. It is recommended that an electronic flow control valve with a flow meter be used to make these small flow adjustments.

5.3.2 Further experimentation

- Testing a range of flow rates

In these experiments only one flow rate of 2 l/min was tested at the centre orifice. It would be beneficial though to test other flow rates as well−say between the range of 1 and 6 l/min. The measurements at the various flow rates could then be compared. This would greatly increase the understanding of the soil - leak interaction which occurs in internal fluidisation.

- Testing with the inclusion of entrapped air in the ballotini bed

As with many experimental studies, the first stage of experiments requires the variables which may affect the results to be limited. One of the variables in this experiment was the entrapped air in the ballotini bed. Further experimentation can be done where this entrapped air is present. In a realistic situation in the field there will be air trapped within the soil medium. Therefore to continue the experiments by obtaining results with entrapped air would be beneficial.

- Testing half of a fluidised jet at the wall orifice

In the experimental setup the wall orifice was in fact described as being away from the wall and not right against it. It would be interesting to theoretically experiment with half a jet. Then the orifice cross section would be a half circle. This will replicate half the jet which was present at the centre orifice. In order to create this theoretical half jet, a thin piece of glass or Perspex sheeting could be placed against the inside wall of the glass tank where the thickness of the sheeting should be equivalent to the distance from the inside face of the glass wall to the centre of the orifice. This will block off half of the orifice and therefore create a theoretical half jet. The flow rate supplied through the half orifice will be of particular interest. Whether the flow rate should be exactly halved as with the orifice, or whether some other fraction of the full flow should be used, would be issues to consider. The effect that the glass or Perspex sheeting has on the internal fluidisation would also need to be considered.

- Flow rate at start of internal fluidisation

The flow rate required to initiate internal fluidisation is an important aspect on which to conduct experiments. This aspect was not tested in this study due to the design of the inlet orifice which consisted of the shoulder, as previously discussed. The shoulder meant that the ballotini beads which fell down into the orifice would get lodged there when the flow was switched on. The blocked orifice prevented internal fluidisation from occurring.

Therefore if the flow rate required for internal fluidisation is to be investigated, then it would be advisable to redesign and manufacture the orifice structure first. An orifice that can"t be blocked by the ballotini beads will perform far better when investigating the flow rate required for internal fluidisation.

References

Abdullah, M., Faruque, A., & Balachandar, R. (2011). Seepage Effects on Turbulence Characteristics in an Open Channel Flow. *Canadian Journal of Civil Engineers,* Vol. 38, pp. 785-799.

Ahmed, N., & Sunada, D.K. (1969). Nonlinear Flow in Porous Media. *Journal of Hydraulics Division, ASCE,* Vol. 95, No. 6, pp. 1847-1857.

Al-Deen, M.F.N., Samways, A.L., & Bruun, H.H. (1996). Water Flow Studies using Split-Film Anemometry. *Measuring Science and Technology,* Vol. 7, pp. 1529-1535.

Alsaydalani, M.O.A. (2010). Internal Fluidisation of Granular Material. *PhD Thesis*, University of Southampton, School of Civil Engineering and the Environment.

Aysen, A. (2002). *Soil Mechanics: Basic concepts and engineering applications.* Tokyo: A.A. Balkema Publishers.

Bagnold, R.A. (1956). The Flow of Cohesionless Grains in Fluids. *Philosophical Transactions of the Royal Society of London. Series A, Mathematical and Physical Sciences*, Vol. 249, No. 964, pp. 235-297.

Bagnold, R.A., *et al.* (1974). Fluid Forces on a Body in Shear-Flow; Experimental Use of 'Stationary Flow'. *Proceedings of the Royal Society of London. Series A, Mathematical and Physical Sciences*, Vol. 340, No. 1621, pp. 147-171.

Barker, M. (1920). On the Use of Very Small Pitot-Tubes for Measuring Wind Velocity. *Royal Society of London*, Vol. 97, pp. 435-445.

Bear, J. (1972). *Dynamics of fluids in Porous Media*. New York: Dover Publications.

Boetcher, S., & Sparrow, E. (2007). Limitations of the Standard Bernoulli Equation Method for Evaluating Pitot/Impact Tube Data. *International Journal of Heat and Mass Transfer, ASCE*, Vol. 50, pp. 782-788.

Brown, G.O. (2003). Henry Darcy‟s Perfection of the Pitot Tube. *Henry P. G. Darcy and Other Pioneers in Hydraulics: Contributions in Celebration of the 200th Birthday of Henry Philibert Gaspard Darcy, ASCE*, Reston, VA. pp. 14-23.

Burnell, D., & Race, J. (2000). Water Distribution Systems Analysis: Patterns in Supply Pipe Leakage. *Proceedings from 2000 ASCE EWRI Conference*, Minneapolis.

Chadwick, A., Morfett, J., & Borthwick, M. (2004). *Hydraulics in Civil and Environmental Engineering*. 4th ed. London: Spon Press – Taylor & Francis.

Chue, S.H. (1975). Pressure Probes of Fluid Measurement. *Progress in Aerospace Science,* Vol. 16, pp. 147-223.

Coetzer, A.J., van Zyl, J.E., & Clayton, C.R.I. (2006). An Experimental Investigation into the Turbulent-Flow Hydraulics of Small Circular Holes in Plastic Pipes. *Water Distribution Systems Analysis Symposium 2006, ASCE*, Vol. 247, No. 171.

Craig, R.F. (2004). *Craig's Soil Mechanics*. 7th ed. London: Spon Press – Taylor & Francis.

Cui, X., Li, J., Chan, A., & Chapman, D. (2014). Coupled DEM-LBM Simulation of Internal Fluidisation Induced by a Leaking Pipe. *Powder Technology*. Vol. 254, pp. 299-306.

Dallavalle, J. (1948). *Micrometrics: The Technology of Fine Particles*. 2nd ed. London: Pitman.

Daugherty, R.L. & Franzini, J.B. (1965). *Fluid Mechanics*. 6th ed. New York: McGraw-Hill, pp. 338-349.

Dey, S. (1999). Sediment Threshold. *Applied Mathematics Modelling,* Vol. 23, pp. 399-417.

Ergun, S. (1952). Fluid Flow through Packed Columns. *Chemical Engineering Progress*, Vol. 48, No. 2, pp. 89-94.

Etemad, S.G., Thibault, J., & Hashemabadi, S.H. (2003). Calculation of the Pitot Tube Correction Factor for Newtonian and Non-Newtonian Fluids. *The Instrumentation, Systems, and Automation Society*, Vol. 42, pp. 505-512.

Farley, M., & Trow, S. (2003). *Losses in Water Distribution Networks*. London: IWA Publishing.

Fingerson, L.M., *et al*. (1993). Data Analysis in Laser Doppler Velocimetry and Particle Image Velocimetry. *Tsi Short Course Text*, St. Paul.

Forchheimer, P. (1901). Wasserbewegung Durch Boden. *Z Ver Deutsch Ing*, Vol. 45, pp. 1782-1788.

Francis, J.R.D. (1973). Experiments on the Motion of Solitary Grains along the Bed of a Water-Stream. *Proceedings of the Royal Society of London. Series A, Mathematical and Physical Sciences*, Vol. 332, No. 1591, pp. 443-471.

Freyberg, T. (2012). Water Leakage? Look to the Clouds. *Water World International, WWi.* Vol. 22, No. 2, pp. 36-38.

George, W. (1985) Liquefaction of Soils during Earthquakes. *Committee on Earthquake Engineering*. Washington, D.C.: National Academy Press.

Goldstein, R.J. (1983). *Fluid Mechanics Measurements*. United States of America: Hemisphere Publishing Corporation.

Greyvenstein, B., & van Zyl, J.E. (2007). An Experimental Investigation into the Pressure-Leakage Relation of some Failed Water Pipes. *Journal of Water Supply: Research and Technology, AQUA*, Vol. 56, No. 2, pp. 117-124.

Hall, I.M. (1956). The Displacement Effect of a Sphere in Two-Dimensional Shear Flow. *Journal of Fluid Mechanics,* Vol. 1, pp. 142-162.

Harr, M.E. (1962). *Groundwater and Seepage*. New York: McGraw Hill.

Hlushkou, D., & Tallarek, U. (2006). Transition from Creeping via Viscous-Inertial to Turbulent Flow in Fixed Beds. *Journal of Chromatography A,* Vol. 1126, pp. 70-85.

Idelchik, I.E. (1994). *Handbook of Hydraulic Resistance*. 3rd ed., New York: Begell House.

Itron. (2014) *Aquadis+ Composite Brochure*. Accessed on 27 January 2015. https://www.itron.com/PublishedContent/AquadisPlus%20Composite%20EN%2006-14.pdf

Kinney, R., & Sparrow, E. (1970). Turbulent Flow, Heat Transfer, and Mass Transfer in a Tube with Surface Suction. *Journal of Heat Transfer, ASME,* Vol. 92, pp. 117 – 125.

Klopfenstein, R. (1998). Air Velocity and Flow Measurement using a Pitot Tube. *King Industries Incorporated,* USA.

Lambert, A. (2001). What Do We Know About Pressure-leakage Relationships in Distribution Systems? *Proc. 2001 IWA Conf.: System Approach to Leakage Control and Water Distribution Systems Management.* Brno, Czech Republic.

Lawrence, A.D. (2008). The Interaction between a Water Pipe-Leak and an Idealized Surrounding Soil. *University of Johannesburg*. BSc in Civil and Urban Engineering Thesis.

Ledwith, C., Weisman, R.N., & Lennon, G.P. (1990). Selection of Hole Size for Fluidization Pipes. *Hydraulic Engineering*, pp. 933-938.

Lighthill, M.J. (1957). Contribution to the Theory of Pitot-Tube Displacement Effect. *Journal of Fluid Mechanics,* Vol. 1, pp. 493-512.

Lima Neto, I.E., Zhu, D.Z., & Rajaratnam, N. (2008). Effect of Tank Size and Geometry on the Flow Induced by Circular Bubble Plumes and Water Jets. *Journal of Hydraulic Engineering, ASCE*, Vol. 134, No. 6, pp. 833-842.

Liu, H., & Graze, H. (1983). Lift and Drag on Stationary Capsule in Pipeline. *Journal of Hydraulic Engineering, ASCE,* Vol. 109(1), pp. 28-47.

Ma, C.H. (2011). Internal Fluidisation due to Horizontal Seepage - A Laboratory Study. *University of Southampton.* MSc Thesis.

Maclean, A., & Willetts, B. (1986). Measurement of Boundary Shear Stress in Non-uniform Open Channel Flow. *Journal of Hydraulic Research,* Vol. 24, No. 1, pp. 39-51.

Maclean, A. (1991). Bed Shear Stress and Scour over Bed-type River Intake. *Journal of Hydraulic Engineering, ASCE,* Vol. 117, No. 4, pp. 436-451.

MacMillan, F.A. (1954). Viscous Effects on Pitot Tubes at Low Speeds. *Journal of Royal Aeronautical Society,* Vol. 58, pp. 837-839.

Marine Aquariums South Africa. (2014). Glass Thickness Calculator. Accessed on 6 February 2014. www.marineaquariumsa.com/general/glasscalculator.xls

McKeon, B., *et al*. (2003). Pitot Probe Corrections in Fully Developed Turbulent Pipe Flow. *Measurement Sience and Technology*, Vol. 14, pp. 1449-1458.

Miyazaki, T. (2006). *Water Flow in Soils*. 2nd ed. Florida: Taylor & Francis.

Muskat, M., & Wyckoff, R.D. (1937). *The Flow of Homogeneous Fluids through Porous Media*. 1st ed. New York: McGraw-Hill.

Nino, Y., & Garcia, M. (1998). Using Lagrangian Particle Saltation Observations for Bedload Sediment Transport Modelling. *Hydrological Processes*, Vol. 12, pp. 1197-1218.

Noack, C., & Ulanicki, B. (2006). Modelling of Soil Diffusibility on Leakage Characterstics of Buried Pipes. *8th Annual Water Distribution Systems Analysis Symposium*. Cincinnati, Ohio, USA.

Oldenziel, D., & Brink, W. (1974). Influence of Suction and Blowing on Entrainment of Sand Particles. *Journal of Hydraulic Division, ASCE*, Vol. 100, No. 7, pp. 935-949.

Ower, E. & Pankhurst, R.C. (1977). *The Measurement of Air Flow*. 5thed. Oxford: Pergamon Press.

Patel, V.C. (1965). Calibration of the Preston Tube and Limitations on its use in Pressure Gradients. *Journal of Fluid Mechanics,* Vol. 23, pp. 185-208.

Powrie, W. (2004). *Soil Mechanics Concepts & Applications*. London and New York: Spon Press.

Prinos, P. (1995). Bed-Suction Effects on Structure of Turbulent Open-Channel Flow. *Journal of Hydraulic Engineering, ASCE,* May, pp. 404-412.

Prohaska, P., Khan, A., & Kaye, N. (2010). Investigation of Flow through Orifices in Riser Pipes. *Journal of Irrigation and Drainage Engineering, ASCE,* Vol. 136, No. 5, pp. 340 – 347.

Rao, A.R., Subrahmanyam, V., Thayumanavan, S., & Damodaran, N. (1994). Seepage Effects on Sand-Bed Channels. *Journal of Irrigation and Drainage Engineering*, *ASCE,* Vol. 120, No. 1, pp. 60–79.

Robertson, G., & Robertson, I. (2013). The Motion of an Arbitrarily Rotating Spherical Projectile and its Application to Ball Games. *Physica Scripta*, Vol. 88, No. 1.

Salter, M.A., Warship, J.H., & Goodman, D.G. (1965). A Discussion of Pitot-Static Tubes and of their Calibration Factors with a Description of Various Versions of a New Design. *Ministry of Aviation, Aeronautical Research Council Reports and Memoranda*. London: Her Majesty's Stationery Office.

Schlichting, H., & Gersten, K. (1999). *Boundary Layer Theory*. 8th ed. New York: Springer.

Stewart, R.L., Fox, J.F., & Harnett, C.K. (2013). Time-Average Velocity and Turbulence Measurement using Wireless Bend Sensors in an Open Channel with a Rough Bed. *Journal of Hydraulic Engineering*, Vol. 139, pp. 696-706.

Terekhov, V.I., *et al*. (2009). Impingement of an Impact Jet onto a Spherical Cavity – Flow Structure and Heat Transfer. *International Journal of Heat and Mass Transfer, ASCE,* Vol. 52, pp. 2498–2506.

Terzaghi, K. (1939). Soil Mechanics: A New Chapter in Engineering Science. *Institution of Civil Engineers*, Vol. 12(1039), pp. 106-141.

Uchiyama, H., & Ide, M. (2009). Development of Hot-Film Anemometer Calibrator for Water Flow Measurement. *Flow Measurement and Instrumentation,* Vol. 20, pp. 75-80.

van Zyl, J.E., & Clayton, C.R.I. (2007). The Effect of Pressure on Leakage in Water Distribution Systems. *Proceedings of the Institution of Civil Engineers, Water Management*, Vol. 160, No. WM2, pp. 109-114.

van Zyl, J.E., *et al*. (2013). Soil Fluidisation Outside Leaks in Water Distribution Pipes – Preliminary Observations. *Proceedings of the Institute of Civil Engineers. Water Management.* Vol. 166, No. 10, pp. 546-555.

Venkataraman, P. & Rama Mohan Rao, P. (1998). Darcian, Transitional, and Turbulent Flow through Porous Media. *Journal of Hydraulic Engineering, ASCE*, Vol. 124, No. 8, pp. 840-846.

Walski, T., *et al*. (2006). Modeling Leakage Reduction through Pressure Control. *Journal of the American Water Works Association,* Vol. 98, No. 4, pp. 147-152.

Ward, J.C. (1964). Turbulent Flow in Porous Media. *Journal of Hydraulics Division, ASCE,* Vol. 90, No. 5, p. 1.

Watters, G. & Rao, V. (1971). Hydrodynamic Effects of Seepage on Bed Particles. *Journal of Hydraulics Division, ASCE,* Vol. 97, No. 3, pp. 421-439.

White, F. (1991). *Viscous Fluid Flows*. 2nd ed. New York :McGraw-Hall.

Yamanoi, K. (2011). Practical Handbook of Tower Flux Observation. *Department of Meteorological Environment.* Ibaraki, Japan.

Zagarola, M.V. (1996). Mean Flow Scaling in Turbulent Pipe Flow. *PhD Thesis*, Princeton University.

Zoueshtiagh, F. & Merlen, A. (2007). Effect of Vertically Flowing Water Jet underneath a Granular Bed. *The American Physical Society*, Vol. 75, No. 5.

Appendix A

Experimental design drawings

Appendix A Layout:

1. Plan view of experimental equipment
2. Front view of experimental equipment
3. Side view of experimental equipment
4. Detail A
5. Detail B
6. Detail C
7. Pitot tubes detail
8. Sight tube stand detail

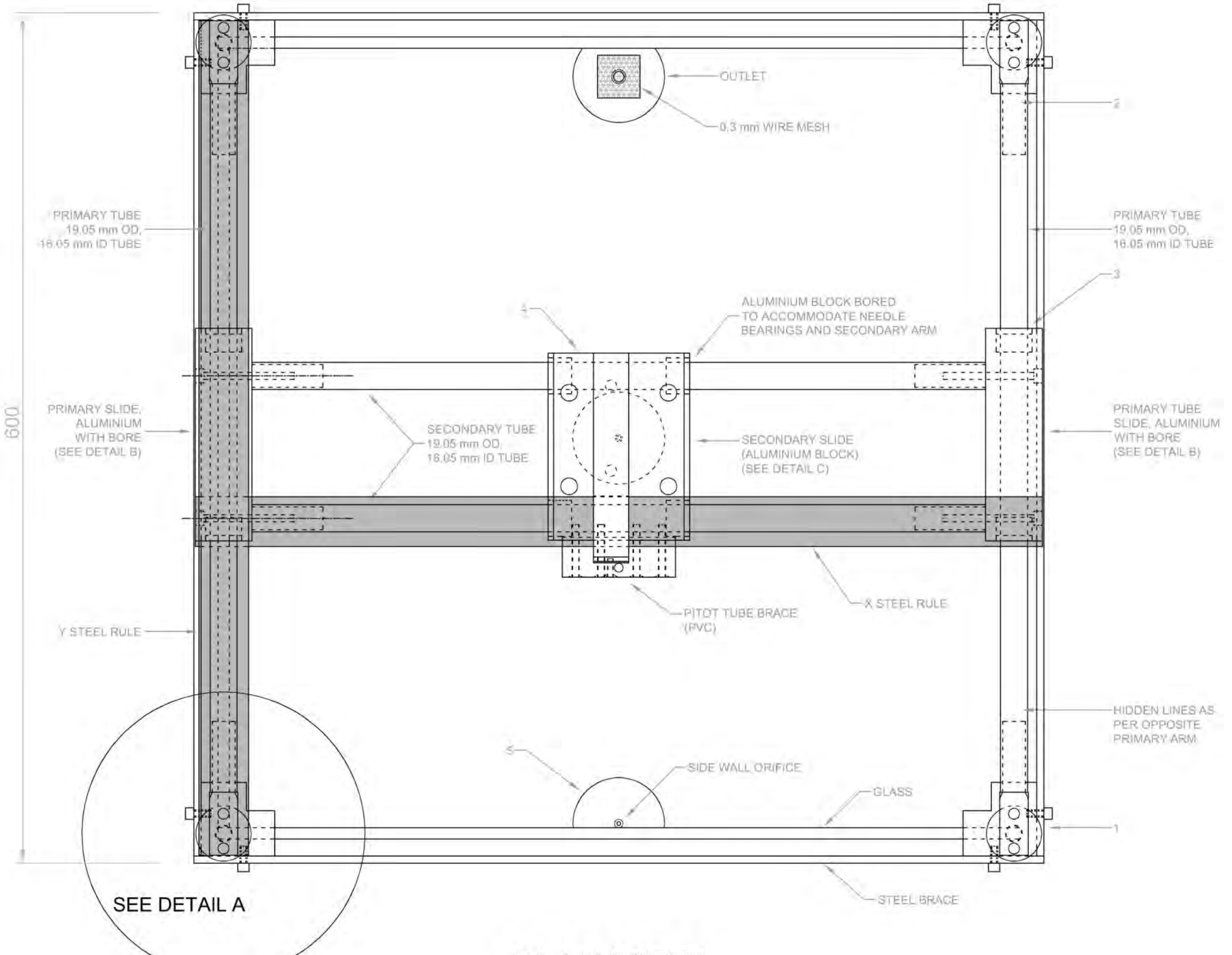

PLAN VIEW

SCALE: 1:4

NOTES:

1	52 mm aliminium cube fitted onto four top corners of the glass tank. Cube filleted as per Section A drawing. 8 mm wide by 25 mm deep slits cut into cube to fit glass corners. 12 mm Ø x 50 mm long threaded pin positioned vertically into cube. Remaining assembly shown in Section A drawing.
2	Both ends of the two Primary tubes fitted with 50 mm long round bar.Round bar forms part of the Primary tube support, as shown in Section AA.
3	Primary tube slide made of 40 x 46 x 150 mm aluminium bar. Each bar bored to accommodate two 25.4 mm OD needle bearings with 4 mm seal. Bearing to house Primary tube.
4	132.2 x 100 x 46 mm thick aluminium block. Block bored at opposite ends of the block's long side, 100.45 mm apart from centers. Each bore accommodates two needle bearings with seals of 25.4 mm OD. A Pitot tube brace is attached to the aluminium block at the center of the block's short side. The brace is a PVC block, consisting of a set screw to fasten Pitot tube. The aluminium block also serves as support for the Z steel rule.
5	Two orifices which create the vertical water jets are located in the base of the glass tank. The orifice locations are, one in the very center of the base of the tank, and the other up against the tank's front side wall. The center orifice's diameter is 3 mm, and the orifice against the wall is 2.8 mm.

SCALE: 1:4

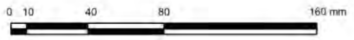

LIST OF DRAWINGS
PLAN VIEW OF EXPERIMENTAL EQUIPMENT
FRONT VIEW OF EXPERIMENTAL EQUIPMENT
SIDE VIEW OF EXPERIMENTAL EQUIPMENT
DETAIL A
DETAIL B
DETAIL C
PITOT TUBES
SIGHT TUBE STAND

UNIVERSITY OF CAPE TOWN
DEPARTMENT OF CIVIL ENGINEERING

UNIVERSITY OF CAPE TOWN
IYUNIVESITHI YASEKAPA • UNIVERSITEIT VAN KAAPSTAD

SUPERVISOR: PROF. J.E. VAN ZYL
DESIGN: N.D. BAILEY
DRAWN: N.D. BAILEY

MASTERS RESEARCH PROJECT

PLAN VIEW OF EXPERIMENTAL EQUIPMENT

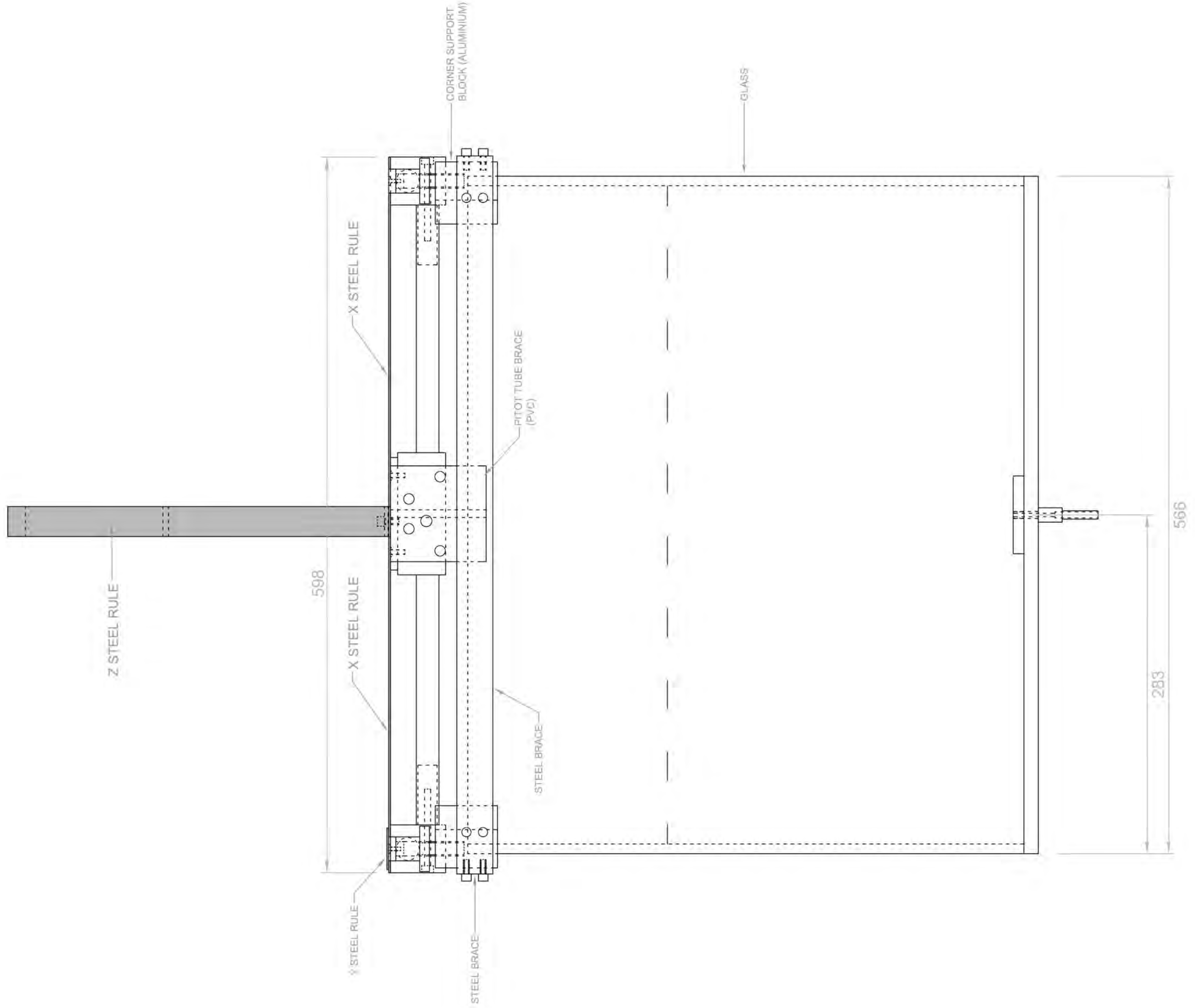

FRONT VIEW

SCALE: 1:4

SCALE: 1:4

0 10 40 80 160 mm

LIST OF DRAWINGS
- PLAN VIEW OF EXPERIMENTAL EQUIPMENT
- FRONT VIEW OF EXPERIMENTAL EQUIPMENT
- SIDE VIEW OF EXPERIMENTAL EQUIPMENT
- DETAIL A
- DETAIL B
- DETAIL C
- PITOT TUBES
- SIGHT TUBE STAND

UNIVERSITY OF CAPE TOWN
DEPARTMENT OF CIVIL ENGINEERING

UNIVERSITY OF CAPE TOWN
IYUNIVESITHI YASEKAPA • UNIVERSITEIT VAN KAAPSTAD

SUPERVISOR: PROF. J.E. VAN ZYL

DESIGN: N.D. BAILEY

DRAWN: N.D. BAILEY

MASTERS RESEARCH PROJECT

FRONT VIEW OF EXPERIMENTAL EQUIPMENT

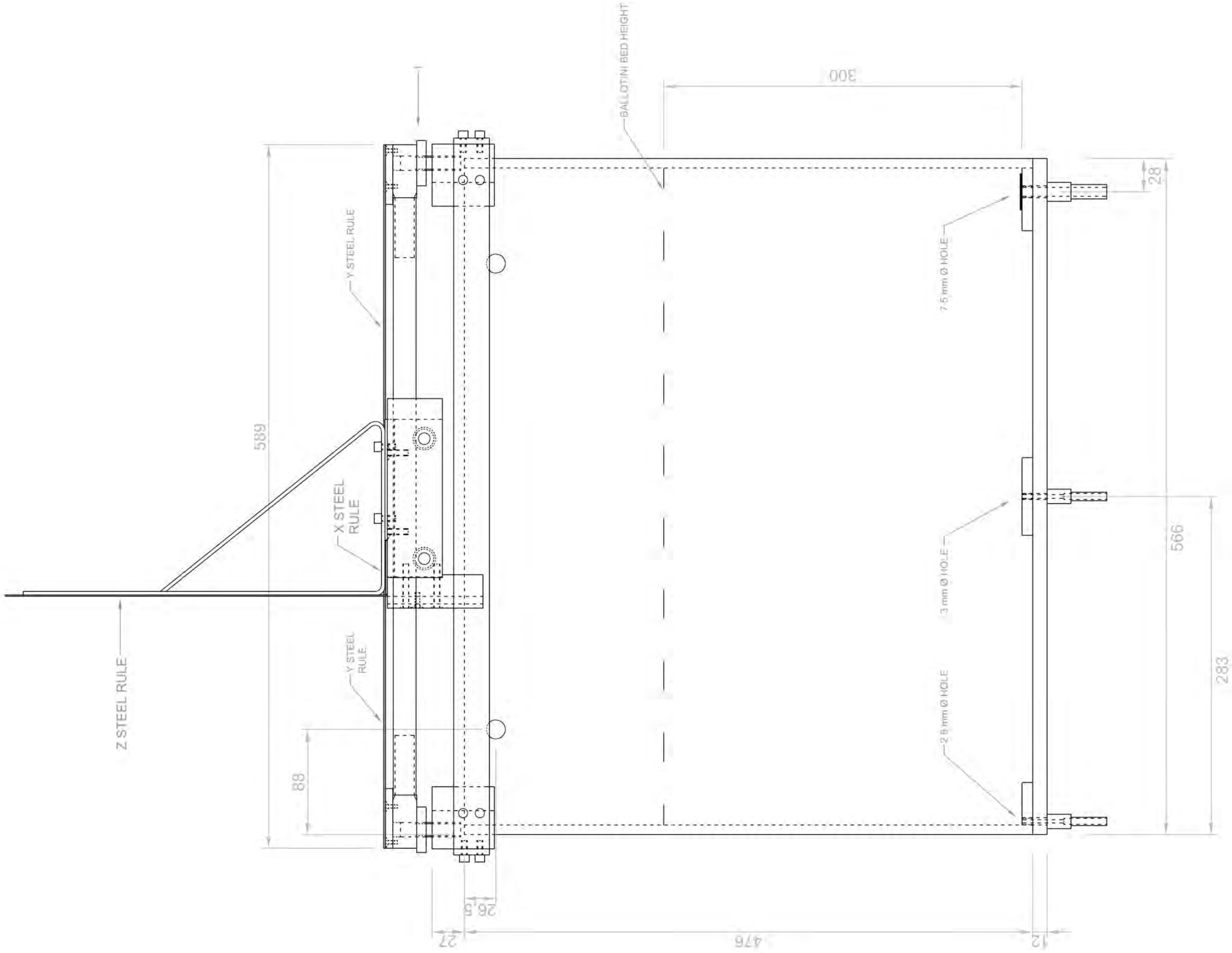

RIGHT SIDE VIEW

SCALE: 1:4

NOTES:

1. 52 mm aliminium cube fitted onto four top corners of the glass tank. Cube filleted as per Section A drawing. 8 mm wide by 25 mm deep slits cut into cube to fit glass corners. 12 mm Ø x 50 mm long threaded pin positioned vertically into cube. Remaining assembly shown in Section A drawing.

SCALE: 1:4

0 10 40 80 160 mm

LIST OF DRAWINGS
PLAN VIEW OF EXPERIMENTAL EQUIPMENT
FRONT VIEW OF EXPERIMENTAL EQUIPMENT
SIDE VIEW OF EXPERIMENTAL EQUIPMENT
DETAIL A
DETAIL B
DETAIL C
PITOT TUBES
SIGHT TUBE STAND

UNIVERSITY OF CAPE TOWN
DEPARTMENT OF CIVIL ENGINEERING

UNIVERSITY OF CAPE TOWN
IYUNIVESITHI YASEKAPA • UNIVERSITEIT VAN KAAPSTAD

SUPERVISOR: PROF. J.E. VAN ZYL
DESIGN: N.D. BAILEY
DRAWN: N.D. BAILEY

MASTERS RESEARCH PROJECT

SIDE VIEW OF EXPERIMENTAL EQUIPMENT

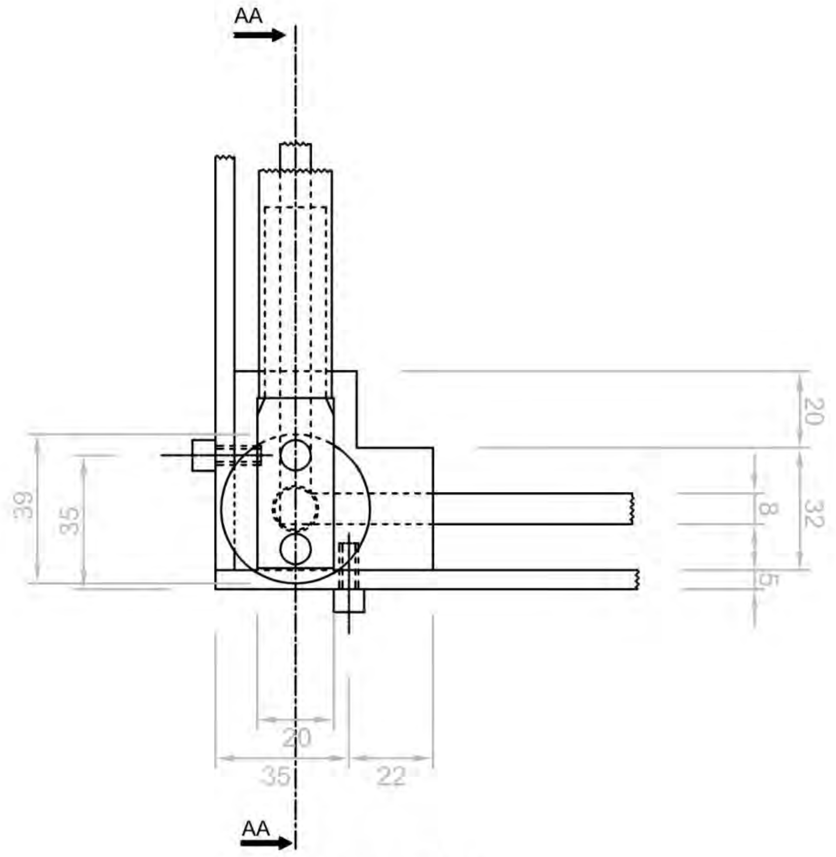

PLAN VIEW

SCALE: 1:2

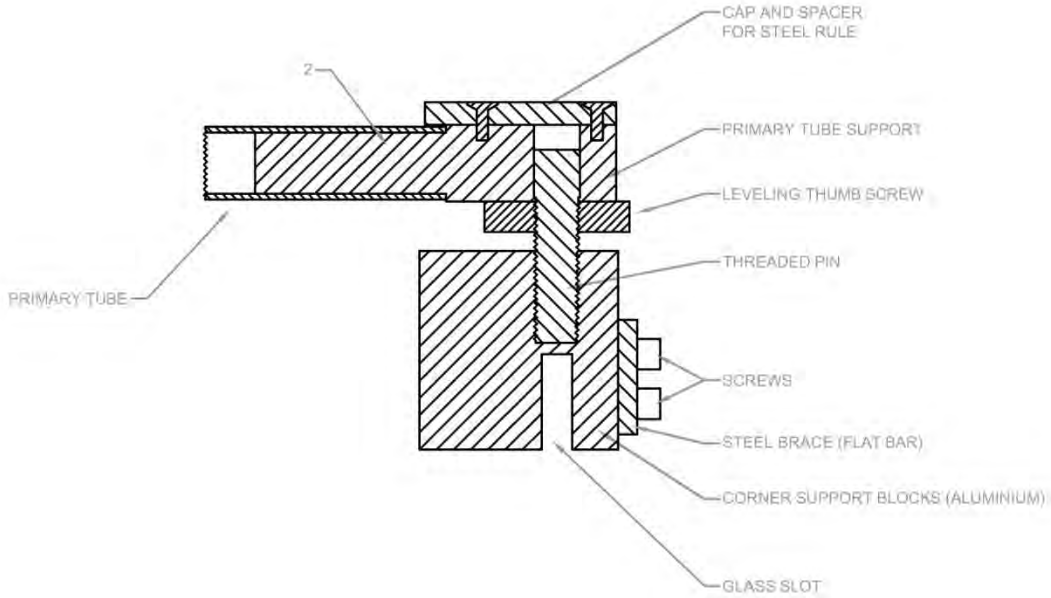

SECTION AA

SCALE: 1:2

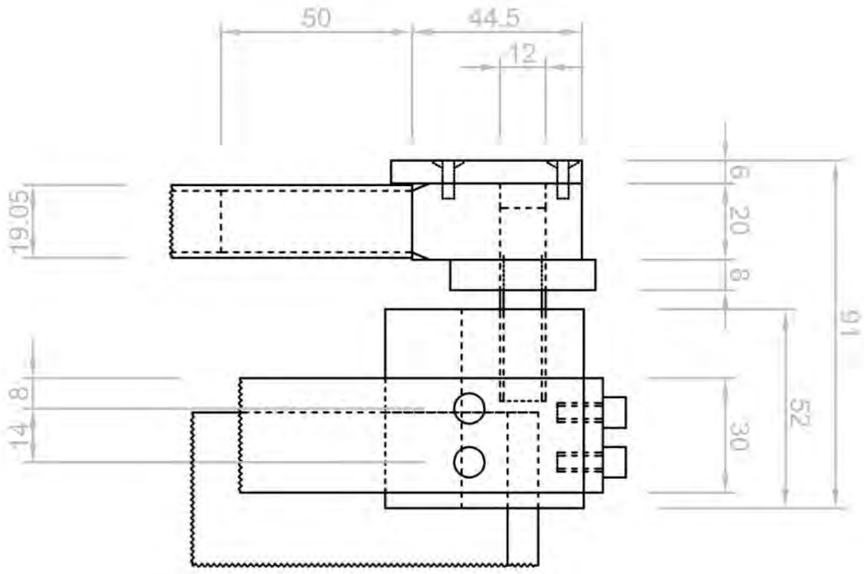

SIDE VIEW

SCALE: 1:2

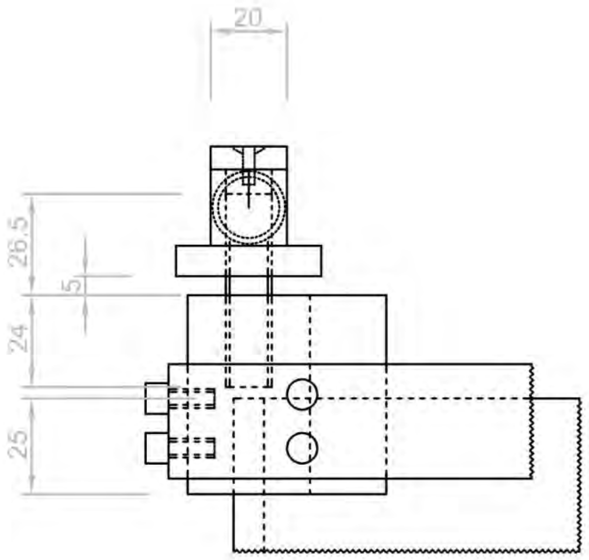

FRONT VIEW

SCALE: 1:2

NOTES:

2. Both ends of the two Primary tubes fitted with 50 mm long round bar. Round bar forms part of the Primary tube support, as shown in Section AA.

SCALE: 1:2

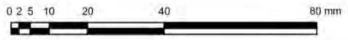

LIST OF DRAWINGS
PLAN VIEW OF EXPERIMENTAL EQUIPMENT
FRONT VIEW OF EXPERIMENTAL EQUIPMENT
SIDE VIEW OF EXPERIMENTAL EQUIPMENT
DETAIL A
DETAIL B
DETAIL C
PITOT TUBES
SIGHT TUBE STAND

UNIVERSITY OF CAPE TOWN
DEPARTMENT OF CIVIL ENGINEERING

UNIVERSITY OF CAPE TOWN
IYUNIVESITHI YASEKAPA • UNIVERSITEIT VAN KAAPSTAD

SUPERVISOR: PROF. J.E. VAN ZYL
DESIGN: N.D. BAILEY
DRAWN: N.D. BAILEY

MASTERS RESEARCH PROJECT

DETAIL A OF EXPERIMENTAL EQUIPMENT

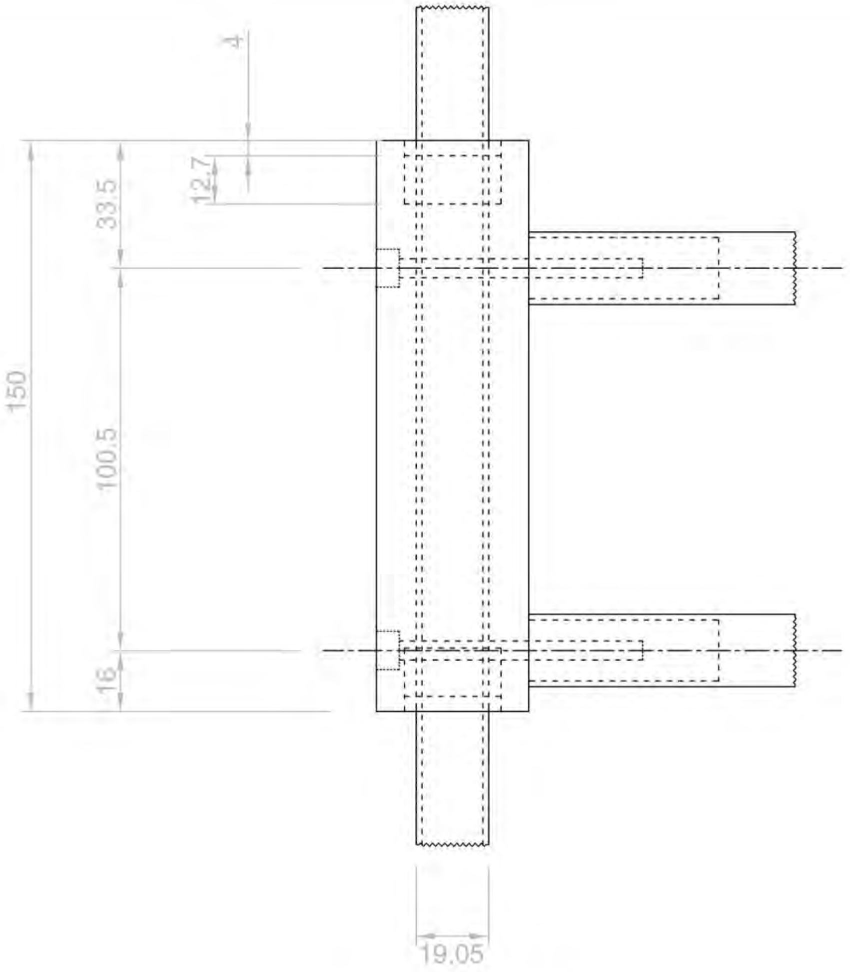

PLAN VIEW

SCALE: 1:2

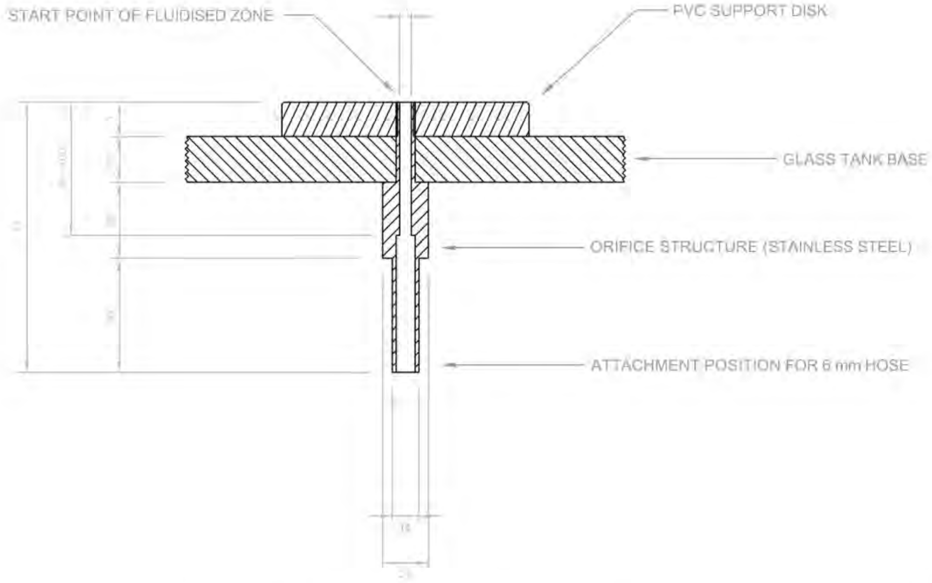

ORIFICE STRUCTURE

SCALE: 1:2

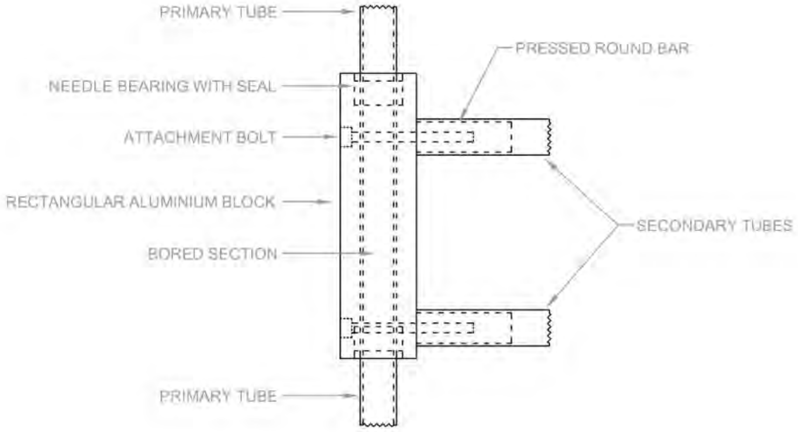

COMPONENT LABELS

SCALE: 1:4

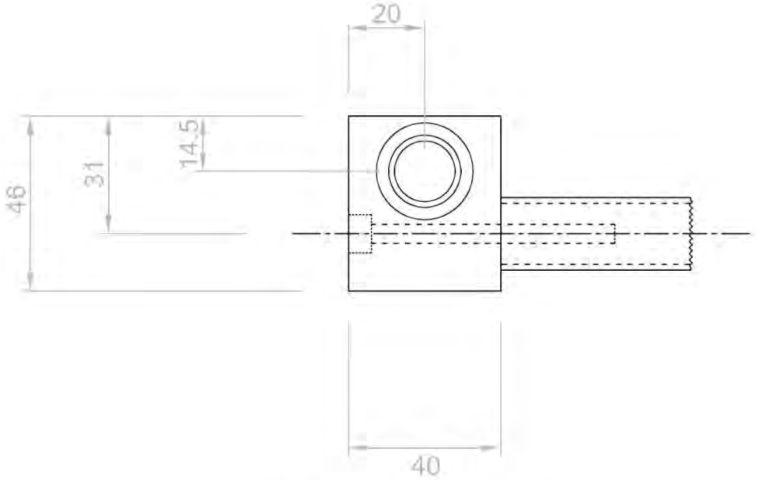

FRONT VIEW

SCALE: 1:2

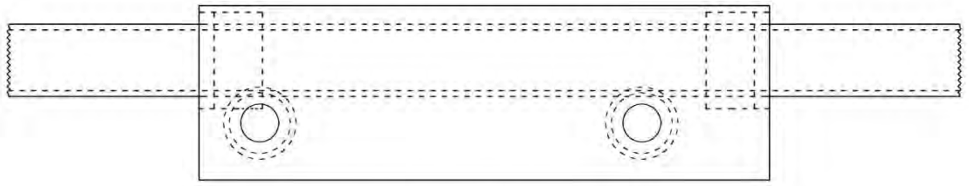

SIDE VIEW

SCALE: 1:2

SCALE: 1:2

SCALE: 1:4

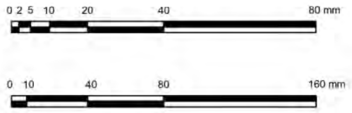

LIST OF DRAWINGS
- PLAN VIEW OF EXPERIMENTAL EQUIPMENT
- FRONT VIEW OF EXPERIMENTAL EQUIPMENT
- SIDE VIEW OF EXPERIMENTAL EQUIPMENT
- DETAIL A
- DETAIL B
- DETAIL C
- PITOT TUBES
- SIGHT TUBE STAND

UNIVERSITY OF CAPE TOWN
DEPARTMENT OF CIVIL ENGINEERING

UNIVERSITY OF CAPE TOWN
IYUNIVESITHI YASEKAPA • UNIVERSITEIT VAN KAAPSTAD

SUPERVISOR: PROF. J.E. VAN ZYL
DESIGN: N.D. BAILEY
DRAWN: N.D. BAILEY

MASTERS RESEARCH PROJECT

DETAIL B AND ORIFICE STRUCTURE OF EXPERIMENTAL EQUIPMENT

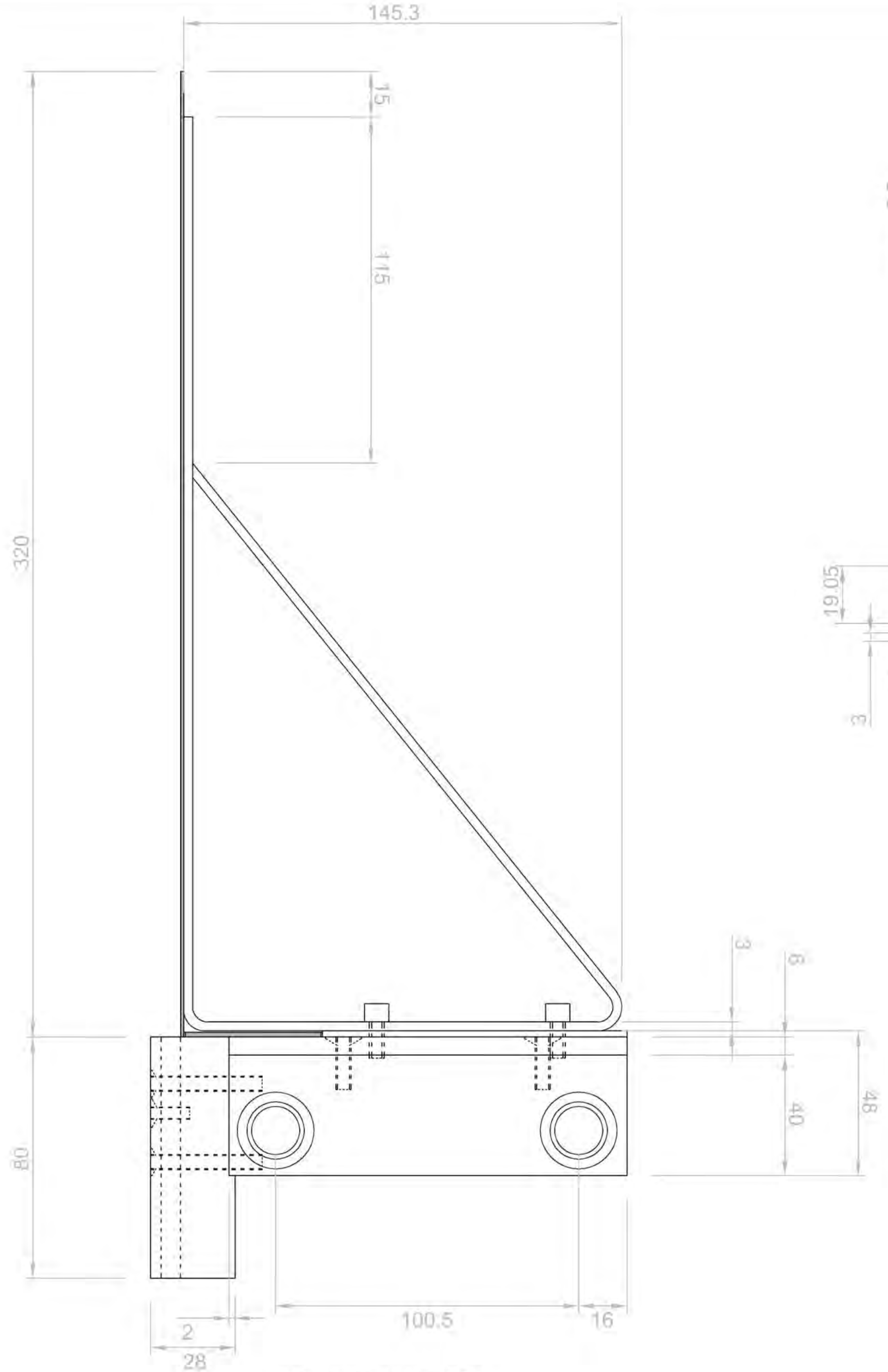

SIDE VIEW

SCALE: 1:2

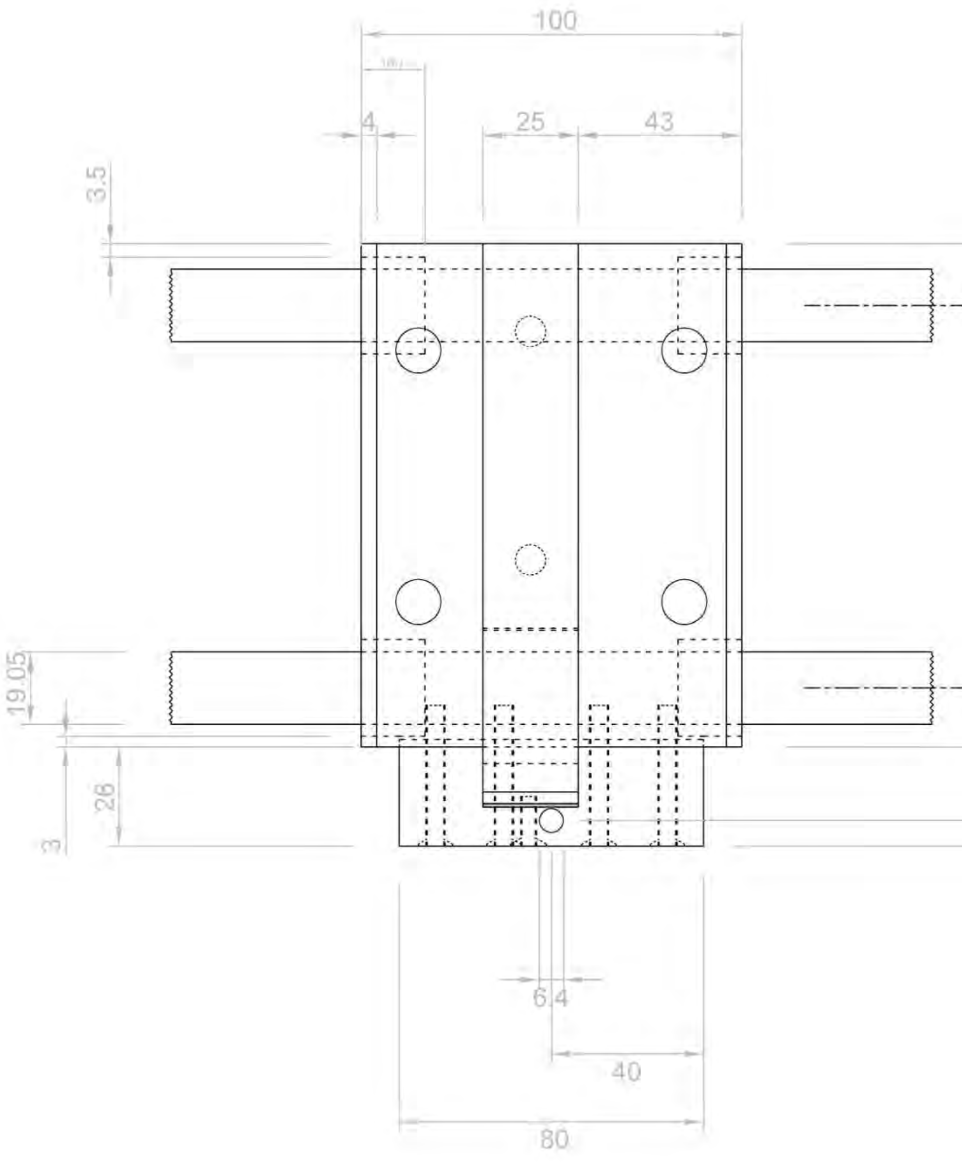

PLAN VIEW

SCALE: 1:2

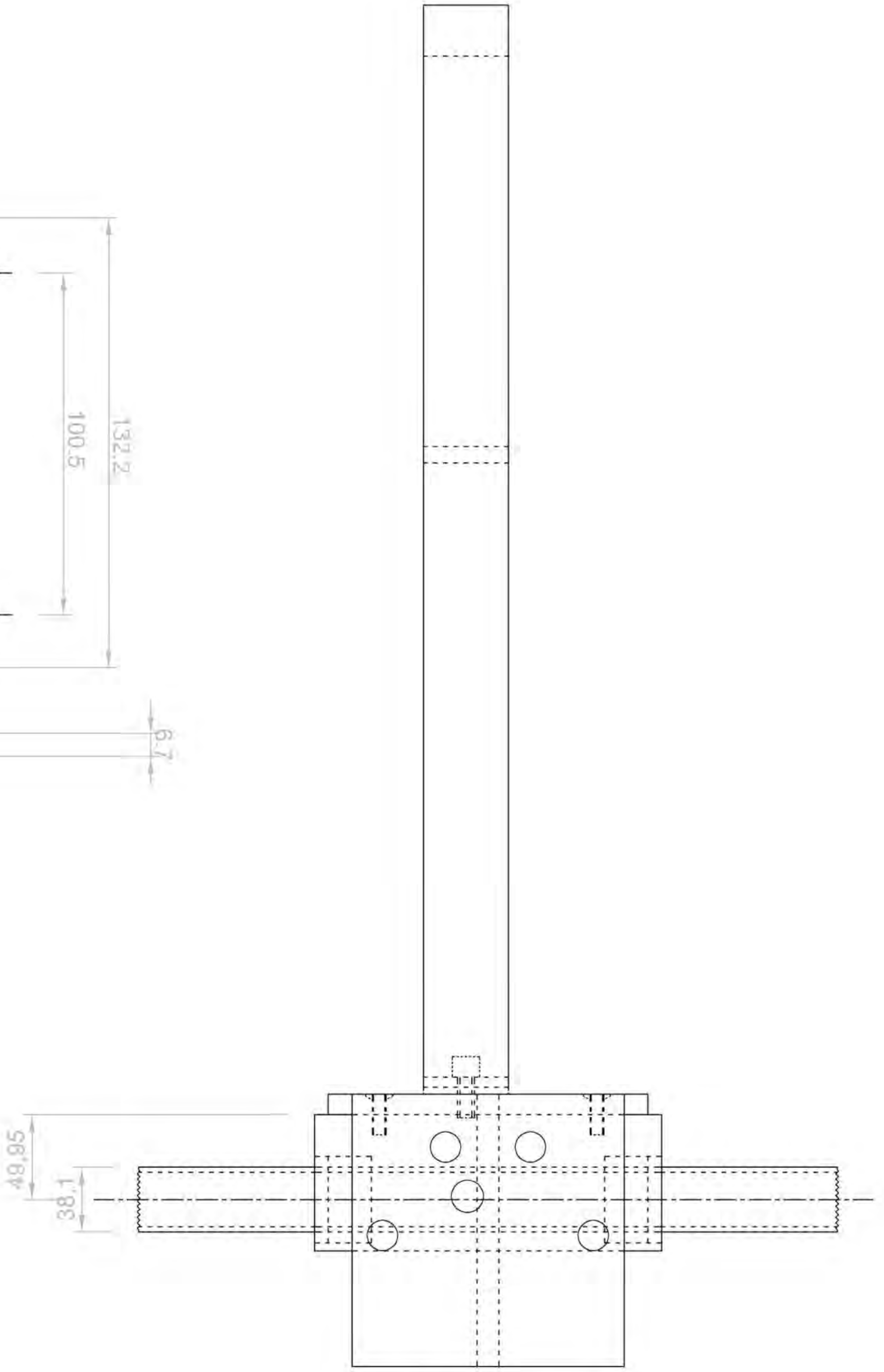

FRONT VIEW

SCALE: 1:2

SCALE: 1:2

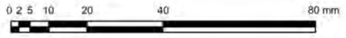

LIST OF DRAWINGS
PLAN VIEW OF EXPERIMENTAL EQUIPMENT
FRONT VIEW OF EXPERIMENTAL EQUIPMENT
SIDE VIEW OF EXPERIMENTAL EQUIPMENT
DETAIL A
DETAIL B
DETAIL C
PITOT TUBES
SIGHT TUBE STAND

UNIVERSITY OF CAPE TOWN
DEPARTMENT OF CIVIL ENGINEERING

UNIVERSITY OF CAPE TOWN
IYUNIVESITHI YASEKAPA • UNIVERSITEIT VAN KAAPSTAD

SUPERVISOR: PROF. J.E. VAN ZYL
DESIGN: N.D. BAILEY
DRAWN: N.D. BAILEY

MASTERS RESEARCH PROJECT

DETAIL C OF EXPERIMENTAL EQUIPMENT

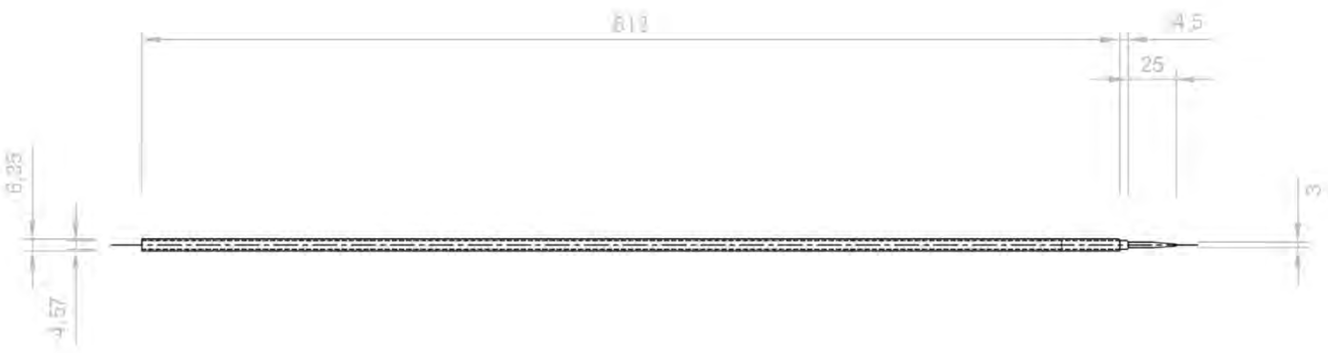

SECTION THROUGH STRAIGHT PITOT TUBE

SCALE: 1:4

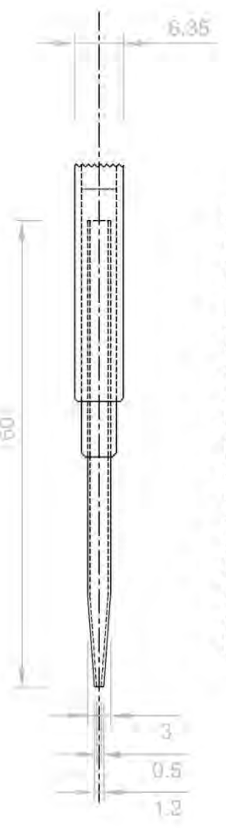

PITOT NOSE DETAIL

SCALE: 1:1

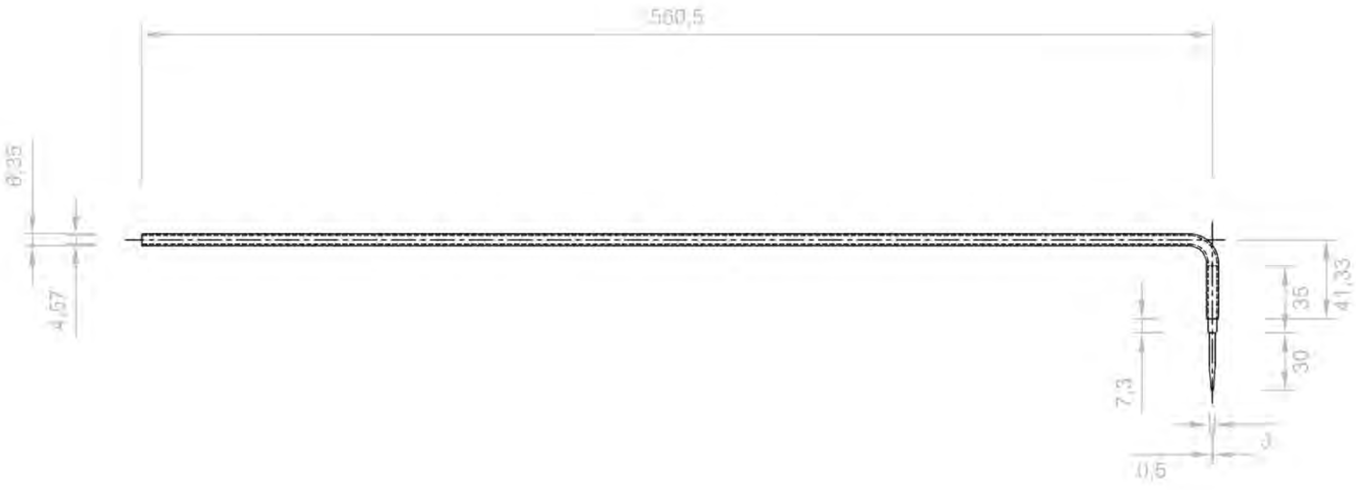

SECTION THROUGH L - TYPE PITOT TUBE

SCALE: 1:4

SCALE: 1:4

SCALE: 1:1

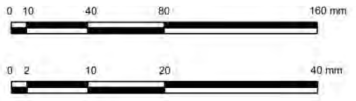

LIST OF DRAWINGS
PLAN VIEW OF EXPERIMENTAL EQUIPMENT
FRONT VIEW OF EXPERIMENTAL EQUIPMENT
SIDE VIEW OF EXPERIMENTAL EQUIPMENT
DETAIL A
DETAIL B
DETAIL C
PITOT TUBES
SIGHT TUBE STAND

UNIVERSITY OF CAPE TOWN
DEPARTMENT OF CIVIL ENGINEERING

UNIVERSITY OF CAPE TOWN
IYUNIVESITHI YASEKAPA · UNIVERSITEIT VAN KAAPSTAD

SUPERVISOR: PROF. J.E. VAN ZYL
DESIGN: N.D. BAILEY
DRAWN: N.D. BAILEY

MASTERS RESEARCH PROJECT

PITOT TUBES DETAIL

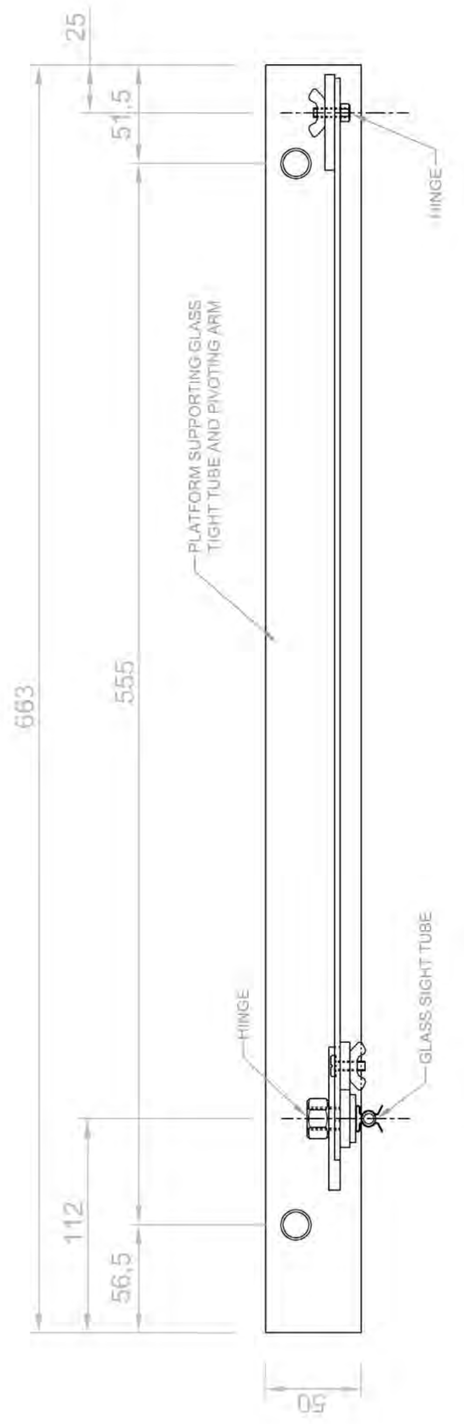

PLAN VIEW

SCALE: 1:4

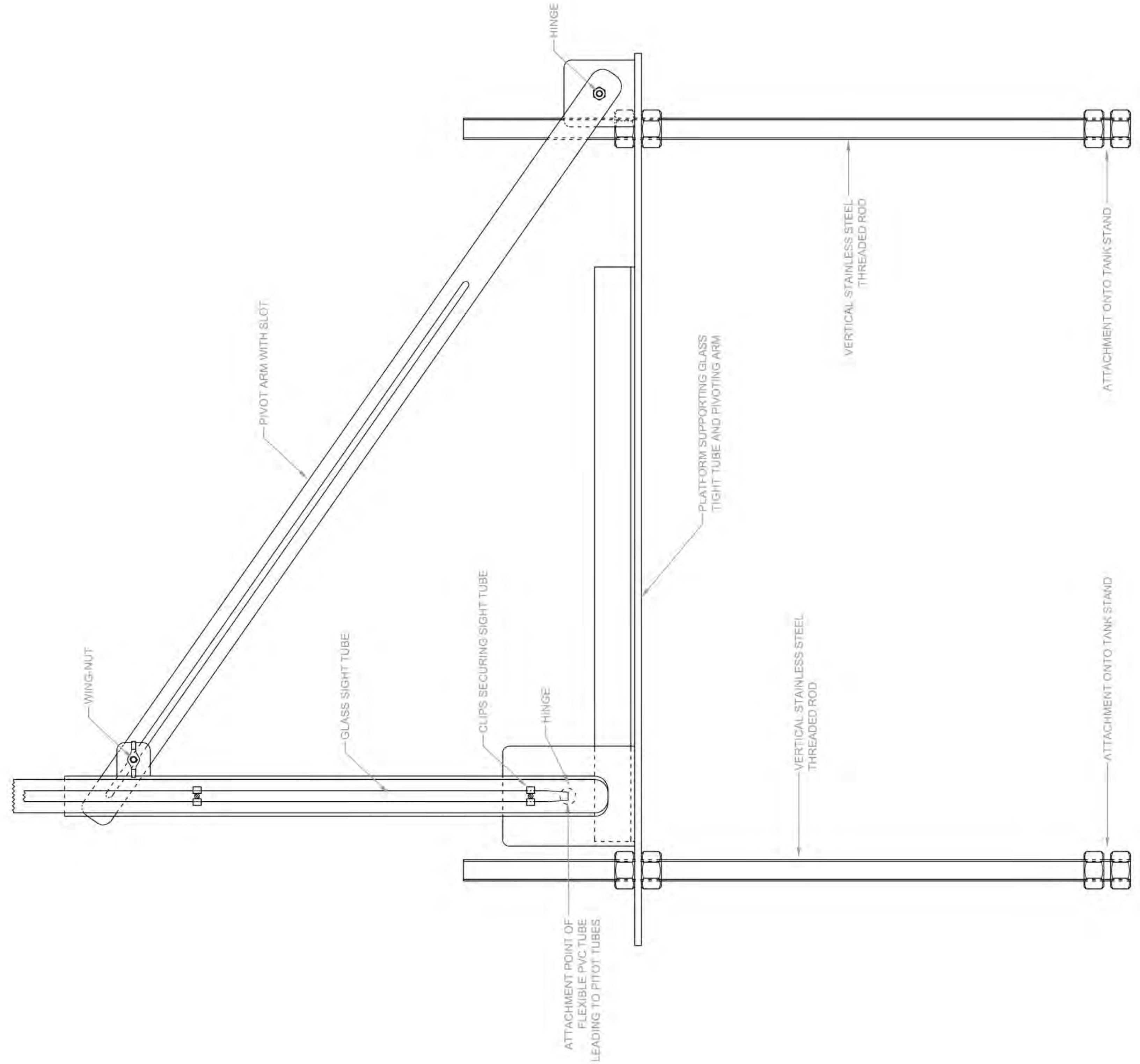

FRONT VIEW

SCALE: 1:4

SCALE: 1:4

0 10 40 80 160 mm

LIST OF DRAWINGS
PLAN VIEW OF EXPERIMENTAL EQUIPMENT
FRONT VIEW OF EXPERIMENTAL EQUIPMENT
SIDE VIEW OF EXPERIMENTAL EQUIPMENT
DETAIL A
DETAIL B
DETAIL C
PITOT TUBES
SIGHT TUBE STAND

UNIVERSITY OF CAPE TOWN
DEPARTMENT OF CIVIL ENGINEERING

UNIVERSITY OF CAPE TOWN
IYUNIVESITHI YASEKAPA • UNIVERSITEIT VAN KAAPSTAD

SUPERVISOR: PROF. J.E. VAN ZYL

DESIGN: N.D. BAILEY

DRAWN: N.D. BAILEY

MASTERS RESEARCH PROJECT

SIGHT TUBE STAND DETAIL

Appendix B

Verification results

Appendix layout:

1. Recorded experimental data
2. Graphs for Test 2
3. Graphs for Test 3

1. Recorded experimental data

Test 1

Weight: 150 g

	Run 1	**Run 2**	**Run 3**	**Run 4**	**Run 5**	**Run 6**	**Run 7**	**Run 8**	**Run 9**	**Run 10**	**Run 11**	**Run 12**	**Run 13**	**Run 14**	**Run 15**	**Run 16**	**Run 17**	**Run 18**	**Run 19**	**Run 20**	**Min**	**Max**	**Average**
Platform velocity																							
Time (sec)	1.78	1.66	1.69	2.03	1.96	2.19	2.1	2	1.84	1.69	1.53	1.53	1.91	1.69	1.62	1.78	1.66	1.68	1.85	1.63	1.530	2.190	1.791
Distance (m)	0.6	0.6	0.6	0.6	0.6	0.6	0.6	0.6	0.6	0.6	0.6	0.6	0.6	0.6	0.6	0.6	0.6	0.6	0.6	0.6			
Velocity (m/s)	0.337	0.361	0.355	0.296	0.306	0.274	0.286	0.300	0.326	0.355	0.392	0.392	0.314	0.355	0.370	0.337	0.361	0.357	0.324	0.368	**0.274**	**0.392**	**0.338**
% Deviation of V from average	-0.392	6.376	4.684	-14.492	-10.544	-23.516	-18.440	-12.800	-3.776	4.684	13.708	13.708	-7.724	4.684	8.632	-0.392	6.376	5.248	-4.340	8.068	**-23.516**	**13.708**	**-1.012**
Reading on pictures																							
Picture reference no.	1317	1318	1319	1320	1321	1322	1323	1324	1326	1327	1328	1329	1330	1331	1332	1333	1334	1335	1336	1337			
Static water height (mm)	24.10	24.10	24.10	24.10	24.10	24.10	24.10	24.10	24.10	24.10	24.10	24.10	24.10	24.10	24.10	24.10	24.10	24.10	24.10	24.10			
Recorded water height (mm)	29.3	30.3	30.2	28.9	29	27.7	28.1	28.7	28.3	30.5	30.5	30.6	28.5	30.4	30.1	29.7	31	30.1	29	29.7	27.700	31.000	29.530
Measured velocity																							
Rise in H, $H=V^2/2g$ (mm)	5.20	6.20	6.10	4.80	4.90	3.60	4.00	4.60	4.20	6.40	6.40	6.50	4.40	6.30	6.00	5.60	6.90	6.00	4.90	5.60	**3.600**	**6.900**	**5.430**
Velocity (m/s)	0.319	0.349	0.346	0.307	0.310	0.266	0.280	0.300	0.287	0.354	0.354	0.357	0.294	0.352	0.343	0.331	0.368	0.343	0.310	0.331	**0.266**	**0.368**	**0.325**
Difference in velocity																							
Difference	-0.018	-0.013	-0.009	0.011	0.004	-0.008	-0.006	0.000	-0.039	-0.001	-0.038	-0.035	-0.020	-0.003	-0.027	-0.006	0.006	-0.014	-0.014	-0.037	**-0.039**	**0.011**	**-0.013**
% Error	-5.531	-3.633	-2.624	3.687	1.270	-3.088	-1.989	0.140	-13.595	-0.190	-10.668	-9.813	-6.916	-0.982	-7.947	-1.692	1.764	-4.092	-4.600	-11.050	**-13.595**	**3.687**	**-4.077**
% Error (Abs)	5.53	3.63	2.62	3.69	1.27	3.09	1.99	0.14	13.60	0.19	10.67	9.81	6.92	0.98	7.95	1.69	1.76	4.09	4.60	11.05	**0.14**	**13.60**	**4.8**

Test 2

Weight: 175 g

	Run 1	**Run 2**	**Run 3**	**Run 4**	**Run 5**	**Run 6**	**Run 7**	**Run 8**	**Run 9**	**Run 10**	**Run 11**	**Run 12**	**Run 13**	**Run 14**	**Run 15**	**Run 16**	**Run 17**	**Run 18**	**Run 19**	**Run 20**	**Min**	**Max**	**Average**
Platform velocity																							
Time (sec)	1.04	0.94	0.97	1.1	1.22	1.03	1.19	1.04	1.25	1.09	0.98	1.15	1.31	1.16	1.15	1.06	1.15	1.21	1.19	1.12	0.940	1.310	1.118
Distance (m)	0.6	0.6	0.6	0.6	0.6	0.6	0.6	0.6	0.6	0.6	0.6	0.7	0.7	0.7	0.7	0.7	0.7	0.7	0.7	0.7			
Velocity (m/s)	0.577	0.638	0.619	0.545	0.492	0.583	0.504	0.577	0.480	0.550	0.612	0.609	0.534	0.603	0.609	0.660	0.609	0.579	0.588	0.625	**0.480**	**0.660**	**0.580**
% Deviation of V from average	-0.476	9.185	6.287	-6.273	-17.866	0.490	-14.968	-0.476	-20.765	-5.307	5.321	4.769	-8.481	3.940	4.769	12.221	4.769	-0.200	1.456	7.253	**-20.765**	**12.221**	**-0.718**
Reading on pictures																							
Picture reference no.	1344	1345	1346	1347	1348	1349	1350	1351	1352	1353	1354	1355	1356	1357	1358	1359	1360	1361	1362	1363			
Static water height (mm)	25.50	25.50	25.50	25.50	25.50	25.50	25.50	25.50	25.50	25.50	25.50	25.50	25.50	25.50	25.50	25.50	25.50	25.50	25.50	25.50			
Recorded water height (mm)	39.4	42.6	45	42.5	36.8	42.9	37.2	41.3	38.5	40.6	42.7	41.9	37.2	42.1	43	43.7	44	41.2	43.8	44	36.800	45.000	41.520
Measured velocity																							
Rise in H, $H=V^2/2g$ (mm)	13.90	17.10	19.50	17.00	11.30	17.40	11.70	15.80	13.00	15.10	17.20	16.40	11.70	16.60	17.50	18.20	18.50	15.70	18.30	18.50	**11.300**	**19.500**	**16.020**
Velocity (m/s)	0.522	0.579	0.619	0.578	0.471	0.584	0.479	0.557	0.505	0.544	0.581	0.567	0.479	0.571	0.586	0.598	0.602	0.555	0.599	0.602	**0.471**	**0.619**	**0.559**
Difference in velocity																							
Difference	-0.055	-0.059	0.000	0.032	-0.021	0.002	-0.025	-0.020	0.025	-0.006	-0.031	-0.041	-0.055	-0.033	-0.023	-0.063	-0.006	-0.024	0.011	-0.023	**-0.063**	**0.032**	**-0.021**
% Error	-10.474	-10.199	-0.003	5.554	-4.449	0.301	-5.235	-3.619	4.957	-1.132	-5.393	-7.307	-11.528	-5.739	-3.880	-10.511	-1.033	-4.235	1.831	-3.740	**-11.528**	**5.554**	**-3.792**
% Error (Abs)	10.47	10.20	0.00	5.55	4.45	0.30	5.24	3.62	4.96	1.13	5.39	7.31	11.53	5.74	3.88	10.51	1.03	4.23	1.83	3.74	**0.00**	**11.53**	**5.1**

Test 3

Weight: 195 g

	Run 1	Run 2	Run 3	Run 4	Run 5	Run 6	Run 7	Run 8	Run 9	Run 10	Run 11	Run 12	Run 13	Run 14	Run 15	Run 16	Run 17	Run 18	Run 19	Run 20	Min	Max	Average
Platform velocity																							
Time (sec)	1.06	1.03	1	1	1.03	1.03	1.1	1.03	1.09	1	0.97	0.97	0.88	1	1	1.19	0.97	0.97	1.16	1	0.880	1.190	1.024
Distance (m)	0.7	0.7	0.7	0.7	0.7	0.7	0.7	0.7	0.7	0.7	0.7	0.7	0.7	0.7	0.7	0.7	0.7	0.7	0.7	0.7			
Velocity (m/s)	0.660	0.680	0.700	0.700	0.680	0.680	0.636	0.680	0.642	0.700	0.722	0.722	0.795	0.700	0.700	0.588	0.722	0.722	0.603	0.700	**0.588**	**0.795**	**0.687**
% Deviation of V from average	-3.964	-1.022	1.921	1.921	-1.022	-1.022	-7.887	-1.022	-6.907	1.921	4.863	4.863	13.690	1.921	1.921	-16.715	4.863	4.863	-13.772	1.921	**-16.715**	**13.690**	**-0.433**
Reading on pictures																							
Picture reference no.	1366	1367	1368	1369	1370	1371	1372	1373	1374	1375	1376	1377	1378	1379	1380	1381	1382	1384	1385	1386			
Static water height (mm)	25.10	25.10	25.10	25.10	25.10	25.10	25.10	25.10	25.10	25.10	25.10	25.10	25.10	25.10	25.10	25.10	25.10	25.10	25.10	25.10			
Recorded water height (mm)	44	46.9	45.1	47.1	48.4	47.6	47.5	49.8	46.3	46.8	50.1	51	53.3	52.6	47.5	46	51.4	48.9	48	48.1	44.000	53.300	48.320
Measured velocity																							
Rise in H, $H=V^2/2g$ (mm)	18.90	21.80	20.00	22.00	23.30	22.50	22.40	24.70	21.20	21.70	25.00	25.90	28.20	27.50	22.40	20.90	26.30	23.80	22.90	23.00	**18.900**	**28.200**	**23.220**
Velocity (m/s)	0.609	0.654	0.626	0.657	0.676	0.664	0.663	0.696	0.645	0.652	0.700	0.713	0.744	0.735	0.663	0.640	0.718	0.683	0.670	0.672	**0.609**	**0.744**	**0.674**
Difference in velocity																							
Difference	-0.051	-0.026	-0.074	-0.043	-0.003	-0.015	0.027	0.017	0.003	-0.048	-0.021	-0.009	-0.052	0.035	-0.037	0.052	-0.003	-0.038	0.067	-0.028	**-0.074**	**0.067**	**-0.012**
% Error	-8.446	-3.916	-11.746	-6.546	-0.516	-2.287	4.009	2.375	0.424	-7.280	-3.040	-1.234	-6.940	4.702	-5.590	8.140	-0.461	-5.606	9.973	-4.204	**-11.746**	**9.973**	**-1.910**
% Error (Abs)	8.45	3.92	11.75	6.55	0.52	2.29	4.01	2.37	0.42	7.28	3.04	1.23	6.94	4.70	5.59	8.14	0.46	5.61	9.97	4.20	**0.42**	**11.75**	**4.9**

2. Test 2 data

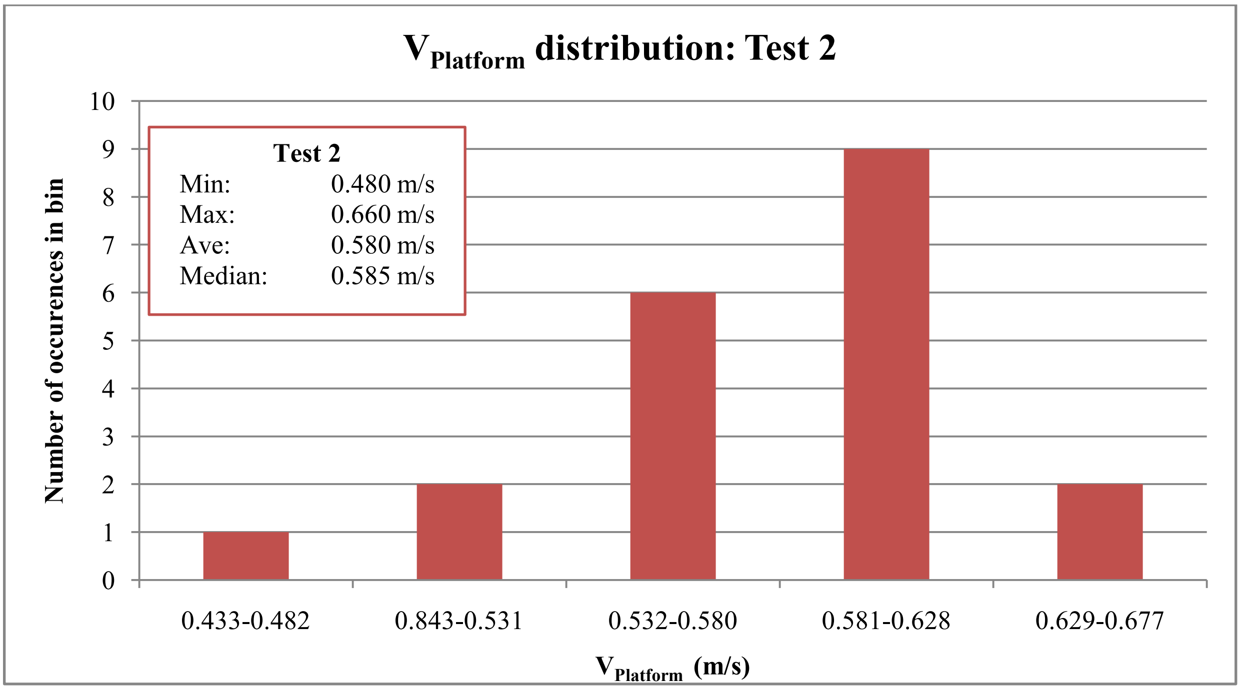

V_Platform distribution: Test 2
Test 2
Min: 0.480 m/s
Max: 0.660 m/s
Ave: 0.580 m/s
Median: 0.585 m/s
Number of occurences in bin
0
1
2
3
4
5
6
7
8
9
10
0.433-0.482
0.843-0.531
0.532-0.580
0.581-0.628
0.629-0.677
V_Platform (m/s)

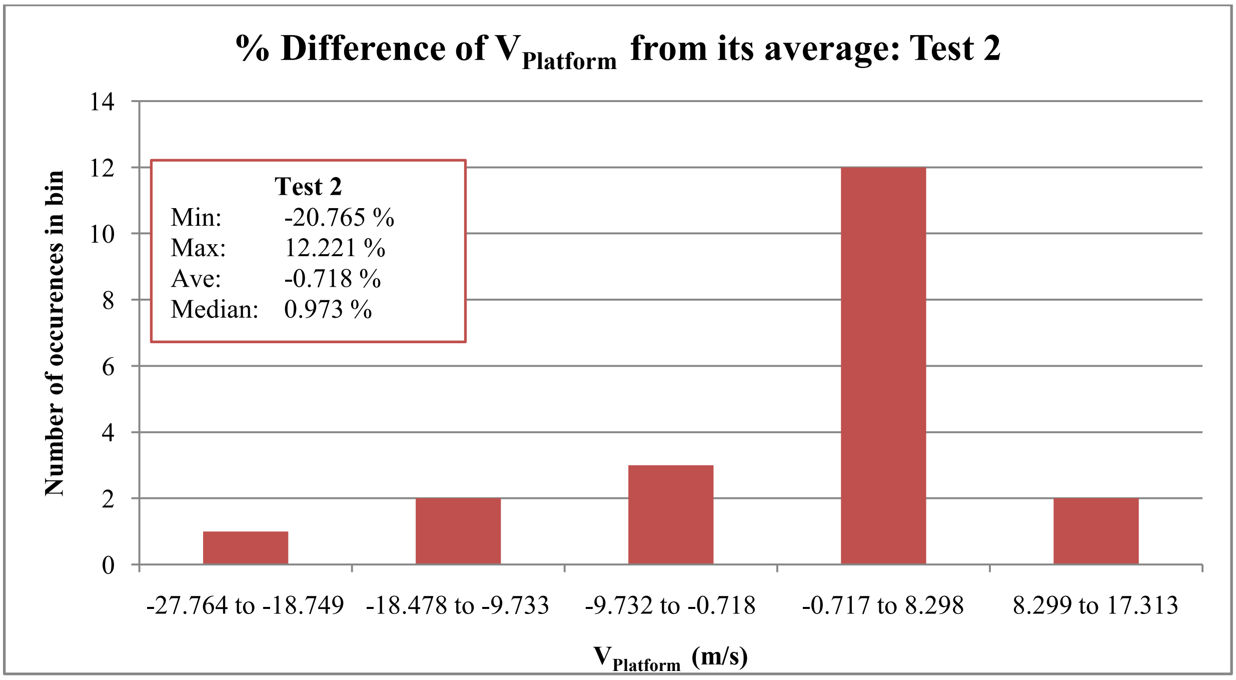

% Difference of V_Platform from its average: Test 2
Test 2
Min: -20.765 %
Max: 12.221 %
Ave: -0.718 %
Median: 0.973 %
Number of occurences in bin
0
2
4
6
8
10
12
14
-27.764 to -18.749
-18.478 to -9.733
-9.732 to -0.718
-0.717 to 8.298
8.299 to 17.313
V_Platform (m/s)

3. Test 3 data

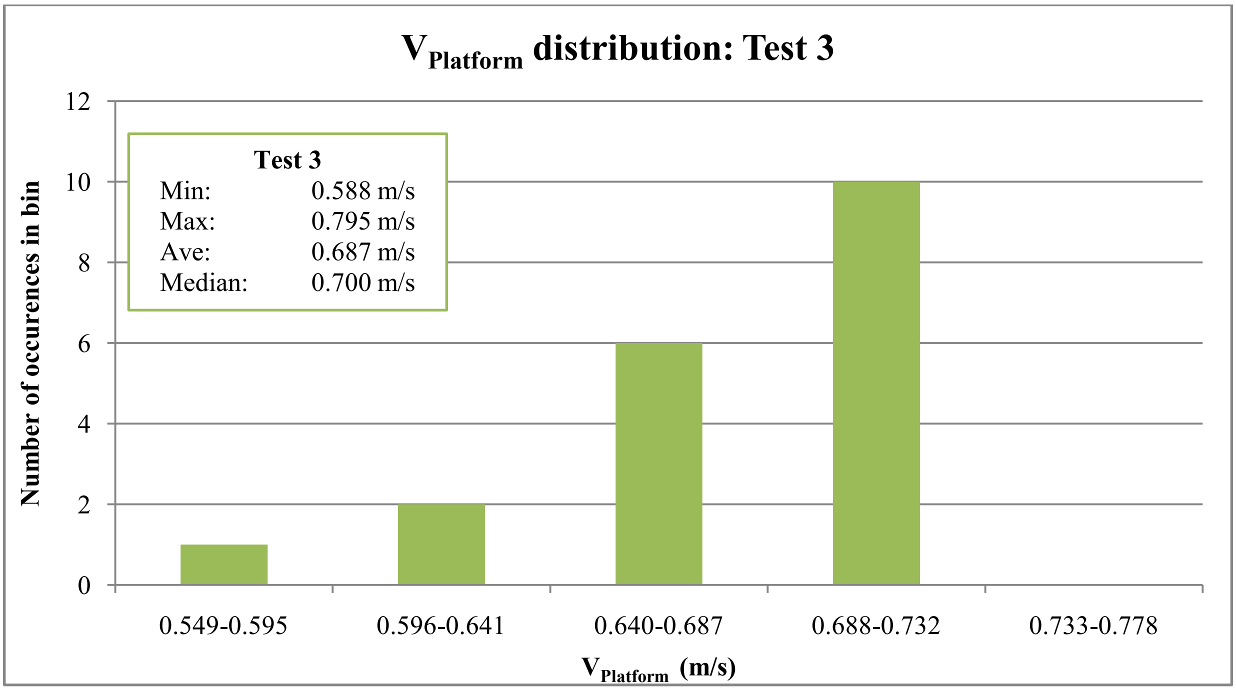
$V_{Platform}$ distribution: Test 3
Test 3
Min: 0.588 m/s
Max: 0.795 m/s
Ave: 0.687 m/s
Median: 0.700 m/s
Number of occurences in bin
0
2
4
6
8
10
12
0.549-0.595
0.596-0.641
0.640-0.687
0.688-0.732
0.733-0.778
$V_{Platform}$ (m/s)

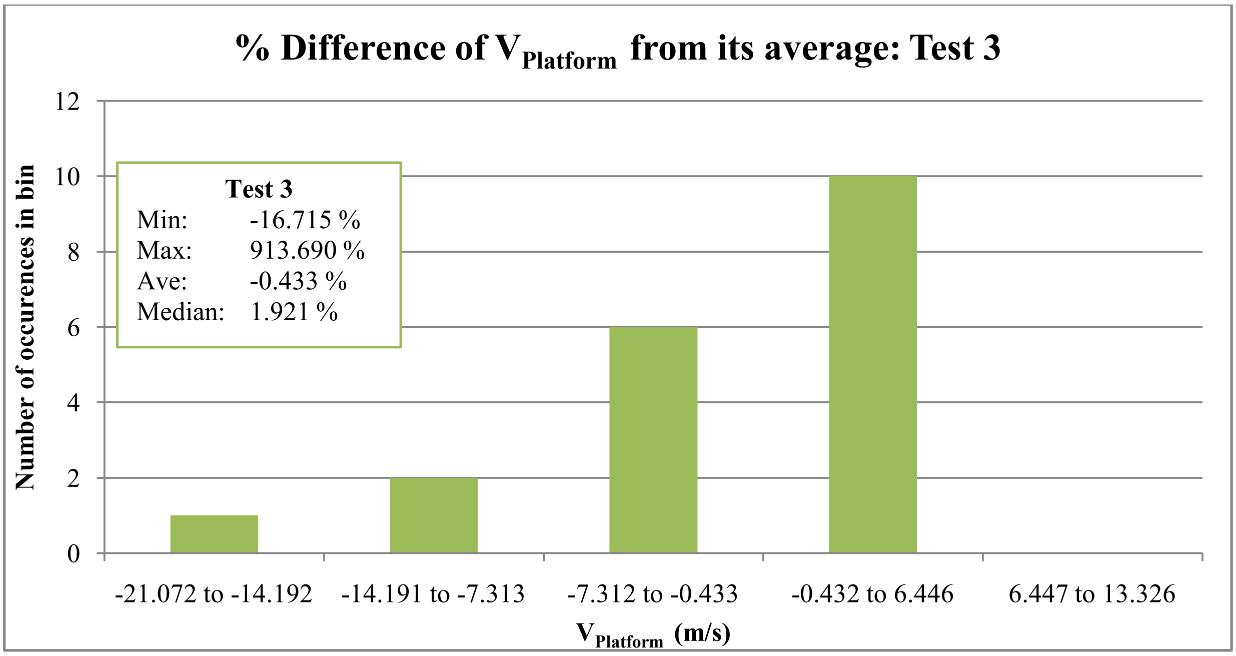
% Difference of $V_{Platform}$ from its average: Test 3
Test 3
Min: -16.715 %
Max: 913.690 %
Ave: -0.433 %
Median: 1.921 %
Number of occurences in bin
0
2
4
6
8
10
12
-21.072 to -14.192
-14.191 to -7.313
-7.312 to -0.433
-0.432 to 6.446
6.447 to 13.326
$V_{Platform}$ (m/s)

Appendix C

Experimental results

Appendix layout:

- Recorded experimental data
- Continued velocity graphs
- Continued pressure graphs
- Continued energy graphs
- Repeatability data

1. Recorded experimental data

Y=0 mm	**Ballotini bed height**	**300 mm**
	Water height	**443.8 mm**

Pitot tube nose location (with respect to centre of orifice/origin) (mm)																								
X				0	0	0	0	0	0	0	0	0	0	0	0	0	0	0	0	0	0	0	0	0
Y				0	0	0	0	0	0	0	0	0	0	0	0	0	0	0	0	0	0	0	0	0
Z				200	190	180	170	160	150	140	130	120	110	100	90	80	70	60	50	40	30	20	10	0
Readings (mm)																								
L type Pitot tube	**Total horizontal pressure (nose facing pos Y)**	**X rule reading**	**Static water reading in sight tube**	360	360	360	360	360	360	360	360	360	360	360	360	360	360	360	360	360	360	360	360	360
		Y rule reading		374.5	374.5	374.5	374.5	374.5	374.5	374.5	374.5	374.5	374.5	374.5	374.5	374.5	374.5	374.5	374.5	374.5	374.5	374.5	374.5	374.5
		Z rule reading		256.0	246.0	236.0	226.0	216.0	206.0	196.0	186.0	176.0	166.0	156.0	146.0	136.0	126.0	116.0	106.0	96.0	86.0	76.0	66.0	56.0
		Reading on sight tube (mm)		21	21.5	21.9	22.5	23	23.7	24.1	25	25.9	27	28	29.7	31.8	35	39.9	47	62	94.4	128.5	94	81.3
		Pressure head (mm)	**17.9**	**3.1**	**3.6**	**4**	**4.6**	**5.1**	**5.8**	**6.2**	**7.1**	**8**	**9.1**	**10.1**	**11.8**	**13.9**	**17.1**	**22**	**29.1**	**44.1**	**76.5**	**110.6**	**76.1**	**63.4**
	Pressure (nose facing pos X)	**X rule reading**	**Static water reading in sight tube**	432	432	432	432	432	432	432	432	432	432	432	432	432	432	432	432	432	432	432	432	432
		Y rule reading		301.9	301.9	301.9	301.9	301.9	301.9	301.9	301.9	301.9	301.9	301.9	301.9	301.9	301.9	301.9	301.9	301.9	301.9	301.9	301.9	301.9
		Z rule reading		256.0	246.0	236.0	226.0	216.0	206.0	196.0	186.0	176.0	166.0	156.0	146.0	136.0	126.0	116.0	106.0	96.0	86.0	76.0	66.0	56.0
		Reading on sight tube (mm)																						
		Pressure head (mm)																						
	Pressure (nose facing neg X)	**X rule reading**	**Static water reading in sight tube**	286	286	286	286	286	286	286	286	286	286	286	286	286	286	286	286	286	286	286	286	286
		Y rule reading		301.9	301.9	301.9	301.9	301.9	301.9	301.9	301.9	301.9	301.9	301.9	301.9	301.9	301.9	301.9	301.9	301.9	301.9	301.9	301.9	301.9
		Z rule reading		256.0	246.0	236.0	226.0	216.0	206.0	196.0	186.0	176.0	166.0	156.0	146.0	136.0	126.0	116.0	106.0	96.0	86.0	76.0	66.0	56.0
		Reading on sight tube (mm)																						
		Pressure head (mm)																						
Straight type Pitot tube	**Total vertical pressure (nose facing neg Z)**	**X rule reading**	**Static water reading in sight tube**	360	360	360	360	360	360	360	360	360	360	360	360	360	360	360	360	360	360	360	360	360
		Y rule reading		301	301	301	301	301	301	301	301	301	301	301	301	301	301	301	301	301	301	301	301	301
		Z rule reading		230.5	220.5	210.5	200.5	190.5	180.5	170.5	160.5	150.5	140.5	130.5	120.5	110.5	100.5	90.5	80.5	70.5	60.5	50.5	40.5	30.5
		Reading on sight tube (mm)		21	21.5	22	22.5	23	23.6	24.1	25.5	25.9	27.2	28.3	30	32.2	35.3	40	47.8	62	100	416.3	627.5	1480
		Pressure head (mm)	**17.9**	**3.1**	**3.6**	**4.1**	**4.6**	**5.1**	**5.7**	**6.2**	**7.6**	**8**	**9.3**	**10.4**	**12.1**	**14.3**	**17.4**	**22.1**	**29.9**	**44.1**	**82.1**	**398.4**	**609.6**	**1462.1**
Calculations																								
Total Mechanical Energy components	**Elevation (Z) (mm)**			200	190	180	170	160	150	140	130	120	110	100	90	80	70	60	50	40	30	20	10	0
	Pressure head (P/ρg) (mm)			3.1	3.6	4.0	4.6	5.1	5.8	6.2	7.1	8.0	9.1	10.1	11.8	13.9	17.1	22.0	29.1	44.1	76.5	110.6	76.1	63.4
	Velocity head - Horizontal component ($V^2/2g$) (mm)			0.0	0.0	0.0	0.0	0.0	0.0	0.0	0.0	0.0	0.0	0.0	0.0	0.0	0.0	0.0	0.0	0.0	0.0	0.0	0.0	0.0
	Velocity head - Vertical component ($V^2/2g$) (mm)			0.0	0.0	0.1	0.0	0.0	-0.1	0.0	0.5	0.0	0.2	0.3	0.3	0.4	0.3	0.1	0.8	0.0	5.6	287.8	533.5	1398.7
	Velocity head - Vector ($V^2/2g$) (mm)			0.00	0.00	0.10	0.00	0.00	0.10	0.00	0.50	0.00	0.20	0.30	0.30	0.40	0.30	0.10	0.80	0.00	5.60	287.80	533.50	1398.70
Energy - Horizontal component				3.1	3.6	4.0	4.6	5.1	5.8	6.2	7.1	8.0	9.1	10.1	11.8	13.9	17.1	22.0	29.1	44.1	76.5	110.6	76.1	63.4
Energy - Vertical component				3.1	3.6	4.1	4.6	5.1	5.7	6.2	7.6	8.0	9.3	10.4	12.1	14.3	17.4	22.1	29.9	44.1	82.1	398.4	609.6	1462.1
Energy - Vector component				3.10	3.60	4.10	4.60	5.10	5.90	6.20	7.60	8.00	9.30	10.40	12.10	14.30	17.40	22.10	29.90	44.10	82.10	398.40	609.60	1462.10
Velocity - Vertical component (m/s)				**0.000**	**0.000**	**0.044**	**0.000**	**0.000**	**-0.044**	**0.000**	**0.099**	**0.000**	**0.063**	**0.077**	**0.077**	**0.089**	**0.077**	**0.044**	**0.125**	**0.000**	**0.331**	**2.376**	**3.235**	**5.239**
Pressure head (mm)				**3.1**	**3.6**	**4.0**	**4.6**	**5.1**	**5.8**	**6.2**	**7.1**	**8.0**	**9.1**	**10.1**	**11.8**	**13.9**	**17.1**	**22.0**	**29.1**	**44.1**	**76.5**	**110.6**	**76.1**	**63.4**
Pressure (Pa)				**30.41**	**35.32**	**39.24**	**45.13**	**50.03**	**56.90**	**60.82**	**69.65**	**78.48**	**89.27**	**99.08**	**115.76**	**136.36**	**167.75**	**215.82**	**285.47**	**432.62**	**750.47**	**1084.99**	**746.54**	**621.95**

Y=10 mm

Ballotini bed height	300 mm
Water height	443.8 mm

Pitot tube nose location (with respect to centre of orifice/origin) (mm)																								
X				0	0	0	0	0	0	0	0	0	0	0	0	0	0	0	0	0	0	0	0	0
Y				-10	-10	-10	-10	-10	-10	-10	-10	-10	-10	-10	-10	-10	-10	-10	-10	-10	-10	-10	-10	-10
Z				200	190	180	170	160	150	140	130	120	110	100	90	80	70	60	50	40	30	20	10	0
Readings (mm)																								
L type Pitot tube	Total horizontal pressure (nose facing pos Y)	X rule reading	Static water reading in sight tube	360	360	360	360	360	360	360	360	360	360	360	360	360	360	360	360	360	360	360	360	360
		Y rule reading		384.5	384.5	384.5	384.5	384.5	384.5	384.5	384.5	384.5	384.5	384.5	384.5	384.5	384.5	384.5	384.5	384.5	384.5	384.5	384.5	384.5
		Z rule reading		256.0	246.0	236.0	226.0	216.0	206.0	196.0	186.0	176.0	166.0	156.0	146.0	136.0	126.0	116.0	106.0	96.0	86.0	76.0	66.0	56.0
		Reading on sight tube (mm)		20.7	21.3	21.8	22.2	22.7	23.1	23.7	24.7	25.5	26.2	27.2	28.7	30.1	32.3	35	40.6	51.1	76.9	97	80.9	66
		Pressure head (mm)	17.9	**2.8**	**3.4**	**3.9**	**4.3**	**4.8**	**5.2**	**5.8**	**6.8**	**7.6**	**8.3**	**9.3**	**10.8**	**12.2**	**14.4**	**17.1**	**22.7**	**33.2**	**59.0**	**79.1**	**63.0**	**48.1**
	Pressure (nose facing pos X)	X rule reading	Static water reading in sight tube	432	432	432	432	432	432	432	432	432	432	432	432	432	432	432	432	432	432	432	432	432
		Y rule reading		311.9	311.9	311.9	311.9	311.9	311.9	311.9	311.9	311.9	311.9	311.9	311.9	311.9	311.9	311.9	311.9	311.9	311.9	311.9	311.9	311.9
		Z rule reading		256.0	246.0	236.0	226.0	216.0	206.0	196.0	186.0	176.0	166.0	156.0	146.0	136.0	126.0	116.0	106.0	96.0	86.0	76.0	66.0	56.0
		Reading on sight tube (mm)		21	21.3	22	22.4	22.8	23.3	23.9	24.7	25.5	26.3	27.4	28.9	30.3	32.7	35.4	40.1	47.3	69.9	81.6	75	66.1
		Pressure head (mm)	17.9	**3.1**	**3.4**	**4.1**	**4.5**	**4.9**	**5.4**	**6.0**	**6.8**	**7.6**	**8.4**	**9.5**	**11.0**	**12.4**	**14.8**	**17.5**	**22.2**	**29.4**	**52.0**	**63.7**	**57.1**	**48.2**
	Pressure (nose facing neg X)	X rule reading	Static water reading in sight tube	286	286	286	286	286	286	286	286	286	286	286	286	286	286	286	286	286	286	286	286	286
		Y rule reading		311.9	311.9	311.9	311.9	311.9	311.9	311.9	311.9	311.9	311.9	311.9	311.9	311.9	311.9	311.9	311.9	311.9	311.9	311.9	311.9	311.9
		Z rule reading		256.0	246.0	236.0	226.0	216.0	206.0	196.0	186.0	176.0	166.0	156.0	146.0	136.0	126.0	116.0	106.0	96.0	86.0	76.0	66.0	56.0
		Reading on sight tube (mm)		21	21.3	21.7	22.2	22.8	23.1	23.4	24.7	25.7	26.4	27.2	28.8	30.5	32.4	35.5	40	47.1	70.4	82.1	75.2	66
		Pressure head (mm)	17.9	**3.1**	**3.4**	**3.8**	**4.3**	**4.9**	**5.2**	**5.5**	**6.8**	**7.8**	**8.5**	**9.3**	**10.9**	**12.6**	**14.5**	**17.6**	**22.1**	**29.2**	**52.5**	**64.2**	**57.3**	**48.1**
	Average pressure head (mm)			**3.1**	**3.4**	**4.0**	**4.4**	**4.9**	**5.3**	**5.8**	**6.8**	**7.7**	**8.5**	**9.4**	**11.0**	**12.5**	**14.7**	**17.6**	**22.2**	**29.3**	**52.3**	**64.0**	**57.2**	**48.2**
Straight type Pitot tube	Total vertical pressure (nose facing neg Z)	X rule reading	Static water reading in sight tube	360	360	360	360	360	360	360	360	360	360	360	360	360	360	360	360	360	360	360	360	360
		Y rule reading		311	311	311	311	311	311	311	311	311	311	311	311	311	311	311	311	311	311	311	311	311
		Z rule reading		230.5	220.5	210.5	200.5	190.5	180.5	170.5	160.5	150.5	140.5	130.5	120.5	110.5	100.5	90.5	80.5	70.5	60.5	50.5	40.5	30.5
		Reading on sight tube (mm)		21	21.3	21.8	22.1	22.6	23	23.8	24.7	25.5	26.2	27.2	28.7	30.2	32.4	36.1	43.6	52.6	66.7	91.5	92	100.4
		Pressure head (mm)	17.9	**3.3**	**3.6**	**4.1**	**4.4**	**4.9**	**5.3**	**6.1**	**7.0**	**7.8**	**8.5**	**9.5**	**11.0**	**12.5**	**14.7**	**18.4**	**25.9**	**34.9**	**49.0**	**73.8**	**74.3**	**82.7**
Calculations																								
Total Mechanical Energy components	Elevation (Z) (mm)			200	190	180	170	160	150	140	130	120	110	100	90	80	70	60	50	40	30	20	10	0
	Pressure head (P/ρg) (mm)			3.1	3.4	4.0	4.4	4.9	5.3	5.8	6.8	7.7	8.5	9.4	11.0	12.5	14.7	17.6	22.2	29.3	52.3	64.0	57.2	48.2
	Velocity head - Horizontal component ($V^2/2g$) (mm)			-0.3	0.0	0.0	-0.1	-0.1	-0.1	0.1	0.0	-0.1	-0.2	-0.1	-0.2	-0.3	-0.3	-0.4	0.6	3.9	6.8	15.2	5.8	0.0
	Velocity head - Vertical component ($V^2/2g$) (mm)			0.2	0.2	0.2	0.0	0.0	0.0	0.4	0.2	0.1	0.0	0.1	0.0	0.0	0.0	0.9	3.8	5.6	-3.3	9.9	17.1	34.6
	Velocity head - Vector ($V^2/2g$) (mm)			0.36	0.20	0.16	0.10	0.10	0.10	0.35	0.20	0.14	0.16	0.14	0.16	0.30	0.25	0.96	3.79	6.82	7.49	18.07	18.06	34.55
Energy - Horizontal component				3.4	3.4	4.0	4.5	5.0	5.4	5.8	6.8	7.8	8.6	9.5	11.1	12.8	14.9	18.0	22.7	33.2	59.0	79.1	63.0	48.2
Energy - Vertical component				3.3	3.6	4.1	4.4	4.9	5.3	6.1	7.0	7.8	8.5	9.5	11.0	12.5	14.7	18.4	25.9	34.9	55.5	73.8	74.3	82.7
Energy - Vector component				3.46	3.60	4.11	4.50	5.00	5.40	6.10	7.00	7.84	8.61	9.54	11.11	12.80	14.90	18.51	25.94	36.12	59.74	82.02	75.26	82.70
Velocity - Horizontal component (m/s)				**-0.077**	**0.000**	**0.031**	**-0.044**	**-0.044**	**-0.044**	**0.031**	**0.000**	**-0.044**	**-0.054**	**-0.044**	**-0.054**	**-0.077**	**-0.070**	**-0.094**	**0.104**	**0.277**	**0.364**	**0.545**	**0.337**	**0.031**
Velocity - Vertical component (m/s)				**0.063**	**0.063**	**0.054**	**0.000**	**0.000**	**0.000**	**0.083**	**0.063**	**0.044**	**0.031**	**0.044**	**0.031**	**0.000**	**0.031**	**0.129**	**0.271**	**0.331**	**-0.253**	**0.440**	**0.579**	**0.823**
Velocity - Vector component (m/s)				**0.099**	**0.063**	**0.063**	**0.044**	**0.044**	**0.044**	**0.089**	**0.063**	**0.063**	**0.063**	**0.063**	**0.063**	**0.077**	**0.077**	**0.160**	**0.290**	**0.432**	**0.443**	**0.700**	**0.670**	**0.824**
Pressure head (mm)				**3.1**	**3.4**	**4.0**	**4.4**	**4.9**	**5.3**	**5.8**	**6.8**	**7.7**	**8.5**	**9.4**	**11.0**	**12.5**	**14.7**	**17.6**	**22.2**	**29.3**	**52.3**	**64.0**	**57.2**	**48.2**
Pressure (Pa)				**30.41**	**33.35**	**38.75**	**43.16**	**48.07**	**51.99**	**56.41**	**66.71**	**75.54**	**82.89**	**92.21**	**107.42**	**122.63**	**143.72**	**172.17**	**217.29**	**287.43**	**512.57**	**627.35**	**561.13**	**472.35**

Y=20 mm		
	Ballotini bed height	300 mm
	Water height	443.8 mm

Pitot tube nose location (with respect to centre of orifice/origin) (mm)																								
X				0	0	0	0	0	0	0	0	0	0	0	0	0	0	0	0	0	0	0	0	0
Y				-20	-20	-20	-20	-20	-20	-20	-20	-20	-20	-20	-20	-20	-20	-20	-20	-20	-20	-20	-20	-20
Z				200	190	180	170	160	150	140	130	120	110	100	90	80	70	60	50	40	30	20	10	0
Readings (mm)																								
L type Pitot tube	Total horizontal pressure (nose facing pos Y)	X rule reading	Static water reading in sight tube	360	360	360	360	360	360	360	360	360	360	360	360	360	360	360	360	360	360	360	360	360
		Y rule reading		394.5	394.5	394.5	394.5	394.5	394.5	394.5	394.5	394.5	394.5	394.5	394.5	394.5	394.5	394.5	394.5	394.5	394.5	394.5	394.5	394.5
		Z rule reading		256.0	246.0	236.0	226.0	216.0	206.0	196.0	186.0	176.0	166.0	156.0	146.0	136.0	126.0	116.0	106.0	96.0	86.0	76.0	66.0	56.0
		Reading on sight tube (mm)		20	21.5	21.9	22.4	23.0	23.7	24.2	25.0	25.5	26.6	27.1	28.0	29.0	31.5	34.6	38.8	45.2	54.7	65.7	71.1	68.0
		Pressure head (mm)	17.9	2.1	3.6	4.0	4.5	5.1	5.8	6.3	7.1	7.6	8.7	9.2	10.1	11.1	13.6	16.7	20.9	27.3	36.8	47.8	53.2	50.1
	Pressure (nose facing pos X)	X rule reading	Static water reading in sight tube	432	432	432	432	432	432	432	432	432	432	432	432	432	432	432	432	432	432	432	432	432
		Y rule reading		321.9	321.9	321.9	321.9	321.9	321.9	321.9	321.9	321.9	321.9	321.9	321.9	321.9	321.9	321.9	321.9	321.9	321.9	321.9	321.9	321.9
		Z rule reading		256.0	246.0	236.0	226.0	216.0	206.0	196.0	186.0	176.0	166.0	156.0	146.0	136.0	126.0	116.0	106.0	96.0	86.0	76.0	66.0	56.0
		Reading on sight tube (mm)		20.1	21.1	21.7	22	22.7	23.1	23.8	24.1	24.9	25.8	26.7	27.3	28.7	30.7	33.3	37	43.8	52	67	75.2	60.8
		Pressure head (mm)	17.9	2.2	3.2	3.8	4.1	4.8	5.2	5.9	6.2	7.0	7.9	8.8	9.4	10.8	12.8	15.4	19.1	25.9	34.1	49.1	57.3	42.9
	Pressure (nose facing neg X)	X rule reading	Static water reading in sight tube	286	286	286	286	286	286	286	286	286	286	286	286	286	286	286	286	286	286	286	286	286
		Y rule reading		321.9	321.9	321.9	321.9	321.9	321.9	321.9	321.9	321.9	321.9	321.9	321.9	321.9	321.9	321.9	321.9	321.9	321.9	321.9	321.9	321.9
		Z rule reading		256.0	246.0	236.0	226.0	216.0	206.0	196.0	186.0	176.0	166.0	156.0	146.0	136.0	126.0	116.0	106.0	96.0	86.0	76.0	66.0	56.0
		Reading on sight tube (mm)		19.8	21.2	21.7	22	22.5	23	23.7	24	24.8	25.4	26.3	27.4	29.3	30.8	32.8	36.8	44.1	55.1	66.2	73.9	62.2
		Pressure head (mm)	17.9	1.9	3.3	3.8	4.1	4.6	5.1	5.8	6.1	6.9	7.5	8.4	9.5	11.4	12.9	14.9	18.9	26.2	37.2	48.3	56.0	44.3
	Average pressure head (mm)			2.1	3.3	3.8	4.1	4.7	5.2	5.9	6.2	7.0	7.7	8.6	9.5	11.1	12.9	15.2	19.0	26.1	35.7	48.7	56.7	43.6
Straight type Pitot tube	Total vertical pressure (nose facing neg Z)	X rule reading	Static water reading in sight tube	360	360	360	360	360	360	360	360	360	360	360	360	360	360	360	360	360	360	360	360	360
		Y rule reading		321	321	321	321	321	321	321	321	321	321	321	321	321	321	321	321	321	321	321	321	321
		Z rule reading		230.5	220.5	210.5	200.5	190.5	180.5	170.5	160.5	150.5	140.5	130.5	120.5	110.5	100.5	90.5	80.5	70.5	60.5	50.5	40.5	30.5
		Reading on sight tube (mm)		19.7	21.1	21.5	21.9	22.9	23.4	23.9	24.3	25.1	26	27.2	28.5	30.2	32.9	36.8	41.7	47.1	54.9	57.9	56.2	55.4
		Pressure head (mm)	17.9	1.8	3.2	3.6	4.0	5.0	5.5	6.0	6.4	7.2	8.1	9.3	10.6	12.3	15.0	18.9	23.8	29.2	37.0	40.0	38.3	37.5
Calculations																								
Total Mechanical Energy components	Elevation (Z) (mm)			0	0	0	0	0	0	0	0	0	0	0	0	0	0	0	0	0	0	0	0	0
	Pressure head (P/ρg) (mm)			2.1	3.2	3.8	4.1	4.8	5.2	5.9	6.2	7.0	7.9	8.8	9.4	10.8	12.8	15.4	19.1	25.9	34.1	49.1	57.3	42.9
	Velocity head - Horizontal component ($V^2/2g$) (mm)			0.0	0.4	0.2	0.4	0.4	0.6	0.4	0.9	0.7	1.0	0.6	0.7	0.0	0.8	1.6	1.9	1.3	1.2	-0.9	-3.5	6.5
	Velocity head - Vertical component ($V^2/2g$) (mm)			-0.3	0.0	-0.2	-0.1	0.3	0.3	0.1	0.3	0.3	0.4	0.7	1.2	1.2	2.2	3.8	4.8	3.2	1.3	-8.7	-18.4	-6.1
	Velocity head - Vector ($V^2/2g$) (mm)			0.25	0.35	0.28	0.41	0.50	0.74	0.47	0.98	0.70	1.08	0.92	1.32	1.20	2.28	4.06	5.16	3.39	1.77	8.75	18.67	8.91
Energy - Horizontal component				2.1	3.6	4.0	4.5	5.2	5.9	6.4	7.2	7.7	8.9	9.4	10.1	10.8	13.6	17.0	21.0	27.2	35.3	50.0	60.8	49.4
Energy - Vertical component				2.3	3.3	4.0	4.2	5.1	5.6	6.1	6.5	7.3	8.3	9.5	10.6	12.0	15.0	19.2	23.9	29.1	35.5	57.8	75.7	49.0
Energy - Vector component				2.30	3.55	4.08	4.51	5.30	5.94	6.37	7.18	7.70	8.98	9.72	10.72	12.00	15.08	19.46	24.26	29.29	35.87	57.85	75.97	51.81
Velocity - Horizontal component (m/s)				0.031	0.083	0.063	0.089	0.089	0.113	0.094	0.137	0.113	0.140	0.108	0.113	0.000	0.121	0.174	0.193	0.157	0.150	-0.133	-0.260	0.357
Velocity - Vertical component (m/s)				-0.070	0.031	-0.063	-0.044	0.077	0.083	0.054	0.070	0.070	0.089	0.117	0.150	0.153	0.205	0.271	0.307	0.249	0.163	-0.413	-0.600	-0.346
Velocity - Vector component (m/s)				0.077	0.089	0.089	0.099	0.117	0.140	0.108	0.153	0.133	0.166	0.160	0.188	0.153	0.239	0.322	0.363	0.294	0.221	0.434	0.654	0.497
Pressure head (mm)				2.1	3.3	3.8	4.1	4.7	5.2	5.9	6.2	7.0	7.7	8.6	9.5	11.1	12.9	15.2	19.0	26.1	35.7	48.7	56.7	43.6
Pressure (Pa)				20.11	31.39	37.28	40.22	47.09	51.01	57.88	60.82	68.67	77.50	86.33	92.21	105.95	125.57	151.07	187.37	254.08	334.52	481.67	562.11	420.85

Y=40 mm	Ballotini bed height	300 mm
	Water height	443.8 mm

Pitot tube nose location (with respect to centre of orifice/origin) (mm)																								
X				0	0	0	0	0	0	0	0	0	0	0	0	0	0	0	0	0	0	0	0	0
Y				-40	-40	-40	-40	-40	-40	-40	-40	-40	-40	-40	-40	-40	-40	-40	-40	-40	-40	-40	-40	-40
Z				200	190	180	170	160	150	140	130	120	110	100	90	80	70	60	50	40	30	20	10	0
Readings (mm)																								
L type Pitot tube	Total horizontal pressure (nose facing pos Y)	X rule reading	Static water reading in sight tube	360	360	360	360	360	360	360	360	360	360	360	360	360	360	360	360	360	360	360	360	360
		Y rule reading		414.5	414.5	414.5	414.5	414.5	414.5	414.5	414.5	414.5	414.5	414.5	414.5	414.5	414.5	414.5	414.5	414.5	414.5	414.5	414.5	414.5
		Z rule reading		256.0	246.0	236.0	226.0	216.0	206.0	196.0	186.0	176.0	166.0	156.0	146.0	136.0	126.0	116.0	106.0	96.0	86.0	76.0	66.0	56.0
		Reading on sight tube (mm)		20.9	21.2	21.6	22.0	22.6	23.0	23.7	24.1	24.9	25.9	26.9	28.0	29.3	31.1	32.1	34.9	38.4	41.0	43.4	44.2	43.5
		Pressure head (mm)	17.9	**3.0**	**3.3**	**3.7**	**4.1**	**4.7**	**5.1**	**5.8**	**6.2**	**7.0**	**8.0**	**9.0**	**10.1**	**11.4**	**13.2**	**14.2**	**17.0**	**20.5**	**23.1**	**25.5**	**26.3**	**25.6**
	Pressure (nose facing pos X)	X rule reading	Static water reading in sight tube	439.5	439.5	439.5	439.5	439.5	439.5	439.5	439.5	439.5	439.5	439.5	439.5	439.5	439.5	439.5	439.5	439.5	439.5	439.5	439.5	439.5
		Y rule reading		341.9	341.9	341.9	341.9	341.9	341.9	341.9	341.9	341.9	341.9	341.9	341.9	341.9	341.9	341.9	341.9	341.9	341.9	341.9	341.9	341.9
		Z rule reading		256.0	246.0	236.0	226.0	216.0	206.0	196.0	186.0	176.0	166.0	156.0	146.0	136.0	126.0	116.0	106.0	96.0	86.0	76.0	66.0	56.0
		Reading on sight tube (mm)		20.6	20.9	21	21.8	22.1	22.8	23.6	24.2	25	26	26.9	27.2	28.5	30	31	33	35.3	38.4	40	41.5	39.1
		Pressure head (mm)	17.9	**2.7**	**3.0**	**3.1**	**3.9**	**4.2**	**4.9**	**5.7**	**6.3**	**7.1**	**8.1**	**9.0**	**9.3**	**10.6**	**12.1**	**13.1**	**15.1**	**17.4**	**20.5**	**22.1**	**23.6**	**21.2**
	Pressure (nose facing neg X)	X rule reading	Static water reading in sight tube	278.5	278.5	278.5	278.5	278.5	278.5	278.5	278.5	278.5	278.5	278.5	278.5	278.5	278.5	278.5	278.5	278.5	278.5	278.5	278.5	278.5
		Y rule reading		341.9	341.9	341.9	341.9	341.9	341.9	341.9	341.9	341.9	341.9	341.9	341.9	341.9	341.9	341.9	341.9	341.9	341.9	341.9	341.9	341.9
		Z rule reading		256.0	246.0	236.0	226.0	216.0	206.0	196.0	186.0	176.0	166.0	156.0	146.0	136.0	126.0	116.0	106.0	96.0	86.0	76.0	66.0	56.0
		Reading on sight tube (mm)												READINGS NOT TAKEN										
		Pressure head (mm)																						
Straight type Pitot tube	Total vertical pressure (nose facing neg Z)	X rule reading	Static water reading in sight tube	360	360	360	360	360	360	360	360	360	360	360	360	360	360	360	360	360	360	360	360	360
		Y rule reading		341	341	341	341	341	341	341	341	341	341	341	341	341	341	341	341	341	341	341	341	341
		Z rule reading		230.5	220.5	210.5	200.5	190.5	180.5	170.5	160.5	150.5	140.5	130.5	120.5	110.5	100.5	90.5	80.5	70.5	60.5	50.5	40.5	30.5
		Reading on sight tube (mm)		20.8	21	21.5	22	22.4	22.9	23.1	23.9	**24.9**	24.9	25.9	27.9	28.3	29.9	31.7	33.7	35.7	**37.5**	**38.7**	**39.0**	**39.1**
		Pressure head (mm)	17.9	**3**	**3.2**	**3.7**	**4.2**	**4.6**	**5.1**	**5.3**	**6.1**	**7.1**	**7.1**	**8.1**	**10.1**	**10.5**	**12.1**	**13.9**	**15.9**	**17.9**	**19.7**	**20.9**	**21.2**	**21.3**
Calculations																								
Total Mechanical Energy components	Elevation (Z) (mm)			200	190	180	170	160	150	140	130	120	110	100	90	80	70	60	50	40	30	20	10	0
	Pressure head (P/ρg) (mm)			2.7	3.0	3.1	3.9	4.2	4.9	5.7	6.3	7.1	8.1	9.0	9.3	10.6	12.1	13.1	15.1	17.4	20.5	22.1	23.6	21.2
	Velocity head - Horizontal component ($V^2/2g$) (mm)			0.3	0.3	0.6	0.2	0.5	0.2	0.1	-0.1	-0.1	-0.1	0.0	0.8	0.8	1.1	1.1	1.9	3.1	2.6	3.4	2.7	4.4
	Velocity head - Vertical component ($V^2/2g$) (mm)			0.3	0.2	0.6	0.3	0.4	0.2	-0.4	-0.2	0.0	-1.0	-0.9	0.8	-0.1	0.0	0.8	0.8	0.5	-0.8	-1.2	-2.4	0.1
	Velocity head - Vector ($V^2/2g$) (mm)			0.42	0.36	0.85	0.36	0.64	0.28	0.41	0.22	0.10	1.00	0.90	1.13	0.81	1.10	1.36	2.06	3.14	2.72	3.61	3.61	4.40
Energy - Horizontal component				3.0	3.3	3.7	4.1	4.7	5.1	5.8	6.4	7.2	8.2	9.0	10.1	11.4	13.2	14.2	17.0	20.5	23.1	25.5	26.3	25.6
Energy - Vertical component				3.0	3.2	3.7	4.2	4.6	5.1	6.1	6.5	7.1	9.1	9.9	10.1	10.7	12.1	13.9	15.9	17.9	21.3	23.3	26.0	21.3
Energy - Vector component				3.12	3.36	3.95	4.26	4.84	5.18	6.11	6.52	7.20	9.10	9.90	10.43	11.41	13.20	14.46	17.16	20.54	23.22	25.71	27.21	25.60
Velocity - Horizontal component (m/s)				**0.077**	**0.077**	**0.108**	**0.063**	**0.099**	**0.063**	**0.044**	**-0.044**	**-0.044**	**-0.044**	**0.000**	**0.125**	**0.125**	**0.147**	**0.147**	**0.193**	**0.247**	**0.226**	**0.258**	**0.230**	**0.294**
Velocity - Vertical component (m/s)				**0.077**	**0.063**	**0.108**	**0.077**	**0.089**	**0.063**	**-0.089**	**-0.063**	**0.000**	**-0.140**	**-0.133**	**0.125**	**-0.044**	**0.000**	**0.125**	**0.125**	**0.099**	**-0.125**	**-0.153**	**-0.217**	**0.044**
Velocity - Vector component (m/s)				**0.1084988**	**0.0990454**	**0.15344054**	**0.09904544**	**0.13288341**	**0.08858894**	**0.09904544**	**0.07672027**	**0.04429447**	**0.14690813**	**0.13288341**	**0.1771779**	**0.13288341**	**0.14690813**	**0.19307511**	**0.230**	**0.26576682**	**0.25827892**	**0.300**	**0.31632578**	**0.29713633**
Pressure head (mm)				**2.7**	**3.0**	**3.1**	**3.9**	**4.2**	**4.9**	**5.7**	**6.3**	**7.1**	**8.1**	**9.0**	**9.3**	**10.6**	**12.1**	**13.1**	**15.1**	**17.4**	**20.5**	**22.1**	**23.6**	**21.2**
Pressure (Pa)				**26.49**	**29.43**	**30.41**	**38.26**	**41.20**	**48.07**	**55.92**	**61.80**	**69.65**	**79.46**	**88.29**	**91.23**	**103.99**	**118.70**	**128.51**	**148.13**	**170.69**	**201.11**	**216.80**	**231.52**	**207.97**

Y=60 mm	**Ballotini bed height**	**300 mm**
	Water height	**443.8 mm**

Pitot tube nose location (with respect to centre of orifice/origin) (mm)																								
X				0	0	0	0	0	0	0	0	0	0	0	0	0	0	0	0	0	0	0	0	0
Y				-60	-60	-60	-60	-60	-60	-60	-60	-60	-60	-60	-60	-60	-60	-60	-60	-60	-60	-60	-60	-60
Z				200	190	180	170	160	150	140	130	120	110	100	90	80	70	60	50	40	30	20	10	0
Readings (mm)																								
L type Pitot tube	**Total horizontal pressure (nose facing pos Y)**	**X rule reading**	**Static water reading in sight tube**	360	360	360	360	360	360	360	360	360	360	360	360	360	360	360	360	360	360	360	360	360
		Y rule reading		442	442	442	442	442	442	442	442	442	442	442	442	442	442	442	442	442	442	442	442	442
		Z rule reading		256.0	246.0	236.0	226.0	216.0	206.0	196.0	186.0	176.0	166.0	156.0	146.0	136.0	126.0	116.0	106.0	96.0	86.0	76.0	66.0	56.0
		Reading on sight tube (mm)		20.2	20.9	21.1	21.7	22.0	22.5	23.0	23.3	24.0	24.8	25.3	26.0	27.0	28.2	29.1	30.2	31.8	32.8	34	34.4	34.8
		Pressure head (mm)	**17.9**	**2.3**	**3.0**	**3.2**	**3.8**	**4.1**	**4.6**	**5.1**	**5.4**	**6.1**	**6.9**	**7.4**	**8.1**	**9.1**	**10.3**	**11.2**	**12.3**	**13.9**	**14.9**	**16.1**	**16.5**	**16.9**
	Pressure (nose facing pos X)	**X rule reading**	**Static water reading in sight tube**	439.5	439.5	439.5	439.5	439.5	439.5	439.5	439.5	439.5	439.5	439.5	439.5	439.5	439.5	439.5	439.5	439.5	439.5	439.5	439.5	439.5
		Y rule reading		361.9	361.9	361.9	361.9	361.9	361.9	361.9	361.9	361.9	361.9	361.9	361.9	361.9	361.9	361.9	361.9	361.9	361.9	361.9	361.9	361.9
		Z rule reading		256.0	246.0	236.0	226.0	216.0	206.0	196.0	186.0	176.0	166.0	156.0	146.0	136.0	126.0	116.0	106.0	96.0	86.0	76.0	66.0	56.0
		Reading on sight tube (mm)		19.9	20.9	21.1	21.8	22.1	22.6	23	23.3	24	24.8	25.3	26	27	28.2	29.2	29.7	31.4	32	33.5	33.3	32.9
		Pressure head (mm)	**17.9**	**2.0**	**3.0**	**3.2**	**3.9**	**4.2**	**4.7**	**5.1**	**5.4**	**6.1**	**6.9**	**7.4**	**8.1**	**9.1**	**10.3**	**11.3**	**11.8**	**13.5**	**14.1**	**15.6**	**15.4**	**15.0**
	Pressure (nose facing neg X)	**X rule reading**	**Static water reading in sight tube**	278.5	278.5	278.5	278.5	278.5	278.5	278.5	278.5	278.5	278.5	278.5	278.5	278.5	278.5	278.5	278.5	278.5	278.5	278.5	278.5	278.5
		Y rule reading		341.9	341.9	341.9	341.9	341.9	341.9	341.9	341.9	341.9	341.9	341.9	341.9	341.9	341.9	341.9	341.9	341.9	341.9	341.9	341.9	341.9
		Z rule reading		256.0	246.0	236.0	226.0	216.0	206.0	196.0	186.0	176.0	166.0	156.0	146.0	136.0	126.0	116.0	106.0	96.0	86.0	76.0	66.0	56.0
		Reading on sight tube (mm)												READINGS NOT TAKEN										
		Pressure head (mm)																						
Straight type Pitot tube	**Total vertical pressure (nose facing neg Z)**	**X rule reading**	**Static water reading in sight tube**	360	360	360	360	360	360	360	360	360	360	360	360	360	360	360	360	360	360	360	360	360
		Y rule reading		361	361	361	361	361	361	361	361	361	361	361	361	361	361	361	361	361	361	361	361	361
		Z rule reading		230.5	220.5	210.5	200.5	190.5	180.5	170.5	160.5	150.5	140.5	130.5	120.5	110.5	100.5	90.5	80.5	70.5	60.5	50.5	40.5	30.5
		Reading on sight tube (mm)		20	20.9	21.1	21.7	21.9	22.6	23	23.1	24	24.8	25.3	26	27	28	29	30	31.2	32.9	33.1	33.2	33.5
		Pressure head (mm)	**17.9**	**2.1**	**3**	**3.2**	**3.8**	**4**	**4.7**	**5.1**	**5.2**	**6.1**	**6.9**	**7.4**	**8.1**	**9.1**	**10.1**	**11.1**	**12.1**	**13.3**	**15**	**15.2**	**15.3**	**15.6**
Calculations																								
Total Mechanical Energy components	**Elevation (Z) (mm)**			200	190	180	170	160	150	140	130	120	110	100	90	80	70	60	50	40	30	20	10	0
	Pressure head ($P/\rho g$) (mm)			2.0	3.0	3.2	3.9	4.2	4.7	5.1	5.4	6.1	6.9	7.4	8.1	9.1	10.3	11.3	11.8	13.5	14.1	15.6	15.4	15.0
	Velocity head - Horizontal component ($V^2/2g$) (mm)			0.3	0.0	0.0	-0.1	-0.1	-0.1	0.0	0.0	0.0	0.0	0.0	0.0	0.0	0.0	-0.1	0.5	0.4	0.8	0.5	1.1	1.9
	Velocity head - Vertical component ($V^2/2g$) (mm)			0.1	0.0	0.0	-0.1	-0.2	0.0	0.0	-0.2	0.0	0.0	0.0	0.0	0.0	-0.2	-0.2	0.3	-0.2	0.9	-0.4	-0.1	0.6
	Velocity head - Vector ($V^2/2g$) (mm)			0.32	0.00	0.00	0.14	0.22	0.10	0.00	0.20	0.00	0.00	0.00	0.00	0.00	0.20	0.22	0.58	0.45	1.20	0.64	1.10	1.99
Energy - Horizontal component				2.3	3.0	3.2	4.0	4.3	4.8	5.1	5.4	6.1	6.9	7.4	8.1	9.1	10.3	11.4	12.3	13.9	14.9	16.1	16.5	16.9
Energy - Vertical component				2.1	3.0	3.2	4.0	4.4	4.7	5.1	5.6	6.1	6.9	7.4	8.1	9.1	10.5	11.5	12.1	13.7	15.0	16.0	15.5	15.6
Energy - Vector component				2.32	3.00	3.20	4.04	4.42	4.80	5.10	5.60	6.10	6.90	7.40	8.10	9.10	10.50	11.52	12.38	13.95	15.30	16.24	16.50	16.99
Velocity - Horizontal component (m/s)				**0.077**	**0.000**	**0.000**	**-0.044**	**-0.044**	**-0.044**	**0.000**	**0.000**	**0.000**	**0.000**	**0.000**	**0.000**	**0.000**	**0.000**	**-0.044**	**0.099**	**0.089**	**0.125**	**0.099**	**0.147**	**0.193**
Velocity - Vertical component (m/s)				**0.044**	**0.000**	**0.000**	**-0.044**	**-0.063**	**0.000**	**0.000**	**-0.063**	**0.000**	**0.000**	**0.000**	**0.000**	**0.000**	**-0.063**	**-0.063**	**0.077**	**-0.063**	**0.133**	**-0.089**	**-0.044**	**0.108**
Velocity - Vector component (m/s)				**0.089**	**0.000**	**0.000**	**0.063**	**0.077**	**0.044**	**0.000**	**0.063**	**0.000**	**0.000**	**0.000**	**0.000**	**0.000**	**0.063**	**0.077**	**0.125**	**0.108**	**0.183**	**0.133**	**0.153**	**0.221**
Pressure head (mm)				**2.0**	**3.0**	**3.2**	**3.9**	**4.2**	**4.7**	**5.1**	**5.4**	**6.1**	**6.9**	**7.4**	**8.1**	**9.1**	**10.3**	**11.3**	**11.8**	**13.5**	**14.1**	**15.6**	**15.4**	**15.0**
Pressure (Pa)				**19.62**	**29.43**	**31.39**	**38.26**	**41.20**	**46.11**	**50.03**	**52.97**	**59.84**	**67.69**	**72.59**	**79.46**	**89.27**	**101.04**	**110.85**	**115.76**	**132.44**	**138.32**	**153.04**	**151.07**	**147.15**

2. Continued velocity graphs

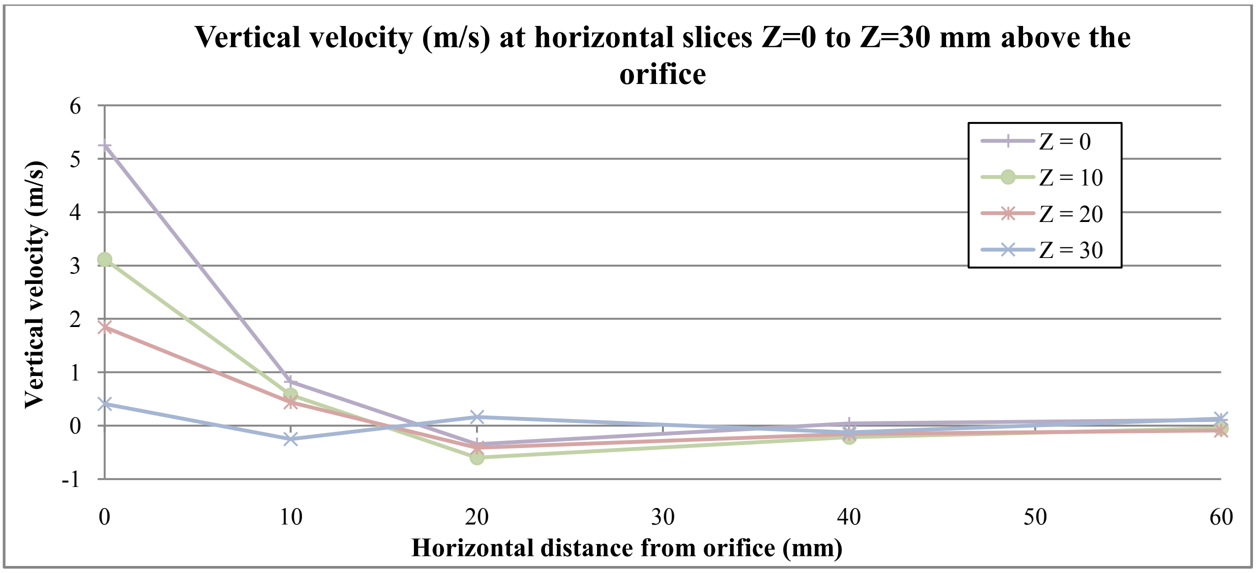

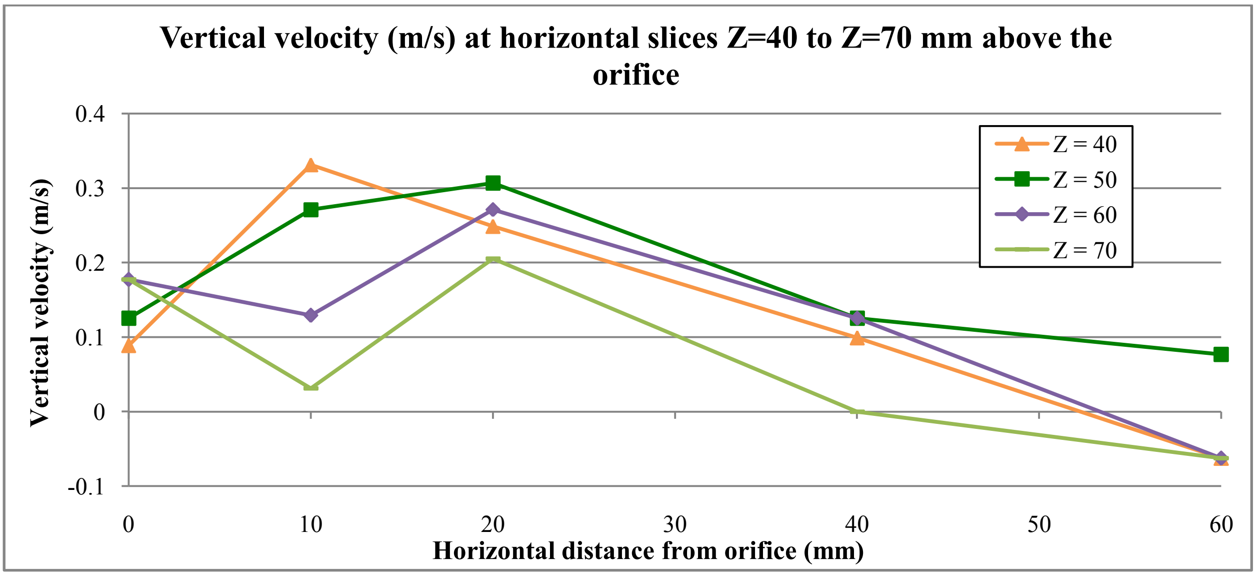

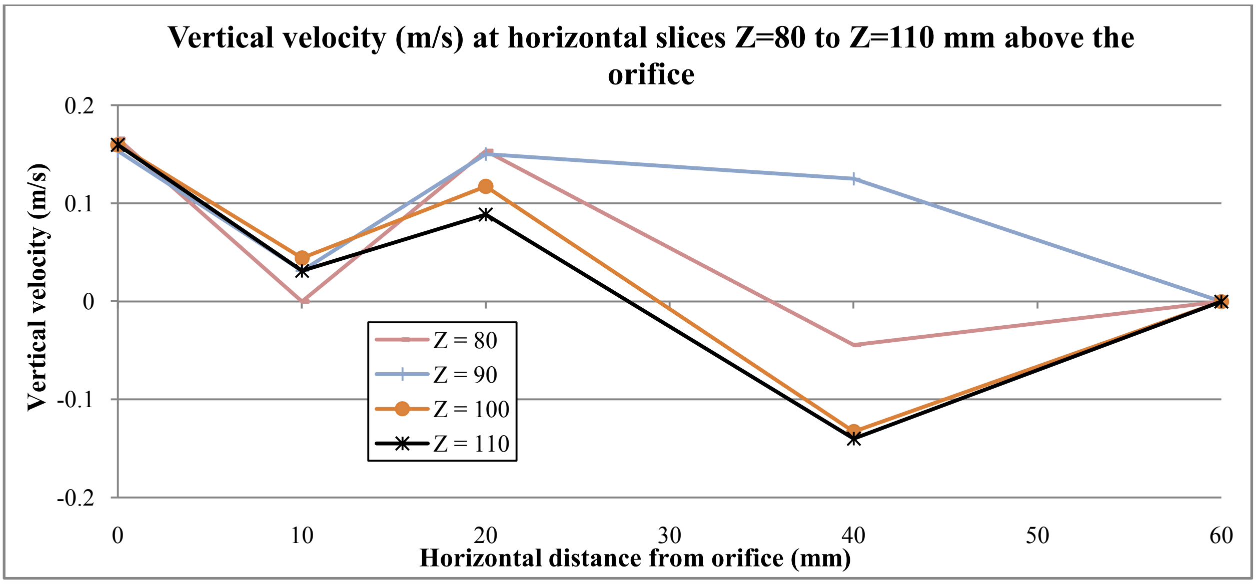
Vertical velocity (m/s) at horizontal slices Z=80 to Z=110 mm above the orifice
Vertical velocity (m/s)
0.2
0.1
0
-0.1
-0.2
0
10
20
30
40
50
60
Horizontal distance from orifice (mm)
Z = 80
Z = 90
Z = 100
Z = 110

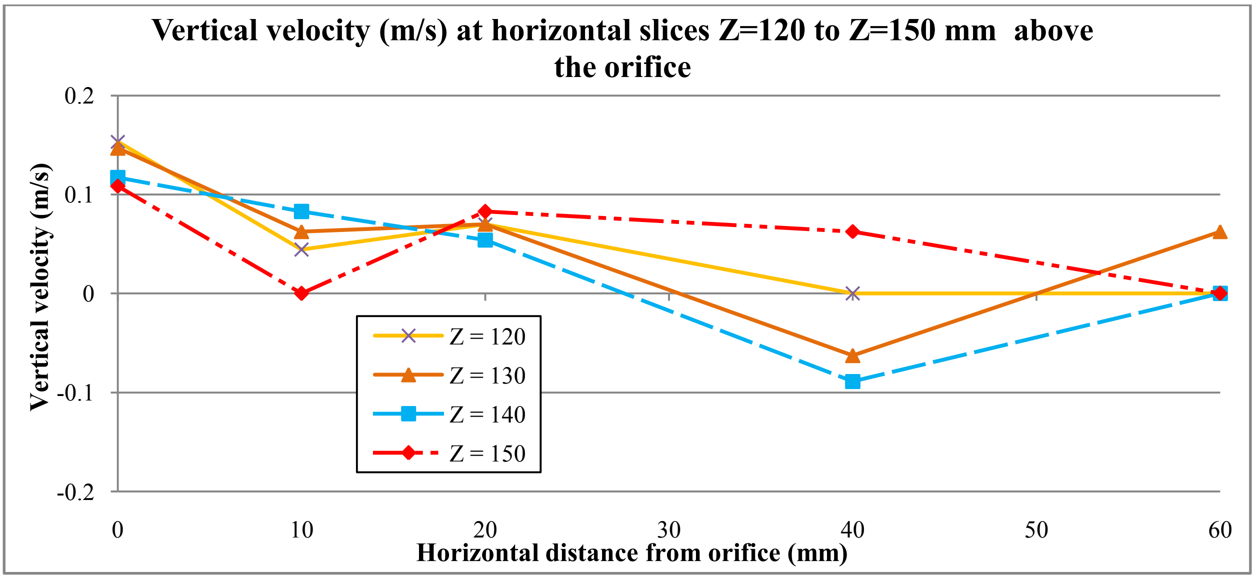
Vertical velocity (m/s) at horizontal slices Z=120 to Z=150 mm above the orifice
Vertical velocity (m/s)
0.2
0.1
0
-0.1
-0.2
0
10
20
30
40
50
60
Horizontal distance from orifice (mm)
Z = 120
Z = 130
Z = 140
Z = 150

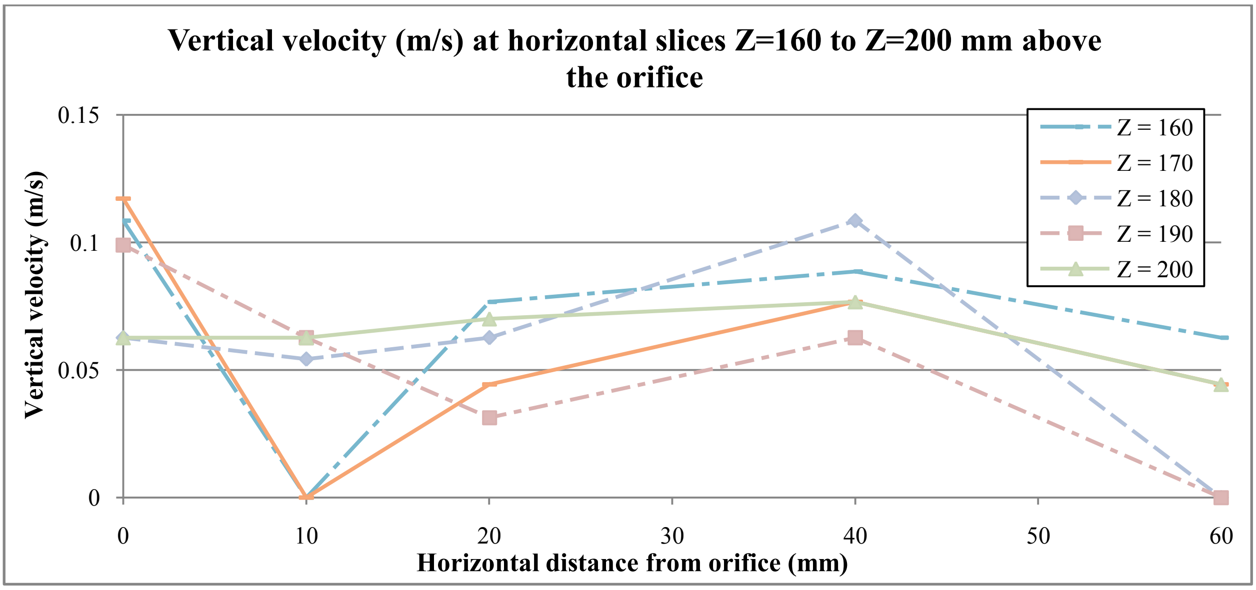
Vertical velocity (m/s) at horizontal slices Z=160 to Z=200 mm above the orifice
Vertical velocity (m/s)
0.15
0.1
0.05
0
0
10
20
30
40
50
60
Horizontal distance from orifice (mm)
Z = 160
Z = 170
Z = 180
Z = 190
Z = 200

3. Continued pressure graphs

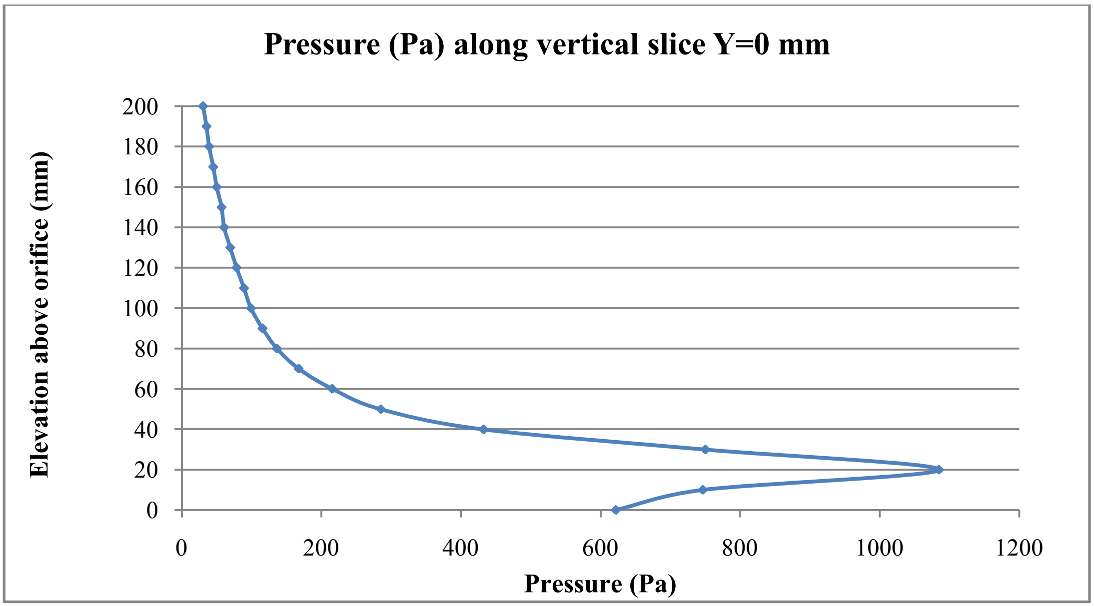

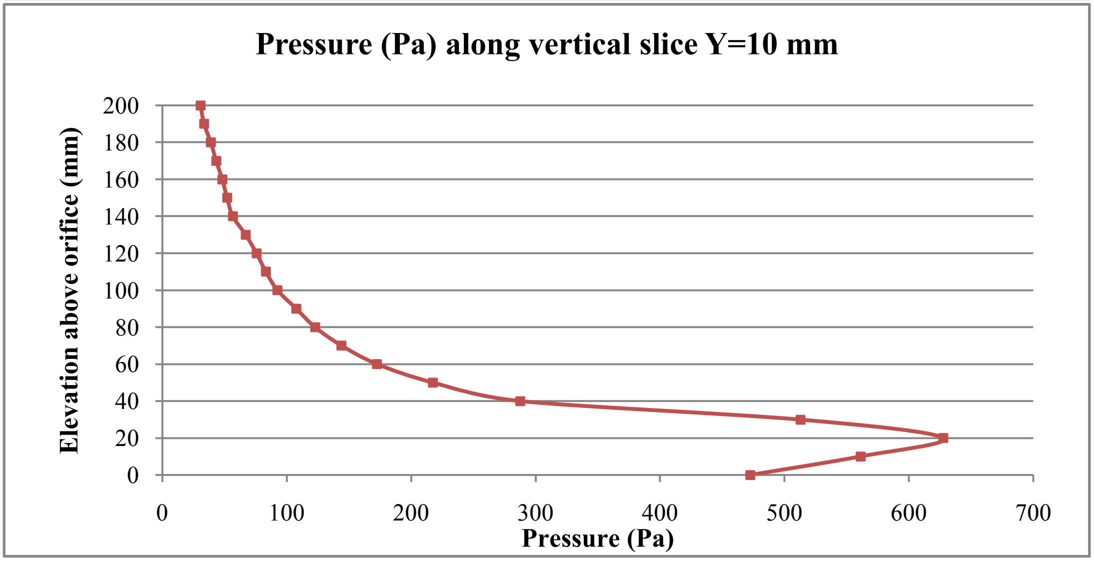

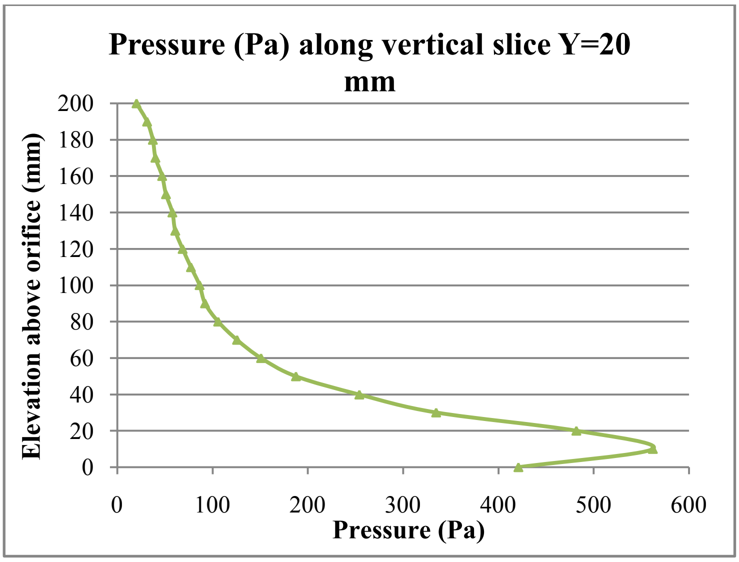
Pressure (Pa) along vertical slice Y=20 mm
Elevation above orifice (mm)
200
180
160
140
120
100
80
60
40
20
0
0
100
200
300
400
500
600
Pressure (Pa)

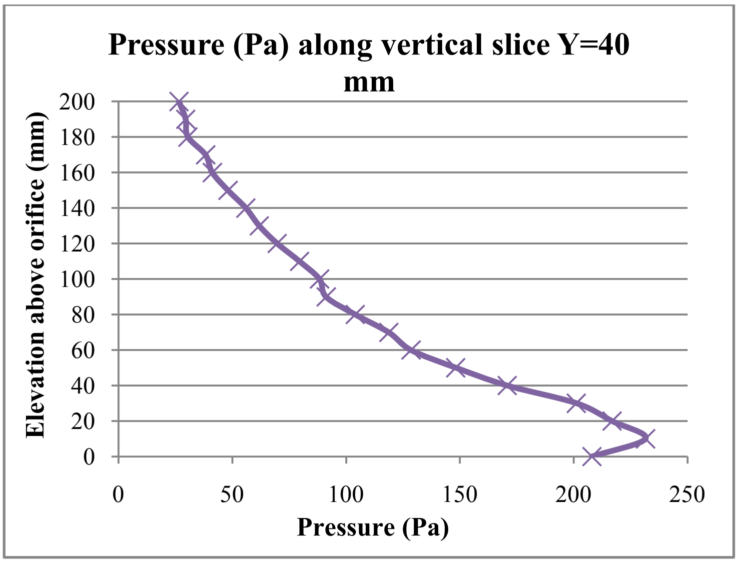
Pressure (Pa) along vertical slice Y=40 mm
Elevation above orifice (mm)
200
180
160
140
120
100
80
60
40
20
0
0
50
100
150
200
250
Pressure (Pa)

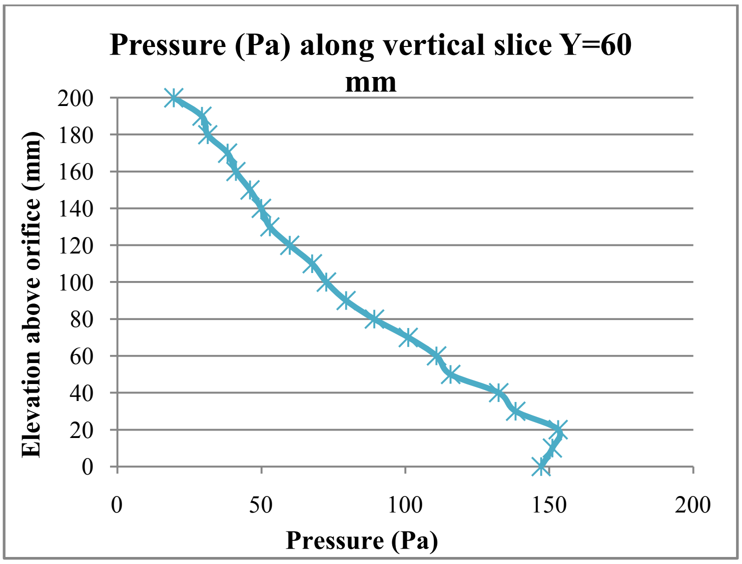
Pressure (Pa) along vertical slice Y=60 mm
Elevation above orifice (mm)
200
180
160
140
120
100
80
60
40
20
0
0
50
100
150
200
Pressure (Pa)

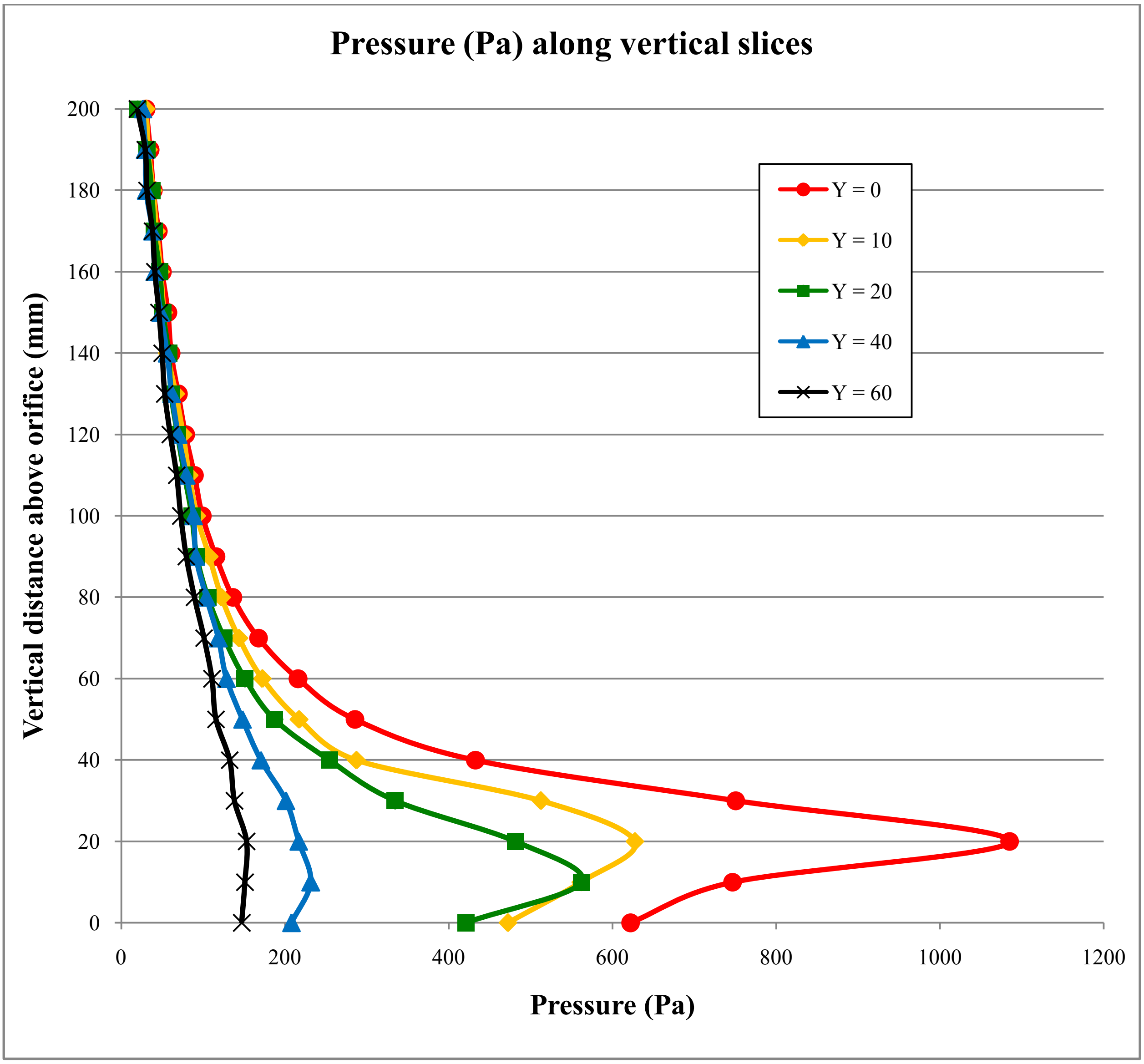
Pressure (Pa) along vertical slices
Vertical distance above orifice (mm)
200
180
160
140
120
100
80
60
40
20
0
0
200
400
600
800
1000
1200
Pressure (Pa)
Y = 0
Y = 10
Y = 20
Y = 40
Y = 60

4. Continued energy graphs

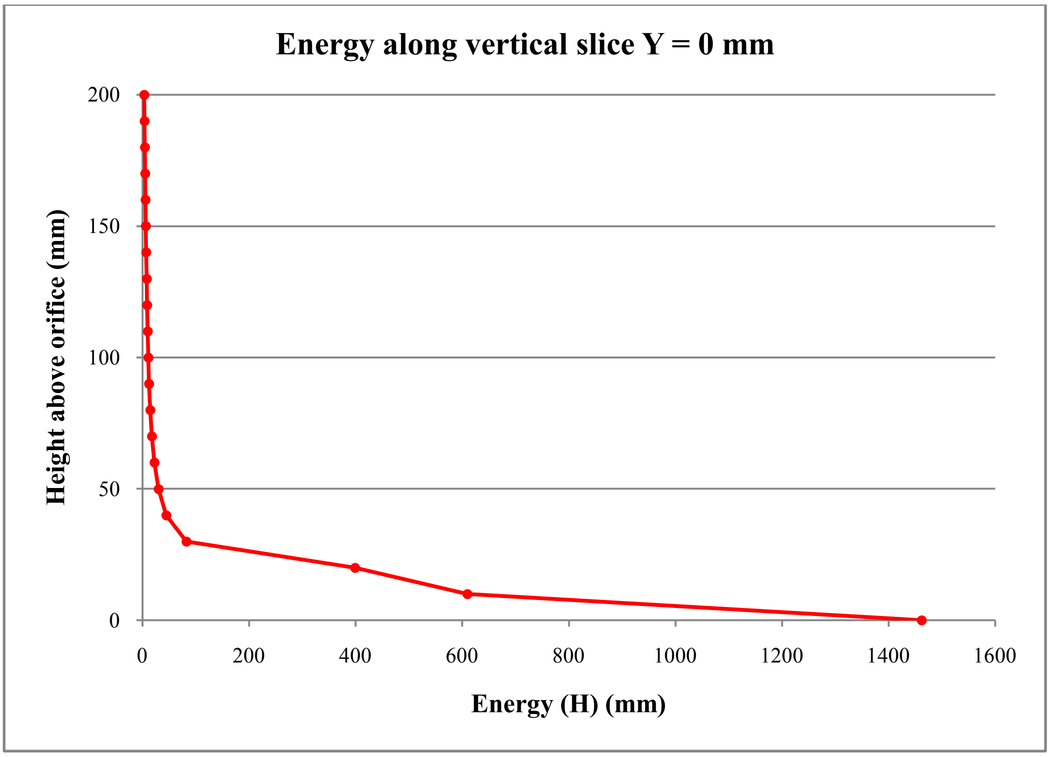

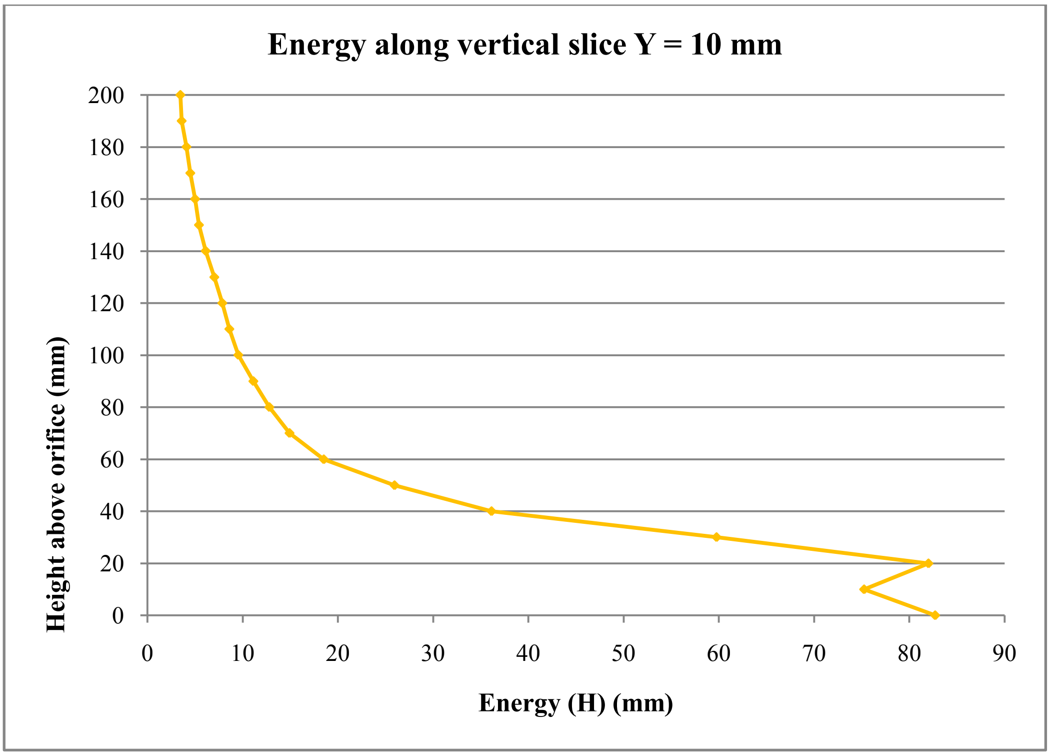

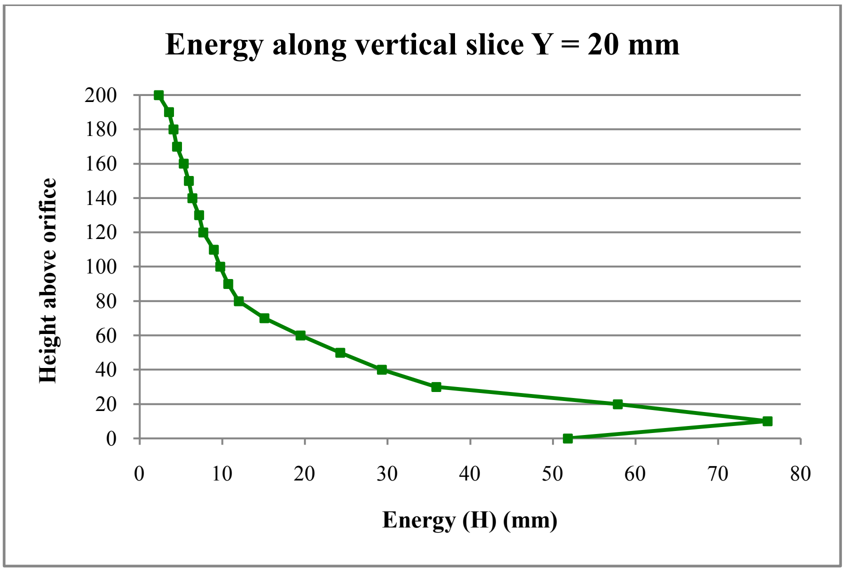
Energy along vertical slice Y = 20 mm
Height above orifice
200
180
160
140
120
100
80
60
40
20
0
0
10
20
30
40
50
60
70
80
Energy (H) (mm)

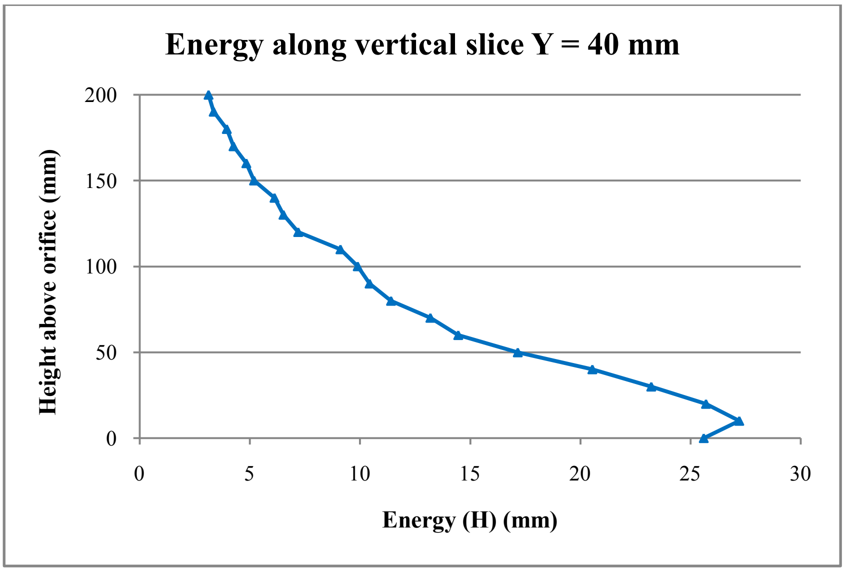
Energy along vertical slice Y = 40 mm
Height above orifice (mm)
200
150
100
50
0
0
5
10
15
20
25
30
Energy (H) (mm)

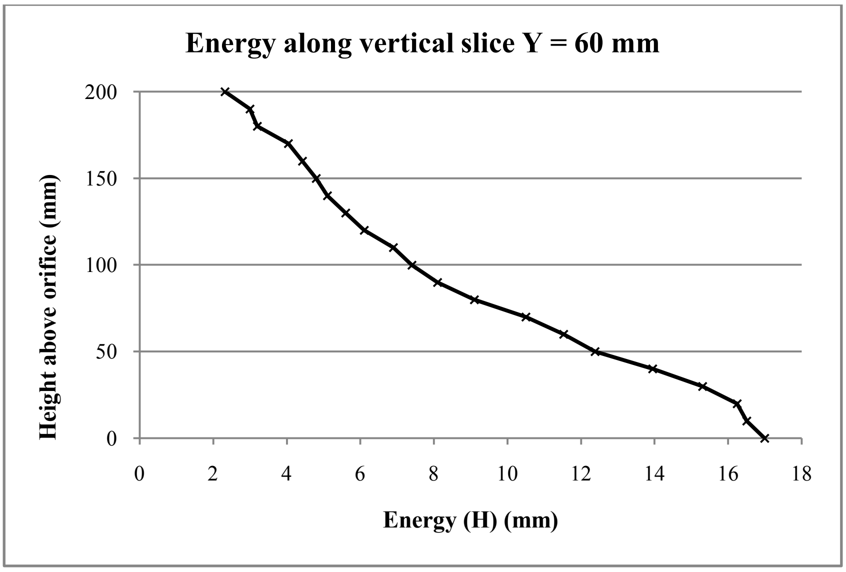
Energy along vertical slice Y = 60 mm
Height above orifice (mm)
200
150
100
50
0
0
2
4
6
8
10
12
14
16
18
Energy (H) (mm)

6. Repeatability data

Repeatability test																						
Pitot type		**L type**											**Straight type**									
Pitot nose direction		**Possitive Y**		**Possitive X**	**Negative X**	**Possitive Y**		**Possitive X**		**Possitive Y**		**Possitive X**	**Negative Z**									
Random readings		**1**	**2**	**3**	**4**	**5**	**6**	**7**	**8**	**9**	**10**	**11**	**12**	**13**	**14**	**15**	**16**	**17**	**18**	**19**	**20**	
Pitot nose possition	**X**	0	0	0	0	0	0	0	0	0	0	0	0	0	0	0	0	0	0	0	0	
	Y	-10	-10	-10	-10	-20	-20	-40	-40	0	0	-60	0	0	0	0	0	-10	-20	-40	-60	
	Z	150	60	40	130	170	30	100	40	70	30	20	190	160	140	20	30	80	10	160	90	
Ruler readings	**X rule reading**	360	360	439.5	278.5	360	360	439.5	439.5	360	360	439.5	360	360	360	360	360	360	360	360	360	
	Y rule reading	392	392	311.9	311.9	402	402	341.9	341.9	374.5	374.5	361.9	301	301	301	301	301	311	321	341	361	
	Z rule reading	206.0	116.0	96.0	186.0	226.0	86.0	156.0	96.0	126.0	86.0	76.0	220.5	190.5	170.5	50.5	60.5	110.5	40.5	190.5	120.5	
Previous readings	**Static reading**	17.9	17.9	17.9	17.9	17.9	17.9	17.9	17.9	17.9	17.9	17.9	17.9	17.9	17.9	17.9	17.9	17.9	17.9	17.9	17.9	
	Reading on sight tube	23.1	35.0	47.3	24.7	22.4	54.7	26.9	35.3	35	94.4	33.5	21.5	23	24.1	416.3	97.0	30.2	56.2	22.4	26.0	
	Pressure head	**5.2**	**17.1**	**29.4**	**6.8**	**4.5**	**36.8**	**9.0**	**17.4**	**17.1**	**76.5**	**15.6**	**3.6**	**5.1**	**6.2**	**398.4**	**79.1**	**12.3**	**38.3**	**4.5**	**8.1**	
Repeated readings	**Static reading**	17.9	17.9	17.9	17.9	17.9	17.9	17.9	17.9	17.7	17.7	17.9	17.3	17.3	17.3	17.9	17.9	17.9	17.9	17.9	17.9	
	Reading on sight tube	22.9	34.0	47.4	25.0	22.5	55.2	26.0	34.2	35	89	34.3	21	22.4	23.8	398.5	98.9	31	54.8	22.2	26.0	
	Pressure head	**5.0**	**16.1**	**29.5**	**7.1**	**4.6**	**37.3**	**8.1**	**16.3**	**17.3**	**71.3**	**16.4**	**3.7**	**5.1**	**6.5**	**380.6**	**81.0**	**13.1**	**36.9**	**4.3**	**8.1**	
Difference in pressure readings		**0.2**	**1.0**	**0.1**	**0.3**	**0.1**	**0.5**	**0.9**	**1.1**	**0.2**	**5.2**	**0.8**	**0.1**	**0.0**	**0.3**	**17.8**	**1.9**	**0.8**	**1.4**	**0.2**	**0.0**	
Percentage difference		**3.8**	**5.8**	**0.3**	**4.4**	**2.2**	**1.4**	**10.0**	**6.3**	**1.2**	**6.8**	**5.1**	**2.8**	**0.0**	**4.8**	**4.5**	**2.4**	**6.5**	**3.7**	**4.4**	**0.0**	
Averages	Previous readings	21.4											61.7									41.6
	Repeated readings	20.8											59.9									40.4
	Difference in pressure readings	0.9											2.5									1.7
	Percentage difference	4.3											3.2									3.8